Politechnika Śląska

Wydział Inżynierii Środowiska i Energetyki

Katedra Inżynierii Wody i Ścieków

Rozprawa Doktorska

Dekoloryzacja roztworów wodnych barwników z wykorzystaniem metod utleniania chemicznego

mgr inż. Sylwester Łoński

PROMOTOR

prof. dr hab. inż. Krzysztof Barbusiński

PROMOTOR POMOCNICZY

dr inż. Maciej Thomas

GLIWICE 2024

Artykuły 1; 2 oraz 4 Prace badawcze związane z badaniem aktywności katalitycznej nanocząstek magnetytu prowadzone były w ramach projektu Diamentowy Grant VII pt. „Wpływ morfologii nanocząstek magnetytu na proces ich izotermicznego wzrostu, właściwości elektryczne oraz aktywność fotokatalityczną”, nr projektu 0220/DIA/2018/470 (kierownik projektu: dr inż. Adrian Radoń; grant realizowany od 07.09.2018 r. do 06.09.2022 r.)

Badania przedstawione w artykule 3 zostały sfinansowane z dotacji statutowej Wydziału Mechaniczno-Technologicznego Politechniki Śląskiej, nr 10.010/BKM22/1114. Publikacja była także wspierana w ramach projakościowej dotacji Rektora Politechniki Śląskiej, nr 08/040/RGJ22/0164.

Podziękowania

Składam serdeczne podziękowanie mojemu Promotorowi,

Prof. dr hab. inż. Krzysztofowi Barbusińskiemu

oraz Promotorowi pomocniczemu

Dr. inż. Maciejowi Thomasowi

za pomoc merytoryczną oraz cierpliwość.

Dziękuję Rodzinie i Znajomym za słowa wsparcia.

„Co my wiemy, to tylko kropelka. Czego nie wiemy, to cały ocean.”
– Isaac Newton

Spis treści

1. Przedmowa

Podstawę niniejszej rozprawy doktorskiej stanowi spójny tematycznie cykl pięciu oryginalnych publikacji naukowych. Przy odwoływaniu się do tych prac w tekście zastosowano oznaczenie **A(x)** gdzie x jest cyfrą rzymską określającą numer artykułu. Pełne testy publikacji zamieszczono na końcu pracy.

Rezultaty zawarte w publikacji **A(I)** stanowią wstępne dane, które zostały opublikowane przed rozpoczęciem doktoratu. Wyniki te są jednak kluczowe dla przedstawienia pełnego przebiegu pracy badawczej, ukazując podstawę i kontekst dla dalszych badań.

A(I)

Adrian Radoń, **Sylwester Łoński**, Tymon Warski, Rafał Babilas, Tomasz Tański, Mariusz Dudziak, Dariusz Łukowiec; Catalytic activity of non-spherical shaped magnetite nanoparticles in degradation of Sudan I, Rhodamine B and Methylene Blue dyes; Applied Surface Science, Volume 487, 1, September 2019, Pages 1018-1025

Doi: 10.1016/j.apsusc.2019.05.091 Impact Factor: **6,3** Punkty MNiSW: 140

A(II)

Adrian Radoń, **Sylwester Łoński**, Mariola Kądziołka-Gaweł, Piotr Gębara, Mateusz Lis, Dariusz Łukowiec, Rafał Babilas; Influence of magnetite nanoparticles surface dissolution, stabilization and functionalization by malonic acid on the catalytic activity, magnetic and electrical properties; Colloids and Surfaces A: Physicochemical and Engineering Aspects, Volume 607, 20, December 2020, 125446

Doi: 10.1016/j.colsurfa.2020.125446 Impact Factor: **4,9** Punkty MNiSW: 70

A(III)

Wojciech Łoński, Monika Spilka, Mariola Kądziołka-Gaweł, Piotr Gębara, Adrian Radoń, Tymon Warski, **Sylwester Łoński**, Krzysztof Barbusiński, Katarzyna Młynarek-Żak, Rafał Babilas; Microstructure, magnetic properties, corrosion resistance and catalytic activity of dual-phase AlCoNiFeTi and AlCoNiFeTiSi high entropy alloys; Journal of Alloys and Compounds, Volume 934, 10, February 2023, 167827

Doi: 10.1016/j.jallcom.2022.167827 Impact Factor: **5,8** Punkty MNiSW: 100

A(IV)

Sylwester Łoński, Dariusz Łukowiec, Krzysztof Barbusiński, Rafał Babilas, Bartosz Szeląg, Adrian Radoń; Flower-like magnetite nanoparticles with unfunctionalized surface as an efficient catalyst in photo-Fenton degradation of chemical dyes; Applied Surface Science Volume 638, 30, November 2023, 158127

Doi: 10.1016/j.apsusc.2023.158127 Impact Factor: **6,3** Punkty MNiSW: 140

A(V)

Sylwester Łoński, Wojciech Łoński, Rafał Babilas, Krzysztof Barbusiński; Photocatalytic Decolourization of Rhodamine B by Modified Photo-Fenton Process with Quasicrystals – Preliminary Research; Architecture, Civil Engineering, Environment, Volume 16 (2023): ISSUE 2 (JUNE 2023)

Doi: 10.2478/acee-2023-0026 Impact Factor: **0,5** Punkty MNiSW: 70

Każdy z artykułów skupiał się na specyficznych aspektach badawczych związanych z procesami dekoloryzacji roztworów barwnych przy użyciu różnych materiałów wykorzystanych jako katalizatory w reakcji Fentona wspomaganej światłem UV, nazywanej również reakcją Foto-Fenton.

W artykułach I-II; IV badano wpływ nanocząstek na procesy dekoloryzacji. Moja rola w tych publikacjach była kluczowa i obejmowała kilka istotnych etapów badawczych. Przede wszystkim, zajmowałem się zaprojektowaniem eksperymentów umożliwiający monitorowanie oraz sterowanie parametrami procesu dekoloryzacji, co wymagało szczegółowego opracowania planów badawczych oraz metodologii. W ramach tych eksperymentów analizowałem różne parametry, jak koncentracja nanocząstek, pH roztworu reakcyjnego oraz przebieg reakcji w czasie, aby dokładnie określić ich wpływ na efektywność procesu dekoloryzacji.

Po zaplanowaniu eksperymentów, przeprowadziłem je osobiście, dbając o precyzję i dokładność każdego eksperymentu. Badania te były kompleksowe i obejmowały zarówno pomiary spektrofotometryczne, jak i analizy chemiczne, co pozwalało na dokładne śledzenie przebiegu procesu oraz na zapis ewentualnych spostrzeżeń. Zakończywszy eksperymenty, zająłem się szczegółowym opisem uzyskanych wyników. Interpretacja wyników była kluczowa, aby zrozumieć mechanizmy zachodzące podczas procesu dekoloryzacji i wyciągnąć odpowiednie wnioski.

Dodatkowo, w ramach tych artykułów, dokonałem obszernego przeglądu literatury. Analizowałem istniejące w literaturze naukowej wyniki badań dotyczące wykorzystania nanocząstek w procesach dekoloryzacji, co pozwoliło na porównanie uzyskanych wyników z danymi literaturowymi oraz ocenę skuteczności i potencjalnych zastosowań badanych materiałów. Dzięki temu, mogłem sformułować wnioski, które nie tylko podsumowywały wyniki moich badań, ale również sugerowały możliwe kierunki dalszych prac.

Artykuły III i V również koncentrowały się na badaniach dekoloryzacji. Badania te jak w pozostałym artykułach dotyczyły katalizy reakcji Foto-Fentona jednak z wykorzystaniem innych materiałów katalitycznych. W artykule III badałem stopy wysokiej entropii, podczas gdy w artykule V kwazikryształy. Podobnie jak w przypadku wcześniejszych artykułów, moja rola obejmowała planowanie i prowadzenie eksperymentów, a następnie interpretację uzyskanych wyników.

W artykule III, zajmowałem się badaniami nad wpływem stopów wysokiej entropii na proces dekoloryzacji. Projektowałem eksperymenty w taki sposób, aby dokładnie zbadać, jak różne składniki stopów wpływają na szybkość i efektywność dekoloryzacji. Przeprowadzałem eksperymenty, monitorując zmiany w barwie roztworu i analizowałem wyniki związane z dekoloryzacją roztworu.

W artykule V, skupiłem się na kwazikryształach jako katalizatorach. Również tutaj byłem odpowiedzialny za zaprojektowanie eksperymentów, ich realizację oraz interpretację wyników. Analizowałem, jak kwazikryształy wpływają na proces dekoloryzacji, badając różne parametry eksperymentalne i oceniając efektywność katalizatorów.

Uzyskane wyniki zostały również przedstawione na konferencjach krajowych oraz międzynarodowych **Bioreaktory w walce o czyste powietrze** Katowice, Lipiec 27, 2021**; 12th International Conference on Materials Science and Engineering** Bramat 2022; **Nowe Trendy w Badaniach Naukowych - Wystąpienie Młodego Naukowca Edycja III**; **Mikrozanieczyszczenia w Środowisku Człowieka** Częstochowa 09.2022.

Podsumowując, moja praca badawcza, której wyniki zostały opublikowane w prezentowanych pięciu artykułach była wszechstronna i obejmowała zaprojektowanie oraz prowadzenie eksperymentów, opis oraz interpretację wyników i wnioski, a także przegląd literatury.

2. Streszczenie

W rozprawie doktorskiej poruszono problem dekoloryzacji roztworów wodnych barwników, skupiając się na wykorzystaniu metod utleniania chemicznego jako potencjalnego rozwiązania. Obecnie stosowane metody usuwania barwników, takie jak adsorpcja, biodegradacja czy flokulacja, mają swoje ograniczenia, dlatego istnieje potrzeba poszukiwania skuteczniejszych technik. W ramach pracy przeanalizowano różne techniki usuwania barwników, takie jak adsorpcja i biosorpcja, procesy biologiczne, flokulacja i koagulacja, procesy pogłębionego utleniania, wymiana jonowa, irradiacja, techniki membranowe oraz ozonowanie, oraz ich zalety i wady, zwracając uwagę na rosnącą tendencję zastępowania sztucznych barwników przez te pochodzenia naturalnego.

Głównym celem pracy było zbadanie potencjału procesów zaawansowanego utleniania w dekoloryzacji wodnych roztworów barwnych. Badania były skoncentrowane na zastosowaniu alternatywnych źródeł jonów żelaza oraz nadtlenku wodoru. Oraz monitorowaniu wpływu tych modyfikacji reakcji Foto-Fentona. Nowością badań było zastosowanie nowatorskich materiałów, jako źródeł jonów żelaza (katalizatorów) w reakcji Fentona, takich jak: **nanocząstki ferrytu, stopy o wysokiej entropii, kwazikryształy i taśmy amorficzne**. W ramach badań przy zastosowaniu modyfikacji reakcji Foto-Fentona, analizowano wpływ różnych parametrów, takich jak: pH, rodzaj utleniacza (H_2O_2 i nadwęglan sodu) oraz dawki reagentów na efektywność odbarwiania.

Wyniki eksperymentów wykazały, że nowe materiały mogą skutecznie katalizować reakcję Fentona, jako alternatywne źródło jonów żelaza, wykorzystaną do dekoloryzacji roztworów wodnych barwników. Wykazano także, że zastosowanie nadwęglanu sodu jako utleniacza w reakcji Foto-Fentona, może stanowić obiecującą alternatywę dla zastosowania nadtlenku wodoru. Główne wnioski wynikające z przeprowadzonych badań wskazują, że procesy zaawansowanego utleniania, w szczególności reakcja Fentona, wspierane nowymi materiałami katalizującymi, mogą efektywnie degradować barwniki w ściekach przemysłowych, przyczyniając się do ochrony środowiska. Dodatkowo zastąpienie nadtlenku wodoru nadwęglanem sodu może być korzystną alternatywą dla stosowania reakcji Fentona. Wyniki badań uzyskane w ramach przedstawionej dysertacji stanowią istotny wkład w poszukiwanie innowacyjnych rozwiązań w dziedzinie oczyszczania ścieków przemysłowych zawierających barwniki, zapewniając podstawy do dalszych ciekawych badań i rozwoju tej tematyki.

3. Wprowadzenie

Problemy z zanieczyszczeniem wód związkami barwnymi pojawiły się, jak tylko człowiek zaczął barwić tkaniny około roku 30000 p.n.e. na terenach dzisiejszej Gruzji [1,2]; już wówczas stosowano barwniki pochodzenia roślinnego. Badania archeologiczne wykazały obecność wielu barwników w różnych kolorach (czarny, szary, turkusowy i różowy). Jak wskazują źródła literaturowe, od najwcześniejszych form barwienia do połowy XIX w. stosowano głównie naturalne barwniki roślinne oraz niektóre minerały. Z czasem zaczęto również stosować syntetyczne barwniki chemiczne. Zgodnie ze źródłami literaturowymi, mogło to jednak nastąpić dopiero po roku 1856, kiedy to William Henry Perkin przeprowadził syntezę pierwszego sztucznego barwnika Mauve [3], znanego jako fiolet malwinowy.

Z biegiem czasu sztuczne barwniki chemiczne zdobyły coraz większą popularność w przemyśle tekstylnym. Od pierwszej syntezy barwnika w 1856 roku do 1924 roku zsyntezowano ponad 1200 innych barwników syntetycznych [4]. Wyraźnie demonstruje to jak bardzo potrzebne były sztuczne barwniki, szczególnie z uwagi na ich dużą trwałość i różnorodność kolorystyczną [2]. W rezultacie stały się one integralną częścią produkcji tkanin. Obecnie dominują na rynku ze względu na łatwość produkcji i niższe koszty w porównaniu do naturalnych barwników roślinnych [5,6]. Generują również problemy związane z ich rozkładem i mogą prowadzić do zanieczyszczenia środowiska [7,8]. Trudności w ich rozkładzie wynikają z faktu, że nawet w bardzo niskich stężeniach znacząco zabarwiają wodę i charakteryzują się wysoką odpornością na degradację [9,10].

Obie te cechy są pożądane podczas stosowania ich w zamierzonym celu, czyli podczas barwienia tekstyliów, jednak po dostaniu się ich do rzek i jezior wraz ze ściekami mogą powodować poważne zanieczyszczenie środowiska wodnego [9–12]. Co więcej, skażenie wody tymi substancjami ma konsekwencje nie tylko dla środowiska, lecz także powoduje dyskwalifikację jej z wykorzystania w innych sektorach przemysłu oraz jako źródło wody dla ludności. Należy podjąć pilne działania w celu oczyszczenia tych zanieczyszczonych wód. Zadanie to nie jest jednak łatwe, ponieważ większość sposobów oczyszczania ścieków jest przygotowywana do rozkładu zanieczyszczeń w stężeniach znacznie większych niż stężenia barwników, które wywołują istotną zmianę barwy. By lepiej zobrazować ten problem, można przytoczyć Rozporządzenie Ministra Gospodarki Morskiej i Żeglugi Śródlądowej z dnia 12 lipca 2019 r., w którym zawarto informację, że zawartość ogólnego węgla organicznego (OWO) w ściekach nie może przekraczać 30 mg/dm^3, a stosowane stężenia barwników w literaturze opisującej wyniki badań ścieków barwnych są zazwyczaj znacznie niższe [10,13]. Barwniki zwykle są obecne w ściekach barwierskich w stężeniu 10-50 mg/dm^3 [14].

Co więcej, barwniki nawet przy tak niewielkim stężeniu mogą być rakotwórcze [6]. Przykłady barwników i wywoływane przez nie problemy chorobotwórcze: Green 1: rak wątroby (zwierzęta); Orange 1 i Orange 2: uszkodzenie narządów wewnętrznych (zwierzęta); Red 1: rak wątroby (zwierzęta); Red 2: możliwy kancerogen; Red 4: wysokie dawki uszkodziły nadnercza u psów; Red 32: uszkadza wewnętrzne organy i może być słabym kancerogenem (od 1956 roku nadal jest używany jedynie jako Citrus Red 2 do barwienia pomarańczy w stężeniu 2 części na milion); Sudan 1: toksyczny i rakotwórczy (zwierzęta);

Violet 1: rak (zwierzęta) – barwnik ten był używany do stemplowania znaku inspekcji Departamentu Rolnictwa USA na tuszki wołowe; Yellow 1 i Yellow 2: wysokie dawki powodowały uszkodzenia jelit (zwierzęta); Yellow 3 i Yellow 4: wysokie dawki powodowały uszkodzenia serca (zwierzęta); [15]. Właściwe wykorzystanie procesów zaawansowanego utleniania może prowadzić do znacznego zmniejszenia ilości barwników w ściekach, co przyczyni się do większej ochrony środowiska naturalnego. Pomimo kosztów związanych z wykorzystaniem reagentów, warto zastosować te procesy ze względu na ich skuteczność w usuwaniu barwników oraz zmniejszenie potencjalnego zagrożenia dla zdrowia ludzkiego. Dlatego też, procesy zaawansowanego utleniania stanowią ważny element w oczyszczaniu ścieków przemysłowych z barwników.

Metoda zaawansowanego utleniania zastosowana w tej pracy jest modyfikacją reakcji opisanej po raz pierwszy w 1894 roku przez Henry'ego Johna Horstmana Fentona [16]. Zbadana jednak bardziej dogłębnie w 1932 [17] (po niemiecku) oraz w 1934 [18] (po angielsku) przez Profesora Fritz Haber wraz z studentem, później również Profesorem, Joseph Joshua Weiss. Przebieg procesu przedstawiono w reakcjach R 1-2.

$$Fe^{2+} + H_2O_2 \rightarrow Fe^{3+} + HO^{\bullet} + OH^{-} \quad \textbf{(R 1)}$$

$$Fe^{3+} + H_2O_2 \rightarrow Fe^{2+} + HOO^{\bullet} + H^{+} \quad \textbf{(R 2)}$$

Reakcja ta może być wspomagania wieloma czynnikami takimi jak: dźwięk (Sono Fenton) [19]; prąd elektryczny (Electro Fenton) [19]; światło (Foto-Fenton/ Photo-Fenton) [19]; światło słoneczne (Solar Fenton) [20] możliwe jest również łączenie dwóch lub większej liczby czynników w np.: Solarphoto Fenton [20] lub Sonophoto Fenton [19].

Reakcje Fentona, oraz jej liczne modyfikacje, można podzielić również pod względem formy dostarczanego żelaza jeżeli jest dostarczane w formie rozpuszczalnej lub dysocjującej mówi się o homogenicznej reakcji Fentona gdy żelazo jest wprowadzane w formie nierozpuszczalnej jest to reakcja heterogeniczna [21]. Czasami spotyka się z wyodrębnieniem procesu przy wykorzystaniu nanocząstek. Na potrzeby niniejszej pracy zdecydowano się, ze względu na wiele podobieństw, zaliczyć je do procesów heterogenicznych.

4. Część teoretyczna

4.1. Rodzaje barwników

Barwniki można podzielić ze względu na ich pochodzenie na naturalne oraz sztuczne. Możliwi jest również podział barwników ze względu na ich budowę. Kryterium w tym podziale jest rodzaj chromoforu. W przedstawionej pracy zastosowano barwniki przedstawione w tabeli 1. Ich wzory strukturalne przedstawiono na rys. 1-3.

Tab. 1. Zestawienie informacji o barwnikach wykorzystanych w badaniach

Nazwa barwnika	Wzór chemiczny	Grupa barwników	Nr CAS	Wzór strukturalny
Rodamina B	$C_{28}H_{31}N_2O_3Cl$	Rodaminy	81-88-9	Rys. 1
Błękit metylenowy	$C_{16}H_{18}ClN_3S$	Tiazyny	61-73-4	Rys. 2
Sudan I	$C_{16}H_{12}N_2O$	Barwniki Azowe	842-07-9	Rys. 3

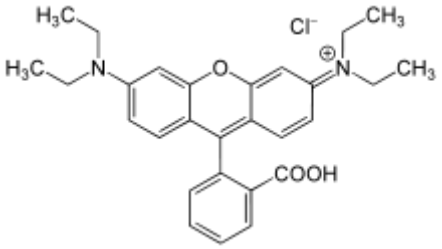

Rys. 1. Wzór strukturalny Rodaminy B

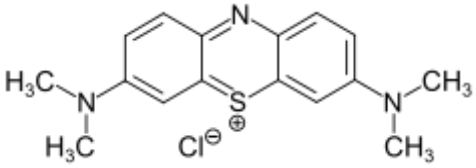

Rys. 2. Wzór strukturalny Błękitu metylenowego

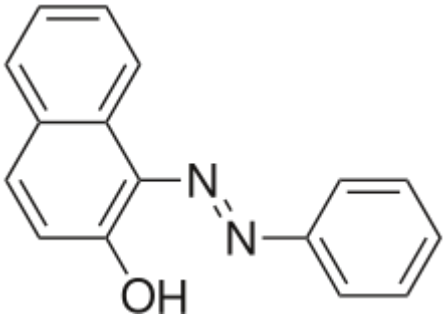

Rys. 3. Wzór strukturalny Sudanu I

4.2. Źródła barwników

Głównym źródłem barwnych zanieczyszczeń jest przemysł włókienniczy [7,22–24], który produkuje i używa znacznych ilości barwników. Barwniki są wykorzystane w tej gałęzi przemysłu do barwienia tkanin, skór, tworzyw sztucznych itp. Kolejnym źródłem jest przemysł

spożywczy, który stosuje barwniki do barwienia żywności oraz napojów. Ta gałąź przemysłu jednak odeszła lub odchodzi od stosowania barwników sztucznych na rzecz naturalnych barwników pochodzenia roślinnego lub zwierzęcego. Jest to wynikiem rosnącej świadomości konsumentów i trendu na zdrowe i naturalne produkty. Jest to również odpowiedź na obawy dotyczące potencjalnych szkodliwych skutków stosowania sztucznych barwników w żywności, takich jak alergie, nadwrażliwość czy nawet rakotwórczość [25]. Przemysł kosmetyczny również korzysta z barwników, używając ich do produkcji makijażu, lakierów do paznokci czy farb do włosów. Jednakże podobnie jak w przypadku przemysłu spożywczego, również w kosmetykach obserwuje się tendencję do zastępowania sztucznych barwników naturalnymi alternatywami, aby spełnić oczekiwania coraz bardziej świadomych konsumentów. Przemysły te odchodzą jednak od bardziej szkodliwych barwników na terenie UE podczas gdy w krajach rozwijających się nadal stosowane są bardziej niebezpieczne substancje.

4.3. Metody usuwania barwników

Istnieje wiele możliwych sposobów usuwania barwników z roztworów wodnych. Wybrane metody przedstawiono wraz z ich zaletami i wadami w tabeli 2. Większość z przedstawionych w tabeli 2 sposobów dekoloryzacji wymaga znacznego nakładu finansowego. Metody te mogą wiązać się z wysokimi kosztami reagentów, koniecznością dużego terenu inwestycyjnego lub innymi znacznymi wydatkami.

Tab.2. Zestawienie przykładowych metod dekoloryzacji barwników

Metoda dekoloryzacji	**Zalety**	**Wady**	**Źródło**
Adsorpcja i biosorpcja	- Prosty proces - Relatywnie wysoki stopień dekoloryzacji - Wysoka powtarzalność wyników	- Wysoki koszt konserwacji - Koszt aktywnego węgla konieczny do prowadzenia procesu - Trudna i konieczna regeneracja	[26–28]
Procesy biologiczne	- Możliwość dekoloryzacji różnych rodzajów barwników - Ekologiczny i konkurencyjny kosztowo - Relatywnie mała produkcja osadu - Nie posiada niebezpiecznych metabolitów - Relatywnie małe zużycie wody	- Nie usuwa wszystkich rodzajów barwników - Niska dekoloryzacja barwników odpornych na biodegradację - Wymaga większego terenu inwestycyjnego niż inne metody	[29]
Flokulacja i koagulacja	- Znaczna redukcja ChZT i BZT - Szeroka gama reagentów dostępnych komercyjnie	- Konieczne dodanie środka chemicznego nienadającego się do ponownego użycia (koagulanty, flokulanty) - Produkcja osadu - Wysoka pozostałość aluminium	[26,27]
Procesy pogłębionego utleniania	- Skuteczne odbarwianie rozpuszczalnych i nierozpuszczalnych barwników - Niewielkie zapotrzebowanie na odczynniki chemiczne - Mineralizacja zanieczyszczeń - Skuteczny względem substancji opornych (leki, barwniki itp.)	- Możliwe postawanie osadów z katalizatora - Ekonomicznie nieopłacalne dla małych i średnich przedsiębiorstw	

Wymiana jonowa	- Osiąga wysoką jakość wody - Po regeneracji brak spadku wydajności absorbancji - Niskie koszty utrzymania	- Skuteczne dla ograniczonej liczby barwników - Efektywność silnie zależy od pH - Konieczność stosowania kosztownych żywic - Wymagana czasochłonna regeneracja	[26,28]
Irradiacja (naświetlanie)	- Skuteczny w skali laboratoryjnej	- Kosztowna - Wymagana jest duża ilość rozpuszczonego O_2	[30]
Techniki membranowe	- Usuwa wszystkie rodzaje barwników - Łatwość łączenia z innymi procesami - Skuteczne w odzyskiwaniu i ponownym wykorzystywaniu wody - Małe zapotrzebowanie na miejsce - Proste, szybkie i praktyczne, nawet przy wysokich poziomach zanieczyszczeń - Zapewnia wysoką jakość permeatu - Brak konieczności stosowania substancji chemicznych - Niski poziom odpadów stałych	- Produkcja zagęszczonego osadu - Koszty sprzętu mogą być wysokie - Wysokie zapotrzebowanie na energię - Różnorodność konstrukcji systemów filtracji membranowej - Wysokie koszty konserwacji - Szybkie zanieczyszczenie membrany (zjawisko foulingu)	[26–28,30]
Ozonowanie	-Dobrze odbarwia i redukuje ChZT -Łatwo można go wdrożyć w istniejących zakładach - Ozon może być stosowany gazowo (ze zbiornika zewnętrznego) lub produkowany na miejscu	- Ekstremalnie droga metoda - Krótka półtrwałość ozonu (20min) - Metoda niestabilna	[28,30]

5. Tezy pracy

W obliczu rosnących wyzwań związanych z ochroną środowiska coraz większą uwagę przywiązuje się do poszukiwania innowacyjnych rozwiązań w dziedzinie oczyszczania ścieków. W tym kontekście, w badaniach obejmujących tematykę pracy doktorskiej zastosowano nowe materiały mogące stanowić alternatywne źródło jonów żelaza w reakcji Fentona wykorzystanej do degradacji barwników w roztworach wodnych. W podobnym celu sprawdzono również możliwość zastosowania do dekoloryzacji barwnych roztworów wodnych nadwęglanu sodu jako alternatywnego, w stosunku do nadtlenku wodoru, utleniacza w zmodyfikowanej reakcji Fentona. Dla realizacji przyjętych założeń pracy doktorskiej postawiono dwie tezy:

1. **Nanocząstki ferrytu (Fe_3O_4), stopy o wysokiej entropii, kwazikryształy i taśmy amorficzne mogą być wykorzystane jako katalizatory, stanowiące alternatywne źródło jonów żelaza w reakcji Foto-Fentona stosowanej w celu efektywnej dekoloryzacji barwnych roztworów wodnych.**
2. **Nadwęglan sodu może stanowić alternatywne źródło nadtlenku wodoru w reakcji Foto-Fentona stosowanej w celu efektywnej dekoloryzacji barwnych roztworów wodnych**.

6. Cele pracy

Głównym celem pracy było zaproponowanie modyfikacji reakcji Fentona, w celu zbadania ich wpływu na efektywność procesu dekoloryzacji roztworów wodnych barwników. Modyfikacje polegały na zastosowaniu następujących nowoczesnych materiałów:

- nanocząstki ferrytu; **A(I, II, IV)**
- stopy wysokiej entropii; (HEA, High entropy alloy), **A(III)**
- kwazikryształy; **A(V)**
- taśmy amorficznych;

oraz na zastąpieniu nadtlenku wodoru nadwęglanem sodu; **A(III-V)**.

Istotą zastosowanych modyfikacji wykorzystujących alternatywne źródła żelaza oraz nadtlenku wodoru, było założenie, że reakcja Fentona katalizowana światłem UV może przebiegać w pH neutralnym bez zmniejszenia efektywności procesu dekoloryzacji.
Zakres badanych parametrów obejmował wpływ:

- pH (4-7),
- rodzaju i dawki utleniacza,
- formy i dawki katalizatora.

7. Materiały i metody

7.1. Opis eksperymentu

Wszystkie eksperymenty prowadzono w zbliżony sposób, różnicując jedynie materiały będące źródłem jonów żelaza oraz rodzaj utleniacza. Prace badawcze realizowano w kontrolowanych warunkach laboratoryjnych w temperaturze otoczenia. Za każdym razem odmierzano 60 ml roztworu wodnego barwnika o określonym stężeniu, korygowano pH z zastosowaniem kwasu siarkowego (VI) lub wodorotlenku sodu. Barwnik Rodamina B (RhB), który wytypowano do dalszych badań, został wybrany na podstawie wstępnych eksperymentów przedstawionych w **A(I)**. Barwnik Sudan I został odrzucony ze względu na jego nierozpuszczalność w wodzie. Ponadto, pomiary wykonane przy użyciu mieszaniny wody z acetonem, w celu wytworzenia roztworu tego barwnika, były obarczone zbyt dużym błędem, co uniemożliwiło uzyskanie wiarygodnych wyników. Z kolei wyniki wstępnych eksperymentów wykazały podobne efekty dekoloryzacji dla Rodaminy B (RhB) oraz błękitu metylenowego (MB). Biorąc to pod uwagę oraz znacznie większą bazę literatury dotyczącą Rodaminy B, zdecydowano dalsze badania prowadzić z wykorzystaniem tego barwnika.

Badane katalizatory (stanowiące alternatywne źródła jonów żelaza) stosowano w różnej formie. Nanocząstki ferrytu, wprowadzano jako dyspersję wodną, natomiast kwazikryształy oraz stopy wysokiej entropii jako metaliczne, nierozpuszczalne w wodzie, granulki o rozmiarach kilku milimetrów. Po dodaniu katalizatora rozpoczynano mieszanie roztworu reakcyjnego mieszadełkiem magnetycznym (400 RPM) oraz jednocześnie wprowadzano utleniacz, którym był nadtlenek wodoru lub nadwęglan sodu. Roztwór naświetlano światłem UV przez cały czas trwania eksperymentu (36 W; λ = 365 nm). Ze względów technicznych lampy UV znajdowały się w stałej odległości (10 cm) nad powierzchnią roztworu, a stanowisko badawcze (Rys. 4) zostało zaprojektowane tak, aby uniemożliwić przenikanie światła zewnętrznego do badanego roztworu.

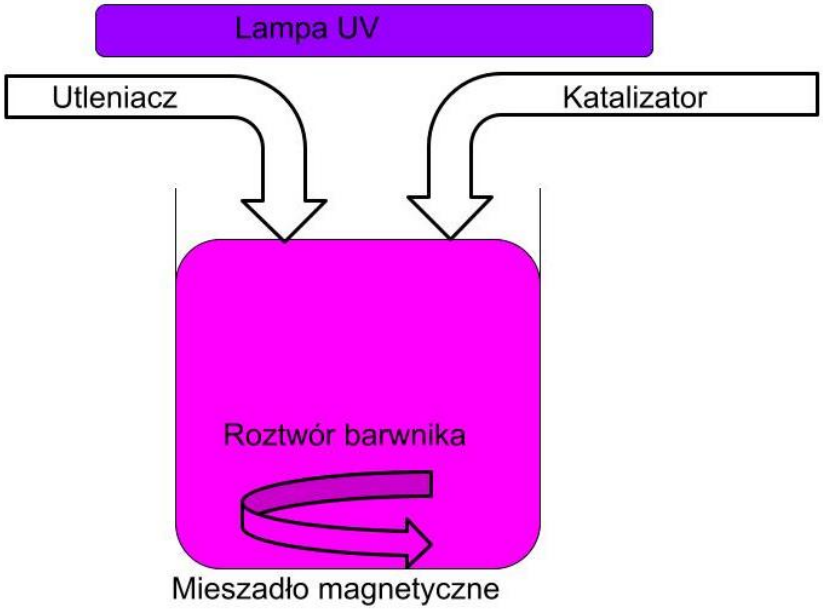

Rys. 4. Schemat stanowiska badawczego

Stężenie barwnika podczas reakcji dekoloryzacji monitorowano poprzez pobieranie próbek w czasie 0, 5, 10, 15, 20, 30, 45 i 60 minut. Następnie dokonywano pomiarów absorbancji przy użyciu spektrofotometrów Thermo Scientific Evolution 220 **A(I)** oraz Shimadzu UV-1800 **A(II, III, IV, V)**. Eksperymentalne wyniki porównywano z rezultatami uzyskanymi dla reakcji referencyjnej realizowanej w systemie UV/H_2O_2.

7.2. Badanie właściwości katalitycznych nanocząstek ferrytu

Rezultaty z publikacji **A(I)** stanowiły wstępne dane, które wykazały zasadność dalszych badań. Przeprowadzone badania wykazały, że zastosowanie nanocząstek ferrytu jako katalizatora w procesach zaawansowanego utleniania przyśpiesza proces odbarwiania barwnika. Nanocząstki wprowadzano w formie dyspersji wodnej. Do przygotowania badanych roztworów zastosowano barwniki Rodamina B (RhB), Błękit metylenowy (MB) oraz Sudan I.

Wyniki dekoloryzacji przy wykorzystaniu nanocząstek jako katalizatora przedstawiono w publikacjach **A(I)**; **A(II)** oraz **A(IV)**. Rezultaty z publikacji **A(I)** są efektem wstępnych eksperymentów, a szczegółowe wyniki przedstawiono w **A(II)** oraz **A(IV)**. W ramach publikacji **A(I)** badano możliwości katalitycznego rozkładu barwników RhB oraz MB. Wyniki badań przedstawiono na Fig. 3 B oraz C w **A(I)**. Brak dekoloryzacji barwnika Sudan I najprawdopodobniej był spowodowany brakiem jego rozpuszczalności w wodzie i koniecznością zastosowania jako rozpuszczalnika 60% roztworu acetonu w wodzie. W publikacjach **A(II, IV)** przedstawiono wyniki bardziej dogłębnej analizy badań nad wpływem funkcjonalizacji, kształtu nanocząstki; stężenia reagentów, pH, jak również wpływem rodzaju utleniacza na przebieg reakcji – Fig. 3 w **A(II)** oraz Fig. 3-6 w **A(IV)**.

Wyniki zamieszczone w publikacji **A(II)** wykazały, że przy wykorzystaniu nadtlenku wodoru jako utleniacza, pH odgrywa ważną rolę i istotnie wpływa na szybkość dekoloryzacji. Wyniki z **A(IV)** wskazują, że podczas zastosowania nadwęglanu sodu w miejsce nadtlenku wodoru nie odnotowano znacznego wpływu pH na szybkość dekoloryzacji. Natomiast odnotowano istotny wpływ mieszania zarówno na przebieg procesu, jak i na stężenie obecnego nadtlenku wodoru. Podczas eksperymentu z mieszaniem badanego roztworu, stężenie obecnego nadtlenku wodoru bardzo szybko osiągnęło maksymalną wartość (1,2%) zaobserwowaną dla tej reakcji. W eksperymencie, w którym mieszadło magnetyczne zostało wyłączone, stężenie wolnego nadtlenku wodoru wzrastało przez pierwsze 30 min procesu, po których nieznacznie zmniejszało się, aż do zakończenia eksperymentu. Efekty zmian stężenia wolnego H_2O_2 widoczne są na wykresie dekoloryzacji dla tych procesów. W procesie bez mieszania, pomimo zaobserwowania większego stężenia nadtlenku wodoru niż w procesie z mieszaniem, przez cały czas trwania eksperymentu osiągano znacznie mniejszy stopień dekoloryzacji, który finalnie wynosił 65% (nie osiągając nawet wizualnego odbarwienia roztworu) w przeciwieństwie do 94% stopnia dekoloryzacji uzyskanego na koniec w procesie z mieszaniem. Było to spowodowane nierównomiernym rozkładem reagentów w objętości reaktora.

7.3. Badanie właściwości katalitycznych stopów o wysokiej entropii

Ze wszystkich materiałów zastosowanych w niniejszej pracy, stopy o wysokiej entropii są materiałem najnowszym, gdyż został po raz pierwszy wytworzony na początku XXI wieku. Charakteryzują się one obecnością wielu pierwiastków w swoim składzie, co w przypadku

stopów metali najczęściej oznacza co najmniej pięć pierwiastków w zbliżonych proporcjach molowych. Wyniki eksperymentów przedstawiono w publikacji **A(III)**. Do badań wybrano stopy **AlCoNiFeTi** oraz **AlCoNiFeTiSi**. Stopy te wybrano ze względu na obecność żelaza oraz tytanu. Tlenki tych metali znane są w literaturze z właściwości katalizujących reakcję Fentona.

Wyniki badań przedstawione w publikacji **A(III)** wykazały, że HEA (High entropy alloy) skutecznie dekoloryzuje roztwór barwnika RhB, osiągając rzędu 90% odbarwienia w czasie 60 min, podczas gdy metoda referencyjna w tych samych warunkach i tym samym czasie zredukowała barwę o 50%, nie osiągając nawet wizualnej dekoloryzacji, co potwierdza jego efektywność dekoloryzacji barwnika RhB. Wykazano również brak znacznego wpływu wartości pH na szybkość dekoloryzacji.

Uzyskane rezultaty dla stopu AlCoFeNiTiSi wykazały, że przy pH 6 uzyskano największą szybkość dekoloryzacji – około 90% degradacji barwnika po 60 minutach. Przy pozostałych wartościach pH (4, 5 i 7) efekty dekoloryzacji były nieco mniejsze i wynosiły, odpowiednio 85-90% dla pH 5 i 7 oraz 80% dla pH 4, po 60 minutach. Podsumowując, zmiany pH miały niewielki wpływ na szybkość i końcowy efekt dekoloryzacji.

Dla stopu AlCoFeNiTiSi przeanalizowano także pięć różnych stężeń nadwęglanu sodu, jako alternatywnego źródła utleniacza w reakcji Foto-Fentona: 1,7 g/dm^3, 4,2 g/dm^3, 8,3 g/dm^3, 16,7g/dm^3 oraz 37,5 g/dm^3. Uzyskane wyniki pokazały, że przy największych stężeniach nadwęglanu sodu (37,5; 16,7 g/dm^3) uzyskano największą szybkość dekoloryzacji, osiągając około 95% odbarwienia po 60 minutach. Natomiast dla kolejnych stężeń (8,3; 4,2 i 1,7 g/dm^3) uzyskano następujące stopnie dekoloryzacji, odpowiednio 60%, 40%, 35% po 60 minutach. Przy stężeniach mniejszych niż 16,7 g/dm^3 nie osiągnięto wizualnego odbarwienia. Wyniki te wskazują, że wyższe stężenia nadwęglanu sodu znacznie przyspieszają proces dekoloryzacji.

Przeanalizowano również pięć różnych stężeń katalizatora (stop AlCoFeNiTiSi): 0 g/dm^3, 4,2 g/dm^3, 8,3 g/dm^3, 16,7 g/dm^3 oraz 33,3 g/dm^3. Wyniki badań pokazały, że przy stężeniu katalizatora (16,7 g/dm^3) proces dekoloryzacji następował najszybciej, osiągając około 90% po 60 minutach. Stężenie 33,3 g/dm^3 również pokazuje wysoką efektywność, osiągając około 80% po 60 minutach. Przy zastosowaniu stężenia 8,3 g/dm^3 i 4,2 g/dm^3 osiągnięto tempo dekoloryzacji, osiągając odpowiednio około 80% i 75% po 60 minutach. Brak katalizatora (0 g/dm^3) wykazuje najniższą efektywność, osiągając jedynie około 50% po 60 minutach, nie osiągając wizualnego odbarwienia. Wyniki te wskazują, że wyższe stężenia katalizatora znacznie przyspieszają proces dekoloryzacji. Osiągając najbardziej sprzyjający wpływ przy stężeniu 16,7 g/dm^3.

Wyniki eksperymentu dla tych samych wartości pH (4, 5, 6, 7) przy zastosowaniu stopu AlCoFeNiTi przedstawiono w **A(IV)** Fig. 10. W tym przypadku, krzywe dla wszystkich wartości pH są bardziej zbliżone do siebie. Przy wartości pH 6 (niebieskie trójkąty) i pH 5 (czerwone okręgi) osiągają najwyższą efektywność dekoloryzacji, zbliżając się do 95-100% po 60 minutach. Dla wartości pH równej 4 (czarne kwadraty) i pH 7 (zielone odwrócone trójkąty) są nieco mniej efektywne, jednak nadal wykazują wysoki stopień dekoloryzacji,

zbliżającą się do 90-95% po 60 minutach. W przypadku tego stopu, różnice między stopniami dekoloryzacji w różnym pH są jeszcze mniejsze.

Wyniki eksperymentu dla różnych stężeń nadwęglanu sodu (1,7; 4,2; 8,3; 16,7; 37,5 g/dm^3) przedstawiono na Fig. 11 w **A(IV)**. Najwyższe stężenie nadwęglanu sodu (37,5 g/dm^3) osiąga prawie 100% dekoloryzacji już po 30 minutach. Stężenie 16,7 g/dm^3, osiągając około 90% odbarwienia po 60 minutach. Stężenie 8,3 g/dm^3 osiąga około 70% odbarwienia po 60 minutach, jest najniższe ze zbadanych stężeń nadwęglanu wykazujących wizualne odbarwienie roztworu barwnika. Stężenia 4,2 g/dm^3 i 1,7 g/dm^3 osiągają odpowiednio około 45% i 20% dekoloryzacji po 60 minutach.

Wyniki eksperymentu dla stężeń katalizatora (0; 4,2; 8,3; 16,7; 33,3 g/dm^3) zestawiono na Fig. 12 w **A(IV)**. Najwyższe stężenie katalizatora (33,3 g/dm^3) osiąga prawie 90% dekoloryzacji po 45 minutach. Stężenie 16,7 g/dm^3 osiągając około 80% po 60 minutach. Stężenie 8,3 g/dm^3 osiąga około 90% po 60 minutach. Stężenia 4,2 g/dm^3 i 0 g/dm^3 osiągają odpowiednio około 90% i 30% po 60 minutach. Wykazując tak samo, jak stop AlCoFeNiTiSi wyższy stopień dekoloryzacji po upływie 60 min, jak i przez cały badany okres. Przedstawione wyniki udowadniają katalityczny wpływ dodatku obu zaproponowanych składów stopów wysokiej entropii.

7.4. Badanie właściwości katalitycznych kwazikryształów

Następnym materiałem, który został przetestowany pod kątem właściwości katalitycznych, były kwazikryształy. Charakteryzują się one strukturą krystaliczną, lecz różnią się od tradycyjnych kryształów swoją unikalną budową. Od zwykłych struktur krystalicznych odróżnia je to, że niemożliwe jest wyznaczenie komórki elementarnej. W kwazikryształach nie ma jednej jednostki komórkowej, która regularnie się powtarza, jak w klasycznych kryształach. Zamiast tego, struktura kwazikrystaliczna może być opisana jako układ atomów, który tworzy unikalne wzory, ale nie jest jednorodny ani regularny w tradycyjny sposób. Wyniki badań nad właściwościami katalitycznymi kwazikryształów przedstawiono w **A(V)**. Wizualny stopień dekoloryzacji osiągnięto w czasie 45 min dla stężenia 16,7 g/dm^3 nadwęglanu sodu oraz 16,7 g/dm^3 kwazikryształu.

Na początku eksperymentu, dla wszystkich dawek kwazikryształów, efektywność dekoloryzacji wzrasta stopniowo wraz z upływem czasu. Najwyższą efektywność dekoloryzacji osiągnięto przy dawce 33,3 g/dm^3, co wskazuje na pozytywny wpływ większej ilości katalizatora na proces dekoloryzacji. Dla dawki 16,7 g/dm^3 i 8,3 g/dm^3, efektywność również znacząco wzrasta, choć jest nieco niższa niż dla najwyższej dawki. Najniższą efektywność dekoloryzacji zaobserwowano dla próbki bez katalizatora (0 g/dm^3), co podkreśla znaczenie obecności katalizatora w procesie.

Na początku eksperymentu, niezależnie od dawki katalizatora, efektywność dekoloryzacji stopniowo wzrasta wraz z upływem czasu. Najwyższą efektywność osiągnięto przy dawce 33,3 g/dm^3, co wskazuje na korzystny wpływ większej ilości katalizatora na proces dekoloryzacji. Efektywność dekoloryzacji również znacząco wzrasta dla dawek 16,7 g/dm^3 oraz 8,3 g/dm^3, choć jest nieco niższa w porównaniu do najwyższej dawki. Najniższą efektywność zaobserwowano w próbce bez katalizatora (0 g/dm^3), co podkreśla kluczową rolę katalizatora w procesie. Po około 30 minutach krzywe dla wszystkich trzech próbek

z katalizatorem zaczynają się zbliżać, osiągając podobne wartości efektywności. Sugeruje to, że przy dłuższym czasie trwania procesu różnice między dawkami katalizatora stają się mniej znaczące. Wszystkie próbki z katalizatorem przekroczyły poziom oznaczony jako "visual discolouration" (około 70% dekoloryzacji roztworu) w ciągu 60 minut, co dowodzi skuteczności procesu dekoloryzacji z użyciem katalizatora.

Wpływ dawki utleniacza badano w trzech seriach różnych stężeń utleniacza: 8,3 ; 16,7 i 33,3 g/dm^3. Każda seria pokazuje, jak efektywność dekoloryzacji, wyrażona w procentach, zmienia się w ciągu 60 minut. Dla stężenia 8,3 g/dm^3, na początku procesu dekoloryzacji efektywność wynosi około 10%. W ciągu pierwszych 20 minut efektywność rośnie do około 40%, a następnie stopniowo wzrasta, osiągając około 60% po 60 minutach. W przypadku stężenia 16,7 g/dm^3, początkowa efektywność jest wyższa niż dla 8,3 g/dm^3, wynosząc około 20%. W ciągu 20 minut efektywność wzrasta do około 60%, a po 60 minutach osiąga około 80%. Dla stężenia 33,3 g/dm^3 początkowa efektywność jest najwyższa spośród wszystkich trzech stężeń, wynosząc około 30%. W ciągu pierwszych 20 minut efektywność wzrasta do około 80%, a po 60 minutach osiąga niemal 100%, co oznacza niemal pełną dekoloryzację.

Porównanie trzech serii danych pokazuje, że wyższe stężenie utleniacza prowadzi do szybszej i bardziej efektywnej dekoloryzacji. Stężenie 33,3 g/dm^3 jest najbardziej efektywne, osiągając prawie całkowitą dekoloryzację w ciągu 60 minut, podczas gdy niższe stężenia 8,3 i 16,7 g/dm^3 również wykazują wzrost efektywności, ale są mniej skuteczne w porównaniu do najwyższego stężenia. Zwiększenie stężenia utleniacza (nadwęglanu sodu) znacznie poprawia efektywność procesu dekoloryzacji.

8. Taśmy amorficzne jako przykład przyszłych badań

W świetle uzyskanych wyników eksperymentalnych kolejnym krokiem w badaniach nad katalizą nowych materiałów jest głębsza analiza wpływu różnych struktur materii na efektywność procesu dekoloryzacji. Następną strukturą materii, która byłaby warta obserwacji, jest forma amorficzna. Ten rodzaj struktury został zbadany pod postacią taśm. Taśmy te zostały wprowadzone do roztworu w postaci zwiniętej. Taśma tak zwinięta przypomina sprężynę płaską. Do jednego eksperymentu wprowadzono taśmę o masie 1 g, w badaniach stosowano skład taśm $Fe_{86-x}Cu_xB_{14}$. Pozostałe parametry eksperymentu pozostały bez zmian. Wyniki określające wpływ pH na proces dekoloryzacji przedstawiono na Rys. 5. Badania wpływu pH przeprowadzono z wykorzystaniem taśm amorficznych o składzie $Fe_{86}B_{14}$. Podczas tych eksperymentów zastosowano stężenie utleniacza wynoszący 33,00 g/dm^3.

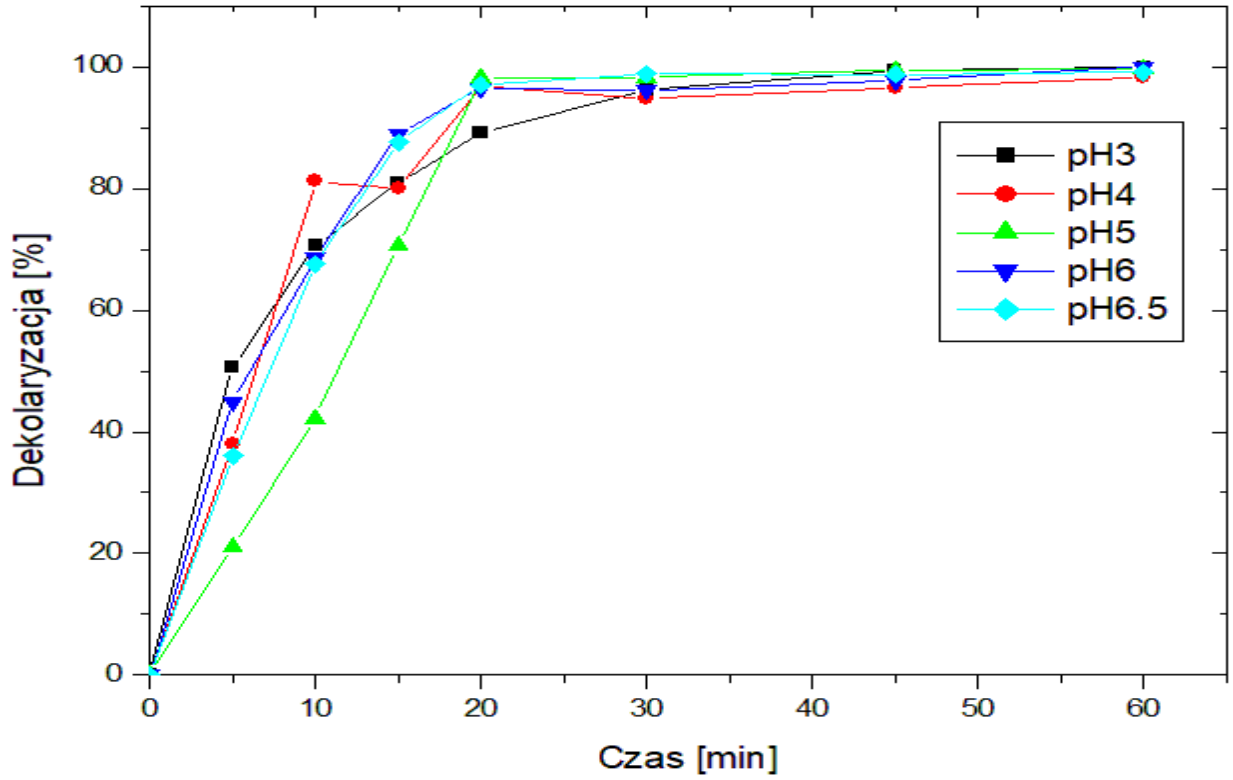

Rys. 5. Wykresy dekoloryzacji w zależności od pH

Analiza wykresu wskazuje, że wpływ pH na dekoloryzację jest znikomy. Wyniki uzyskane przy wszystkich przebadanych wartościach pH wykazują podobny trend, zbliżając się do niemal pełnej dekoloryzacji (około 100%) w ciągu 20-25 minut. Różnice w stopniu dekoloryzacji pomiędzy różnymi wartościami pH są minimalne, co sugeruje, że proces dekoloryzacji jest skuteczny w szerokim zakresie pH. Jedynie przy pH 5 proces dekoloryzacji jest nieco wolniejszy w pierwszych minutach eksperymentu, ale ostatecznie także osiąga blisko 100% po 60 minutach. Wartości pH 6,5; 6; 5 i 4 wykazują bardzo zbliżone wyniki, co podkreśla, że pH w przedziale 4-6,5 nie ma znaczącego wpływu na efektywność dekoloryzacji. Wnioski z analizy wykresu przedstawionego na Rys. 5. sugerują,

że dekoloryzacja roztworu jest skuteczna niezależnie od pH w przedziale 3-6,5, a wpływ pH na tempo i efektywność dekoloryzacji jest minimalny.

Wpływ dawki nadwęglanu sodu określono również wykorzystując taśmy amorficzne o składzie $Fe_{86}B_{14}$. Wyniki przedstawiono na Rys. 6. Eksperymenty wykonano w pH 4.

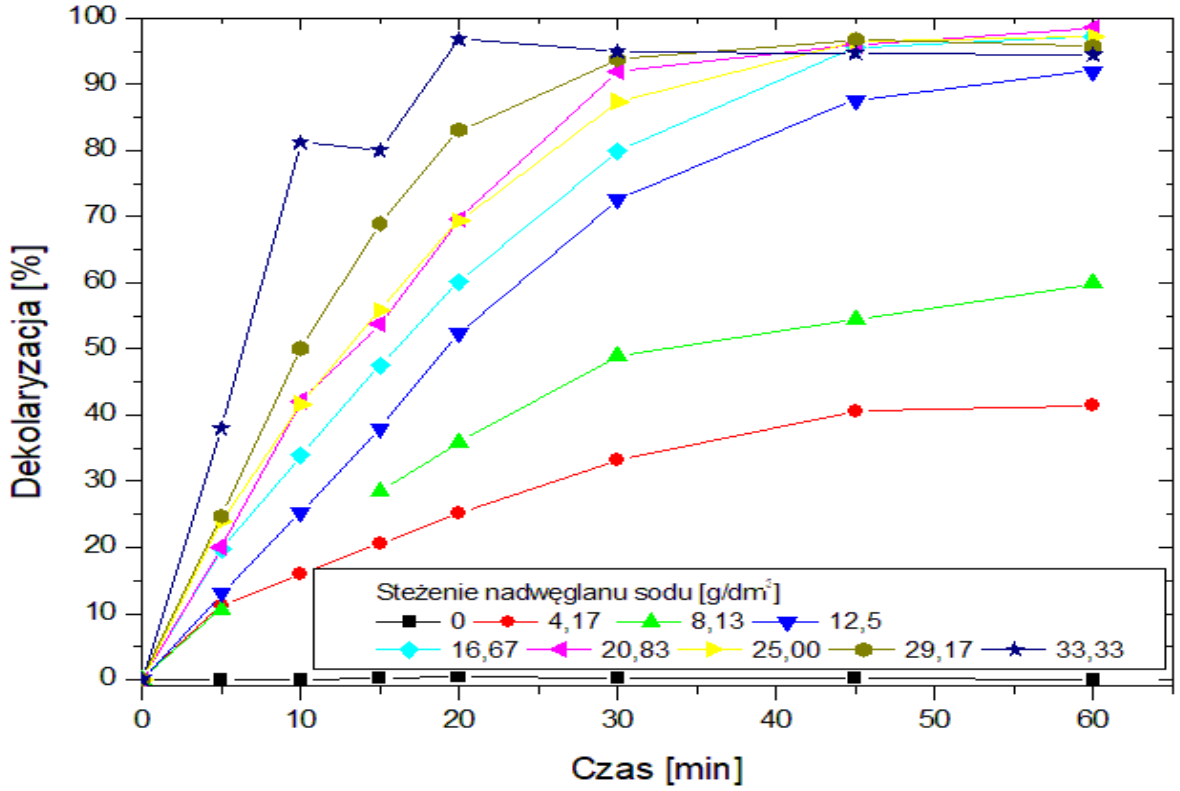

Rys. 6. Wykresy dekoloryzacji w zależności od stężenia nadwęglanu sodu

Rys. 6 ilustruje, jak zwiększanie stężenia nadwęglanu sodu wpływa na efektywność dekoloryzacji, z wyraźnym wzrostem efektywności przy wyższych stężeniach. W miarę zwiększania się stężenia nadwęglanu sodu, tempo dekoloryzacji wyraźnie wzrasta. Najwyższe stężenia nadwęglanu sodu (33,33; 29,17; 25,00 g/dm^3) powodują szybkie i wysokie wartości dekoloryzacji, osiągając, dla największego stężenia, ponad 80% w ciągu 10 minut i stabilizując się blisko 90% w ciągu 60 minut. Przy średnich stężeniach (20,83; 16,67 g/dm^3) tempo dekoloryzacji jest wolniejsze, osiągając około 60-80% w ciągu 20 minut. Osiągając 90% w czasie 60 min. Niższe stężenia (12,50; 8,33; 4,17 g/dm^3) prowadzą do zauważalnie wolniejszej dekoloryzacji, osiągając odpowiednio około 80%, 50% i 30% po 60 minutach. Brak nadwęglanu sodu (0,00 g/dm^3) skutkuje praktycznie zerową dekoloryzacją przez cały okres trwania eksperymentu. Efektywność dekoloryzacji jest więc silnie zależna od stężenia nadwęglanu sodu. Najwyższe stężenia nadwęglanu sodu (33,33 i 29,17 g/dm^3) są najskuteczniejsze w szybkim usuwaniu barwnika z roztworu podkreśla to kluczową rolę tego reagenta w procesie.

Wpływ składu taśm określono, badając sześć składów taśm amorficznych $Fe_{86-x}Cu_xB_{14}$ X=0; 0,25; 0,4; 0,55; 0,7; 1. Wyniki przedstawiono na Rys. 7. Eksperymenty wykonano w pH 4 oraz dawce utleniacza 33,33 g/dm^3.

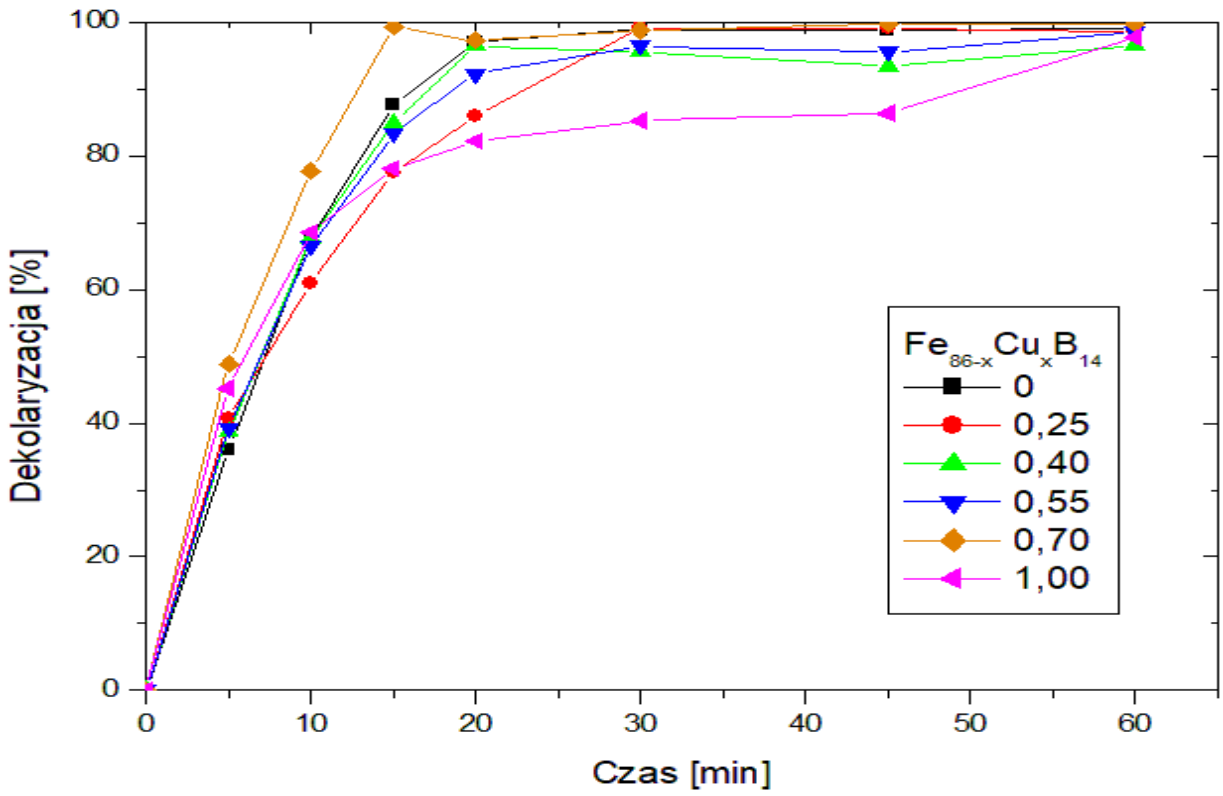

Rys. 7. Krzywe dekoloryzacje dla różnych rodzajów stopów amorficznych

Wszystkie badane składy taśm amorficznych prowadzą do wysokiego stopnia dekoloryzacji, osiągającego blisko 100% w ciągu 20-30 minut. Najszybszą dekoloryzację zaobserwowano dla składu o zawartości miedzi 0,7% (pomarańczowy). Osiągając około 10 minutach dekoloryzację wynoszącą ponad 80%, a maksymalny stopień dekoloryzacji (około 95-100%) osiągnięto po około 20 minutach.

Składy z zawartością miedzi 0,55% (niebieski) oraz 0,4% (zielony) również wykazały wysoką efektywność, osiągając maksymalną dekoloryzację nieco wolniej, ale nadal w granicach 20-30 minut.

Składy z mniejszą zawartością miedzi, 0,25% (czerwony), wykazał się najwolniejszą dekoloryzacją, osiągając około 80-90% po 20-25 minutach. Mimo to, wszystkie badane składy taśm amorficznych ostatecznie osiągnęły wysoki stopień dekoloryzacji po 60 minutach.

Podsumowując, wyniki wskazują, że zawartość miedzi w taśmach amorficznych ma pewien wpływ na tempo dekoloryzacji, ale wszystkie badane składy są skuteczne w osiągnięciu wysokiego stopnia dekoloryzacji. Najwyższą efektywność wykazały składy z zawartością miedzi 0,7%.

9. Dyskusja wyników

W niniejszej pracy doktorskiej skoncentrowano się na dekoloryzacji roztworów wodnych barwników przy użyciu metod zaawansowanego utleniania. Badania przeprowadzono z zastosowaniem różnych nowoczesnych materiałów katalitycznych, takich jak nanocząstki ferrytu, stopy o wysokiej entropii oraz kwazikryształy. Otrzymane wyniki dostarczają istotnych informacji na temat efektywności tych materiałów w procesach dekoloryzacji oraz potencjalnych korzyści związanych z ich zastosowaniem.

9.1. Efektywność materiałów katalitycznych

W badaniach wykazano, że zastosowane materiały katalityczne mają istotny wpływ na efektywność procesu dekoloryzacji. Nanocząstki ferrytu **A(I, II, IV)** okazały się szczególnie efektywne w katalizie dekoloryzacji barwnika, co wykazano znacznym zwiększeniem efektywności procesu. Wyniki te są zgodne z wcześniejszymi badaniami, które wskazują na wysoką aktywność katalityczną ferrytów w reakcjach Fentona.

Stopy o wysokiej entropii **A(III)** wykazały również znaczną efektywność w procesach utleniania, co można przypisać ich unikalnym właściwościom fizykochemicznym.

Kwazikryształy **A(V)**, choć mniej efektywne niż nanocząstki ferrytu, nadal wykazały znaczący potencjał katalityczny.

9.2. Wpływ parametrów reakcji

Badania nad modyfikacją reakcji Fentona wykazały, że optymalizacja parametrów takich jak rodzaj i dawka utleniacza oraz dawka katalizatora jest kluczowa dla maksymalizacji efektywności procesu dekoloryzacji. Wyniki **A(III-V)** pokazały, że wpływ pH w zakresie 4-7 na szybkość dekoloryzacji przy zastosowaniu nadwęglanu sodu jest mały.

Zastosowanie nadwęglanu sodu jako alternatywnego źródła nadtlenku wodoru okazało się obiecujące, oferując korzyści związane z łatwością przechowywania i transportu, a także zmniejszonym ryzykiem związanym z bezpieczeństwem. Jest to ważne odkrycie, które może mieć praktyczne znaczenie dla przemysłowych zastosowań metod zaawansowanego utleniania.

9.3. Porównanie z istniejącymi metodami

Wyniki badań sugerują, że metody zaawansowanego utleniania wspierane nowymi materiałami katalitycznymi mogą być bardziej efektywne niż tradycyjne metody usuwania barwników, takie jak adsorpcja, biosorpcja czy procesy biologiczne. Chociaż koszty związane z wykorzystaniem reagentów chemicznych mogą być wyższe, efektywność dekoloryzacji i możliwość pełnej mineralizacji zanieczyszczeń stanowią istotne przewagi tych metod. Kolejną zaletą jest, relatywnie, małe zapotrzebowanie na powierzchnię co może pozwolić na zastosowanie tej metody tam gdzie mała ilość miejsca jest kluczowym ograniczeniem.

9.4. Znaczenie dla ochrony środowiska

Zastosowanie metod zaawansowanego utleniania w usuwaniu barwników ze ścieków przemysłowych ma znaczący potencjał w kontekście ochrony środowiska. Wysoka efektywność tych procesów może przyczynić się do zmniejszenia ilości szkodliwych substancji wprowadzanych do ekosystemów wodnych, co ma bezpośredni wpływ na zdrowie ludzkie i bioróżnorodność środowiska naturalnego.

10. Wnioski

W ramach niniejszej rozprawy doktorskiej badano procesy dekoloryzacji roztworów wodnych barwników, skupiając się na wykorzystaniu metod utleniania chemicznego, a w szczególności na reakcji Foto-Fentona. Wyniki uzyskane w pięciu opublikowanych artykułach naukowych pozwalają na sformułowanie następujących wniosków:

- **Wykorzystanie nowatorskich materiałów katalitycznych**:
    - Nanocząstki ferrytu (Fe_3O_4) okazały się wysoce efektywnymi katalizatorami w procesie dekoloryzacji roztworów barwnych. Badania wykazały, że ich zastosowanie w reakcjach Foto-Fentona znacząco przyspieszało proces odbarwiania barwników takich jak Rodamina B (RhB) **A(I, II, IV)** i Błękit metylenowy (MB) **A(I).**
    - Badania nad funkcjonalizacją kształtu nanocząstek **A(IV)**, stężenia reagentów oraz pH wykazały, że optymalizacja tych parametrów jest kluczowa dla maksymalizacji efektywności procesu dekoloryzacji. Szczególnie pH okazało się mieć istotny wpływ na szybkość dekoloryzacji przy użyciu nadtlenku wodoru jako utleniacza **A(II)**.
    - Stopy wysokiej entropii, choć mniej efektywne niż nanocząstki ferrytu, wykazały znaczący potencjał katalityczny. Szczególnie stopy wysokiej entropii o składzie AlCoNiFeTi, wykazały wysoką efektywność w dekoloryzacji roztworu barwnika RhB, osiągając 90% odbarwienia w czasie 30 minut **A(III)**.
    - W badaniach katalitycznych dotyczących dekoloryzacji roztworu barwnika, kwazikryształy wykazały zbliżoną skuteczność do stopów wysokiej entropii, osiągając porównywalne wyniki w zakresie efektywności katalitycznej **A(V)**.
- **Nadwęglan sodu jako alternatywny utleniacz**:
    - Wyniki badań wykazały, że nadwęglan sodu może stanowić efektywne alternatywne źródło nadtlenku wodoru w reakcji Foto-Fentona. Zastosowanie nadwęglanu sodu oferuje korzyści związane z łatwością przechowywania i transportu **A(III-V)**.
    - Badania wykazały, że wpływ pH na szybkość dekoloryzacji przy zastosowaniu nadwęglanu sodu był minimalny, co sugeruje, że może on być stosowany w szerszym zakresie warunków pH niż nadtlenek wodoru **A(III-V)**.

Podsumowując, badania wykazały, że zastosowanie nowoczesnych materiałów katalitycznych oraz optymalizacja parametrów procesu dekoloryzacji może znacząco zwiększyć efektywność reakcji Foto-Fentona. Wyniki te mają istotne znaczenie dla przyszłych badań i potencjalnych zastosowań przemysłowych w dziedzinie dekoloryzacji roztworów barwnych.

11. Kierunki dalszych badań

Na podstawie przeprowadzonych badań można stwierdzić, że procesy zaawansowanego utleniania z wykorzystaniem nowoczesnych materiałów katalitycznych są obiecującym rozwiązaniem w zakresie dekoloryzacji roztworów wodnych barwników. W przyszłości warto skoncentrować się na dalszej optymalizacji parametrów reakcji oraz badaniach nad trwałością i możliwością regeneracji materiałów katalitycznych.

Następne badania mogłyby zawierać analizę materiałów takich jak Ferrocen, nanokompozyty żelazowo-grafenowe czy materiały żelazowo-azotkowe.

Ferrocen ($Fe(C_5H_5)_2$) jest organometalicznym związkiem, który składa się z dwóch cyklopentadienylowych pierścieni związanych z centralnym atomem żelaza. Badania wykazały możliwość zmiany stopnia utlenienia centralnego atomu żelaza z +2 do +3 i odwrotnie [31]. Udowodniono również możliwość zastosowania tego związku w katalizie dekoloryzacji barwnika [13] przy zastosowaniu reakcji Fentona. Co więcej, Ferrocen jest stabilny w różnych warunkach reakcji, co zwiększa jego potencjalną użyteczności w katalizie dekoloryzacji.

Nanokompozyty żelazowo-grafenowe łączą właściwości żelaza i grafenu, tworząc materiały o unikalnych właściwościach chemicznych i fizycznych. Grafen, będący płaską warstwą atomów węgla ułożonych w heksagonalną sieć, zapewnia dużą powierzchnię, bardzo dobrą przewodność elektryczną i stabilność chemiczną. Nanokompozyty te mogą działać jako katalizatory heterogeniczne, gdzie żelazo uczestniczy w reakcjach redoks, a grafen zwiększa powierzchnię aktywną oraz poprawia przewodnictwo elektronów. W procesach takich jak fotokataliza nanokompozyty żelazowo-grafenowe mogłyby być używane do generowania, wspomaganego światłem, reaktywnych form tlenu, które utleniają barwniki w roztworach wodnych.

Materiały żelazowo-azotkowe (FeN) to związki żelaza i azotu, które wykazują interesujące właściwości chemiczne, mechaniczne i magnetyczne. Żelazowe azotki mogą działać jako katalizatory w reakcji Fentona i Foto-Fentona lub podobnych reakcjach, gdzie generują reaktywne formy tlenu zdolne do degradacji barwników w roztworach wodnych. Materiały te są chemicznie stabilne, co jest, korzystne w trudnych warunkach reakcji.

Wszystkie z wymienionych materiałów, dzięki swoim unikalnym właściwościom, oferują nowe możliwości w procesach dekoloryzacji, poprawiając efektywność i stabilność reakcji katalitycznych. Integracja z innymi technologiami oczyszczania ścieków, takimi jak procesy membranowe czy biodegradacja, może dodatkowo zwiększyć efektywność, ekonomiczność i wszechstronność tych metod.

12. Bibliografia

[1] M. Balter, Clothes make the (Hu) man, Science (1979) 325 (2009) 1329. https://doi.org/10.1126/SCIENCE.325_1329A/ASSET/4617CF3E-5E00-4590-B646-9CF7071307A4/ASSETS/GRAPHIC/325_1329A_F1.GIF.

[2] D. Cristea, G. Vilarem, Improving light fastness of natural dyes on cotton yarn, Dyes and Pigments 70 (2006) 238–245. https://doi.org/10.1016/J.DYEPIG.2005.03.006.

[3] W.H. Perkin, XIX. On colouring matters derived from coal tar, Quarterly Journal of the Chemical Society of London 14 (1862) 230–255. https://doi.org/10.1039/QJ8621400230.

[4] E. Hagan, J. Poulin, Statistics of the early synthetic dye industry, Herit Sci 9 (2021) 1–14. https://doi.org/10.1186/S40494-021-00493-5/TABLES/3.

[5] S. Nishijima, S. Eckroad, A. Marian, al -, Y. Zhang, Y. Wang -, Q. Liu, Pollution and Treatment of Dye Waste-Water, IOP Conf Ser Earth Environ Sci 514 (2020) 052001. https://doi.org/10.1088/1755-1315/514/5/052001.

[6] E. B.M. Adesanmi, Y.-T. Hung, H. Paul, C. Huhnke, Comparison of dye wastewater treatment methods: A review., GSC Advanced Research and Reviews, 10(2) 10 (2022) 126. https://doi.org/https://doi.org/10.5281/zenodo.6331586.

[7] S. Khan, A. Malik, Environmental and health effects of textile industry wastewater, Environmental Deterioration and Human Health: Natural and Anthropogenic Determinants 9789400778900 (2014) 55–71. https://doi.org/10.1007/978-94-007-7890-0_4/FIGURES/2.

[8] S.S. Affat, Classifications, Advantages, Disadvantages, Toxicity Effects of Natural and Synthetic Dyes: A review, Classifications, Advantages, Disadvantages, Toxicity Effects of Natural and Synthetic Dyes: A Review. University of Thi-Qar Journal of Science 8 (2021).

[9] R. Kant, Textile dyeing industry an environmental hazard, Nat Sci (Irvine) 2012 (2011) 22–26. https://doi.org/10.4236/NS.2012.41004.

[10] A.K. Al-Buriahi, A.A. Al-Gheethi, P. Senthil Kumar, R.M.S. Radin Mohamed, H. Yusof, A.F. Alshalif, N.A. Khalifa, Elimination of rhodamine B from textile wastewater using nanoparticle photocatalysts: A review for sustainable approaches, Chemosphere 287 (2022) 132162. https://doi.org/10.1016/J.CHEMOSPHERE.2021.132162.

[11] Y. Zhang, Y. Zhang -, H. Hui, J. Liu, G. Dong, al -, Q. Li, K. Dong, Y. Tu, Q. Liu, Pollution and Treatment of Dye Waste-Water, IOP Conf Ser Earth Environ Sci 514 (2020) 052001. https://doi.org/10.1088/1755-1315/514/5/052001.

[12] L.D. Ardila-Leal, R.A. Poutou-Piñales, A.M. Pedroza-Rodríguez, B.E. Quevedo-Hidalgo, I. Capela, M. Kamali, A. Zuorro, A Brief History of Colour, the Environmental Impact of Synthetic Dyes and Removal by Using Laccases, Molecules 2021, Vol. 26, Page 3813 26 (2021) 3813. https://doi.org/10.3390/MOLECULES26133813.

[13] Q. Wang, S. Tian, P. Ning, Degradation Mechanism of Methylene Blue in a Heterogeneous Fenton-like Reaction Catalyzed by Ferrocene, Ind Eng Chem Res 53 (2013) 643–649. https://doi.org/10.1021/IE403402Q.

[14] I.G. Laing, The impact of effluent regulations on the dyeing industry, Review of Progress in Coloration and Related Topics 21 (1991) 56–71. https://doi.org/10.1111/J.1478-4408.1991.TB00081.X.

[15] S. Kobylewski, M.F. Jacobson, Toxicology of food dyes, Int J Occup Environ Health 18 (2012) 220–246. https://doi.org/10.1179/1077352512Z.00000000034.

[16] H.J.H. Fenton, LXXIII.—Oxidation of tartaric acid in presence of iron, Journal of the Chemical Society, Transactions 65 (1894) 899–910. https://doi.org/10.1039/CT8946500899.

[17] F. Haber, J. Weiss, Über die Katalyse des Hydroperoxydes, Naturwissenschaften 20 (1932) 948–950. https://doi.org/10.1007/BF01504715/METRICS.

[18] F. Haber, J. Weiss, J.O. Seph, W. Eiss, The catalytic decomposition of hydrogen peroxide by iron salts, Proc R Soc Lond A Math Phys Sci 147 (1934) 332–351. https://doi.org/10.1098/RSPA.1934.0221.

[19] A. Babuponnusami, K. Muthukumar, A review on Fenton and improvements to the Fenton process for wastewater treatment, J Environ Chem Eng 2 (2014) 557–572. https://doi.org/10.1016/J.JECE.2013.10.011.

[20] A.G. Gutierrez-Mata, S. Velazquez-Martínez, A. Álvarez-Gallegos, M. Ahmadi, J.A. Hernández-Pérez, F. Ghanbari, S. Silva-Martínez, Recent Overview of Solar Photocatalysis and Solar Photo-Fenton Processes for Wastewater Treatment, International Journal of Photoenergy 2017 (2017) 8528063. https://doi.org/10.1155/2017/8528063.

[21] A. Zecchina, S. Bordiga, E. Groppo, Selective Nanocatalysts and Nanoscience: Concepts for Heterogeneous and Homogeneous Catalysis, Selective Nanocatalysts and Nanoscience: Concepts for Heterogeneous and Homogeneous Catalysis (2011). https://doi.org/10.1002/9783527635689.

[22] E. Rápó, S. Tonk, Factors Affecting Synthetic Dye Adsorption; Desorption Studies: A Review of Results from the Last Five Years (2017–2021), Molecules 2021, Vol. 26, Page 5419 26 (2021) 5419. https://doi.org/10.3390/MOLECULES26175419.

[23] V. Katheresan, J. Kansedo, S.Y. Lau, Efficiency of various recent wastewater dye removal methods: A review, J Environ Chem Eng 6 (2018) 4676–4697. https://doi.org/10.1016/J.JECE.2018.06.060.

[24] Z. Carmen, S. Daniela, Z. Carmen, S. Daniela, Textile Organic Dyes – Characteristics, Polluting Effects and Separation/Elimination Procedures from Industrial Effluents – A Critical Overview, Organic Pollutants Ten Years After the Stockholm Convention - Environmental and Analytical Update (2012). https://doi.org/10.5772/32373.

[25] E. Eren, Investigation of a basic dye removal from aqueous solution onto chemically modified Unye bentonite, J Hazard Mater 166 (2009) 88–93. https://doi.org/10.1016/J.JHAZMAT.2008.11.011.

[26] K.Y. Foo, B.H. Hameed, Decontamination of textile wastewater via TiO2/activated carbon composite materials, Adv Colloid Interface Sci 159 (2010) 130–143. https://doi.org/10.1016/J.CIS.2010.06.002.

[27] G. Crini, E. Lichtfouse, Advantages and disadvantages of techniques used for wastewater treatment, Environ Chem Lett 17 (2019) 145–155. https://doi.org/10.1007/S10311-018-0785-9/TABLES/1.

[28] T. Islam, M.R. Repon, T. Islam, Z. Sarwar, M.M. Rahman, Impact of textile dyes on health and ecosystem: a review of structure, causes, and potential solutions, Environmental Science and Pollution Research 2022 30:4 30 (2022) 9207–9242. https://doi.org/10.1007/S11356-022-24398-3.

[29] M.A.M. Salleh, D.K. Mahmoud, W.A.W.A. Karim, A. Idris, Cationic and anionic dye adsorption by agricultural solid wastes: A comprehensive review, Desalination 280 (2011) 1–13. https://doi.org/10.1016/J.DESAL.2011.07.019.

[30] N. Sivarajasekar, R. Baskar, Agriculture waste biomass valorisation for cationic dyes sequestration: A concise review, Available Online Www.Jocpr.Com Journal of Chemical and Pharmaceutical Research 7 (2015).

[31] Z. Urbanczyk-Lipkowska, A.-M. Caminade, C. Ornelas, D. Astruc, Ferrocene-Based Drugs, Delivery Nanomaterials and Fenton Mechanism: State of the Art, Recent Developments and Prospects, Pharmaceutics 2023, Vol. 15, Page 2044 15 (2023) 2044. https://doi.org/10.3390/PHARMACEUTICS15082044.

13. Załączniki

Załącznik I

A(I)

Adrian Radoń, **Sylwester Łoński**, Tymon Warski, Rafał Babilas, Tomasz Tański, Mariusz Dudziak, Dariusz Łukowiec;

Catalytic activity of non-spherical shaped magnetite nanoparticles in degradation of Sudan I, Rhodamine B and Methylene Blue dyes

Applied Surface Science, Volume 487, 1, September 2019, Pages 1018-1025

Doi: 10.1016/j.apsusc.2019.05.091 Impact Factor: **6,3** Punkty MNiSW: 140

Applied Surface Science 487 (2019) 1018–1025

Contents lists available at ScienceDirect

Applied Surface Science

journal homepage: www.elsevier.com/locate/apsusc

Full length article

Catalytic activity of non-spherical shaped magnetite nanoparticles in degradation of Sudan I, Rhodamine B and Methylene Blue dyes

Adrian Radoń[a], Sylwester Łoński[b], Tymon Warski[a], Rafał Babilas[a], Tomasz Tański[a], Mariusz Dudziak[b], Dariusz Łukowiec[a,*]

[a] Faculty of Mechanical Engineering, Silesian University of Technology, Konarskiego 18 a St., 44-100 Gliwice, Poland
[b] Faculty of Energy and Environmental Engineering, Silesian University of Technology, Konarskiego 18 St., 44-100 Gliwice, Poland

ARTICLE INFO

Keywords:
Magnetite nanoparticles
Azo dyes
Photo-Fenton
Water treatment
Degradation mechanism

ABSTRACT

The catalytic activity of non-spherical shaped Fe_3O_4 nanoparticles synthesized by low cost co-precipitation method was tested. It was presented, that magnetite nanoparticles can be used to degrade not only Rhodamine B and Methylene Blue, but above all cancerogenic azo dye – Sudan I. It was confirmed, that the degradation of Rhodamine B can be described by pseudo-zero-order kinetic model, whereas degradation of Methylene Blue by pseudo-first-order kinetic model. The degradation mechanism of Sudan I by photo-Fenton reaction was proposed. It was noted, that this double-stage process can be associated with hydroxylation of Sudan I and degradation of derivates, such as 4′-OH-Sudan I and 6-OH-Sudan I. Therefore, it cannot be simple describe by one kinetic model. The introduction of hydroxyl group results in an increase of the absorbance, which in turn is associated with hyperchromic effect.

1. Introduction

Azo dyes are synthetic organic compounds with an azo bond (—N=N—) in their structure [1]. These dyes are the main group of compounds used for dyeing purposes, mostly in textile and food industry, and make up for near 70% of all commercial dyes [2]. They are generally considered to be xenobiotic compounds and can cause hyperactivity or photophobia [3,4]. It was confirmed, that Sudan I can cause cancer in the liver or bladder tumors, in the liver or urinary bladder in rats, mice, and rabbits. Therefore is classified in the 3rd degree of carcinogenicity [5,6]. However despite this, and the prohibition of adding to food, it happens to be added to powdered pepper [7,8]. According to that, many research groups addressed the problem of a degradation of azo-compounds [9–11]. The decomposition of dyes can occur in the presence of other nanostructures such as Ag_2CrO_4 and $AgCr_2O_7$ [12], ZrO_2 [13], $ZnTiO_3$ [14], $Pr_2Zr_2O_7$ [15], $Cu_3V_2O_8$ [16], NiO [17] or $Nd_2Zr_2O_7$-Nd_2O_3 nanocomposite [18]. For example, Paramasivama et al. presented degradation results of azo compound Acid Orange 7 in the presence of TiO_2 nanotube layers loaded with Ag and Au nanoparticles [19]. Safajou et al. presented similar results of the degradation of Rhodamine B (RhB) using graphene/Pd/TiO_2 composites [20]. To degrade chemical dyes, such as azo dyes, many different processes were proposed in literature. Few of the most commonly used are advanced oxidation processes such as: electrochemical oxidation, anodic oxidation, Fenton reaction [21,22]. The most commonly used, Fenton reaction, is a catalytic process that converts hydrogen peroxide into a highly reactive hydroxyl radicals [23]. The Fenton reaction was used to decompose different azo-dyes such as: Reactive Yellow 84, Reactive Red 120 and Red MX-5B [11,24]. Additionally, this process was used for example by Yang et al. to degrade Methylene Blue (MB) in the presence of magnetite particles [25].

According to Kefeni et al. near 73% of scientific papers from 2004 to 2017 related to water and wastewater treatment by spinel ferrite nanoparticles were connected with Fe_3O_4 nanoparticles [26]. Magnetite nanoparticles (Fe_3O_4 NPs) can be used in Fenton reaction as a heterogeneous catalyst, which is associated with their highly reactive surface. Different methods synthesis of Fe_3O_4 NPs such as: co-precipitation [27], sol-gel [28], hydrothermal [29], electrochemical [30] and sonochemical [31] methods were proposed. However, synthesis of non-spherical shaped magnetite NPs is difficult. Vaysylkiv et al. used co-precipitation method with and without chitosan addition to obtain various morphologies of Fe_3O_4 NPs from cubic, octahedral, flower-like, rod-like, quasi-spherical to rice-seed-like [32]. Difference in magnetic properties of rod-shape and spherical-shaped Fe_3O_4NPs synthesized using piperidine was described by Singh et al. They reported, that the rod-shaped NPs had higher magnetization than spherical-shaped ones

* Corresponding author.
E-mail address: dariusz.lukowiec@polsl.pl (D. Łukowiec).

https://doi.org/10.1016/j.apsusc.2019.05.091
Received 9 November 2018; Received in revised form 8 April 2019; Accepted 8 May 2019
Available online 09 May 2019
0169-4332/

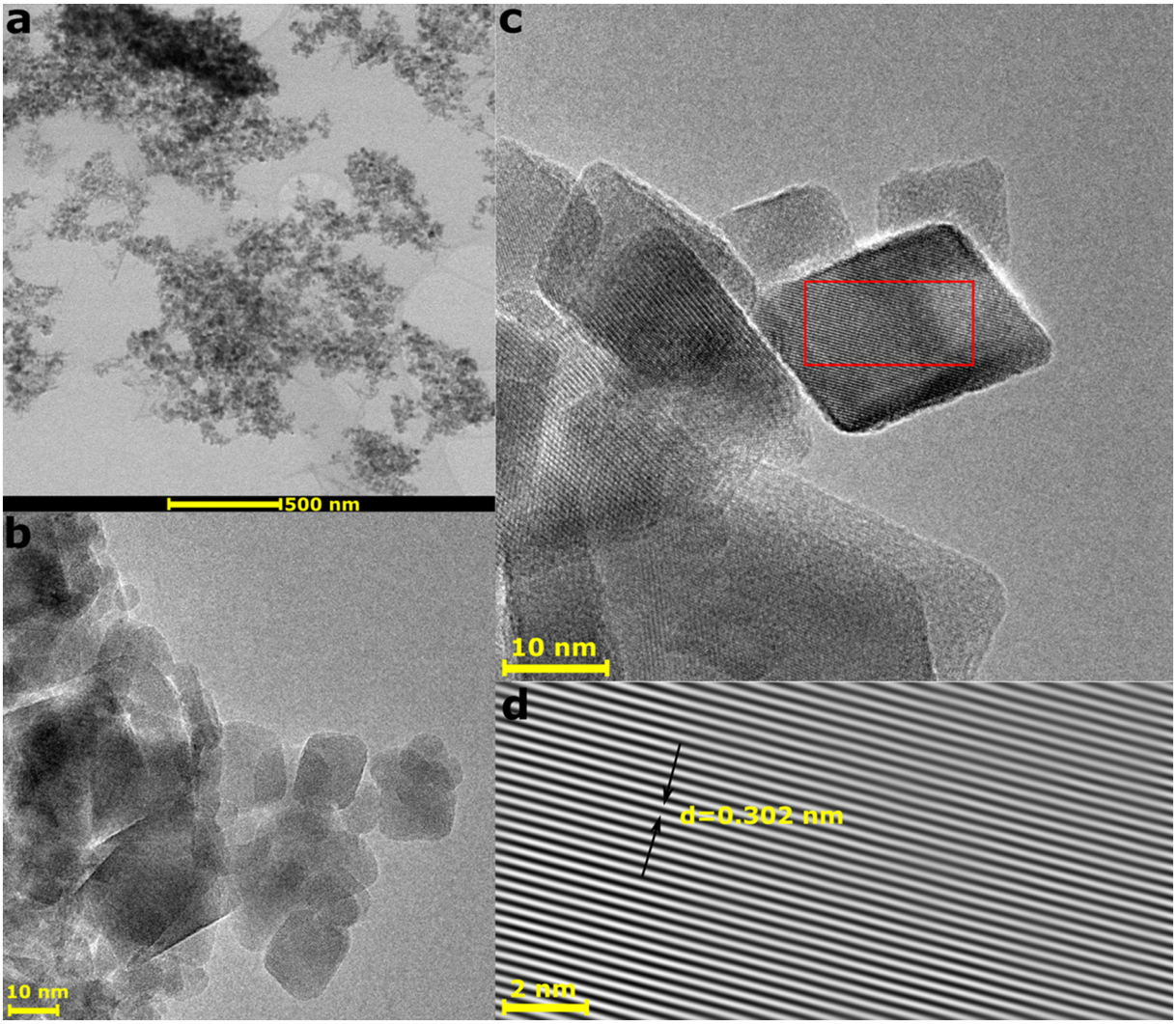

Fig. 1. Results of TEM images analysis: a) STEM image of ultrafine, agglomerated magnetite nanoparticles; b) and c) TEM images of octahedral and cubic shaped Fe_3O_4 NPs; d) lattice spacing characterized for Fe_3O_4 identified in red marked region on TEM image (c) corresponding to the (222) lattice planes (theoretical value $d = 0.296$ nm).

and can be used as electromagnetic interference shielding materials [33]. Martinez-Boubeta et al. recently reported, that the cubic shaped Fe_3O_4 NPs synthesized by a one-pot method are characterized by superior heat induction power and can be used for magnetic hyperthermia applications. These properties were related to the high surface magnetic anisotropy and tendency to aggregation into chains [34]. Moreover, influence of size on magnetic hyperthermia for cubic shape Fe_3O_4 NPs synthesized by similar method was described in detail [35]. Wang et al. described the method of synthesis of octahedral and cubic nanocages from Cu_2O NPs. The hollow nanostructures can be used in various applications like nanoscale reactors, drug delivery etc. [36]. On the other hand, cubic shape Fe_3O_4 NPs obtained by co-precipitation method was used for heat transfer applications due to their surprising thermal conductivity property. Sundar et al. described the enchantment of thermal conductivity of Fe_3O_4 ferrofluid based on ethylene glycol and water mixture increased with the number of nanoparticles and temperature [37]. Qian et al. reported, that polygonal Fe_3O_4 NPs obtained by solvothermal method can be used to synthesis of polygonised carbon nanotubes. They described inhomogeneous catalyst activity of hexagonal magnetite NPs [38]. Moreover, the catalytic activity of magnetite nanoparticles was tested and describe; especially in degradation of different dyes. For example, Wand et al. synthesized Fe_3O_4 NPs by co-precipitation method and described influence of pH on their catalytic activity in decolorization process of Rhodamine B [39]. Similar researches carried out by Khorshidi et al. confirmed that the magnetite NPs synthesized by the same method can be used as catalyst to degrade MB [40].

In this work, non-spherical shaped Fe_3O_4 NPs were synthesized by simple co-precipitation method without usage of organic modifiers. Their structure and catalytic properties were described. It was confirmed, that these nanoparticles can be used to degrade different dyes in alkaline pH and can be also used to perform hydroxylation of Sudan I azo dye. Moreover, according to our knowledge this is the first study, in which mechanism degradation and hydroxylation of Sudan I by photo-Fenton reaction was proposed.

2. Experimental section

2.1. Synthesis of non-spherical shaped Fe_3O_4 NPs

The Fe_3O_4 nanoparticles were synthesized by co-precipitation method. For this purpose $FeCl_3$ and $FeSO_4{\cdot}7H_2O$ (molar ratio 2:1) were dissolved in 50 ml distilled water. At the same time second solution containing 3.2 g KOH and 50 ml distilled water was prepared. Both solutions were added dropwise to vigorous stirring 50 ml distilled water. Afterwards, to increase pH 40 ml of solution containing 4 g KOH

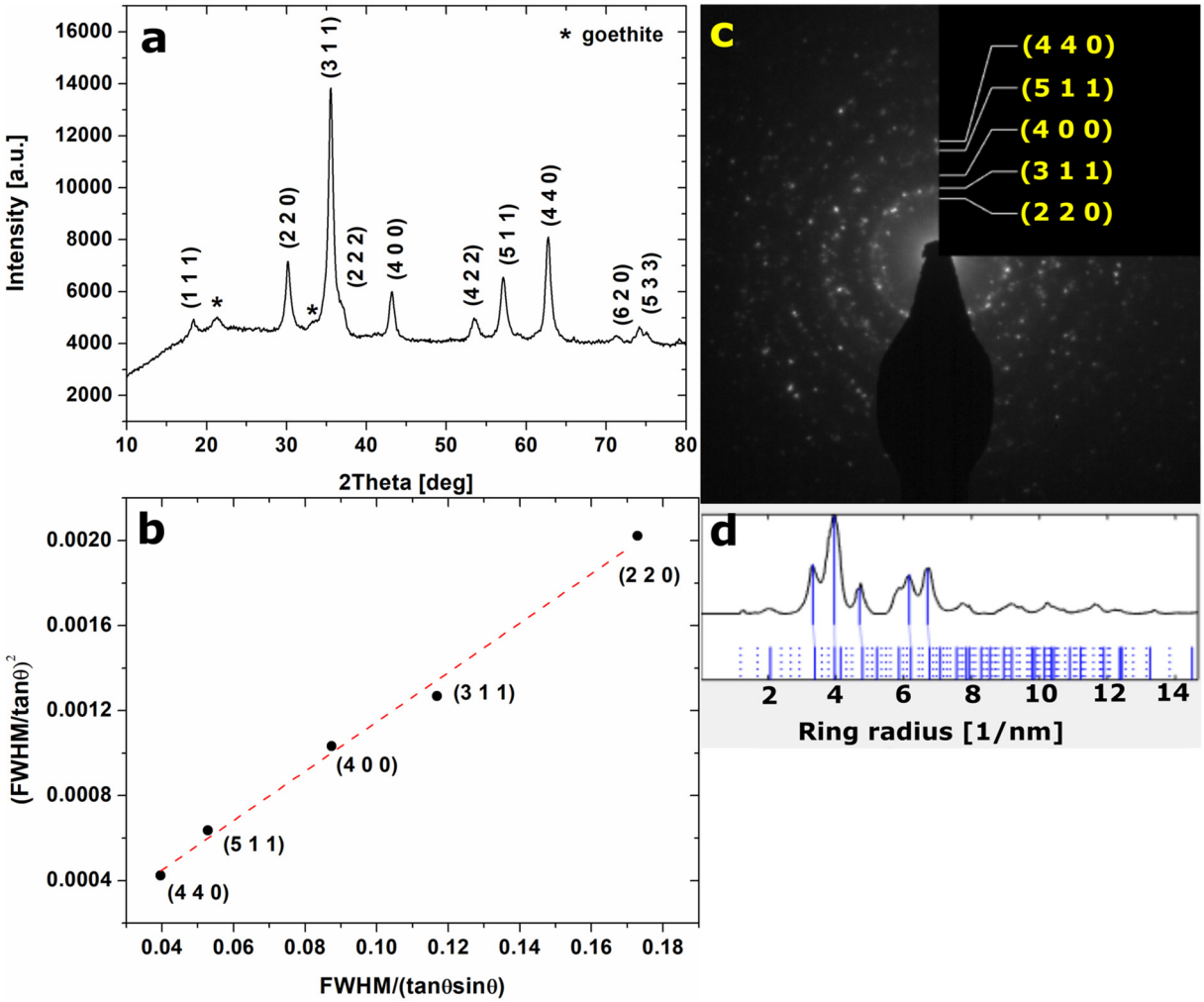

Fig. 2. Results of structure analysis of Fe_3O_4 NPs: a) XRD pattern of Fe_3O_4 NPs with marked Miller indices; b) Halder-Wagner plot received from five different reflexes with the highest intensity presented on (b); c) and d) SAED pattern and corresponding linear pattern with marked Miller indices characteristic for Fe_3O_4

was added dropwise to the stirring mixture. Finally, the mixture had undergone a sonification process (40 kHz, 120 W) by 15 min in 50 °C. The precipitate was collected and filtered, washed 3 times by distilled water then by ethanol, acetone and once again ethanol. The synthesized Fe_3O_4 nanoparticles were dried at 60 °C.

2.2. Materials characterization

Transmission electron microscopy (TEM), scanning transmission electron microscopy (STEM) as well as selected area electron diffraction (SAED) patterns were used to determine chemical composition, structure and morphology of Fe_3O_4 NPs. For this purpose, nanoparticles were dispersed in analytical grade ethanol and few drops were placed on the copper TEM grid with a carbon film and examined using transmission electron microscope S/TEM TITAN 80-300. The X-ray diffraction (XRD) patterns were collected using X-ray diffractometer Rigaku MiniFlex 600 with a copper tube Cu Kα ($\lambda = 0.15406$ nm), a tube voltage of 40 kV, and a current of 15 mA, using a D/teX Ultra silicon strip detector.

2.3. Degradation process

The 0.05 mM solution of MB, 0.025 mM of RhB and 0.05 mM of Sudan I were prepared. To dissolve Sudan I mixture of water and acetone in a volume ratio 2:3 was chosen as a solvent. The analysis of dyes degradation process was carried out using Thermo Scientific Evolution 220 spectrophotometer. For this purpose 0.5 ml H_2O_2 (30%), 2 ml of water dispersion of Fe_3O_4 NPs (4 g/L) and 3 ml of dyes solutions were mixed. Degradation of dyes was carried out under UV irradiation using an UV lamp with $\lambda = 365$ nm and $P = 36$ W at ambient temperature. The same experimental conditions were used to perform degradation without catalyst (UV/H_2O_2) using 2 ml of water instead Fe_3O_4 dispersion. The pH value equaled to 10 was obtained by NaOH addition. The blank test was performer for solution containing the same amount of H_2O instead H_2O_2. The adsorption of dyes on the surface of Fe_3O_4 NPs was performed in the same solution as for blank test. Time of adsorption was equal to 60 min.

3. Results and discussion

3.1. Structure of Fe_3O_4 NPs

The structure and morphology of Fe_3O_4 NPs were presented in Fig. 1. The observed agglomeration of magnetite nanoparticles (Fig. 1a) can be associated with high surface energy provided by the surface ratio to the total amount of nanoparticles and is typical for nanoparticles. To maintain balance of energy Van der Waals forces connection between separated nanoparticles is created, which results in uncontrolled agglomerations [41]. TEM images (Fig. 1b and c) show non-spherical shaped morphology of NPs; the most of them have octahedral or cubic shapes. Well-formed crystal structure of nanoparticles can be observed in Fig. 1d. The identified interplanar distance was related to the lattice

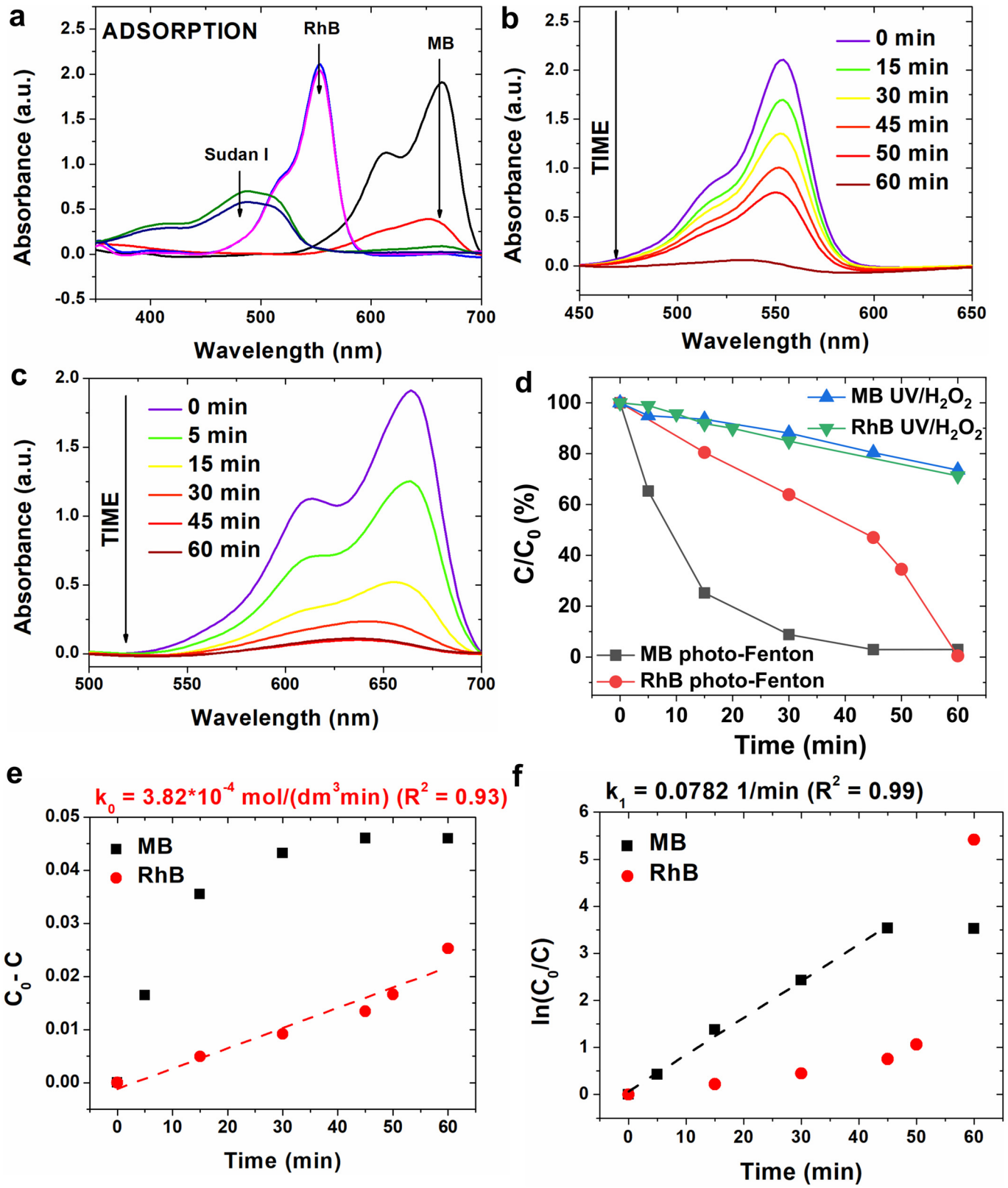

Fig. 3. UV–Vis spectra of a) dyes after adsorption process; b) RhB as a function of time over Fe_3O_4 nanoparticles under UV illumination; c) MB as a function of time over Fe_3O_4 nanoparticles under UV illumination; d) decolorization curves determined for MB and RhB degraded by photo-Fenton and UV/H_2O_2; e) C_0-C vs t plots for MB and RhB; linear relationship was observed only for RhB; f) ln(C_0/C) vs t plots for MB and RhB; linear relationship was observed only for MB (in the plots marked rate constants).

Table 1
Comparison of various catalytic systems for RhB and MB degradation by different Fenton and Fenton-like processes.

Catalyst	Dye	Reaction condition	Degradation (%)	Time (min)	Reference
Fe_2O_3–Kaolin	RhB	[dye] = 15.0 mg·L^{-1} [catalyst] = 1.0 g·L^{-1} pH = 2.21 [H_2O_2] = 0.05 mol·L^{-1}	98	120	[53]
Poly-hydroxyl-iron/sepiolite (H-Fe-S)	RhB	[dye] = 95.80 mg·L^{-1} ($2.0{\cdot}10^{-4}$ M) [catalyst] = 2.0 g·L^{-1} [H_2O_2] = 0.012 mol·L^{-1} pH = 4.25 t = 25 °C	99.8	100	[54]
Cu-doped $LaTiO_3$	RhB	[dye] = 8 mg·L^{-1} [catalyst] = 1.4 g·L^{-1} [H_2O_2] = 0.02 mol·L^{-1}	94	120	[55]
$NiFe_2O_4$	RhB	[dye] = 10.0 mg·L^{-1} [catalyst] = 4 g·L^{-1} pH = 3.0 [$H_2C_2O_4$] = 0.001 mol·L^{-1} t = 25 °C	98.7	60	[56]
Fe@Fe_2O_3 core-shell nanowires	RhB	[dye] = 5 mg·L^{-1} [catalyst] = 0.018 mol·L^{-1} pH = 2.0 sonochemical-assisted Fenton	almost 100	60	[57]
Fe_3O_4	RhB	[dye] = 13 mg·L^{-1} [catalyst] = 1.5 g·L^{-1} pH = 10	99.5	60	This article
$FeSO_4$	MB	[dye] = $3.13{\cdot}10^{-1}$ mol·L^{-1} [catalyst] = 3.58×10^{-5} mol·L^{-1} [H_2O_2] = 4.41×10^{-4} mol·L^{-1} T = 25.85 °C pH = 2.5	99	120	[58]
Fe_3O_4	MB	[dye] = 100 mg·L^{-1} pH = 6.8 [H_2O_2] = 0.3 mol·L^{-1} t = 25 °C	20	60	[25]
$Fe_{2.77}Ti_{0.23}O_4$	MB	[dye] = 100 mg·L^{-1} pH = 6.8 [H_2O_2] = 0.3 mol·L^{-1} t = 25 °C	29	60	[25]
$Fe_{2.5}Ti_{0.5}O_4$	MB	[dye] = 100 mg·L^{-1} pH = 6.8 [H_2O_2] = 0.3 mol·L^{-1} t = 25 °C	65	60	[25]
$Fe_{2.22}Ti_{0.78}O_4$	MB	[dye] = 100 mg·L^{-1} pH = 6.8 [H_2O_2] = 0.3 mol·L^{-1} t = 25 °C	90	60	[25]
Fe_3O_4	MB	[dye] = 17.5 mg·L^{-1} [catalyst] = 1.5 g·L^{-1} pH = 10	97	60	This article

spacing between the (222) lattice planes in crystalline magnetite.

In Fig. 2a presented XRD pattern of synthesized nanoparticles with marked characteristic diffraction peaks. The magnetite structure (space groups: *Fd-3m*, DB card number: 9005812) was observed. Moreover, two additional diffraction peaks with low intensity were assigned to the goethite structure (space groups: *Pbnm*, DB card number: 9003078). However, it can be treated as an impurity formed during the magnetite synthesis without the using of a protective atmosphere. The average crystallite size (D) of Fe_3O_4 NPs and strain (ε) were calculated based on Halder-Wagner method [42,43]:

$$\left(\frac{\beta^*}{d}\right)^2 = \frac{1}{D}\frac{\beta^*}{d^2} + \left(\frac{\varepsilon}{2}\right)^2 \quad (1)$$

$$\beta^* = \frac{(FWHM)cos\theta}{\lambda} \quad (2)$$

$$d = \frac{2sin\theta}{\lambda} \quad (3)$$

where: FWHM is the full-width at half maximum, λ is the wavelength of X-ray and θ is the diffraction angle. On the assumption that the Lorentzian and Gaussian components of β^* are due to the size and strain, Eq. (3) can be rewritten as:

$$\left(\frac{FWHM}{tan\theta}\right)^2 = \frac{K\lambda}{D}\frac{FWHM}{tan\theta sin\theta} + \left(\frac{\varepsilon}{2}\right)^2 \quad (4)$$

where K is a constant.

The values of average crystallite size and strain can be determined based on the plot of $(FWHM/tan\theta)^2$ vs $FWHM/(tan\theta sin\theta)$ as slope and intercept, respectively. The calculated average crystallite size and strain were equaled to 12.47 nm and 0, respectively. Additionally, to confirm presence of magnetite structure SAED pattern and corresponding linear plot were presented in Fig. 2c and d. The characteristic diffraction rings related to the magnetite structure confirm polycrystalline structure of sample.

3.2. Catalytic activity in degradation of Methylene Blue and Rhodamine B

The adsorption ability of nanomaterials depends on physical and chemical properties along with surface area of the adsorbent

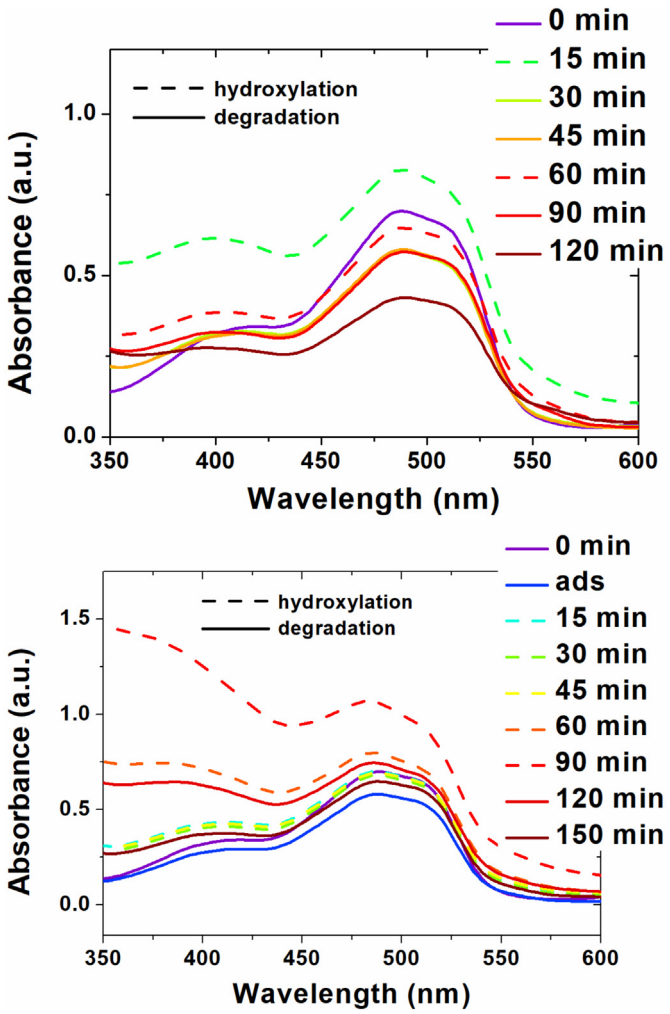

Fig. 4. UV–vis spectra of Sudan I as a function of time over Fe_3O_4 nanoparticles under UV illumination (a) and in absence of UV illumination – experiment in the dark (b) with marked hydroxylation and degradation processes of Sudan I.

responsible for mass transfer rate [44]. Low adsorption capacity of Fe_3O_4 NPs is associated with low amount of chemical bonds between dyes molecules and nanoparticles [45]. Additionally, concentration of adsorbent, pH and temperature have high impact on adsorption ability. Adsorption studies of Fe_3O_4 NPs showed, that among three dyes: Methylene Blue, Sudan I and Rhodamine B, the last one had the worst ability to sorption on the NPs surface. Average adsorption capacity for RhB was 10% (1.0 g L^{-1}) after 60 min [46]. Similar results were obtained for synthesized non-spherical shaped Fe_3O_4 NPs. The changes in absorbance associated with adsorption of molecules on the surface of catalyst were presented in Fig. 3a for three tested dyes. It can be noticed, that the Sudan I and MB can be adsorbed on the surface of nanoparticles, whereas slightly changes in absorbance can be observed for RhB adsorption process.

Fig. 3b and c show the UV–Vis spectra at the various stages of degradation of RhB and MB, respectively. Decreasing of absorbance peak intensity is related to the removing of the dyes from the solutions. This was clearly presented in the Fig. 3d as C_0/C ratio and compared with results of the same experiments, however without magnetite nanoparticles. After 60 min, almost complete degradation of the RhB and MB was observed for heterogeneous photo-Fenton process (97% RhB and 99.5% of MB), whereas only 29% of RhB and 26% of MB degraded without usage of catalyst. These results are comparable and even better than for other nanoparticles and nanocomposites (see Table 1). The kinetics of these dyes degradation was studied based on the three kinetics models, supposing that, the reaction of degradation is zero-order, first-order or second-order. For this purpose, plots of C_0-C (for zero order reaction), $\ln(C_0/C)$ (for first-order reaction) and $1/C$-$1/C_0$ (for second-order reaction) versus time were prepared and based on linear regression mechanism of degradation was chosen [47,48]. The plots of $ln(C_0/C_t)$ vs t were presented in Fig. 3f. It can be noticed, that only degradation of MB can be described by this kinetic model. The determined pseudo-first-order rate constant $k_1 = 0.0782\,min^{-1}$ is about 2.7 times higher than that for the conventional $FeCl_2$ [49]. It can be noticed, that degradation of RhB can be described by pseudo-zero-order kinetic model (R^2 equalled to 0.93, whereas for first-order only 0.67). This difference between degradation of RhB and MB can be associated with interaction between surface of non-spherical shaped Fe_3O_4 NPs and dyes molecules. It can be concluded, that for RhB, which cannot be adsorbed on the surface of nanoparticles reaction degradation can be described by pseudo-zero-order, in which the reaction rate does not depend on the concentration of substrates, whereas for MB, which can be easily adsorbed on the Fe_3O_4 NPs surface by pseudo-first-order, in which the reaction rate depends on the concentration of one of the substrates.

Degradation of Rhodamine B and Methylene Blue is well known and described in literature. AlHamedi et al. showed that the degradation of RhB is based on decomposition of the dyes molecules into shorter carbon chains, aliphatic compounds, alcohols and ketones. These products are smaller, less toxic and less colouring than the RhB. Moreover, Nidheesh et al. presented in their studies, that the decomposition of RhB can results in formation of benzene, benzoic acid, ethamine, diethyloammonium and penta-1,4-dien-3-ylium. They also postulated full mineralization of these compounds to carbon dioxide, water and ammonia [50,51]. Wang et al. proposed degradation mechanism of MB. The first possible path is associated with breaking up C—S and C—N bonds and the oxidation of the remaining products. The other way is related to the breaking up C—N bond, further oxidation and degradation of this intermediate compound. The last degradation pathway was related to the hydroxylation of MB and formation of 4*aH*-phenothiazine-4,6-disulfonic acid 5-oxide. They also postulated full mineralization of these compounds [52].

3.3. Degradation of Sudan I

The degradation of Sudan I dye was tested under UV illumination and in the dark. The catalytic degradation by non-spherical shaped Fe_3O_4 NPs was presented in Fig. 4a and b. Non-linear changes in absorbance can be observed for reactions in the dark and under UV illumination. This behavior can be associated with two different processes: degradation and hydroxylation. Therefore, double-step mechanism decolorization of Sudan I in alkaline environment was proposed and presented in Fig. 5. First of all, azo (OH) ➔ hydrazo (NH) tautomeric displacement occurs [59]. Afterwards, $HO^{\bullet}$ radicals produced by Fenton (in the dark) or photo-Fenton (under UV-illumination) reactions react with the Sudan I molecules and two new derivates can be formed: 4′-OH Sudan I and 6-OH Sudan I. Introduction of hydroxyl group results in an increase of the absorbance, which in turn is associated with hyperchromic effect [60] (process marked by dash line in Fig. 5a and b). These compounds were also found to be the major product of hydroxylation of Sudan I in vivo and excreted in urine [6]. In the next stage $HO^{\bullet}$ radicals react with Sudan I derivates and break hydrazone bond – two new compounds with hydroxylamine and oxime groups can be formed. Moreover, photo-Fenton reaction is faster than Fenton reaction in dark, therefore in absorbance spectra presented in Fig. 4 a degradation and hydroxylation reactions can be observed as step by step process, whereas in dark (Fig. 4b) hydroxylation of Sudan I is a dominant process and degradation of Sudan I derivates occurs at 120 min.

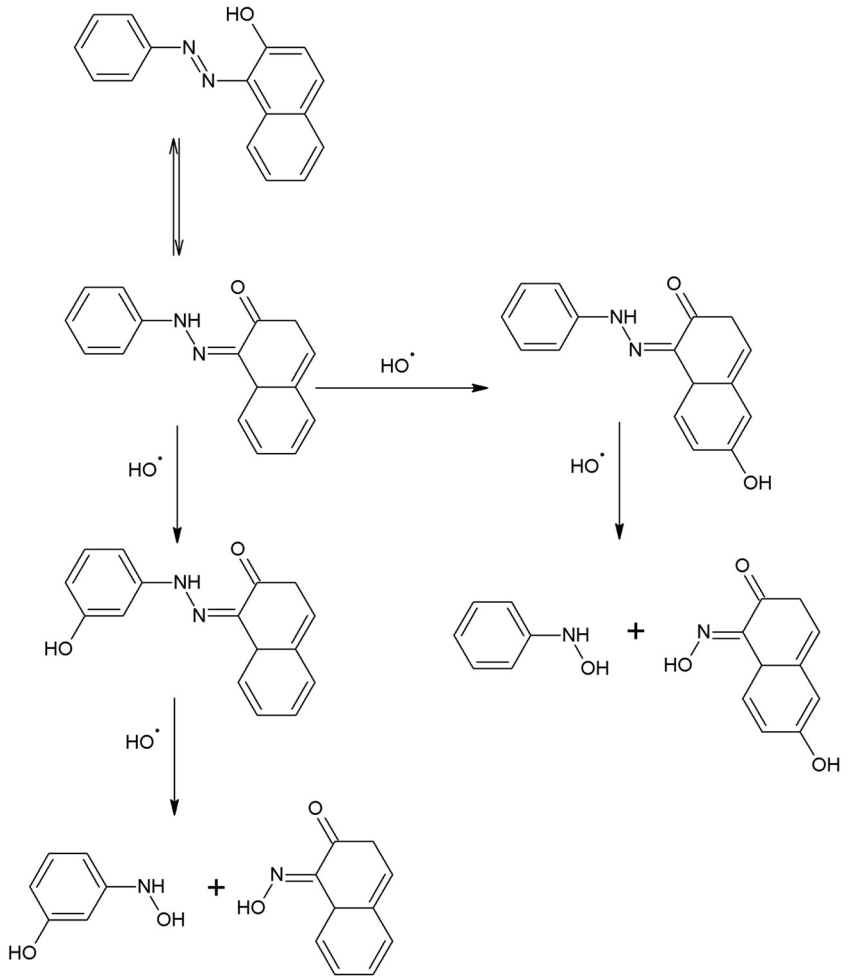

Fig. 5. Proposed hydroxylation and degradation mechanism of Sudan I developed based on performed experiments and literature data.

4. Conclusions

Octahedral and cubic shaped Fe_3O_4 NPs with average crystallite size equaled to 12.47 nm were synthesized by co-precipitation method in very high pH solution without usage of any modifiers. The degradation of Rhodamine B and Methylene Blue by photo-Fenton reaction over Fe_3O_4 NPs surface was confirmed. It was noted, that the degradation of RhB and MB proceeds differently which is related to absorption of dyes on the surface of nanoparticles. The 97% of MB and 99.5% of RhB were degraded at 60 min. It can be concluded, that for RhB, which cannot be adsorbed on the surface of nanoparticles reaction degradation can be described by pseudo-zero-order, whereas for MB, which can be easy adsorbed on the Fe_3O_4 NPs surface by pseudo-first-order. From the other hand, the nonlinear changes observed in UV–Vis spectra of Sudan I under UV and without UV irradiation were related to the 2 different reactions: hydroxylation and degradation of this dye. The degradation mechanism of Sudan I by photo-Fenton reaction was proposed for the first time. It was concluded, that the two derivates can be formed: 4′-OH Sudan I and 6-OH Sudan I in the intermediate stage of degradation of this azo compound. However, there are some disadvantages of this degradation method such as necessity to adjust the pH to a high value, the necessity of continuous UV light exposure and the requirement of receiving the catalyst from the post-reaction solution. Therefore, the catalyst removal should be performed by usage of magnetic field or by filtration.

Funding

This work was supported by the grant from Polish Ministry of Science and Higher Education - Diamond Grant (0220/DIA/2018/47).

References

[1] L. Gomathi Devi, S. Girish Kumar, K. Mohan Reddy, C. Munikrishnappa, Photo degradation of methyl orange an azo dye by advanced Fenton process using zero valent metallic iron: influence of various reaction parameters and its degradation mechanism, J. Hazard. Mater. (2009), https://doi.org/10.1016/j.jhazmat.2008.08.017.
[2] M.A. Hassaan, A. El Nemr, Health and environmental impacts of dyes: mini review, Org. Consum. Assoc. 1 (2017) 64–67, https://doi.org/10.11648/j.ajese.20170103.11.
[3] A. Stolz, Basic and applied aspects in the microbial degradation of azo dyes, Appl. Microbiol. Biotechnol. (2001), https://doi.org/10.1007/s002530100686.
[4] T.J. Rosol, R.A. DeLellis, P.W. Harvey, C. Sutcliffe, Endocrine system, Haschek Rousseaux's Handb, Toxicol. Pathol. (2013) 2391–2492, https://doi.org/10.1016/B978-0-12-415759-0.00058-3.
[5] Y. Lian, W. Gao, L. Zhou, N. Wu, Q. Lu, W. Han, X. Tie, Occurrence of Sudan I in paprika fruits caused by agricultural environmental contamination, J. Agric. Food Chem. (2014), https://doi.org/10.1021/jf5013067.
[6] M. Stiborová, V. Martínek, H. Rýdlová, P. Hodek, E. Frei, Sudan I is a potential carcinogen for humans: evidence for its metabolic activation and detoxication by human recombinant cytochrome P450 1A1 and liver microsomes, Cancer Res. 62 (2002) 5678–5684.
[7] S. Genualdi, S. MacMahon, K. Robbins, S. Farris, N. Shyong, L. DeJager, Method development and survey of Sudan I–IV in palm oil and chilli spices in the Washington, DC, area, Food Addit. Contam. - Part A Chem. Anal. Control. Expo. Risk Assess. (2016), https://doi.org/10.1080/19440049.2016.1147986.
[8] D. Taverna, L. Di Donna, F. Mazzotti, B. Policicchio, G. Sindona, High-throughput determination of Sudan Azo-dyes within powdered chili pepper by paper spray mass spectrometry, J. Mass Spectrom. (2013), https://doi.org/10.1002/jms.3181.
[9] S. Wang, A comparative study of Fenton and Fenton-like reaction kinetics in

decolourisation of wastewater, Dyes Pigments 76 (2008) 714–720, https://doi.org/10.1016/j.dyepig.2007.01.012.
[10] M.S. Lucas, J.A. Peres, Decolorization of the azo dye reactive black 5 by Fenton and photo-Fenton oxidation, Dyes Pigments 71 (2006) 236–244, https://doi.org/10.1016/j.dyepig.2005.07.007.
[11] C.L. Hsueh, Y.H. Huang, C.C. Wang, C.Y. Chen, Degradation of azo dyes using low iron concentration of Fenton and Fenton-like system, Chemosphere 58 (2005) 1409–1414, https://doi.org/10.1016/j.chemosphere.2004.09.091.
[12] F. Soofivand, F. Mohandes, M. Salavati-Niasari, Silver chromate and silver dichromate nanostructures: sonochemical synthesis, characterization, and photocatalytic properties, Mater. Res. Bull. (2013), https://doi.org/10.1016/j.materresbull.2013.02.025.
[13] S. Zinatloo-Ajabshir, M. Salavati-Niasari, Facile route to synthesize zirconium dioxide (ZrO_2) nanostructures: structural, optical and photocatalytic studies, J. Mol. Liq. (2016), https://doi.org/10.1016/j.molliq.2016.01.062.
[14] M. Salavati-Niasari, F. Soofivand, A. Sobhani-Nasab, M. Shakouri-Arani, A. Yeganeh Faal, S. Bagheri, Synthesis, characterization, and morphological control of $ZnTiO_3$ nanoparticles through sol-gel processes and its photocatalyst application, Adv. Powder Technol. (2016), https://doi.org/10.1016/j.apt.2016.07.018.
[15] S. Zinatloo-Ajabshir, M. Salavati-Niasari, Z. Zinatloo-Ajabshir, Facile size-controlled preparation of highly photocatalytically active praseodymium zirconate nanostructures for degradation and removal of organic pollutants, Sep. Purif. Technol. (2017), https://doi.org/10.1016/j.seppur.2016.12.043.
[16] M. Ghiyasiyan-Arani, M. Masjedi-Arani, M. Salavati-Niasari, Facile synthesis, characterization and optical properties of copper vanadate nanostructures for enhanced photocatalytic activity, J. Mater. Sci. Mater. Electron. (2016), https://doi.org/10.1007/s10854-016-4370-3.
[17] F. Motahari, M.R. Mozdianfard, F. Soofivand, M. Salavati-Niasari, NiO nanostructures: synthesis, characterization and photocatalyst application in dye wastewater treatment, RSC Adv. (2014), https://doi.org/10.1039/c4ra02697g.
[18] S. Zinatloo-Ajabshir, S. Mortazavi-Derazkola, M. Salavati-Niasari, Nd_2O_3-SiO_2 nanocomposites: a simple sonochemical preparation, characterization and photocatalytic activity, Ultrason. Sonochem. (2018), https://doi.org/10.1016/j.ultsonch.2017.11.026.
[19] I. Paramasivam, J.M. Macak, P. Schmuki, Photocatalytic activity of TiO_2 nanotube layers loaded with Ag and Au nanoparticles, Electrochem. Commun. (2008), https://doi.org/10.1016/j.elecom.2007.11.001.
[20] H. Safajou, H. Khojasteh, M. Salavati-Niasari, S. Mortazavi-Derazkola, Enhanced photocatalytic degradation of dyes over graphene/Pd/TiO_2 nanocomposites: TiO_2 nanowires versus TiO_2 nanoparticles, J. Colloid Interface Sci. (2017), https://doi.org/10.1016/j.jcis.2017.03.078.
[21] P.V. Nidheesh, M. Zhou, M.A. Oturan, An overview on the removal of synthetic dyes from water by electrochemical advanced oxidation processes, Chemosphere (2018), https://doi.org/10.1016/j.chemosphere.2017.12.195.
[22] C. Salazar, C. Ridruejo, E. Brillas, J. Yáñez, H.D. Mansilla, I. Sirés, Abatement of the fluorinated antidepressant fluoxetine (Prozac) and its reaction by-products by electrochemical advanced methods, Appl. Catal. B Environ. (2017), https://doi.org/10.1016/j.apcatb.2016.10.026.
[23] H.J.H. Fenton, Oxidation of tartaric acid in presence of iron, J. Chem. Soc. (1894), https://doi.org/10.1039/ct8946500899.
[24] M. Neamtu, A. Yediler, I. Siminiceanu, A. Kettrup, Oxidation of commercial reactive azo dye aqueous solutions by the photo-Fenton and Fenton-like processes, J. Photochem. Photobiol. A Chem. (2003), https://doi.org/10.1016/S1010-6030(03)00270-3.
[25] S. Yang, H. He, D. Wu, D. Chen, X. Liang, Z. Qin, M. Fan, J. Zhu, P. Yuan, Y. Ma, X. Li, J. Zhu, P. Yuan, Decolorization of methylene blue by heterogeneous Fenton reaction using $Fe_{3-x}Ti_xO_4$ ($0 \le x \le 0.78$) at neutral pH values, Appl. Catal. B Environ. 89 (2009) 527–535, https://doi.org/10.1021/ie900666b.
[26] K.K. Kefeni, B.B. Mamba, T.A.M. Msagati, Application of spinel ferrite nanoparticles in water and wastewater treatment: a review, Sep. Purif. Technol. (2017), https://doi.org/10.1016/j.seppur.2017.07.015.
[27] L. Barbosa, T. Michelle, G. Cordeiro, Microstructural assessment of magnetite nanoparticles (Fe_3O_4) obtained by chemical precipitation under different synthesis conditions, Mater. Res. 21 (2018) 1–7.
[28] O.M. Lemine, K. Omri, B. Zhang, L. El Mir, M. Sajieddine, A. Alyamani, M. Bououdina, Sol–gel synthesis of 8nm magnetite (Fe_3O_4) nanoparticles and their magnetic properties, Superlattice. Microst. 52 (2012) 793–799, https://doi.org/10.1016/j.spmi.2012.07.009.
[29] K. Hedayati, M. Goodarzi, D. Ghanbari, Hydrothermal synthesis of Fe_3O_4 nanoparticles and flame resistance magnetic poly styrene nanocomposite, J Nanostruct 7 (2017) 32–39, https://doi.org/10.22052/jns.2017.01.004.
[30] D. Ramimoghadam, S. Bagheri, S.B.A. Hamid, Progress in electrochemical synthesis of magnetic iron oxide nanoparticles, J. Magn. Magn. Mater. 368 (2014) 207–229, https://doi.org/10.1016/j.jmmm.2014.05.015.
[31] D. Ghanbari, M. Salavati-Niasari, M. Ghasemi-Kooch, A sonochemical method for synthesis of Fe_3O_4 nanoparticles and thermal stable PVA-based magnetic nanocomposite, J. Ind. Eng. Chem. (2014), https://doi.org/10.1016/j.jiec.2013.12.098.
[32] O. Vasylkiv, O. Bezdorozhev, Y. Sakka, Synthesis of iron oxide nanoparticles with different morphologies by precipitation method with and without chitosan addition, J. Ceram. Soc. Japan. 124 (2016) 489–494, https://doi.org/10.2109/jcersj2.15288.
[33] A.K. Singh, O.N. Srivastava, K. Singh, Shape and size-dependent magnetic properties of Fe_3O_4 nanoparticles synthesized using piperidine, Nanoscale Res. Lett. 12 (2017), https://doi.org/10.1186/s11671-017-2039-3.
[34] C. Martinez-Boubeta, K. Simeonidis, A. Makridis, M. Angelakeris, O. Iglesias, P. Guardia, A. Cabot, L. Yedra, S. Estradé, F. Peiró, Z. Saghi, P.A. Midgley, I. Conde-Leborán, D. Serantes, D. Baldomir, Learning from nature to improve the heat generation of iron-oxide nanoparticles for magnetic hyperthermia applications, Sci. Rep. 3 (2013), https://doi.org/10.1038/srep01652.
[35] P. Guardia, R. Di Corato, L. Lartigue, C. Wilhelm, A. Espinosa, M. Garcia-Hernandez, F. Gazeau, L. Manna, T. Pellegrino, Water-soluble iron oxide nanocubes with high values of specific absorption rate for cancer cell hyperthermia treatment, ACS Nano 6 (2012) 3080–3091, https://doi.org/10.1021/nn2048137.
[36] Z. Wang, D. Luan, C.M. Li, F. Su, S. Madhavi, F.Y.C. Boey, X.W. Lou, Engineering nonspherical hollow structures with complex interiors by template-engaged redox etching, J. Am. Chem. Soc. 132 (2010) 16271–16277, https://doi.org/10.1021/ja107871r.
[37] L.S. Sundar, M.K. Singh, A.C.M. Sousa, Thermal conductivity of ethylene glycol and water mixture based Fe_3O_4 nanofluid, Int. Commun. Heat Mass Transf. 49 (2013) 17–24, https://doi.org/10.1016/j.icheatmasstransfer.2013.08.026.
[38] W. Qian, J. Chen, L. Wu, F. Cao, Q. Chen, Synthesis of polygonized carbon nanotubes utilizing inhomogeneous catalyst activity of nonspherical Fe_3O_4 nanoparticles, J. Phys. Chem. B 110 (2006) 16404–16407, https://doi.org/10.1021/jp062690k.
[39] G.H. Wang, K. Chen, W.B. Li, D. Wan, Q. Hu, L.L. Lu, Synthesis and catalysis of Fe_3O_4 nanoparticles for degradation of rhodamine B, Adv. Mater. Res. 734–737 (2013) 2200–2203, https://doi.org/10.4028/www.scientific.net/AMR.734-737.2200.
[40] A. Khorshidi, A.F. Shojaei, S. Shariati, R. Amin, Efficient Fenton like Degradation of Methylene Blue in Aqueous Solution by Using Fe_3O_4 Nanoparticles as Catalyst, vol. 2, (2015).
[41] G. Sharma, V. Kodali, M. Gaffrey, W. Wang, K.R. Minard, N.J. Karin, J.G. Teeguarden, B.D. Thrall, Iron oxide nanoparticle agglomeration influences dose rates and modulates oxidative stress-mediated dose–response profiles in vitro, Nanotoxicology 8 (2014) 663–675, https://doi.org/10.3109/17435390.2013.822115.
[42] A. Rebhi, T. Makhlouf, N. Njah, X-ray diffraction analysis of 99.1% recycled aluminium subjected to equal channel angular extrusion, Phys. Procedia 2 (2009) 1263–1270, https://doi.org/10.1016/j.phpro.2009.11.090.
[43] C.M. Patel, M. Chakraborty, Z.V.P. Murthy, Study on the stability and microstructural properties of barium sulfate nanoparticles produced by nanomilling, Adv. Powder Technol. 25 (2014) 226–235, https://doi.org/10.1016/j.apt.2013.04.003.
[44] H. Mittal, S.B. Mishra, Gum Ghatti and Fe_3O_4 magnetic nanoparticles based nanocomposites for the effective adsorption of rhodamine B, Carbohydr. Polym. 101 (2014) 1255–1264, https://doi.org/10.1016/j.carbpol.2013.09.045.
[45] Y. Qin, M. Long, B. Tan, B. Zhou, RhB adsorption performance of magnetic adsorbent Fe_3O_4/RGO composite and its regeneration through a Fenton-like reaction, Nano-Micro Lett 6 (2014) 125–135, https://doi.org/10.1007/BF03353776.
[46] D. Wan, W. Li, G. Wang, K. Chen, L. Lu, Q. Hu, Adsorption and heterogeneous degradation of rhodamine B on the surface of magnetic bentonite material, Appl. Surf. Sci. 349 (2015) 988–996, https://doi.org/10.1016/j.apsusc.2015.05.004.
[47] Y. Chen, Y.F. Song, Immobilization of LaW10 onto ionic-liquid-modified mesoporous silica: deep desulfurization with zero-order reaction kinetics, Chempluschem (2014), https://doi.org/10.1002/cplu.201300323.
[48] D. Malwal, P. Gopinath, Fabrication and characterization of poly(ethylene oxide) templated nickel oxide nanofibers for dye degradation, Environ. Sci. Nano. (2015), https://doi.org/10.1039/C4EN00107A.
[49] T.M. Do, J.Y. Byun, S.H. Kim, An electro-Fenton system using magnetite coated metallic foams as cathode for dye degradation, Catal. Today (2017), https://doi.org/10.1016/j.cattod.2017.05.016.
[50] F.H. AlHamedi, M.A. Rauf, S.S. Ashraf, Degradation studies of rhodamine B in the presence of UV/H_2O_2, Desalination (2009), https://doi.org/10.1016/j.desal.2008.03.016.
[51] P.V. Nidheesh, R. Gandhimathi, N.S. Sanjini, $NaHCO_3$ enhanced Rhodamine B removal from aqueous solution by graphite-graphite electro Fenton system, Sep. Purif. Technol. (2014), https://doi.org/10.1016/j.seppur.2014.06.009.
[52] Q. Wang, S. Tian, P. Ning, Degradation mechanism of methylene blue in a heterogeneous Fenton-like reaction catalyzed by ferrocene, Ind. Eng. Chem. Res. (2014), https://doi.org/10.1021/ie403402q.
[53] S. Guo, G. Zhang, J. Wang, Photo-Fenton degradation of rhodamine B using Fe_2O_3-kaolin as heterogeneous catalyst: characterization, process optimization and mechanism, J. Colloid Interface Sci. 433 (2014) 1–8, https://doi.org/10.1016/j.jcis.2014.07.017.
[54] Y. Gao, H. Gan, G. Zhang, Y. Guo, Visible light assisted Fenton-like degradation of rhodamine B and 4-nitrophenol solutions with a stable poly-hydroxyl-iron/sepiolite catalyst, Chem. Eng. J. 217 (2013) 221–230, https://doi.org/10.1016/j.cej.2012.11.115.
[55] L. Zhang, Y. Nie, C. Hu, J. Qu, Enhanced Fenton degradation of Rhodamine B over nanoscaled Cu-doped $LaTiO_3$ perovskite, Appl. Catal. B Environ. 125 (2012) 418–424, https://doi.org/10.1016/j.apcatb.2012.06.015.
[56] S.Q. Liu, L.R. Feng, N. Xu, Z.G. Chen, X.M. Wang, Magnetic nickel ferrite as a heterogeneous photo-Fenton catalyst for the degradation of rhodamine B in the presence of oxalic acid, Chem. Eng. J. 203 (2012) 432–439, https://doi.org/10.1016/j.cej.2012.07.071.
[57] Z. Ai, L. Lu, J. Li, L. Zhang, J. Qiu, M. Wu, Fe@Fe_2O_3 Core-shell nanowires as iron reagent. 1. Efficient degradation of rhodamine by a novel sono-Fenton process, J. Phys. Chem. C 111 (2007) 4087–4093, https://doi.org/10.1021/jp065559l.
[58] K. Dutta, S. Mukhopadhyay, S. Bhattacharjee, B. Chaudhuri, Chemical oxidation of methylene blue using a Fenton-like reaction, J. Hazard. Mater. 84 (2001) 57–71, https://doi.org/10.1016/S0304-3894(01)00202-3.
[59] G.R. Ferreira, H.C. Garcia, M.R.C. Couri, H.F. Dos Santos, L.F.C. De Oliveira, On the azo/hydrazo equilibrium in Sudan I azo dye derivatives, J. Phys. Chem. A (2013), https://doi.org/10.1021/jp310229h.
[60] H. Tamta, S. Kalra, R. Thilagavathi, A.K. Chakraborti, A.K. Mukhopadhyay, Nature and position of functional group on thiopurine substrates influence activity of xanthine oxidase–enzymatic reaction pathways of 6-mercaptopurine and 2-mercaptopurine are different, Biokhimiya/Biochemistry (2007), https://doi.org/10.1134/S000629790702006X.

Załącznik II

A(II)

Adrian Radoń, **Sylwester Łoński**, Mariola Kądziołka-Gaweł, Piotr Gębara, Mateusz Lis, Dariusz Łukowiec, Rafał Babilas

Influence of magnetite nanoparticles surface dissolution, stabilization and functionalization by malonic acid on the catalytic activity, magnetic and electrical properties

Colloids and Surfaces A: Physicochemical and Engineering Aspects, Volume 607, 20, December 2020, 125446

Doi: 10.1016/j.colsurfa.2020.125446 Impact Factor: **4,9** Punkty MNiSW: 70

Colloids and Surfaces A 607 (2020) 125446

Contents lists available at ScienceDirect

Colloids and Surfaces A

journal homepage: www.elsevier.com/locate/colsurfa

Influence of magnetite nanoparticles surface dissolution, stabilization and functionalization by malonic acid on the catalytic activity, magnetic and electrical properties

Adrian Radoń[a,*], Sylwester Łoński[b], Mariola Kądziołka-Gaweł[c], Piotr Gębara[d], Mateusz Lis[e], Dariusz Łukowiec[e], Rafał Babilas[e]

[a] Łukasiewicz Research Network - Institute of Non-Ferrous Metals, Sowinskiego 5 St., 44-100 Gliwice, Poland
[b] Faculty of Energy and Environmental Engineering, Silesian University of Technology, Konarskiego 18 St., 44-100 Gliwice, Poland
[c] A. Chelkowski Institute of Physics, University of Silesia, 75 Pułku Piechoty 1A St., 41-500 Chorzów, Poland
[d] Institute of Physics, Czestochowa University of Technology, al. Armii Krajowej 19, 42-200 Czestochowa, Poland
[e] Faculty of Mechanical Engineering, Silesian University of Technology, Konarskiego18 a St., 44-100 Gliwice, Poland

GRAPHICAL ABSTRACT

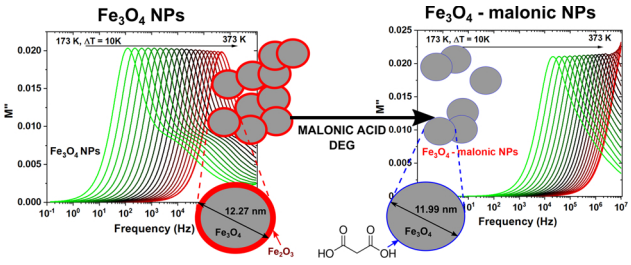

ARTICLE INFO

Keywords:
magnetite nanoparticles
Fenton process
functionalization
electrical conductivity
capping agent

ABSTRACT

Stabilization and modification of magnetite nanoparticles synthesized by the co-precipitation method were presented in these studies. The role of chemical treatment on the structure and properties of Fe_3O_4 nanoparticles was described. It was noted, that the functionalization of nanoparticles surface by malonic acid has a negative impact on the catalytic activity in Fenton and photo-Fenton processes. The decolorization rate decreases from 86% to 35% and from 93% to 85.5 % at the same reaction time for these processes, respectively. However, the magnetite nanoparticles stabilized by malonic acid have higher saturation magnetization and electrical conductivity. These changes were related to the removal of the oxidized surface layer and to the stabilization of iron ions by malonic acid molecules, which was confirmed by the analysis of Mössbauer spectra. The proposed modification also allowed to reduce the size of the agglomerated nanoparticles 10 times and to produce stable Fe_3O_4 NPs.

1. Introduction

Among oxide nanoparticles such as titanium oxide and zinc oxide nanoparticles, magnetite nanoparticles (Fe_3O_4 NPs) are the subject of many studies. The interest in them is associated with many possible low-cost synthesis methods, the possibility of modifying the structure and morphology and in some unique properties. The Fe_3O_4 NPs are characterized by superparamagnetic properties, therefore they can find

* Corresponding author.
E-mail address: adrianr@imn.gliwce.pl (A. Radoń).

https://doi.org/10.1016/j.colsurfa.2020.125446
Received 19 June 2020; Received in revised form 8 August 2020; Accepted 8 August 2020
Available online 20 August 2020

applications in medicine and electronic devices. It was previously reported, that the electrical properties of magnetite nanoparticles and other ferrites are associated with two different mechanisms. First of all, in high-frequency region conductivity by nanoparticles occurs. According to that, this type of conduction can be modified by chemical composition and structural defects. On the other hand, in the low-frequency region (in which is used in typical electronic devices) the electrical conductivity is strongly dependent on the grain boundaries (nanoparticles surface). Therefore, it can be modified by shape and by modification of the surface by different ligands or coatings [1]. The superparamagnetic properties of magnetite nanoparticles have been confirmed for particles of various shapes such as cubic and flower-shaped nanoparticles [2]. Moreover, magnetite nanoparticles are biocompatible and therefore can be used as contrast agents for magnetic resonance imaging (MRI) [3,4]. Their surface can be easily modified to change their properties and nanostructures such as core-shell nanoparticles and hollow-shell NPs can be synthesized [5,6]. The second way to the modify properties of nanoparticles is the functionalization of their surface. This process was used to prevent the agglomeration of magnetite nanoparticles and allows the synthesis of long-term stable particles with unique properties [7–9]. Many different organic molecules such as oleic acid and chitosan were recently used as a stabilizing agent for magnetite nanoparticles [10]. Good stabilization is associated with strong chemical bonds between acidic organic molecules and the surface of iron oxide NPs.

It is well known, that the highly reactive surface of Fe_3O_4 NPs can be oxidized even by air. Therefore, the functionalization of the surface of nanoparticles can also prevent their oxidation. Moreover, the introduction of organic molecules on the surface of nanoparticles can result in the formation of the nanostructured system with multifunctional properties [11]. For example, natural oxidants such as gallic acid can be used to reduce the size of magnetite nanoparticles by selectively dissolving them during synthesis and to improve their antimicrobial properties [12]. Moreover, the functionalized nanoparticles can bind to drugs, enzymes, antibodies, or proteins and can be used in targeted therapy [13–15]. Recently, functionalization by different organic molecules such as carboxymethyl chitosan, hyaluronic acid, folic acid, or poly(ethylene glycol) was proposed to load different drugs (doxorubicin, irinotecan, 5-Fluorouracil, curcumin, ciprofloxacin). For example, functionalization of magnetite nanoparticles by chitosan-grafted-poly(ethylene glycol) methyl ether allows delivering paclitaxel drug [16]. Moreover, the highly reactive surface of Fe_3O_4 NPs can be functionalized by specific organic molecules and used as a catalyst in organic synthesis. Riente et al. synthesized the superparamagnetic Fe_3O_4 NPs functionalized by (S)-α,α-Diphenylprolinol trimethylsilyl ether, which can be used as the highly reactive, magnetically recoverable and reusable catalyst for organocatalytic Michael addition reaction [17]. However, the functionalization of the surface of magnetite nanoparticles may also have a negative impact on the properties. The Fenton process is one of the most promising catalyst reaction, in which Fe_3O_4 NPs can be used as a catalyst [2,18,19]. Fenton reaction is a simple reaction, in which Fe^{2+} acts as catalysts, but the reduction of Fe^{3+} ions back to Fe^{2+} is a very slow process. It has been reported, that the photo treatment of solid iron oxides can accelerate this process and further increase the production of $^{\bullet}OH$ (hydroxyl radicals). Hence, reduction of the Fe^{2+} rich free surface area may reduce the rate of this reaction. On the other hand, reducing agglomeration may increase the surface area and number of reactive Fe^{2+} ions. It has recently been confirmed, that the use of various organic acids can be used to synthesize ultrafine magnetite nanoparticles [20]. Moreover, the use of these types of molecules can prevent agglomeration. The carboxylic acids and their salts act as electrostatic stabilizers. Sone of them, such as citric acid or malonic acid have a strong coordination affinity for iron ions on the surface of magnetite nanoparticles, thanks to which they increase the stability of functionalized nanoparticles and prevent their agglomeration [21]. Therefore, in this studies, the role of chemical treatment with malonic acid on agglomeration, catalytic activity, and electrical properties was investigated in detail.

2. Materials and methods

2.1. Magnetite nanoparticles (Fe_3O_4 NPs) synthesis

Magnetite nanoparticles were synthesized by a simple and low-cost co-precipitation method. For this purpose 4 mmol of $FeCl_3$ and 2 mmol of $FeSO_4{\cdot}7H_2O$ were dissolved in 200 ml of deionized (DI) water. To obtain an acidic environment 2 ml of 35% HCl were added. The solution was sonicated at 328 K to remove oxygen. Afterward, 50 ml of 4 M NaOH solution was added dropwise under continuous sonication. The synthesized nanoparticles marked as Fe_3O_4 NPs were collected by filtration and washed three times by DI water, ethanol and acetone.

2.2. Functionalization of magnetite nanoparticles by malonic acid

0.7 g of the synthesized Fe_3O_4 NPs was sonicated for 15 min in 100 ml of diethylene glycol (DEG). Then 1 mmol of malonic acid dissolved in 10 ml of DEG was added. This dispersion was heated up to reflux and held at that temperature for 1 hour. The synthesized nanoparticles marked as Fe_3O_4 - malonic NPs were collected by filtration and washed three times by DI water, ethanol and acetone.

2.3. Materials characterization

X-ray diffraction (XRD) patterns of nanoparticles were collected using X-ray diffractometer Rigaku MiniFlex 600 with a copper tube Cu Kα ($\lambda = 0.15406$ nm), a tube voltage of 40 kV, and a current of 15 mA, using a D/teX Ultra silicon strip detector. The scanning transmission electron microscope (STEM) images in the bright field-dark field (BF-DF) and high-angle annular dark-field imaging (HAADF) modes were obtained using a transmission electron microscope S/TEM TITAN 80-300. For this purpose, Fe_3O_4 NPs were redispersed in ethanol and sonicated by a few minutes. Two drops of this dispersion were placed into the copper grid with a carbon film and dried at ambient temperature. The Fourier transform infrared (FTIR) spectra were recorded for each material at room temperature using spectrophotometer FTIR Nicolet 6700/8700. Measurements of samples were conducted in the transmission mode in the mid-infrared range of 4000 - 400 cm^{-1}. The hysteresis loops were measured at room temperature using a LakeShore 7307 vibrating sample magnetometer (VSM) at external magnetic fields up to 20000 Oe. The ^{57}Fe Mössbauer spectra (MS) were recorded at room temperature with a constant acceleration spectrometer with ^{57}Co:Rh source (activity ~ 25 mCi), a multichannel analyzer with 1024 channels and a linear arrangement of the ^{57}Co source, absorber, and detector. A metallic iron foil (α-Fe) absorber was used for velocity and isomer shift calibration of the Mössbauer spectrometer. The electrical properties were studied using Concept 81 dielectric spectrometer equipped with Alpha analyzer and Novo-cool temperature control system. The compressed samples with a diameter of 10 mm were placed in an acid-resistant steel capacitor. Measurements were carried out in the frequency range 10^{-1}–10^{7} Hz, and in the temperature range from 173 K to 373 K.

2.4. Catalytic activity measurements

The catalytic and photocatalytic activity measurements of Fe_3O_4 NPs towards the degradation of rhodamine B (RhB) dye was carried out under a UV irradiation using the UV lamp with $\lambda = 365$ nm and $P = 36$ W. The experiments were performed in a solution containing 10 mg/l of RhB and Fe_3O_4 NPs dispersions with different concentration at room temperatures under continuous stirring. Generally, the 30 ml of RhB solution was mixed together with 20 ml of Fe_3O_4 nanoparticles dispersion and then 30% H_2O_2 was added to the solution. To compensate

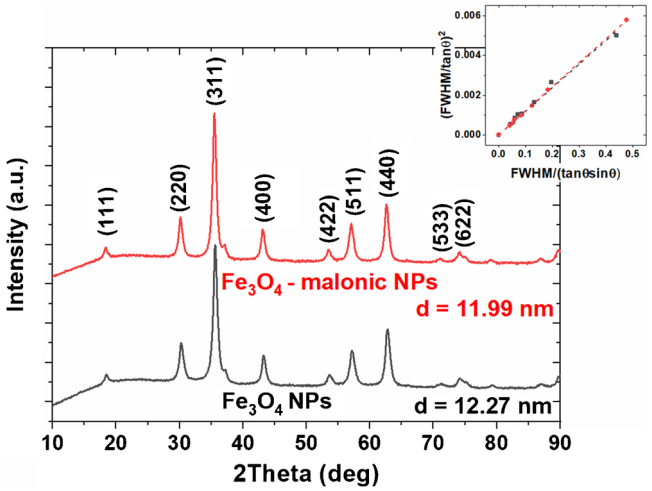

Fig. 1. XRD patterns of Fe_3O_4 NPs and Fe_3O_4 - malonic NPs; inset shows Halder-Wagner plots with the best linear fit.

for changes in the volume of hydrogen peroxide, the DI water was added to obtain 60 ml of the final solution. The adsorption-desorption equilibrium was achieved in the dark with constant stirring. The role of pH has been tested for Fenton and photo-Fenton processes. For this purpose, the pH of the solutions was adjusted to 2.8, 6.5, and 8.7 with NaOH or H_2SO_4. After the degradation process, 3 ml of the solution was received and the nanoparticles were collected by centrifugation. Finally, after the degradation process, UV-vis spectra were collected and RhB concentration was calculated based on the performed experiment. The UV-vis spectra for solutions after the decolorization process were obtained in the wavelength range 350-700 nm using Thermo Scientific Evolution 220 spectrophotometer.

3. Results and discussion

3.1. Structure and morphology analysis

The influence of chemical treatment of Fe_3O_4 NPs by malonic acid in DEG on the structure and morphology was studied by analysis of XRD patterns and TEM images. In Fig. 1 XRD patterns of samples have been presented. It can be noticed, that the proposed methods of synthesis allowed us to prepare pure magnetite nanoparticles without any impurities. The obtained plots were used to calculate average crystallite size using the Halder-Wagner method. In this method broadening of the diffraction peaks observed for nanoparticles with small crystalline size is approximated by the Cauchy function and the broadening related to the microstrain is given by the Gaussian function. The crystallite size (D) and strain (ε) are related to full-width at half maximum ($FWHM$) according to the equations [22]:

$$\left(\frac{\beta^*}{d}\right)^2 = \frac{1}{D}\frac{\beta^*}{d^2} + \left(\frac{\varepsilon}{2}\right)^2 \quad (1)$$

$$\beta^* = \frac{(FWHM)cos\theta}{\lambda} \quad (2)$$

$$d = \frac{2sin\theta}{\lambda} \quad (3)$$

where: λ is the wavelength of X-ray and θ is the diffraction angle. Assuming that the Lorentzian and Gaussian components of β^* result from size and strain, equation (3) can be rewritten as:

$$\left(\frac{FWHM}{tan\theta}\right)^2 = \frac{K\lambda}{D}\frac{FWHM}{tan\theta sin\theta} + \left(\frac{\varepsilon}{2}\right)^2 \quad (4)$$

where K is a constant (0.94 for magnetite).

From Eq. (4) the slope and intercept of the plot of $(FWHM/tan\theta)^2$ vs $FWHM/(tan\theta sin\theta)$ (Fig. 1) give the value of the crystallite size and strain. The small changes in the size of nanoparticles were observed. It was noted, that after treatment with malonic acid the size decreased

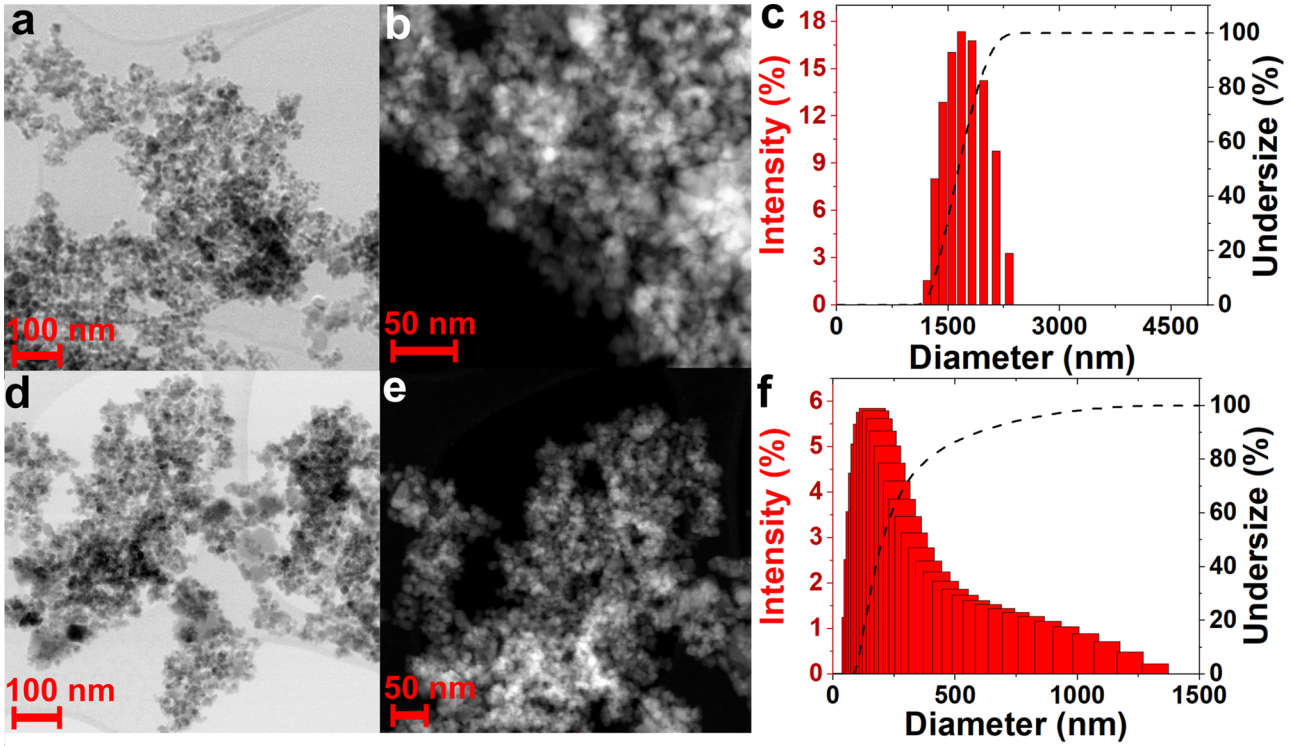

Fig. 2. Analysis of morphology and agglomeration of magnetite nanoparticles: **(a)** BF-DF and **(b)** HAADF STEM images of Fe_3O_4 NPs; **(d)** BF-DF and **(e)** HAADF STEM images of Fe_3O_4 - malonic NPs ; **(c)** and **(f)** variation of the size distribution of Fe_3O_4 NPs and Fe_3O_4 - malonic NPs, respectively.

from 12.27 nm to 11.99 nm, which may be related to the dissolution of the nanoparticles surface and will be discussed later.

It is well known, that the synthesis of magnetite nanoparticles by the co-precipitation method results in the formation of agglomerated structures composed of Fe_3O_4 NPs [23]. Therefore, post-reaction treatment such as functionalization must be performed to obtain nanoparticles with higher surface area [24]. The proposed dissolution of the magnetite nanoparticles surface by malonic acid may result in lower agglomeration. To confirm this, the analysis of TEM images and size distribution variation was performed. In Fig. 2 a, b and d, e STEM images of Fe_3O_4 NPs before and after chemical treatment by malonic acid were presented. It can be noticed, that the ultrafine nanoparticles are presented in both samples. It was found that in both Fe_3O_4 NPs and Fe_3O_4 – malonic NPs agglomeration takes place, therefore in order to confirm the changes generated by malonic acid, the size variation was measured using the DLS technique and shown in Fig. 2 c and f for nanoparticles, respectively, before and after chemical treatment. It can be easily noticed, that the larger agglomerates occur in the as-synthesized sample. The calculated hydrodynamic diameter of these agglomerates was equal to 2384 nm and 240 nm for Fe_3O_4 NPs and Fe_3O_4 - malonic NPs, respectively. Moreover, parameter D_{50} obtained from DLS was equal to 1713 nm and 324 nm for these samples. According to that, it was stated, that the Fe_3O_4 - malonic NPs should have much higher catalytic activity than untreated ones, which should be associated with their higher surface area..

3.2. Catalytic activity

To confirm that the reaction degradation of rhodamine B was performed using the synthesized nanoparticles as a catalyst in Fenton and photo-Fenton processes. Fenton reaction with H_2O_2 is a simple reaction, in which Fe^{2+} acts as catalyst, but the reduction of Fe^{3+} ions back to Fe^{2+} is a very slow process. To accelerate this process the photo-treatment of solid iron oxides can be used. Additionally, the same process results in the formation of $^{\bullet}OH$ (hydroxyl radicals). These radicals are associated with the degradation of different organic compounds and can be produced not only in Fenton reaction [25–28]. The literature shows that the heterogeneous photo-Fenton can be used in a wide pH without loss of iron, which is related to the reaction on the surface of different iron oxides. In the case of uncapped Fe_3O_4 nanoparticles the mechanism of producing $^{\bullet}OH$ can be described as follows [29,30]:

$$(5))\text{-}Fe^{2+} + H_2O_2 \rightarrow)\text{-}Fe^{3+} + {}^{\bullet}OH + OH^-$$

$$(6))\text{-}Fe^{3+} + H_2O + h\upsilon \rightarrow)\text{-}Fe^{2+} + {}^{\bullet}OH + H^+$$

where)- represents the surface of Fe_3O_4 nanoparticles.

Additionally, reactions, in which radicals such as $HO_2^{\bullet}$ and oxygen are formed can occur if we use magnetite nanoparticles as photo-Fenton catalyst. The production mechanism of these radicals is described below [29]:

$$(7))\text{-}Fe^{3+} + H_2O_2 \rightarrow)\text{-}Fe^{2+} + HO_2^{\bullet} + H^+$$

$$(8))\text{-}Fe^{3+} + HO_2^{\bullet} \rightarrow)\text{-}Fe^{2+} + O_2 + H^+$$

The reduction of Fe^{3+} ions is possible due to the consumption of H_2O_2, which is an unnecessary process. To avoid this reaction, photo-reduction of these ions must be used to increase the efficiency of dyes degradation. According to that, both Fenton and photo-Fenton processes were tested in this study. First of all, the optimal reaction conditions were determined on the basis of experiments performed with the use of Fe_3O_4 NPs as a catalyst. The role of pH in the degradation efficiency was tested. In all the conducted experiments, the highest decolorization rate was observed for the acidic pH of 2.8 (Fig. 3 a and b). In case of the Fenton and photo-Fenton reaction, this may be related to the surface activation of nanoparticles in an acidic environment [29]. Similar behaviour was observed for the composite with graphene oxide and magnetite nanoparticles synthesized using triethanolamine as reductive agent and surfactant. Low catalytic activity at high pH was related to the precipitation of $Fe(OH)_3$. The highest activity was observed at pH lower than 4 [31]. In the case of the degradation in the alkaline pH and in the solution without the addition of any ions, some changes can be observed, but the decolorization is very low. In photo-Fenton the degradation in the solution with NaOH was slightly lower than in pH equal to 6.5, which can be related to the recombination of $^{\bullet}OH$ radicals with OH- ions. The second, important parameter in photo-Fenton and Fenton processes is the concentration of catalyst, i.e. Fe_3O_4 NPs. It was previously described, that the too high concentration of catalysts has a negative impact on the degradation rate of dyes [32]. According to that, concentrations of nanoparticles lower than 4 g/L were tested and the results have been presented in Fig. 3 c and d for the Fenton and photo-Fenton, respectively. Interestingly, the decreases in the concentration of Fe_3O_4 NPs reduces the degradation efficiency in the Fenton process. This may be associated with a reduction in the production of $^{\bullet}OH$ radicals. The nanoparticles synthesized by the co-precipitation method should have an oxidized surface, therefore their activation and reduction of Fe^{3+} ions to Fe^{2+} must take place. Consequently, a higher concentration of Fe_3O_4 NPs generates a greater probability of Fe^{2+} ions on the surface of nanoparticles. A similar tendency can be observed for the photo-Fenton reaction, however, due to the rapid reduction of Fe^{3+} to Fe^{2+} ions by UV light, the changes are not so visible. The last optimized parameter was the concentration of H_2O_2, which has the same impact on the degradation rate as the magnetite nanoparticles. As presented in Fig. 3 e and f optimal volume of 30% H_2O_2 was 5 ml for Fenton and 2.5 ml for the photo-Fenton reaction. In the case of a higher concentration of hydrogen peroxide the efficiency of degradation decreases. This can be related to the recombination of $^{\bullet}OH$ radicals into water and oxygen and to the reaction between Fe^{2+} ions and $^{\bullet}OH$ radicals, in which Fe^{3+} ions are being generated [31,33]. The optimal reaction condition was chosen for the experiment, in which the catalytic activity of Fe_3O_4 - malonic NPs was tested. For the Fenton process the concentration of Fe_3O_4 - malonic NPs was 4 g/L, pH was 2.8 and the volume of 30% H_2O_2 was 5 ml. For photo-Fenton reaction $C_{Fe3O4} = 4$ g/L, pH = 2.8, and $V_{H2O2} = 2.5$ ml. The results are presented in Fig. 3 g. It can be noticed, that the degradation efficiency decreases in the Fenton and photo-Fenton reaction when chemical treatment of Fe_3O_4 NPs with malonic acid was applied. The changes are the most visible for Fenton-process. The efficiency of decolorization of this process decreases from 86% to 35% (at 90 min of reaction). The decreasing tendency was also observed for the photo-Fenton process, for which efficiency decreases from 93% to 85.5 % at the same time. Moreover, the decreasing tendency can be observed in the whole reaction time, therefore some changes on the surface of nanoparticles treated by malonic acid can result in reduced catalytic activity.

3.3. Analysis of surface modification

The hypothesis, that the lower catalytic activity of Fe_3O_4-malonic nanoparticles is associated with functionalization of the surface was proposed. It is possible, that the molecules of malonic acid not only cause the changes in the agglomeration but above all functionalize the surface of nanoparticles. This functionalization can result in decreasing the catalytic activity by the bonding of Fe^{2+} ions on the surface. Therefore, the Fenton process cannot occur so easily and the oxidation of the surface can be also stopped. This, in turn, should be manifested by higher magnetic properties and stability of Fe_3O_4 NPs. To confirm that, the analysis of the surface of nanoparticles, as well as the analysis of their magnetic properties were performed. As can be seen in Fig. 4 the FTIR spectra of pure Fe_3O_4 nanoparticles and Fe_3O_4-malonic nanoparticles are different. For nanoparticles after malonic acid treatment new bands associated with vibrations of O-H, C = O, and C-O in

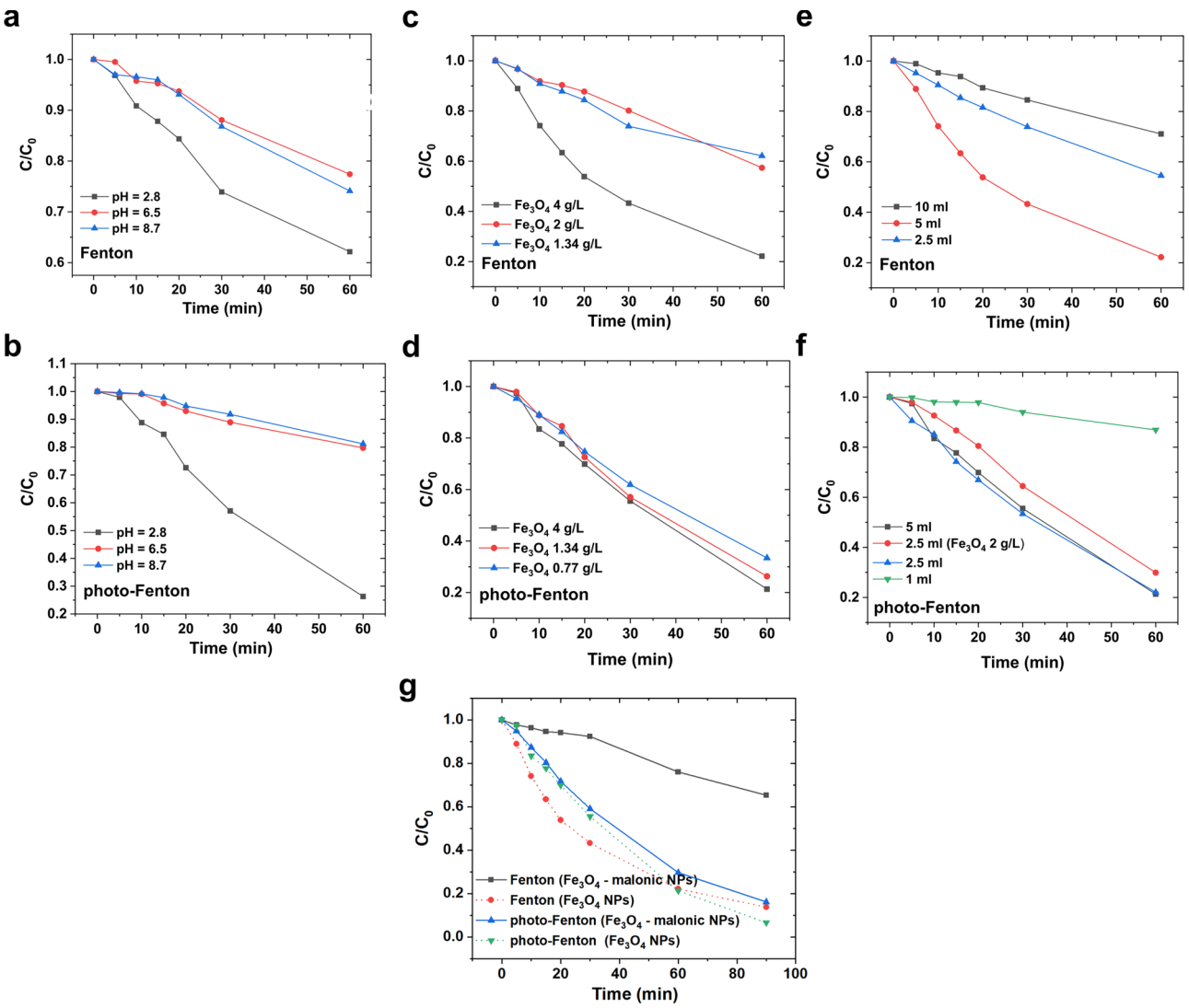

Fig. 3. Decolorization curves obtained from Fenton and photo-Fenton degradation process of RhB; Fenton process in different pH (**a**), Fe_3O_4 concentration (c) and volume of H_2O_2 (e); photo-Fenton process in different pH (b), Fe_3O_4 concentration (d) and volume of H_2O_2 (**f**); **g** comparison of decolorization efficiency of Fe_3O_4 NPs and Fe_3O_4 - malonic NPs.

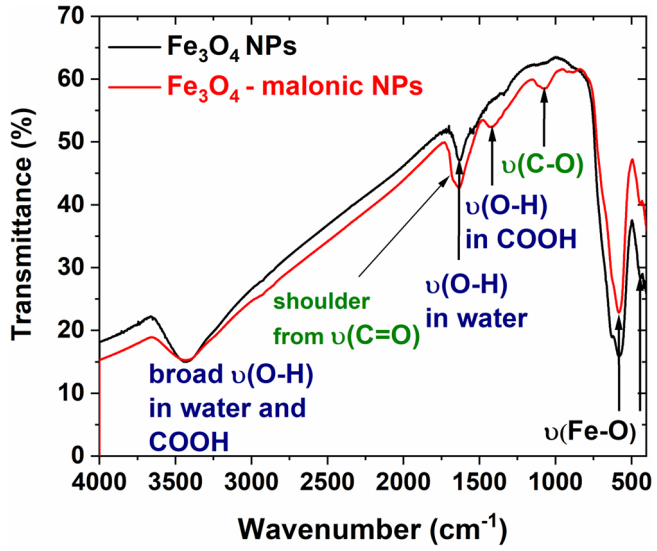

Fig. 4. FTIR spectra of pure magnetite nanoparticles and magnetite nanoparticles after treatment by malonic acid.

carboxyl groups have appeared. As was stated, this is associated with the formation of an organic protective layer on the surface of nanoparticles. These functionalized nanoparticles have a lower tendency to agglomeration, however also lower catalytic activity.

Taking into account, that the malonic acid can react with Fe^{2+} ions the magnetic properties of nanoparticles stored in the air can be higher than pure Fe_3O_4 NPs. Recorded in the room temperature VSM curves presented in Fig. 5 a confirm, that the Fe_3O_4-malonic NPs have higher magnetization (equal to 68 emu/g) than Fe_3O_4 NPs, for which magnetization was 64 emu/g. These changes are not so high, as was expected. However, it can be also related to the reduction of the level of surface spin disorder, which was observed for magnetite nanoparticles functionalized by oleic acid [34]. Moreover, the difference in the coercivity is also very low and reverse. The H_c for Fe_3O_4-malonic NPs was equal to 31.3 Oe, whereas for pure magnetite nanoparticles 28.5 Oe. If we treat the nanoparticle as a single magnetic domain, this phenomenon can be related to the impeded movement of nanoparticles which have been additionally functionalized on the surface. To understand these changes Mössbauer spectra (MS) were collected and presented in Fig. 5 b and c for pure Fe_3O_4 NPs and Fe_3O_4-malonic NPs, respectively. The MS were studied by fitting with magnetic sextets. The values of isomer shift (I_s), quadrupole splitting (Q_s), hyperfine magnetic

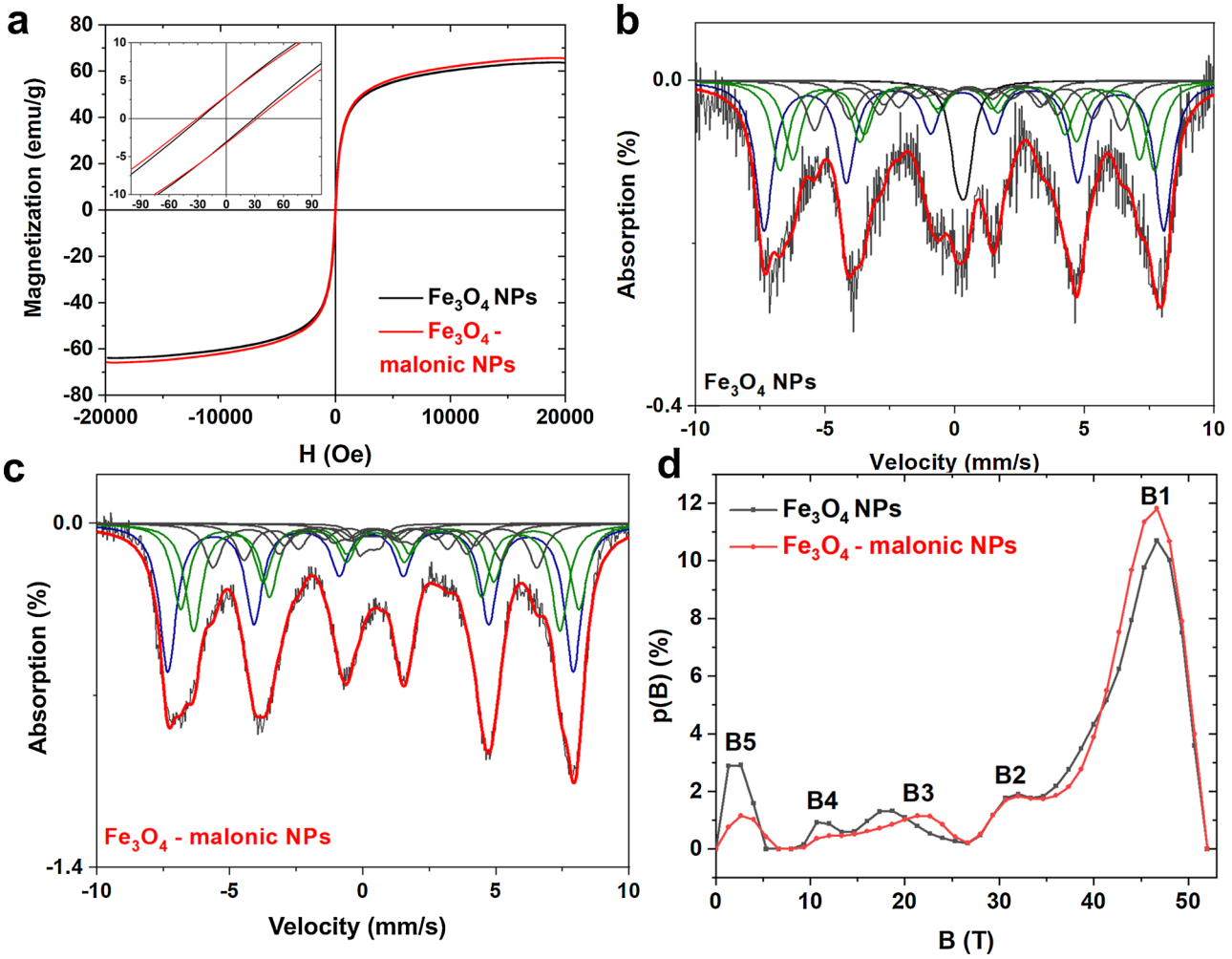

Fig. 5. Magnetic properties of Fe_3O_4 NPs and Fe_3O_4 - malonic NPs: (**a**) VSM curves recorded at room temperature, (**b**) and (**c**) Mössbauer spectra before and after chemical treatment by malonic acid, respectively, (**d**) distribution function of effective magnetic fields for iron nuclei.

Table 1
Hyperfine parameters of synthesized samples (isomer shift (I_s), quadrupole splitting (Q_s), hyperfine magnetic field (B_{hf}) and relative area (A))

Sample	Parameters	Sextet A	Sextet B	Sextet C	Sextet D	Sextet E	Sextet F	Sextet G	Sextet H
Fe_3O_4 NPs	I_s (mm/s)	0.32	0.50	0.41	0.52	0.60	0.37	0.43	0.28
	Q_s (mm/)	0.02	−0.04	0.04	−0.02	0.07	−0.03	0.07	−0.04
	B_{hf} (T)	48.0	45.0	41.6	36.9	29.2	19.3	10.1	1.5
	A (%)	32	19	17	10	8	5	3	7
Fe_3O_4 -malonic NPs	I_s (mm/s)	0.30	0.61	0.50	0.42	0.37	0.63	0.43	0.22
	Q_s (mm/)	−0.03	0.05	0.05	0.06	−0.02	−0.02	−0.05	0.07
	B_{hf} (T)	47.4	46.6	42.9	38.0	30.1	22.3	9.4	2.6
	A (%)	31	19	22	9	8	5	4	2

field (B_{hf}), and relative area (A) of each subspectrum are listed in Table 1. The broad line width of sextets confirms the superparamagnetic size of nanoparticles [35]. First of all, the MS of bulk magnetite is different than for nanoparticles, and the shape of this spectrum for NPs is strongly related to the size of the magnetite particle [36]. This is related to the contribution from the surface, which plays a crucial role in the magnetic properties of nanoparticles. This surface contribution can result in the appearance of much more sextets than for bulk magnetite, for which two sextets from tetrahedral and octahedral sites appear [36]. Three main sextets: sextet A: Tetrahedral site (Fe^{3+}), Sextet B and C: Octahedral site ($Fe^{2.5+}$) were identified in recorded spectra [37] and assigned to magnetite. The obtained values of isomer shift and quadrupole splitting are very close to the bulk parameters. The hyperfine magnetic fields are slightly lower than in bulk. However, the five more sextets (marked as D-H) were also observed. These sextets have a hyperfine magnetic field, isomer shift, and quadrupole splitting not belonging to either tetrahedral or octahedral position. It seems that this sextet may be assigned to the surface part of the particles and/or the existence of the relaxation process [38]. The fraction in the middle part of the spectra is different for Fe_3O_4 NPs and Fe_3O_4-malonic NPs and indicates some changes made by malonic acid. The collapsed part of the spectrum may come from the particles which are close to the transition from superparamagnetic to ferrimagnetic state. To explain the changes in the structure and properties of Fe_3O_4 NPs the distribution function of effective magnetic fields for iron nuclei was presented in Fig. 5 d. As can be seen, five maxima can be observed. This distribution reflects the complex magnetic structure of nanoparticles (for bulk sample only two maxima can be observed). In the previous studies,

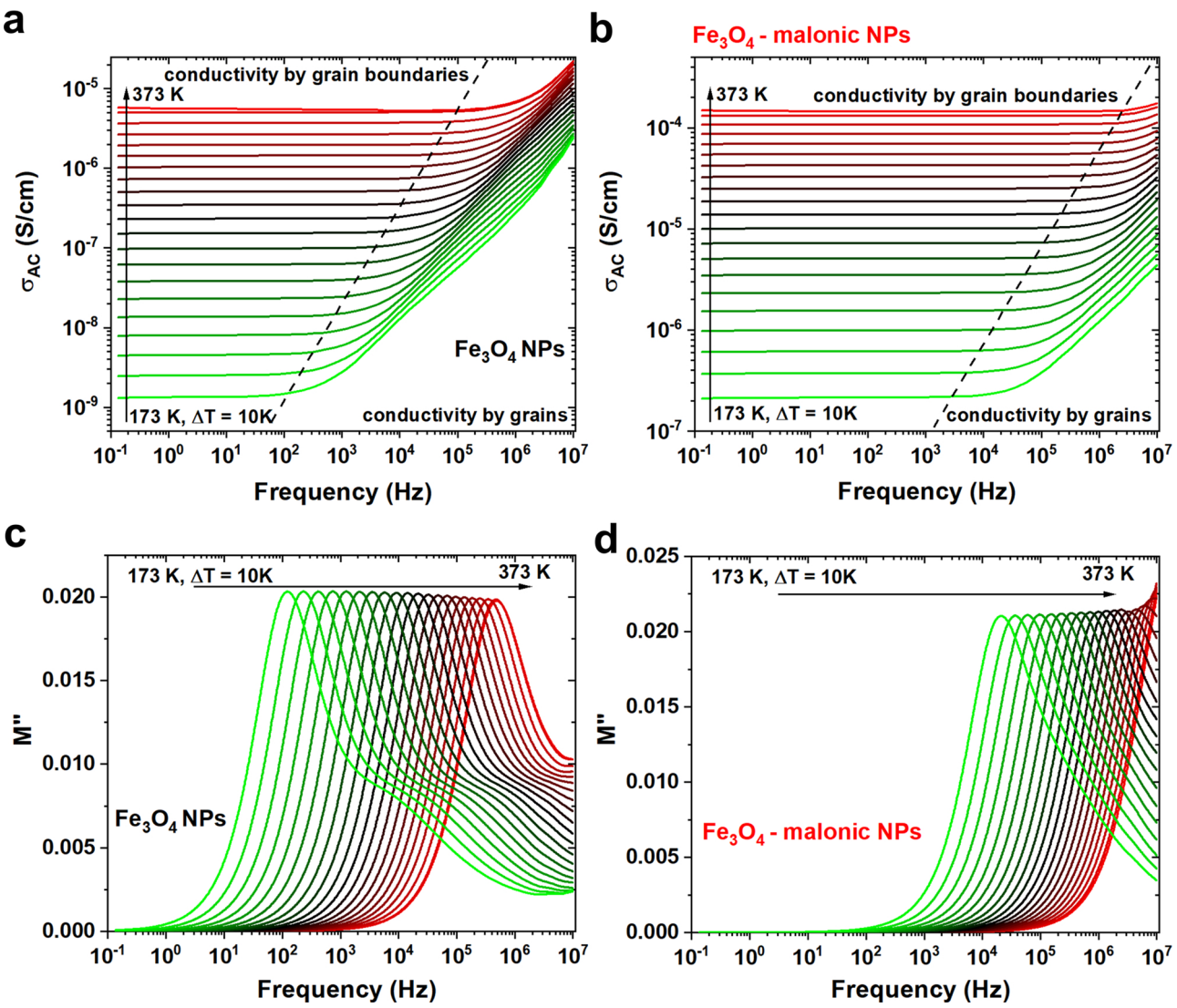

Fig. 6. Electrical properties of Fe_3O_4 NPs and Fe_3O_4 - malonic NPs: (**a**) and (**b**) AC electrical conductivity in function of temperature and frequency in wide temperature range; (**c**) and (**d**) *M"(f)* plots in wide temperature and frequency range.

these maxima were related to the different regions in nanoparticles [36]. The first two (B_1 and B_2) are the fields for iron-ion nuclei in the internal region of nanoparticles. Therefore, the changes between them for untreated and Fe_3O_4-malonic NPs are negligible. The shift and change of the shape of maxima B_3 and B_4 can be easily observed. These maxima represent the fields for Fe^{3+} and $Fe^{2.5+}$ nuclei belonging to the transition layer between internal and external regions. The last, B_5 maximum, which intensity decreases rapidly after functionalization is related to the surface layer of nanoparticles. According to that, the hypothesis, that the heat treatment in diethylene glycol in the presence of malonic acid changes the surface of nanoparticles can be clearly confirmed. The observed differences in the spectra can be related to the changes in their surface. It can be concluded, that three different processes appear: the disordering surface dissolution by malonic acid, reordering of the surface by high-temperature heat treatment in reducing diethylene glycol, and functionalization of nanoparticles by the bonding of Fe^{2+} ions by malonic molecules.

3.4. Electric properties

The reorganization and functionalization of the surface of magnetite nanoparticles should generate the visible changes in the electrical conductivity. Previously, it was reported, that the electrical conductivity in the magnetite nanoparticles can be related to two different processes. Conductivity at low temperatures and in the low-frequency region is associated with the movement of charge carriers through the grain boundaries, whereas in higher frequencies and temperature region it is associated with conduction through the grains [1]. According to that, broadband dielectric spectroscopy was used to measure AC electrical conductivity (σ_{AC}) and complex permittivity. Then the imaginary part of electric modulus (*M"*) was calculated. The obtained results at a broad temperature range from 173 to 373 K were presented in Fig. 6 Two regions can be observed (Fig. 6 a,b). The first one, in which σ_{AC} is frequency independent, but depends on the temperature is associated with the conductivity through the grain boundaries. The second one, observed in the high-frequency region is related to the conduction through the grains [39]. The analysis of transition between them can be performed on the basis of *M"(f)* plots (see in Fig.6 c and d). The $M"_{peak}$ is related to the changes in electrical conductivity. First of all, in Fig. 6 c double nature of this peak can be observed. If we assume that on the surface of the nanoparticles exist the thin layer of Fe_2O_3, which was formed by oxidation of Fe_3O_4 in air, the two peaks should occur. One of them is associated with changes in electrical conductivity in magnetite, the second one with changes in the conductivity of Fe_2O_3. As was stated before, the surface of Fe_3O_4 - malonic NPs was reordered and stabilized by malonic acid. Therefore, the $M"_{peak}$

observed in Fig. 6 d can be related strictly to the transition between conductivity in Fe_3O_4 NPs and by the surface of magnetite NPs. On the other hand, presented in Fig. 6 c M''_{peak} can be associated with the transition between conductivity in thin Fe_2O_3 layer and by the oxidized surface, whereas shoulder can be associated with the transition between conductivity in Fe_3O_4 NPs and by the surface of magnetite NPs. Therefore, the activation energies of these processes should be different. The calculated activation energy from the M''_{peak} ($\Delta E_{M''}$) according to the Arrhenius law was equal to 0.21 eV for the Fe_3O_4 NPs and 0.17 eV for the Fe_3O_4 -malonic NPs. It can be noticed, that the $\Delta E_{M''}$ is lower for Fe_3O_4 -malonic NPs than Fe_3O_4 NPs. This can be related to the differences in surface conductivity of the oxidized nanoparticles. The charge carriers movements are much easier on the surface of Fe_3O_4, in which both, Fe^{2+} and Fe^{3+} ions exist, than on the surface of Fe_2O_3, in which only Fe^{3+} ions are presented.

4. Conclusions

Magnetite nanoparticles stabilized by malonic acid with an average crystallite size equal to 11.99 nm were successfully synthesized in presented studies. The dissolution and surface reorganization under chemical treatment was confirmed. The functionalized nanoparticles have much lower catalytic activity than uncapped ones. This decrease was related to the chemical bonding between Fe^{2+} ions and malonic acid molecules. The same interaction stabilizes their surface and prevents oxidation. This, in turn, improves saturation magnetization from 64 to 68 emu/g and greatly increases electrical conductivity. Taking into account fact, that the average crystallite size decreased after chemical treatment by malonic acid the thickness of the oxidized layer can be approximated and was equal to 0.28 nm. According to that, the difference in saturation magnetization was not so visible, however, this oxidized layer has a great impact on the other properties and can be detected using Mössbauer spectroscopy or broadband dielectric spectroscopy. Performed dielectric measurements allowed to state that the double nature of *M''* peak is associated with the existence of a thin layer of Fe_2O_3 on the surface of magnetite nanoparticles. The dissolution of this oxidized layer improves electrical conductivity through the grain boundaries. This process additionally reduces the agglomeration ratio. It was confirmed by DLS studies, that the size of agglomerates have been reduced 10 times. The dissolution process results with the surface reorganization, which was clearly confirmed by Mössbauer spectroscopy. According to that further surface modification of magnetite nanoparticles can be easily described by the use of this technique.

Funding

This work was supported by the grant from Polish Ministry of Science and Higher Education - Diamond Grant (0220/DIA/2018/47).

Data Availability

The raw/processed data required to reproduce these findings cannot be shared at this time due to technical or time limitations.

CRediT authorship contribution statement

Adrian Radoń: Conceptualization, Methodology, Investigation, Writing - original draft, Visualization. **Sylwester Łoński:** Investigation, Methodology, Formal analysis. **Mariola Kądziołka-Gaweł:** Investigation, Formal analysis, Writing - original draft. **Piotr Gębara:** Investigation. **Mateusz Lis:** Investigation. **Dariusz Łukowiec:** Investigation. **Rafał Babilas:** Writing - review & editing, Supervision.

Declaration of Competing Interest

None

References

[1] A. Radoń, D. Łukowiec, M. Kremzer, J. Mikuła, P. Włodarczyk, Electrical conduction mechanism and dielectric properties of spherical shaped Fe_3O_4 nanoparticles synthesized by co-precipitation method, Materials (Basel). (2018), https://doi.org/10.3390/ma11050735.
[2] F. Hu, K.W. MacRenaris, E.A. Waters, E.A. Schultz-Sikma, A.L. Eckermann, T.J. Meade, Highly dispersible, superparamagnetic magnetite nanoflowers for magnetic resonance imaging, Chem. Commun. (2010), https://doi.org/10.1039/b916562b.
[3] Z.R. Stephen, F.M. Kievit, M. Zhang, Magnetite nanoparticles for medical MR imaging, Mater. Today. (2011), https://doi.org/10.1016/S1369-7021(11)70163-8.
[4] M. Barrow, A. Taylor, P. Murray, M.J. Rosseinsky, D.J. Adams, Design considerations for the synthesis of polymer coated iron oxide nanoparticles for stem cell labelling and tracking using MRI, Chem. Soc. Rev. (2015), https://doi.org/10.1039/c5cs00331h.
[5] A.L. Morel, S.I. Nikitenko, K. Gionnet, A. Wattiaux, J. Lai-Kee-Him, C. Labrugere, B. Chevalier, G. Deleris, C. Petibois, A. Brisson, M. Simonoff, Sonochemical approach to the synthesis of Fe_3O_4@SiO_2 core - Shell nanoparticles with tunable properties, ACS Nano. (2008), https://doi.org/10.1021/nn800091q.
[6] B. Luo, S. Xu, W.F. Ma, W.R. Wang, S.L. Wang, J. Guo, W.L. Yang, J.H. Hu, C.C. Wang, Fabrication of magnetite hollow porous nanocrystal shells as a drug carrier for paclitaxel, J. Mater. Chem. (2010), https://doi.org/10.1039/c0jm00726a.
[7] A.G. Magdalena, I.M.B. Silva, R.F.C. Marques, A.R.F. Pipi, P.N. Lisboa-Filho, M. Jafelicci, EDTA-functionalized Fe_3O_4 nanoparticles, J. Phys. Chem. Solids. (2018), https://doi.org/10.1016/j.jpcs.2017.10.002.
[8] A. Zhu, L. Yuan, T. Liao, Suspension of Fe_3O_4 nanoparticles stabilized by chitosan and o-carboxymethylchitosan, Int. J. Pharm. (2008), https://doi.org/10.1016/j.ijpharm.2007.09.004.
[9] L. Shen, B. Li, Y. Qiao, Fe_3O_4 nanoparticles in targeted drug/gene delivery systems, Materials (Basel). (2018), https://doi.org/10.3390/ma11020324.
[10] P. Nicolás, M. Saleta, H. Troiani, R. Zysler, V. Lassalle, M.L. Ferreira, Preparation of iron oxide nanoparticles stabilized with biomolecules: Experimental and mechanistic issues, Acta Biomater. (2013), https://doi.org/10.1016/j.actbio.2012.09.040.
[11] K. Hola, Z. Markova, G. Zoppellaro, J. Tucek, R. Zboril, Tailored functionalization of iron oxide nanoparticles for MRI, drug delivery, magnetic separation and immobilization of biosubstances, Biotechnol. Adv. (2015), https://doi.org/10.1016/j.biotechadv.2015.02.003.
[12] S.T. Shah, W.A. Yehya, O. Saad, K. Simarani, Z. Chowdhury, A.A. Alhadi, L. Al-Ani, Surface Functionalization of Iron Oxide Nanoparticles with Gallic Acid as Potential Antioxidant and Antimicrobial Agents, Nanomaterials. (2017), https://doi.org/10.3390/nano7100306.
[13] M. Mahmoudi, S. Sant, B. Wang, S. Laurent, T. Sen, Superparamagnetic iron oxide nanoparticles (SPIONs): Development, surface modification and applications in chemotherapy, Adv. Drug Deliv. Rev. (2011), https://doi.org/10.1016/j.addr.2010.05.006.
[14] A.K. Gupta, M. Gupta, Synthesis and surface engineering of iron oxide nanoparticles for biomedical applications, Biomaterials. (2005), https://doi.org/10.1016/j.biomaterials.2004.10.012.
[15] Y.P. Yew, K. Shameli, M. Miyake, N.B.B. Ahmad Khairudin, S.E.B. Mohamad, T. Naiki, K.X. Lee, Green biosynthesis of superparamagnetic magnetite Fe_3O_4 nanoparticles and biomedical applications in targeted anticancer drug delivery system: A review, Arab. J. Chem. (2018), https://doi.org/10.1016/j.arabjc.2018.04.013.
[16] D.Q. Hoang, T.V. Tran, N.Q. Tran, C.K. Nguyen, T.H. Nguyen, M.D. Truong, D.L. Tran, L. Van Thu, D.H. Nguyen, Functionalization of Fe_3O_4 nanoparticles with biodegradable chitosan-grafted-mPEG for paclitaxel delivery, Green Process. Synth. (2016), https://doi.org/10.1515/gps-2016-0093.
[17] P. Riente, C. Mendoza, M.A. Pericás, Functionalization of Fe_3O_4 magnetic nanoparticles for organocatalytic Michael reactions, J. Mater. Chem. (2011), https://doi.org/10.1039/c1jm10535c.
[18] A. Hassani, M. Karaca, S. Karaca, A. Khataee, Ö. Açışlı, B. Yılmaz, Preparation of magnetite nanoparticles by high-energy planetary ball mill and its application for ciprofloxacin degradation through heterogeneous Fenton process, J. Environ. Manage. (2018), https://doi.org/10.1016/j.jenvman.2018.01.014.
[19] W. Wang, Q. Mao, H. He, M. Zhou, Fe_3O_4 nanoparticles as an efficient heterogeneous Fenton catalyst for phenol removal at relatively wide pH values, Water Sci. Technol. (2013), https://doi.org/10.2166/wst.2013.497.
[20] A. Radoń, A. Drygała, Ł. Hawełek, D. Łukowiec, Structure and optical properties of Fe_3O_4 nanoparticles synthesized by co-precipitation method with different organic modifiers, Mater. Charact. (2017), https://doi.org/10.1016/j.matchar.2017.06.034.
[21] J. Liu, Z. Sun, Y. Deng, Y. Zou, C. Li, X. Guo, L. Xiong, Y. Gao, F. Li, D. Zhao, Highly water-dispersible biocompatible magnetite particles with low cytotoxicity stabilized by citrate groups, Angew. Chemie - Int. Ed. (2009), https://doi.org/10.1002/anie.200901566.
[22] C.M. Patel, M. Chakraborty, Z.V.P. Murthy, Study on the stability and microstructural properties of barium sulfate nanoparticles produced by nanomilling, Adv. Powder Technol. 25 (2014) 226–235, https://doi.org/10.1016/j.apt.2013.04.003.

[23] S.P. Yeap, J.K. Lim, B.S. Ooi, A.L. Ahmad, Agglomeration, colloidal stability, and magnetic separation of magnetic nanoparticles: collective influences on environmental engineering applications, J. Nanoparticle Res. (2017), https://doi.org/10.1007/s11051-017-4065-6.

[24] S.E. Favela-Camacho, E.J. Samaniego-Benítez, A. Godínez-García, L.M. Avilés-Arellano, J.F. Pérez-Robles, How to decrease the agglomeration of magnetite nanoparticles and increase their stability using surface properties, Colloids Surfaces A Physicochem, Eng. Asp. (2019), https://doi.org/10.1016/j.colsurfa.2019.04.016.

[25] X. Chen, J. Dai, G. Shi, L. Li, G. Wang, H. Yang, Sonocatalytic degradation of Rhodamine B catalyzed by β-Bi_2O_3 particles under ultrasonic irradiation, Ultrason. Sonochem. 29 (2016) 172–177, https://doi.org/10.1016/j.ultsonch.2015.08.010.

[26] H. Bouya, M. Al Rashidi, E. Roth, R. Salghi, A. Chakir, Atmospheric degradation of 2- nitrobenzaldehyde: Photolysis and reaction with OH radicals, Atmos. Environ. 171 (2017) 221–228, https://doi.org/10.1016/j.atmosenv.2017.10.021.

[27] E.E. Ebrahiem, M.N. Al-Maghrabi, A.R. Mobarki, Removal of organic pollutants from industrial wastewater by applying photo-Fenton oxidation technology, Arab. J. Chem. 10 (2017) S1674–S1679, https://doi.org/10.1016/j.arabjc.2013.06.012.

[28] X.J. Yang, X.M. Xu, J. Xu, Y.F. Han, Iron oxychloride (FeOCl): An efficient fenton-like catalyst for producing hydroxyl radicals in degradation of organic contaminants, J. Am. Chem. Soc. 135 (2013) 16058–16061, https://doi.org/10.1021/ja409130c.

[29] C. Wang, H. Liu, Z. Sun, Heterogeneous photo-Fenton reaction catalyzed by nano-sized iron oxides for water treatment, Int. J. Photoenergy. 2012 (2012), https://doi.org/10.1155/2012/801694.

[30] F. Chen, S. Xie, X. Huang, X. Qiu, Ionothermal synthesis of Fe_3O_4 magnetic nanoparticles as efficient heterogeneous Fenton-like catalysts for degradation of organic pollutants with H_2O_2, J. Hazard. Mater. 322 (2017) 152–162, https://doi.org/10.1016/j.jhazmat.2016.02.073.

[31] Z. fang Cao, X. Wen, P. Chen, F. Yang, X. li Ou, S. Wang, H. Zhong, Synthesis of a novel heterogeneous fenton catalyst and promote the degradation of methylene blue by fast regeneration of Fe^{2+}, Colloids Surfaces A Physicochem. Eng. Asp. (2018), https://doi.org/10.1016/j.colsurfa.2018.04.009.

[32] M. Neamtu, C. Nadejde, V.D. Hodoroaba, R.J. Schneider, L. Verestiuc, U. Panne, Functionalized magnetic nanoparticles: Synthesis, characterization, catalytic application and assessment of toxicity, Sci. Rep. (2018), https://doi.org/10.1038/s41598-018-24721-4.

[33] M. Munoz, Z.M. de Pedro, J.A. Casas, J.J. Rodriguez, Preparation of magnetite-based catalysts and their application in heterogeneous Fenton oxidation - A review, Appl. Catal. B Environ. (2015), https://doi.org/10.1016/j.apcatb.2015.04.003.

[34] P. Guardia, B. Batlle-Brugal, A.G. Roca, O. Iglesias, M.P. Morales, C.J. Serna, A. Labarta, X. Batlle, Surfactant effects in magnetite nanoparticles of controlled size, J. Magn. Magn. Mater. (2007), https://doi.org/10.1016/j.jmmm.2007.03.085.

[35] C. Lu, Z.-S. Quan, J.C. Sur, S.-H. Kim, C.H. Lee, K.Y. Chai, One-pot fabrication of carboxyl-functionalized biocompatible magnetic nanocrystals for conjugation with targeting agents, New J. Chem. 34 (2010) 2040–2046, https://doi.org/10.1039/C0NJ00067A.

[36] M.A. Shipilin, I.N. Zakharova, A.M. Shipilin, V.I. Bachurin, Mössbauer studies of magnetite nanoparticles, J. Surf. Investig. X-Ray, Synchrotron Neutron Tech. (2014), https://doi.org/10.1134/s1027451014030343.

[37] P.B. Rathod, A.K. Pandey, S.S. Meena, A.A. Athawale, Quaternary ammonium bearing hyper-crosslinked polymer encapsulation on Fe_3O_4 nanoparticles, RSC Adv. (2016), https://doi.org/10.1039/c6ra01543c.

[38] V.A.J. Silva, P.L. Andrade, M.P.C. Silva, A.D. Bustamante, L. De Los Santos Valladares, J. Albino Aguiar, Synthesis and characterization of Fe_3O_4 nanoparticles coated with fucan polysaccharides, J. Magn. Magn. Mater. (2013), https://doi.org/10.1016/j.jmmm.2013.04.062.

[39] C.G. Koops, On the dispersion of resistivity and dielectric constant of some semiconductors at audiofrequencies, Phys. Rev. (1951), https://doi.org/10.1103/PhysRev.83.121.

Załącznik III

A(III)

Wojciech Łoński, Monika Spilka, Mariola Kądziołka-Gaweł, Piotr Gębara, Adrian Radoń, Tymon Warski, **Sylwester Łoński**, Krzysztof Barbusiński, Katarzyna Młynarek-Żak, Rafał Babilas

Microstructure, magnetic properties, corrosion resistance and catalytic activity of dual-phase AlCoNiFeTi and AlCoNiFeTiSi high entropy alloys

Journal of Alloys and Compounds, Volume 934, 10, February 2023, 167827

Doi: 10.1016/j.jallcom.2022.167827 Impact Factor: **5,8** Punkty MNiSW: 100

Journal of Alloys and Compounds 934 (2023) 167827

Contents lists available at ScienceDirect

Journal of Alloys and Compounds

journal homepage: www.elsevier.com/locate/jalcom

Microstructure, magnetic properties, corrosion resistance and catalytic activity of dual-phase AlCoNiFeTi and AlCoNiFeTiSi high entropy alloys

Wojciech Łoński [a,*], Monika Spilka [a], Mariola Kądziołka-Gaweł [b], Piotr Gębara [c], Adrian Radoń [a,d], Tymon Warski [d], Sylwester Łoński [e], Krzysztof Barbusiński [e], Katarzyna Młynarek-Żak [a], Rafał Babilas [a,*]

[a] Department of Engineering Materials and Biomaterials, Silesian University of Technology, Konarskiego 18a St., Gliwice 44-100, Poland
[b] Institute of Physics, University of Silesia, Uniwersytecka 4, 40-007 Katowice, Poland
[c] Department of Physics, Częstochowa University of Technology, Armii Krajowej 19, 42-200 Częstochowa, Poland
[d] Łukasiewicz Research Network - Institute of Non-Ferrous Metals, Sowińskiego 5 St., 44-100 Gliwice, Poland
[e] Faculty of Energy and Environmental Engineering, Silesian University of Technology, Konarskiego 18 St., 44-100 Gliwice, Poland

ARTICLE INFO

Article history:
Received 29 August 2022
Received in revised form 27 October 2022
Accepted 31 October 2022
Available online 1 November 2022

Keywords:
High entropy alloys
X-ray diffraction
Thermal analysis
Mössbauer spectroscopy
Electrochemical measurements
Advanced oxidation processes

ABSTRACT

The high entropy AlCoFeNiTi and AlCoFeNiTiSi alloys were prepared by two methods to determine the influence of the cooling rate on the structure and properties. The Mössbauer spectra of AlCoFeNiTi alloys showed the coexistence of a nonmagnetic part with a magnetic hyperfine portion. The spectra for AlCoFeNiTiSi alloy in an as-cast and plate states contain only nonmagnetic components. The X-ray diffraction analysis confirmed that the silicon addition drastically changes the phase composition of AlCoFeNiTi alloy. Whereas alloy without Si was characterised by the coexistence of $L2_1$ and BCC phases, the addition of silicon resulted in the formation of Ti-rich HCP and Al-rich B2 phases. AlCoFeNiTi plate exhibits a high saturation magnetisation value of 29.83 emu/g and the best corrosion resistance (polarisation resistance of about 38.6 kΩcm^2 and corrosion current density of 0.77 μA/cm^2). The highest hardness (1096 HV) was achieved for AlCoFeNiTiSi plate, which is related to the phase composition changes generated by Si addition. The influence of the Si addition on the properties of studied alloys was also confirmed in the decolourisation of Rhodamine B using a modified photo-Fenton process. The decolourisation efficiency within 60 min was 92% for AlCoFeNiTiSi alloy, and 95.5% for the AlCoFeNiTi alloy.

1. Introduction

High entropy alloys (HEAs) constitute a group of multi-component alloys composed of several major alloying elements, such as aluminium, nickel, chromium, iron, cobalt, copper, titanium molybdenum and manganese [1]. HEAs with structural homogeneity show superior properties over conventional alloys [2,3] and therefore have various possible uses [4]. For example, high entropy alloys are excellent materials for compressors, combustion chambers, exhaust nozzles and gas turbines. On the contrary, alloys with excellent mechanical, electrical, electrochemical, and anticorrosion properties offer an alternative for biomedical applications [5] and hydrogen storage materials [6]. Furthermore, HEAs alloys have properties that will allow their use as catalysts (e.g., ammonia oxidation catalyst) [7]. Furthermore, HEAs are expected to be used as thermoelectric materials with high thermoelectric efficiency [8] and solar absorber coating [7]. Interestingly, HEA with titanium can also be used in specialised and extreme applications in Generation IV nuclear reactors [9].

The alloying elements introduced into the high entropy alloys strongly influence the microstructure and phase composition. The microstructure of Ti-containing HEAs is complex and tends to form intermetallic compounds [10]. The authors of the work [11] reported that, in the titanium-free alloy, one BCC phase was formed, and the addition of Ti caused the formation of two different BCC phases as the main phases. At 0.5% Ti content, a minor phase with FCC structure was formed in the alloy. The further addition of titanium led to the formation of complex phases [11]. Some authors have noted that titanium additions modify the phase composition of HEAs and properties such as wear resistance and hardness [12]. For example, adding 0.25% Ti to the $Al_{0.75}$FeNiCrCo alloy increased strength and

* Corresponding authors.
E-mail addresses: wojciech.lonski@polsl.pl (W. Łoński), rafal.babilas@polsl.pl (R. Babilas).

https://doi.org/10.1016/j.jallcom.2022.167827
0925-8388/

hardness but decreased ductility [13]. However, when Ti exceeds the equimolar composition, many intermetallic phases that generate brittleness and material deterioration are formed [14]. Titanium added to HEA can also improve the corrosion resistance of the alloys because of its beneficial role in enhancing the surface film. Ti-containing HEAs usually exhibit higher pitting corrosion resistance than 304 stainless steel in chloride-containing environments [15]. For example, the $Al_{2-x}CoCrFeNiTi_x$ alloys had a wider passive region and a higher breakdown potential than Ti-free $Al_2CoCrFeNi$ alloy in a 3.5% NaCl solution. This result was due to the formation of TiO_2 incorporated into the passive film of the HEAs that improved the resistance to pitting. Furthermore, non-oxidised metal atoms, especially Ti, in the passive film hindered the transport of point defects, which also benefitted the protective ability of the passive film [10,15,16].

In addition to metallic elements, non-metallic elements such as boron or silicon are added to high entropy alloys to change their physical and chemical properties [17,18]. For example, Si is usually added to improve wear, oxidation, and corrosion resistance [14]. In addition, adding silicon to high entropy alloys improves mechanical properties, including compressive strength and fracture toughness [19]. For example, the $AlCoCrFeNiSi_x$ alloy, after introducing 0.4 Si, obtained a yield stress of 1481 MPa, a fracture strength of 2444 MPa, and a plastic strain of 13.38%, respectively [18]. However, the addition of a large amount of Si (> 7.4%) to HEA causes a decrease in strength and ductility [20]. In work [21], with increasing Si content in the $AlCoCrFeNiSi_x$ alloy, a visible tendency for the saturation magnetisation value to decrease and increase the hardness was observed. Furthermore, the excessive introduction of the Si element leads to precipitation of the δ phase at the grain boundary, which is responsible for the transition of alloy from plastic fracture to brittle fracture [18].

Although high entropy alloys contain multiple elements, they frequently solidify into simple crystal types, such as face-centred-cubic (FCC), body-centred-cubic (BCC), and hexagonal-close-packed (HCP) solid-solution structures. The FCC structure HEAs are generally ductile but insufficiently strong, while the BCC/HCP structure HEAs can be very strong but also brittle [22]. However, in reality, only a limited number of high entropy alloys can form as single-phase solid solutions. Most fabricated HEAs have second phases, including complex or intermetallic phases [15]. The literature has shown that HEAs with dual phases generally exhibit better mechanical properties than those with a single structure. In single-phase high entropy alloys, it is difficult to strike a balance between high strength and high ductility. For example, single-phase HEAs with an FCC structure have high ductility but low strength, and single-phase HEAs with a BCC structure have high strength but limited ductility [23]. Therefore, for the engineering applications of HEA, it is recommended to produce eutectic high entropy alloys consisting of soft phases (FCC) and hard phases (B2) [24]. For example, in work [25], an excellent combination of yield strength (~980 MPa), ultimate tensile strength (~1160 MPa), and tensile elongation (~15%) were achieved in dual phase $Al_{0.45}CoCrFeNi$ high entropy alloys. In turn, the $CoCrFeNiAl_{0.5}$ HEA with the FCC + BCC microstructure showed a combined high strength of 1280 MPa and reasonable ductility of 7.1% [26].

Moreover, dual-phase high-entropy casting alloys by tuning the volume fraction of the BCC and FCC phases as damping materials used in machine parts, such as submarine propeller, brake disc, shield machine, gear and crusher [27]. These alloys are also promising as multifunctional electrocatalysts due to their inherent compositional and structural complexity [28]. Furthermore, double-phase HEAs, with the Laves phase's participation as the phase structure's second component, possess many exciting properties in superconductivity, magnetism, and magnetocaloric fields [29].

The potential applications of the HEAs are wide and depend on the chemical and phase composition, producing technology, and their physicochemical properties. Accordingly, this study aims to determine the influence of the cooling rate on the structure and selected properties of the AlCoFeNiTi and AlCoFeNiTiSi high entropy alloys. As mentioned above, the addition of Si can influence structure and properties. Moreover, HEAs containing Ti are characterised by unique properties, which are generally related to the formation of dual-phase alloys. Therefore, to better understand the relationships between chemical composition, phase composition and properties, in this study, a comprehensive analysis of AlCoFeNiTi and AlCoFeNiTiSi HEAs was performed using various techniques. Although most studies concentrate on the mechanical properties of HEAs, the magnetic and anticorrosion properties and catalytic activity were tested herein. Due to their composition, high-entropy alloys can be used as a source of metals that catalyse the Fenton reaction [30]. Accordingly, it is reasonable to test the catalytic activity of HEAs, which can be easily removed from the reaction solution using a magnetic field. Therefore, in this work, the catalytic activity of HEAs in the photo-Fenton reaction using sodium percarbonate as hydroxyl radical source was tested and described.

2. Materials and methods

The work describes the results of investigations on the AlCoFeNiTi and AlCoFeNiTiSi high entropy alloys in the form of ingots and plates. The alloys in an as-cast state (ingots) were produced by induction melting using an NG-40 induction generator in an argon atmosphere. Plates of 1 mm thickness were prepared by remelting the ingots and then cast by high-pressure to copper die (with a cooling rate ~10^3 K/s). The ingots were produced using a low cooling rate of molten alloy (argon-cooled in a ceramic Al_2O_3 crucible).

The phase analysis of the HEAs was conducted using an X-ray diffractometer, Rigaku MiniFlex 600, equipped with a copper tube (Cu Kα, λ = 0.15406 nm) and a D/TEX strip detector. The measurements were performed on powder samples in the Bragg-Brentano geometry over an angular range of 2Θ = 20–90° at room temperature. In addition, the microstructures of the ingots and plates were observed using a Supra 35 Carl Zeiss scanning electron microscope (SEM) equipped with energy-dispersive X-ray spectroscopy (EDX).

^{57}Fe Mössbauer transmission spectra for ingots and plates were recorded at room temperature using an MS96 spectrometer and a linear arrangement of a ^{57}Co:Rh (40 mCi) source, a multichannel analyser, an absorber and a detector. The spectrometer was calibrated at room temperature with a 30 μm thick α-Fe foil. Numerical analysis of the Mössbauer spectra was performed using the MossWinn4.0i programme.

Differential thermal analysis (DTA) of ingots and plates was provided to determine the crystallisation mechanism using a NETSCH Jupiter STA 449 F3 thermal analyser. The DTA curves were recorded at 20 °C/min for heating and cooling under a protective argon atmosphere.

Measurements of magnetic parameters were carried out at room temperature. The study of magnetic properties included the field of coercive force (H_c), saturation magnetisation (M_s), and remaining magnetisation (M_r), which were determined from hysteresis loops by the LakeShore 7307 vibrating sample magnetometer (VSM) in magnetic fields up to 10 kOe.

The electrochemical measurements were conducted in a 3.5% NaCl solution using a potentiostat Autolab 302 N instrument equipped with a three-electrode cell. The potentiostat was controlled using the NOVA 1.11 software. A saturated calomel electrode (SCE) was used as the reference electrode and a platinum rod as the counter electrode. The corrosion resistance was evaluated by recording the variation of the open-circuit potential (E_{OCP}) versus the SCE. The corrosion potential (E_{corr}) and corrosion current density (j_{corr}) were also determined using the Tafel extrapolation method.

The samples were measured after a period of open-circuit potential stabilisation of 3600 s was reached, at a scan rate of 1 $mV{\cdot}s^{-1}$. Surface morphology of ingots after electrochemical tests was observed by using Leica DVM6 digital microscope. Microhardness tests were conducted using a Future Tech FM-700 Vickers hardness testing instrument with a load of 1000 g for 15 s.

In addition, dye decomposition tests were carried out using alloys in the as-cast state. Due to the lack of research in decolourising dyes using high entropy alloys, the authors used the parameters of experiments from previous studies with another material [31]. Sodium percarbonate has already demonstrated its potential to carry the Fenton reaction [32]. The experiment was carried out in a solution containing the dye Rhodamine B (RhB) with a concentration equal to 0.005 g/l. Sodium percarbonate and the test alloys were introduced into the test solution. The appropriate pH was obtained by adding sulphuric acid. The initial values for the experiment were: pH 7, sodium percarbonate (SPC) concentration of 16.7 g/l and one of the two tested alloys concentration of 16.7 g/l. To standardise the decolourisation processes and to enable precise dosing of the material, a high entropy alloy in the as-cast state was added to the reaction solution in fragmented form. The reaction solution was irradiated with a UV light source (36 W, λ = 365 nm) and stirred (400 rpm) for 60 min. The process was carried out at ambient temperature. The reference method to assess the catalytic effect of the alloy was the UV/sodium percarbonate process, an identical experiment except for the presence of a high-entropy alloy in the solution. The degree of decolourisation was measured using the UV/Vis method (Shimadzu UV-1800 UV/Visible Scanning Spectrophotometer).

3. Results and discussion

3.1. Structure analysis

Firstly, to obtain detailed information about the arrangements of the atoms in the structure of high entropy alloys, the ^{57}Fe Mössbauer spectra for the AlCoFeNiTi and AlCoFeNiTiSi alloys in an as-cast state and form of plates were measured and are displayed in Fig. 1. The obtained hyperfine parameters are listed in Table 1.

The spectra for AlCoFeNiTi alloys showed the coexistence of a nonmagnetic part (singlet) with a magnetic hyperfine portion (sextets). The nonmagnetic component in the form of a single line dominates the spectrum. This component represents the ordered Heusler phase with $L2_1$ structure [33,34]. The magnetic part of the Mössbauer spectra was resolved on the four magnetic Zemann's sextets with different values of magnetic hyperfine field (Table 1). These sextets correspond to the Fe atom in the body-centred crystal structure and are surrounded by the Fe, Co, Ni, Al or Ti atoms. The sextets with hyperfine magnetic fields ~35 T and ~ 34 T arise from iron atoms surrounded by Co or Ni [35–37]. In BCC Fe-Ni or Fe-Co alloy, an Ni or Co atom causes an increase of Fe moments near the atom [38]. Sextets with hyperfine magnetic fields lower than 33 T result from the surrounding of Fe atom primarily by Al and Ti atoms [39,40]. For the AlCoFeNiTi alloy in the form of the plate, the line width of sextets is much higher than those observed for this alloy in the as-cast state (Table 1). Also, calculated hyperfine magnetic field values for AlCoFeNiTi alloy in the plate form are smaller than for this alloy in the as-cast state. It can result from the disordered phases related to these components and the substitution of Fe, Co and Ni atoms by Al and Ti atoms.

The Mössbauer spectra for AlCoFeNiTiSi alloy in an as-cast state and the form of plates contain only nonmagnetic components (doublets). Hyperfine parameters of quadrupole doublets with negative isomer shift values indicate the presence of some Ti-rich phase [33,41–43]. The physical properties of Ti-alloys are very sensitive to their stoichiometry [41,44,45]. Due to the above, we associated this component with some $Ti_2Co_3Si_1$-like phase, where Fe substitutes Ti. Hyperfine parameters of second doublets are typical for Al-rich Al-Fe alloys [46–48]. This component is related to the Al-rich B2 phase. These doublets are two primary components visible on the Mössbauer spectra for AlCoFeNiTiSi alloys (Table 1, Fig. 1). Hyperfine parameters of third quadrupole doublet with isomer shift ~0.27 mm/s indicate the presence of α-$(Fe,Co)Si_2$ phase [49,50]. Narrow line width calculated for components on Mössbauer spectra of AlCoFeNiTiSi alloys indicates that phases related to them are well crystallised.

The structure analysis of alloys with and without the addition of silicon was performed to describe the influence of both silicon and cooling rate on the changes in the phase composition, chemical elements distribution and segregation. The changes generated by the cooling rate were determined for AlCoFeNiTi HEA and presented in Fig. 2. As can be seen, both samples (in the as-cast state and the form of plate) are characterised by the double-phase nature related to the presence of $L2_1$ and BCC phases. However, the changes in the BCC phase's chemical composition are responsible for shifting the character of diffraction peaks. For example, the 2θ position of (110) shifts from 45.57 to 43.72, while a higher cooling rate was used to cast the alloy. 2D EDX maps were presented in Fig. 2b and c for master alloy and sample in the form of the plate to support this analysis. As can be seen, the Ni and Co are nearly uniformly distributed in both phases, and some segregation of Ti can be observed for alloy in the as-cast state, while for the sample in the plate form, Ni, Co, and Ti are uniformly disturbed between the two phases. Generally, the presence of $L2_1$ Heusler in high entropy alloys is related to the formation of multicomponent TM_2TiAl phase, in which TM is Co, Fe, Cr and Ni [51]. As can be seen, in Fig. 2b and c, in the AlCoFeNiTi HEAs, this $L2_1$ phase appears in Al-reach regions and contain Ni, Fe and Co. The same situation appears when the sample is cast using a higher cooling rate. Despite the presence of $(Fe,Co,Ni)_2TiAl$ phase, the second one, the BCC phase associated with Fe-rich regions, can be observed on the XRD pattern recorded for as-cast AlCoFeNiTi HEA. This phase contains all chemical elements, i.e. Co, Ni, Al and Ti and also is presented in a sample in the form of a plate, which can be visible especially under analysing of the 2D EDX maps (Fig. 2c). The previously presented analysis of Mössbauer spectra additionally confirms these findings.

A similar analysis was prepared for AlCoFeNiTiSi HEA and presented in Fig. 3. Interestingly, the addition of silicon drastically changes the phase composition and results in the formation of a double-phase alloy. The observed phases are related to Al-rich B2 and Ti-rich HCP phases. The cooling rate does not influence the phase composition; however, it changes the structure and chemical distribution in the alloy. As a result, only Co is uniformly distributed between these two phases for the sample in the as-cast state. The 2D EDX maps confirm that the master alloy B2 phase contains mainly Al and Ni, while the Ti-rich HCP phase is also composed of Fe and Si.

Moreover, some segregation of Fe and Si also can be noted. A higher cooling rate also results in the presence of the B2 and HCP phases, while Si and Ti are distributed in both phases. Also, Ni is nearly uniformly distributed between these two identified phases. Some chemical element segregations can also be observed for Fe and Si. This segregation can be attributed to forming the α-$(Fe,Co)Si_2$ phase identified in Mössbauer spectra. The B2 phase presented in this alloy can be related to the Al(TM) phase, in which TM is Co, Fe and Ni, while the HCP with a $Ti_2Co_3Si_1$-like phase contains both Fe and Ni. The influence of Si on the phase composition and structure can be observed. The changes in the phase composition are strictly related to the segregation between Al and Si, which can be observed for alloys casted using two different cooling rates.

The SEM images show both the influence of the cooling rate and the presence of Si on the structure of the analysed alloys (Fig. 4). In the case of the discussed alloys, the structure was refined by

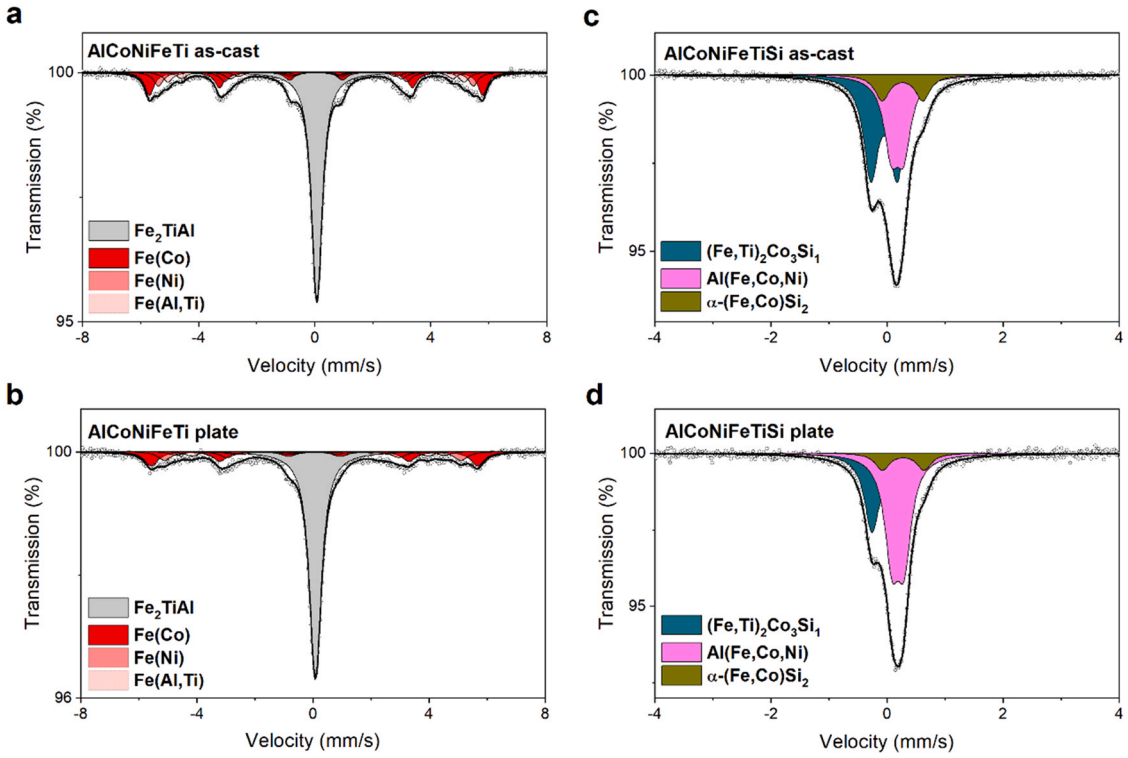

Fig. 1. Mössbauer spectra together with the fitted subspectra for the alloys in an as-cast state and plates recorded for AlCoFeNiTi (a,b), AlCoFeNiTiSi (c,d) (sextets represent the magnetic part and the single lines and doublets are the non-magnetic part).

Table 1
The Mössbauer hyperfine parameters of the investigated alloys. Isomer shift (*IS*), quadrupole splitting (*QS*), hyperfine magnetic field (*H*), full line width (FWHM) and relative area from the spectra (*A*) for the studied samples. Estimated errors are ± 0.01 mm/s for IS, QS and G; for H, the error is ± 0.5 T, and for A is ± 0.5%.

Component	IS (mm/s)	QS (mm/s)	G (mm/s)	H (T)	A (%)	Compound
AlCoNiFeTi as-cast						
Singlet	0.08	–	0.43	–	54.4	$L2_1$ Fe_2TiAl
Sextet	0.05	0.00	0.39	35.7	19.7	BCC Fe(Co)
Sextet	0.04	0.00		33.7	11.8	BCC Fe(Ni)
Sextet	0.05	0.00		31.7	8.6	BCC Fe(Al,Ti)
Sextet	0.09	0.00		29.0	5.5	BCC Fe(Al,Ti)
AlCoNiFeTi plate						
Singlet	0.08	–	0.49	–	61.5	$L2_1$ Fe_2TiAl
Sextet	0.05	0.00	0.56	35.0	17.7	BCC Fe(Co)
Sextet	-0.01	0.00		31.7	10.8	BCC Fe(Ni)
Sextet	-0.09	0.00		28.7	4.7	BCC Fe(Al,Ti)
Sextet	-0.11	0.00		25.3	5.5	BCC Fe(Al,Ti)
AlCoNiFeTiSi as-cast						
Doublet	-0.05	0.45	0.31	–	51.1	HCP $(Fe,Ti)_2Co_3Si_1$
Doublet	0.17	0.21		–	35.8	B2 Al-(Fe,Co,Ni)
Doublet	0.27	0.67		–	13.1	α-$(Fe,Co)Si_2$
AlCoNiFeTiSi plate						
Doublet	-0.03	0.46	0.30	–	39.3	HCP $(Fe,Ti)_2Co_3Si_1$
Doublet	0.18	0.21		–	51.7	B2 Al-(Fe,Co,Ni)
Doublet	0.28	0.69		–	9.0	α-$(Fe,Co)Si_2$

increasing the cooling rate. In the samples, the precipitation has a dense shape, with larger dimensions in the slowly cool ones and much smaller in the case of the fast cooling plates. In the case of the AlCoFeNiTiSi alloy, and especially in the case of plates, complex alternating light and dark areas are noticeable; they are probably the effect of spinodal decomposition and quick freezing of the structure.

3.2. Thermal analysis

The crystallisation mechanism of AlCoFeNiTi and AlCoFeNiTiSi HEAs in an as-cast state and the form of plates were described based on the DTA curves presented for heating and cooling (Fig. 5). It can be seen that the course of the curves was similar between the used cooling rates. Differences in the course of the DTA curves for chemical compositions result from the phase composition. In the case of the AlCoFeNiTi alloy in the as-cast state, during heating, there were three thermal events with low enthalpies at temperatures: 1037 °C, 1146 °C, 1210 °C and one distinct peak at 1401 °C. The thermal events for the high-pressure cast alloy were observed at the following temperatures: 829 °C, 1054 °C, 1214 °C, and 1429 °C. The recorded DTA curve during the cooling of the as-casted alloy was characterised by three exothermic peaks: 1389 °C, 1211 °C, and 1129 °C. In the case of the plate, a shift of thermal events towards positive values was recorded: 1415 °C, 1229 °C, 1146 °C and a small peak was observed at 966 °C. The AlCoFeNiTiSi, both in the form of as-cast and plates, during heating, was characterised by the occurrence of a single thermal event at temperatures similar to ~1375 °C. During cooling, the alloy with the addition of silicon, produced in both technologies, was characterised by a DTA curve consisting of a double thermal event. The highest enthalpy values were recorded at ~1376 °C and 1350 °C.

According to the literature [52], the solid state transformations for AlxCoCrFeNi alloys should be considered up to 1400 °C. The article [53] describes the Fe-Al-Ti alloys after heat treatment, for which the presence of α-Fe, Al (A2) + Fe_2AlTi ($L2_1$) phases was identified. Based on the DTA results, the authors [53] determined the transition temperatures: $L2_1$ ↔ B2 (950 °C), B2 ↔ A2 (1137 and 1100 °C), solvus temperature (1330 and 1342 °C) as well as liquidus temperature (1393 and 1402 °C). According to another source in the literature [54], the temperature about 1000 °C is the transformation temperature of the solvus B2 (NiAl) from the FCC and $L1_2$ (Ni_3Al) phases. Moreover, Stryzhyboroda et al. [52] indicate that the thermal event

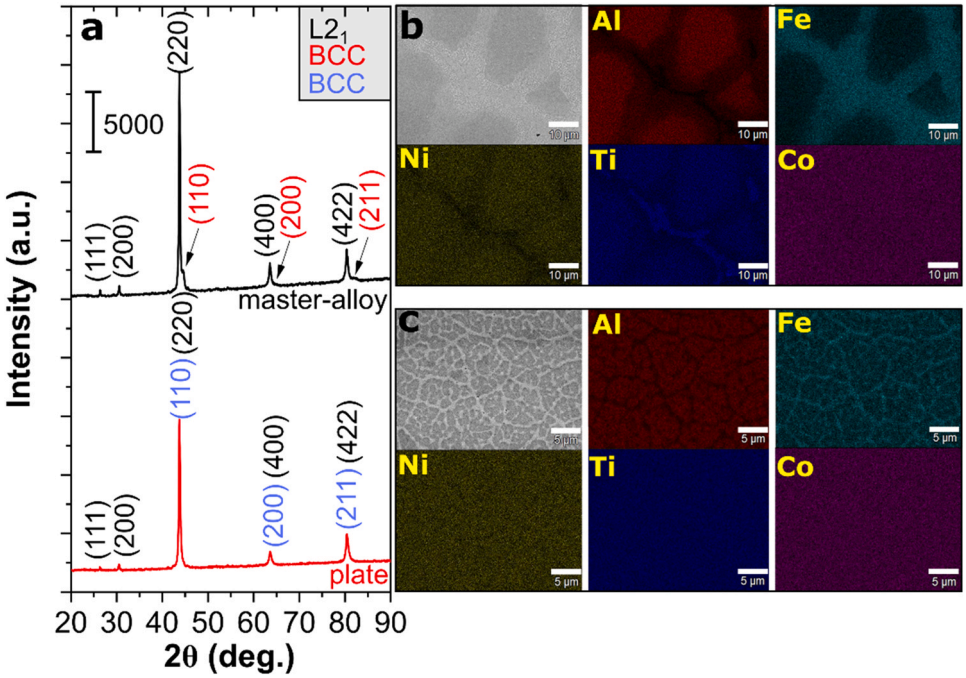

Fig. 2. XRD patterns (a) and EDX maps (b) for the AlCoFeNiTi HEAs in an as-cast state (ingot) and the form of plates (c).

of approximately 1200 °C for the share of aluminium $0.8 \geq x \geq 1$ is related to the dissolution of the disordered phase of the solid solution of BCC-A2 and FCC-A1. The heat event above 1350 °C corresponds to mass melting [52]. For the AlCoFeNiTi alloys analysed in this article, it can be assumed that during heating the transformation of $L2_1$ into the B2 phases took place first, then B2 to A2 and at the end the dissolution of BCC-A2 before melting in the mass [52–54]. Based on the previous work [21], it can be assumed that the highest enthalpy value at the temperature of ~1350–1400 °C and the corresponding thermal events during cooling in the range of 1300–1400 °C are characteristic of AlCoFeNi HEA. In the literature, these thermal events have been described as the melting point of the dendritic and interdendritic phases [54,55]. The double thermal event during heating and cooling of AlCFeNiTiSi alloys is related to the addition of silicon, which was also observed in previous work [21]. The addition of titanium to the AlCoNiFe HEA alloys influenced the formation of the B2 and HCP phases. Therefore, thermal effects related to the transformations of 1037 °C, 1146 °C, and 1210 °C may be related to the transformations of these phases.

3.3. Magnetic properties

The magnetic hysteresis loops of the AlCoFeNiTi and AlCoFeNiTiSi HEAs in the form of ingots and plates measured by the VSM method at room temperature are presented in Fig. 6. Furthermore, the values of saturated magnetisations (M_s), remanence (M_r), and coercivity (H_c) are listed in Table 2. The effect of silicon addition to the AlCoFeNiTi alloy on the magnetic properties is noticeable. The addition of Si significantly reduces the saturation magnetisation. AlCoFeNiTi HEA in plate form exhibits a high M_s value of 29.83 emu/g, while

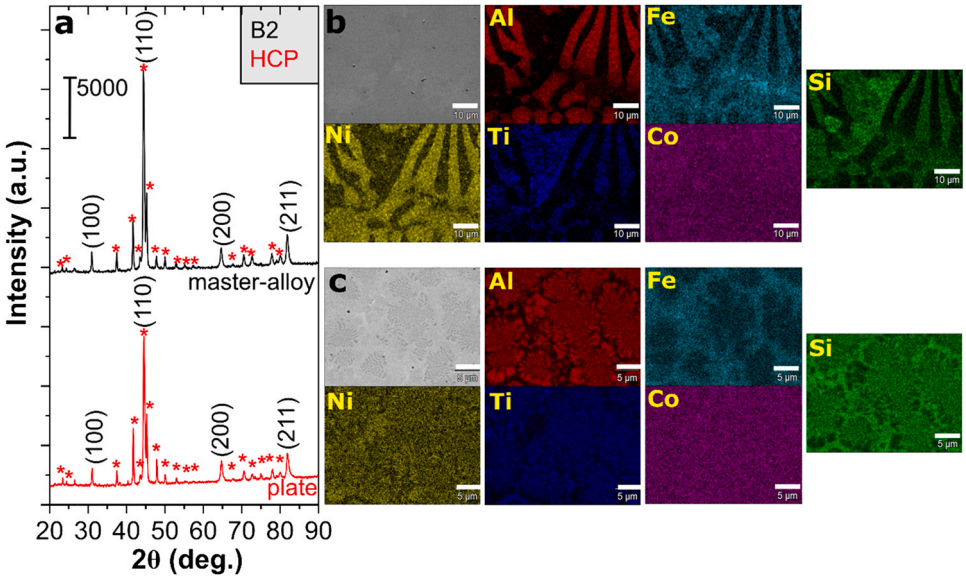

Fig. 3. XRD patterns (a) and EDX maps (b) for the AlCoFeNiTiSi HEAs in an as-cast state (ingot) and the form of plates (c).

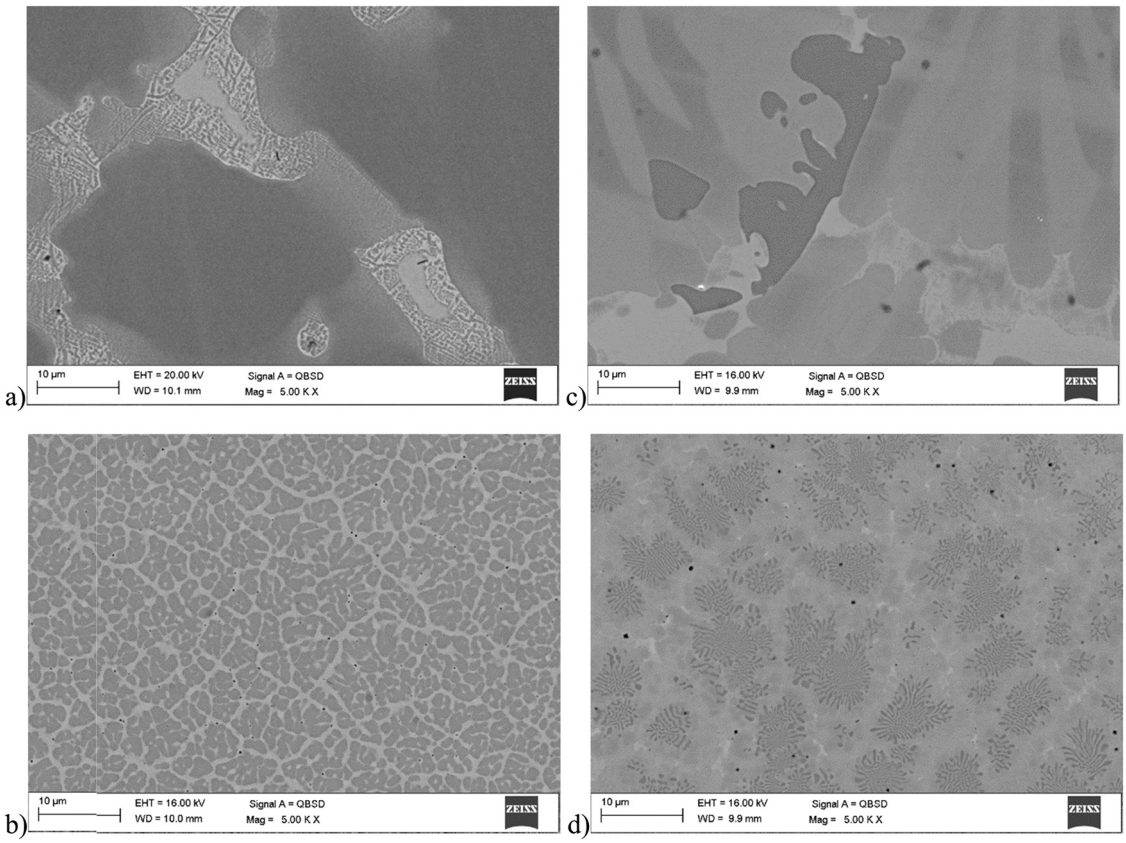

Fig. 4. SEM images of AlCoFeNiTi HEA (ingot: a, plate: b) and AlCoFeNiTiSi HEA (ingot: c, plate: d).

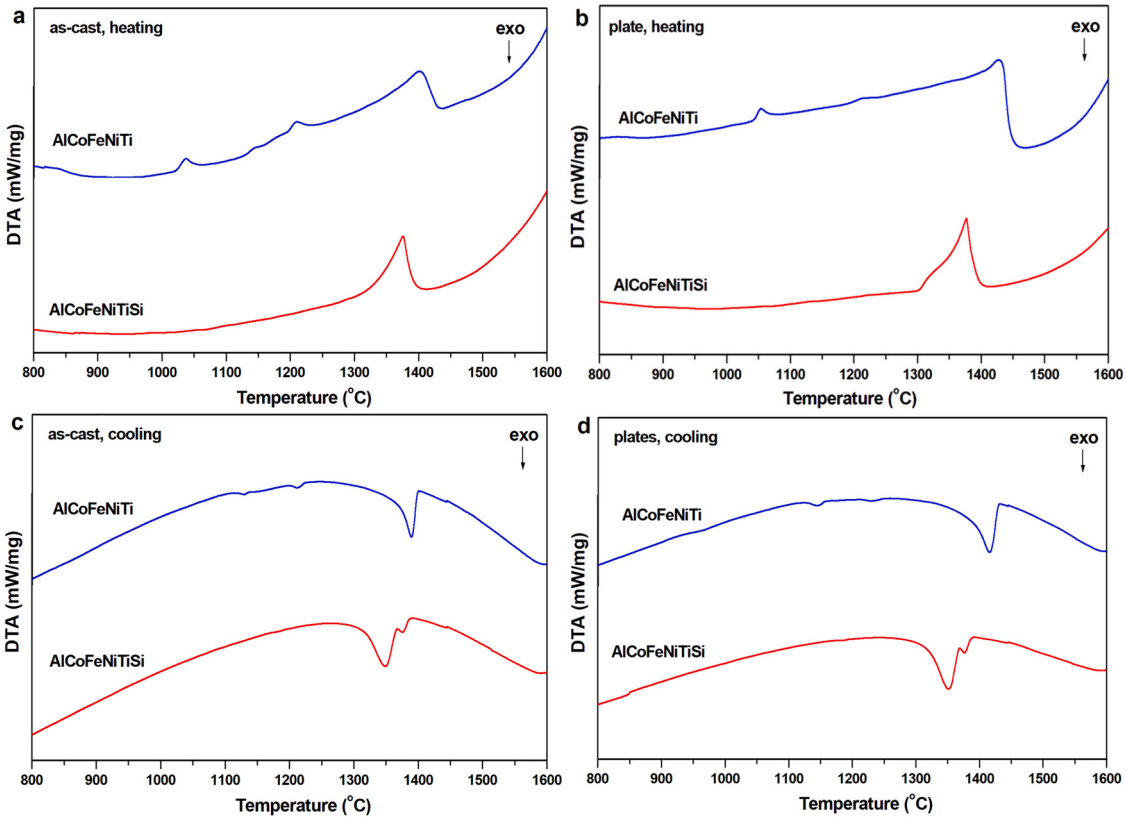

Fig. 5. DTA curves of the AlCoFeNiTi(Si) HEAs in an as-cast state (a,c) and in the form of plates (b,d), heating and cooling at 20 °C /min.

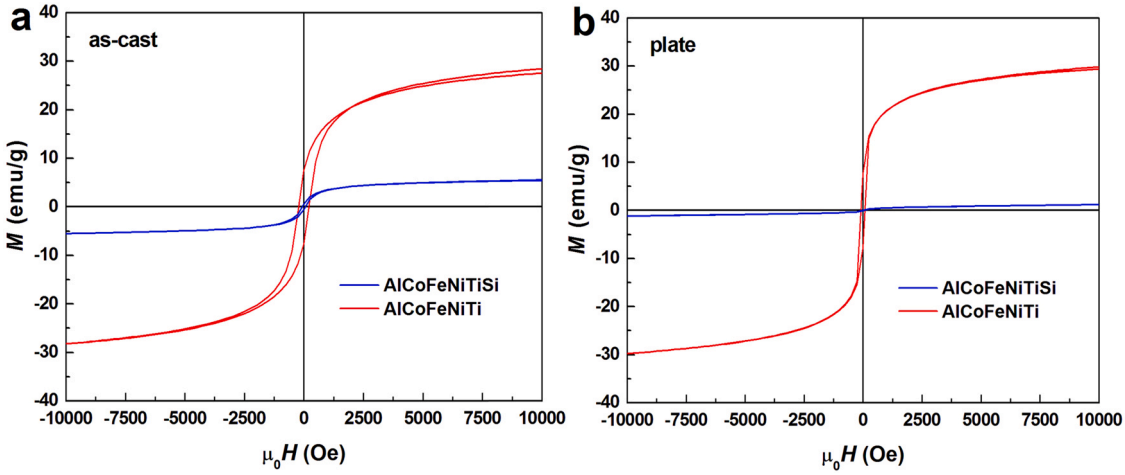

Fig. 6. Magnetic hysteresis loops of the AlCoFeNiTiSi HEAs in (a) an as-cast state and (b) in the form of plates.

Table 2
The magnetic properties of the AlCoCrFeNiSix HEAs determined by analysis of the hysteresis loops (M_s – saturation magnetisation, M_r – remanence, H_c – coercivity).

Sample	Type	M_s (emu/g)	M_r (emu/g)	H_c (Oe)
AlCoFeNiTi	as-cast	28.47	7.53	217.44
	plate	29.83	7.61	117.66
AlCoFeNiTiSi	as-cast	5.52	0.56	72.19
	plate	1.18	0.06	48.15

AlCoFeNiTiSi HEA shows a low M_s value of 1.18 emu/g. A significant reduction in saturation magnetisation is also observed in an as-cast state alloys from 28.47 emu/g for the alloy without the addition of silicon to 5.52 emu/g for the alloy with the silicon content. The values of remanence and coercivity show a similar trend. A much higher value of M_r is characteristic of AlCoFeNiTi alloys. The sample in the plate obtained M_r value of 7.61 emu/g, while the AlCoFeNiTiSi alloy in the form of the plate had a remanence value of 0.06 emu/g. In the case of coercivity, the AlCoFeNiTi as-cast alloy is characterised by a higher H_c value than the plate, which is 217.44 Oe and 117.66 Oe, respectively. There was also a significant decrease in the coercivity value after adding Si to the alloy. The AlCoFeNiTiSi alloy showed the lowest coercivity value of 48.15 Oe in the form of a plate.

Earlier works confirm the effect of silicon addition on the magnetic properties of high entropy alloys. For example, in work [21], there was a clear tendency for a decrease in saturation magnetisation with an increase of Si content in the AlCoCrFeNiSi$_x$ alloy. Similarly, in [56], the addition of Si significantly reduced the saturation magnetisation in the CoFeNiSi$_x$ alloy. Thus, the characteristics of the magnetic properties and hysteresis loops showed that the AlCoFeNiTi alloys show typical ferromagnetic behaviour, and the introduction of Si causes deterioration of the magnetic properties of these alloys, both in the as-cast state and in the form of plates.

3.4. Corrosion resistance

The electrochemical tests were carried out in 3.5% NaCl aqueous solution at 25 °C to describe and compare the corrosion resistance of the studied alloys from the point of view of the chemical composition and the solidification rates from the liquid state. Fig. 7a shows the dependence curves of the open circuit potential as a function of time (3600 s), while Fig. 7b presents the polarisation curves. Based on the conducted tests, the best corrosion resistance is indicated by the AlCoFeNiTi alloy in the form of plate due to the highest value of polarisation resistance (38.6 kΩcm^2) and the lowest corrosion current density (0.77 μA/cm^2). The worst corrosion behaviour was observed for the AlCoFeNiTiSi alloy in the as-cast state due to the inverse relationship, like the lowest polarisation resistance (2 kΩcm^2) and the highest corrosion current density (12.49 μA/cm^2). The positive effect of increasing the cooling rate from the liquid state on the corrosion resistance is visible for both tested chemical compositions. In the case of the AlCoFeNiTi alloy, all the analysed corrosion parameters were characterised by better values, f.e. the shift of the E_{OCP} and E_{corr} towards positive values, higher polarisation resistance and lower corrosion current density. The AlCoFeNiTiSi alloy in the form of plate showed a better value of the corrosion potential, while the other three parameters indicated a slight improvement or were practically comparable (see Table 3).

The improvement of the corrosion resistance of AlCoFeNiTi is visible in comparison with the mechanically alloyed AlNiCoCrFe HEAs described by Parakh et al. [57]. In that article [57], the value of the corrosion potential was − 524 mV, and the corrosion density was 12 μA/cm^2. In previous work [21], we compared the chemical compositions of AlCoCrFeNiSi$_x$ (x = 0; 0.25; 0.5; 0.75) HEAs and the effect of solidification from the liquid state (also as-cast alloys and high pressure cast plates). This effect of increasing the cooling rate on corrosion resistance improvement was visible [21]. In the article [21], the best corrosion resistance in terms of chemical composition was demonstrated by the AlCoCrFeNiSi$_{0.75}$ alloy. In this work, it could be concluded that the corrosion behaviour was different due to the use of Ti addition. Among others, the values of polarisation resistances are significantly lower compared to AlCoCrFeNiSi$_x$ alloys (x = 0; 0.25; 0.5; 0.75) [21]. Similar observations could be seen to the results presented in publication [58], because for AlCoCrFeNiSix alloys (x = 0; 0.3; 0.6; 0.9) more positive values of the corrosion potential were recorded. However, a more favourable j_{corr} value could be observed for the AlCoFeNiTi plate analysed in this work. The influence of Ti addition on the corrosion properties of AlCoCrFeNi alloys was investigated in the article by Huang et al. [59]. The results for the corrosion potential obtained by the authors for the AlCoCrFeNi (−0.355 V) and AlCoCrFeNiTi$_{0.4}$ (−0.3266 V) alloys were much more favourable, although in our study we obtained lower corrosion current density values than AlCoCrFeNi (223 μA/cm^2), AlNiCiFeNiTi$_{0.4}$ (73.6 μA/cm2), AlCoCrFeNiTi$_{0.8}$ (128 μA/cm^2), AlCoCrFeNiTi (114 μA/cm^2) [59]. The visible improvement of the corrosion parameters for the AlCoFeNiTi alloy presented in this paper and the critical assessment of an article [21] is a hint for future research on optimising the chemical composition of high-entropy alloys with the addition of Ti.

Fig. 8 presents the surface morphology of AlCoFeNiTi and AlCoFeNiTiSi ingots after electrochemical measurements. The surface of alloys after corrosion contains pores and cracks. The visible brighter areas suggest the formation of local galvanic microcells resulting

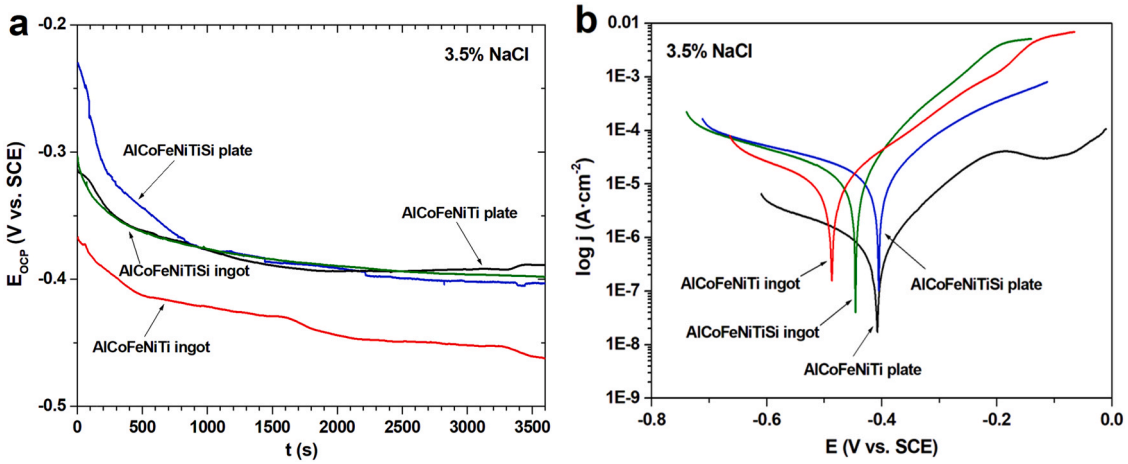

Fig. 7. Variation in the open-circuit potential with time (a,b) and polarisation curves (b,d) for samples in an as-cast state and plates in 3.5% NaCl solution at 25 °C.

Table 3
Polarisation results of the AlCoFeNiTiSi HEAs in 3.5% NaCl solution.

Sample	Type	E_{OCP} [V] (± 0.01)	E_{corr} [V] (± 0.01)	R_p [kΩcm^2] (± 0.1)	j_{corr} [μA/cm^2] (± 0.1)
AlCoFeNiTi	as-cast	-0.462	-0.487	3.1	10.29
	plate	-0.389	-0.407	38.6	0.77
AlCoFeNiTiSi	as-cast	-0.398	-0.445	2.0	12.49
	plate	-0.403	-0.405	2.2	11.7

from the difference in the potentials of individual phases. However, it could be seen that the AlCoFeNiTi alloy is characterised by a less corrosive degradation compared to that of the AlCoFeNiTiSi ingot. The literature [60] also presents the results of observations of surface morphology after electrochemical tests. Dada et al. [60] describe that the coarse-grained AlTiCrFeCoNi HEA microstructure helped to create kinetic barriers that reduced the corrosion rate by forming passive layers on the surface of the HEA. The formation of passive layers in the morphology images using light microscopy was not visible for the alloys studied in this work. Other works [61,62] describe the corrosion mechanisms for high entropy alloys, including $Al_{0.5}CoCrFeNi$. Pitting corrosion was observed after immersion tests in an aqueous environment with 3.5% NaCl at 25 °C [61,62].

In this work, especially for the AlCoFeNiTiSi ingot, corrosion pitting was visible after electrochemical tests carried out in the same environment as in the work [61,62]. The articles [61,63] also reported that the phases rich in aluminium and nickel in compositionally complex alloys (CCAs) were dissolved in acid environments. The AlTiCrFeCoNi and AlTiCrFeCoNiSi alloys were characterised by the presence of lighter areas on the morphology images after corrosion tests that may indicate selective corrosion resulting from differences in the phase potentials of the alloys. Interestingly, according to the literature [61,64], the addition of small amounts of Ti (x = 0.2) or Si (x = 0.2) negatively affects the corrosion resistance of both the $Al_{0.3}CrFe_{1.5}MnNi_{0.5}Ti_x$ and $Al_{0.3}CrFe_{1.5}MnNi_{0.5}Si_x$ systems in NaCl solutions. This phenomenon is attributed to the formation of intermetallic compounds that can promote local corrosion [61,64].

3.5. Hardness measurements

The results of the hardness tests of AlCoFeNiTi and AlCoFeNiTiSi HEA in the ingot and plate form are presented in Fig. 9a. An apparent increase in hardness can be observed in both forms of samples with silicon addition. The highest hardness (1096 HV) was achieved for the AlCoFeNiTiSi alloy in the form of a plate. A hardness of 930 HV was noted for the AlCoFeNiTiSi ingot. The AlCoFeNiTi alloy exhibits a much lower hardness value (632 HV for the ingot and 699 HV for the plate, respectively). The selected images of the hardness test indentation are presented in Fig. 9b. Fine cracks can be observed for the plate of the AlCoFeNiTiSi alloy with the highest hardness. According to Martin et al. [65] who studied $Al_xCoCrCu_yFeNi$ alloys in terms of weld solidification and weldability, brittle fracture is caused by the accumulation of stresses during cooling. The increase in the cooling rate from the liquid state of the AlCoFeNiTiSi alloys probably influences higher hardness at the expense of plastic properties. Furthermore, Al-Si-(Fe,Mn) alloys are brittle due to the high

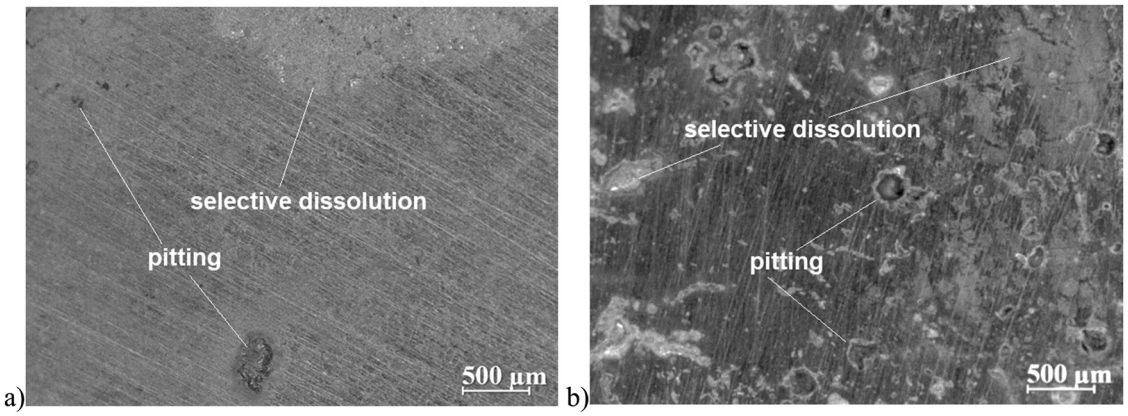

Fig. 8. Surface morphology of AlCoFeNiTi (a) and AlCoFeNiTiSi (b) ingots after electrochemical tests.

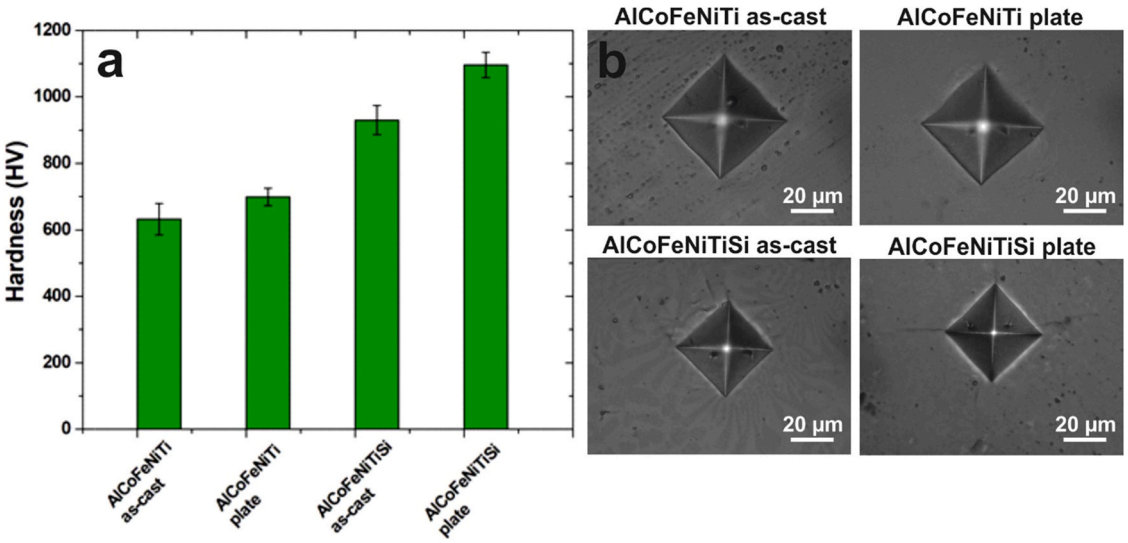

Fig. 9. Variation of Vickers hardness (a) and indentation images (b) of samples in an as-cast state and plates.

dissolution of Si in the aluminium matrix [66]. Strengthening mechanisms in HEAs can be related to solid solution hardening, precipitation hardening, grain boundary strengthening, and dislocation hardening [67]. Ren et al. [30] observed that after adding a high content of Ti or Si elements ($x < 0.5$), intermetallic compounds appear in the HEA microstructure, making the alloys of high hardness. After casting, the AlCoFeNi alloy without Ti content had a hardness of 350 HV [1]. The introduction of Ti into the AlCoFeNiTi alloy in the as-cast state increased the hardness value to 644 HV [68].

Similarly, in work [69], the hardness of the AlCoCuFeNiTi alloy was shown at 623 HV after adding Ti. Löbel et al. [11] obtained a hardness value of 730 HV in $AlCoCrFeNiTi_{1.5}$ HEA samples prepared in the arc melting process. In turn, for the $Al_{0.75}FeNiCrCoTi_{0.25}$ alloy prepared by a combination of mechanical alloying and spark plasma sintering, the hardness was 609 HV [13]. In another work [70], Ti led to the hardness of the $Al_{0.9}CoCrFeNiTi_{0.5}$ alloy of 620 HV due to the strengthening of the solid solution by Ti and the phase presence of the BCC and B2 phase. The literature also shows the effect of Si on the increase in the value of HEA microhardness. In our previous work [21], the hardness of $AlCoCrFeNiSi_x$ alloys increased with Si concentration. In the case of the HEAs analysed herein, the hardness changes can be related to differences in the phase composition between AlCoFeNiTi and AlCoFeNiTiSi alloys. The presence of the HCP $Ti_2Co_3Si_1$-like phase results in the observed significant improvement of the hardness compared to the alloy containing $L2_1$ and disordered BCC phases. Moreover, as observed under the Mössbauer spectra analysis, the HEA containing Si can also be hardened by the intermetallic α-$(Fe,Co)Si_2$ phases.

Strengthening mechanisms in high entropy alloys show that the spinodal distribution of the BCC phase with a high content of aluminium for AlxCoCrFeNi HEA alloys ($x = 0.7$) in the random A2 phase and the ordered B2 phase caused spinodal hardening effects [71]. Moreover, the effect of the addition of silicon on the increase in segregation would also be visible in the increase in the hardness of the AlCoFeNiTiSi alloy. The spinodal structure causes a high densification of the interfacial boundaries. It may also be a response to the higher hardness of the rapidly cooled alloy. Large disintegration, especially observed for the AlCoFeNiTiSi alloy in the form of plate, results in a high concentration of boundaries between the phases and causes a large increase in the hardness. Multicomponent alloys can be expected as alloys with elements having different atomic radius, which cause distortions of the lattice. Tian et al. [72] reported that a hardness value in monophasic HEAs depends on the variation of the atomic size. The increase in hardness value was also observed in the $AlCoCrFeNiSi_x$ ($x = 0$, 0.3, 0.6 and 0.9) cast [58] where it was found that it may be caused by the phase evolution of the BCC/B2 phases in place of the FCC phase, and the improvement in hardness may be attributed to the smaller atomic size compared to other components, which resulted in a limitation of dislocation.

Moreover, Jin et al. [73] attributed the increase in microhardness in AlxCoCrFeNiSi HEA to the decrease in the concentration of valence electrons (VEC). Also in this case, the phenomenon of improving the microhardness of these alloys was attributed to the transformation of the ductile FCC structure into the nano-spaced spinodal structure of the BCC phase, which provides the strengthening effect. Zhu et al. [18] indicate that the solid solution of the strengthening of the Si element and the precipitation of the cellular structure at the nanoscale responsible for improving the mechanical properties of the $AlCoCrFeNiSi_x$ alloys.

3.6. Decolourisation analysis

Removing organic pollutants from wastewater is one of the major challenges related to the high growth of various industries. Generally, dyes, hormones and antibiotics are widely studied in the literature, and their decomposition is tested using nanoparticles and newly-developed alloys. Herein, the possibility of application of high entropy alloys in these processes was studied, and the optimal reaction condition was determined based on the degradation of the widely studied chemical dye – Rhodamine B. Accordingly, initial pH, oxidant concentration, and catalyst (high entropy alloy) concentration were considered. The first factor was pH, which can significantly affect the efficiency of the oxidation process of the organic substance [74]. The results of this series of experiments can be seen in Fig. 10. For both tested alloys in an as-cast state, the pH did not significantly influence the decolourisation process, which may be due to the absence of the pH-induced activation of the alloy surface. The difference between the reaction rate constants (assuming the 1st order reaction) is also negligible (Table 4). For example, in the case of the AlCoFeNiTiSi HEA, the reaction rate constant is equal to 0.043 min^{-1} and 0.042 min^{-1} for pH 7 and 4, respectively.

Another parameter that influences the photo-Fenton process is the concentration of the oxidant [78]. Quan et al. [75] showed that the concentration of oxidant in the Fenton reaction has its maximum, over which the efficiency decreases. A similar effect was observed by Wang et al.[76]. Herein, the optimum oxidant - sodium

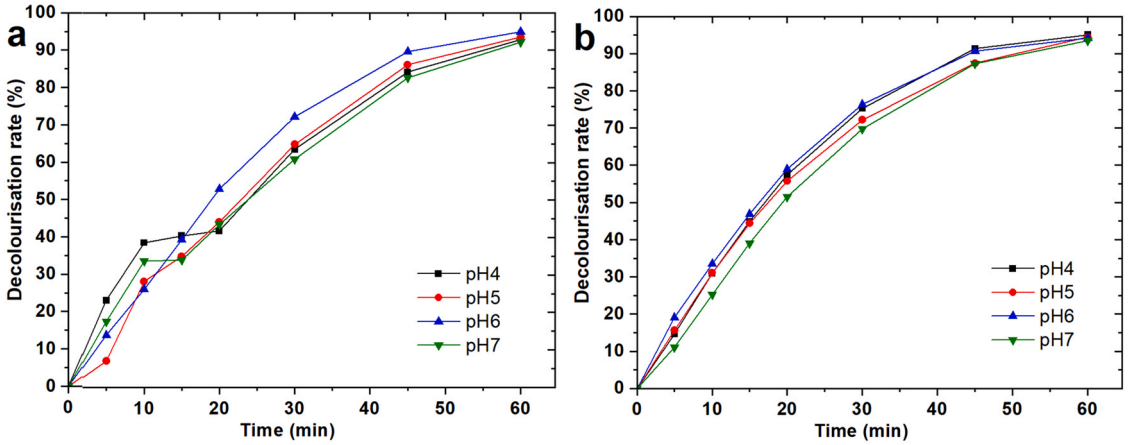

Fig. 10. Influence of the initial pH on the decolourisation process for AlCoFeNiTiSi (a) and AlCoFeNiTi (b) HEAs.

Table 4
The reaction rate constant (k) values determined for various initial pH.

Alloy	pH	k (min^{-1})
AlCoFeNiTi	7	0.053
	6	0.049
	5	0.050
	4	0.047
AlCoFeNiTiSi	7	0.043
	6	0.047
	5	0.052
	4	0.042

percarbonate concentration was determined for five various dosages (Fig. 11). The effect of sodium percarbonate concentration was significant. Increasing the dose of oxidant increases the rate of decolourisation. The AlCoFeNiTiSi alloy showed the highest degree of decolourisation for the highest oxidant concentration; however, for shorter reaction times, better results were obtained for two times lower concentration of sodium percarbonate. During the first 30 min of the process, the decolourisation rate of about 54% was observed for the 16.7 g/l, while the higher concentration allowed to decolourise only 38% of the dye. In the case of the AlCoFeNiTi alloy, no such relationship was demonstrated, and the increase in the concentration caused an increase in the decolourisation rate. For the AlCoFeNiTi HEA reaction rate constant increases from 0.006 min^{-1} to 0.058 min^{-1}. Interestingly, for sodium percarbonate concentration equal to 16.7 g/l and in the case of AlCoFeNiTiSi HEA, the degradation reaction is the reaction of 1st order, and the reaction rate constant increases gradually from 0.004 to 0.042 min^{-1}, while for the highest oxidant concentration the reaction order changes to the zero order, with the reaction rate equal to 0.089 $mol \cdot l^{-1} \cdot min^{-1}$.

The last parameter checked was the concentration of the catalyst – high entropy alloy. Due to that, the decolourisation rate (at 60 min) for the highest and two times lower oxidant concentration is similar; the two times lower concentration was chosen as much privilege in the further applications. The experiment was performed separately for AlCoFeNiTiSi and AlCoFeNiTi HEAs. The concentration of 0 g/l is the reference method (without HEAs). The results are shown in Fig. 12. The alloy concentration affects the decolourisation rate; however, almost all proposed concentrations achieve a similar level of decolourisation after 60 min. For example, the process catalysed by AlCoFeNiTiSi alloy shows a much higher decolourisation rate (92%) than the reference method without the addition of catalysts (52%). The most favourable among the tested concentrations is 16.7 g/l. This catalyst (AlCoFeNiTiSi) concentration allowed to decolourise 92% of RhB after 60 min. The concentration of the AlCoFeNiTi alloy turned out to have a less significant effect than that of the AlCoFeNiTiSi alloy (see Fig. 11b). All tested concentrations achieved more than 90% decolourisation after 60 min, while the highest decolourisation rate for the reaction catalysed by AlCoFeNiTiSi alloy was equal to 95.5%. However, for the reference reaction (i.e. without catalyst addition), the decolourisation rate at 60 min was equal to 52%. Accordingly, both alloys increase the degree of decolourisation compared to the reference method.

Moreover, in the case of the AlCoFeNiTi HEA, the reaction rate constant increases from 0.001 min^{-1} to 0.058 min^{-1} when the alloy concentration increases from 0 to 33.3 g/l. As previously mentioned,

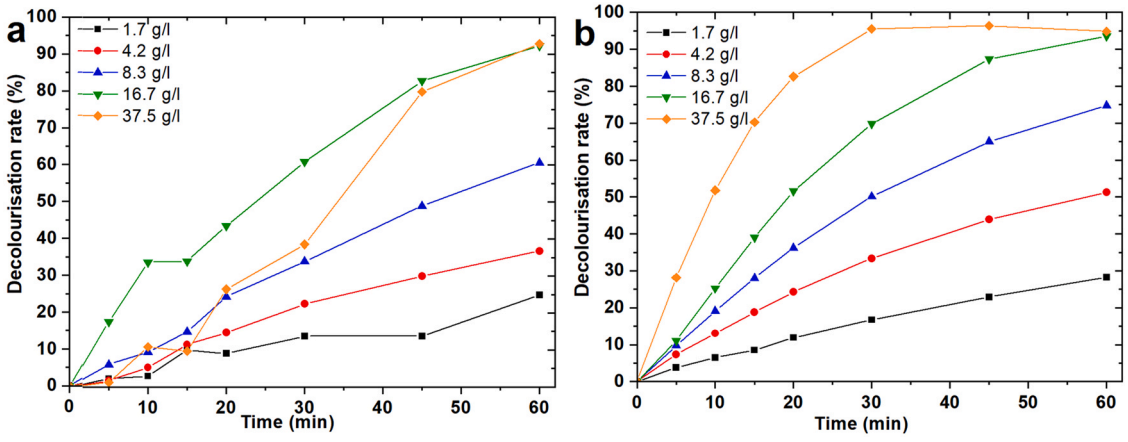

Fig. 11. Influence of sodium percarbonate concentration on the decolourisation process in the presence of AlCoFeNiTiSi (a) and AlCoFeNiTi (b) HEAs.

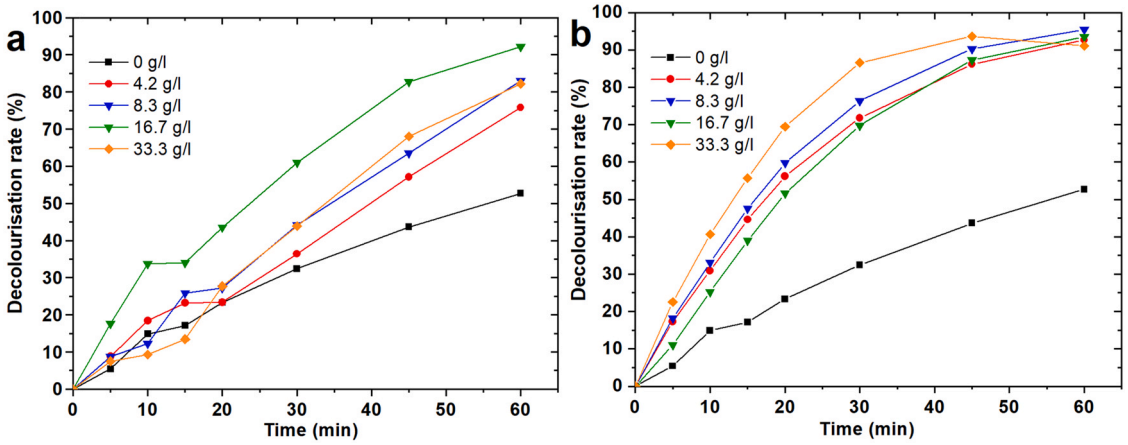

Fig. 12. Effect of AlCoFeNiTiSi (a) and AlCoFeNiTi (b) HEAs concentration.

Table 5
Comparison of results obtained in this work with the values from the literature.

Catalyst	Dye	Reaction condition	Decolourisation rate [%]	Time [min]	Ref.
Cu-doped $LaTiO_3$	RhB	[dye] = 8 mg/l [catalyst] = 1.4 g/l [H_2O_2] = 0.02 mol/l pH = 4	94	120	[82]
Fe_2O_3–Kaolin	RhB	[dye] = 15 mg/l [catalyst] = 1 g/l [H_2O_2] = 0.05 mol/l pH = 2.21	98	120	[83]
Ag_2CrO_4–$LaFeO_3$ nanocomposite	RhB	[dye] = 5 mg/l [catalyst] = 0.5 g/l [H_2O_2] = 0.064 mol/l	96	60	[84]
Fe_3O_4/CuO	RhB	[dye] = 10 mg/l [catalyst] = 0.02 g/l [H_2O_2] = 0.03 mol/l pH = 2	98	60	[85]
Fe_3O_4/SiO_2	RhB	[dye] = 20 mg/l [catalyst] = 0.2 g/l [H_2O_2] = 0.256 mol/l pH = 6.12	97	180	[86]
Fe_3O_4@Prussian blue	RhB	[dye] = 10 mg/l [catalyst] = 0.16 g/l [H_2O_2] = 0.587 mol/l pH = 6.5 T = 318 K	~ 100	15	[76]
$Fe_{41}Co_7Cr_{15}Mo_{14}C_{15}B_6Y_2$ amorphous alloy	RhB	[dye] = 20 mg/l [catalyst] = 1 g/l [H_2O_2] = 0.003 mol/l pH = 3 T = 313 K	100	6	[87]
AlCoFeNiTiSi	RhB	[dye] = 5 mg/l [catalyst] = 16.7 g/l [sodium percarbonate] = 0.106 mol/l pH = 7	92	60	This work
AlCoFeNiTi	RhB	[dye] = 5 mg/l [catalyst] = 8.3 g/l [sodium percarbonate] = 0.106 mol/l pH = 7	95.5	60	This work

Ti ions positively influence the production of OH radicals [77]. In the case of the examined alloys, the difference in the achieved effects of decolourisation is probably related to the content of Ti and Fe. Better effects of decolourisation were achieved for the AlCoFeNiTi alloy, which contained 20% Fe and Ti by weight in its composition, as opposed to the AlCoFeNiTiSi alloy with 16.66% by weight of Fe and Ti. Moreover, it was found that pH slightly influenced the effectiveness of the decolourisation process, and both alloys showed catalytic activity even at a neutral pH. This allows using the investigated alloys to treat coloured wastewater without the initial pH correction. When the wastewater needs to be treated with a modified Fenton reagent using other alternative iron sources (e.g. steel swarf) [78] or zero-valent iron [79], and at low pH, the dissolution of iron is a significant problem. Therefore, the advantage of the tested alloys is their increased corrosion resistance and, thus, low susceptibility to dissolution. The tested alloys can also be used as a modified Fenton process in continuous flow reactors similar to that proposed in [80], which offers greater possibilities for the practical application of the Fenton reagent. The continuous Fenton process

can be easier to operate, allowing the catalyst in the process, and thus, the catalyst can be used repeatedly.

Finally, the results of the experiments were compared with the literature data (Table 5). The small influence of pH on the decolourisation process and the use of sodium percarbonate in place of hydrogen peroxide distinguished them. Due to its chemical properties, sodium percarbonate is safer than hydrogen peroxide [81]. Moreover, high entropy alloys showed catalytic abilities comparable to Fe_3O_4 nanoparticles. However, there are similar decolourisation effects at neutral pH. All presented literature studies, not only of Fe_3O_4 nanoparticles, showed a decrease in decolourisation with increasing pH, while this factor had little effect on the decolourisation process using high entropy alloys as a catalyst. The research was also compared with amorphous alloys as a similar material group. Amorphous alloys achieve very high decolourisation rate in a short time; however, they require a low pH (reaching the value of 3).

4. Conclusions

The formation of double-phase HEAs was confirmed for the AlCoFeNiTi and AlCoFeNiTiSi alloys cast using two different cooling rates. As presented, adding Si changes the phase composition, whereas the cooling rate does not affect the phase composition of both alloys. However, a higher cooling rate results in a much higher homogeneity in the distribution of the chemical elements. The AlCoFeNiTi alloy was composed of the $(Fe,Co,Ni)_2TiAl$ $L2_1$ Heusler phase and the BCC phase associated with Fe-rich regions observed on the 2D EDX maps. The addition of silicon causes the formation of the $Ti_2Co_3Si_1$-like HCP and Al-rich B2 phases. The AlCoFeNiTi alloy indicates the best corrosion resistance in the form of a plate due to the highest value of polarisation resistance (38.6 $k\Omega cm^2$) and the lowest corrosion current density (0.77 $\mu A/cm^2$). The addition of Si significantly reduces the M_s, M_r, and H_c values for samples in the as-cast state and plates. The AlCoFeNiTiSi alloy showed the lowest coercivity value of 48.15 Oe in the form of a plate.

A significant increase in hardness can be observed in both forms of samples with silicon addition. The highest hardness (1096 HV) was achieved for the AlCoFeNiTiSi alloy in the form of a plate, which can be mainly related to the formation of the $Ti_2Co_3Si_1$-like HCP phase. However, fine cracks can be observed for rapidly solidified AlCoFeNiTiSi. This could mean that, by changing the cooling rate from the liquid state of high entropy alloys with the addition of silicon, it is possible to control the value of hardness and strength. A slight influence of pH on the effectiveness of the decolourisation process was found, and both alloys showed high catalytic activity even at a neutral pH. This allows the investigated alloys to treat coloured wastewater without the initial pH correction. Furthermore, the AlCoFeNiTi alloy in the as-cast state shows catalytic properties that are different from those of HEA containing Si. A near two times higher decolourisation rate (95.5%) than for the reference reaction without catalyst addition was achieved for the optimal reaction condition (pH 7, sodium percarbonate and catalyst concentrations equal to 16.7 g/l and 8.3 g/l, respectively).

CRediT authorship contribution statement

W. Łoński: Conceptualization, Investigation, Writing – original draft. **M. Spilka**: Data curation, Writing – original draft. **M. Kądziołka-Gaweł**: Investigation, Writing – original draft. **P. Gębara**: Investigation. **A. Radoń**: Investigation, Writing – original draft. **T. Warski**: Investigation. **S. Łoński**: Investigation, Writing – original draft. **K. Barbusiński**: Supervision. **K. Młynarek-Żak**: Investigation, Writing – original draft. **R. Babilas**: Methodology, Writing – review & editing, Supervision.

Data availability

Data will be made available on request.

Declaration of Competing Interest

The authors declare that they have no known competing financial interests or personal relationships that could have appeared to influence the work reported in this paper.

Acknowledgements

The work was financed from the statutory subsidy of the Faculty of Mechanical Engineering of the Silesian University of Technology 10/010/BKM22/1114. Publication was also supported under the rector's pro-quality grant. Silesian University of Technology, Poland, grant number: 08/040/RGJ22/0164.

References

[1] P.S. Hari, C. Mathew, J. Kuriakose, V.Y. Baby, Comparative study of high entropy alloys- AlCoCrFeNi, AlCoFeNi and CoCrFeNi with 304SS, Int. J. Eng. Innov. Technol. 6 (2016) 29–33, https://doi.org/10.17605/OSF.IO/SDRCG
[2] M. Asadikiya, S. Yang, Y. Zhang, C. Lemay, D. Apelian, Y. Zhong, A review of the design of high-entropy aluminum alloys: a pathway for novel Al alloys, J. Mater. Sci. 56 (2021) 12093–12110, https://doi.org/10.1007/s10853-021-06042-6
[3] C.B. Nascimento, U. Donatus, C.T. Ríos, M.C. Lopes de Oliveira, R.A. Antunes, A review on corrosion of high entropy alloys: exploring the interplay between corrosion properties, alloy composition, passive film stability and materials selection, Mater. Res. 25 (2022), https://doi.org/10.1590/1980-5373-MR-2021-0442
[4] P.A. Ibrahim, İ. Özkul, C.A. Canbay, An overview of high entropy alloys, Emergent Mater. (2022) 1–18, https://doi.org/10.1007/s42247-022-00349-z
[5] M. Dada, P. Popoola, S. Adeosun, N. Mathe, High entropy alloys for aerospace applications, Aerodynamics (2021) 1–16, https://doi.org/10.5772/intechopen.84982
[6] R.R. Shahi, A.K. Gupta, P. Kumari, Perspectives of high entropy alloys as hydrogen storage materials, Int. J. Hydrog. Energy (2022) 1–17, https://doi.org/10.1016/j.ijhydene.2022.02.113
[7] X. Yan, Y. Zhang, Functional properties and promising applications of high entropy alloys, Scr. Mater. 187 (2020) 188–193, https://doi.org/10.1016/j.scriptamat.2020.06.017
[8] M.C. Gao, D.B. Miracle, D. Maurice, X. Yan, Y. Zhang, J.A. Hawk, High-entropy functional materials, J. Mater. Res. 33 (2018) 3138–3155, https://doi.org/10.1557/jmr.2018.323
[9] E.J. Pickering, A.W. Carruthers, P.J. Barron, S.C. Middleburgh, D.E.J. Armstrong, A.S. Gandy, High-entropy alloys for advanced nuclear applications, Entropy 23 (2021) 1–28, https://doi.org/10.3390/e23010098
[10] Y. Fu, J. Li, H. Luo, C. Du, X. Li, Recent advances on environmental corrosion behavior and mechanism of high-entropy alloys, J. Mater. Sci. Technol. 80 (2021) 217–233, https://doi.org/10.1016/j.jmst.2020.11.044
[11] M. Löbel, T. Lindner, T. Mehner, T. Lampke, Influence of titanium on microstructure, phase formation and wear behaviour of AlCoCrFeNiTix high-entropy alloy, Entropy 20 (2018) 1–11, https://doi.org/10.3390/e20070505
[12] M.A. Avila-Rubio, J.A. Baldenebro-Lopez, R. Soto-Rojo, L.G. Ceballos-Mendivil, Carreño-Gallardo, N.F. Garza-Montes-de-Oca, F.J. Baldenebro-Lopez, Effect of Mo and Ti on the microstructure and microhardness in AlCoFeNiMoTi high entropy alloys prepared by mechanical alloying and conventional sintering, Adv. Powder Technol. 31 (2020) 1693–1701, https://doi.org/10.1016/j.apt.2020.02.008
[13] Z. Chen, W. Chen, B. Wu, X. Cao, L. Liu, Z. Fu, Effects of Co and Ti on microstructure and mechanical behavior of Al0.75FeNiCrCo high entropy alloy prepared by mechanical alloying and spark plasma sintering, Mater. Sci. Eng. A 648 (2015) 217–224, https://doi.org/10.1016/j.msea.2015.08.056
[14] D. Mitrica, M.T. Olaru, V. Dragut, C. Predescu, A. Berbecaru, M. Ghita, I. Carcea, M. Burada, D. Dumitrescu, B.A. Serban, I.C. Banica, Influence of composition and as-cast structure on the mechanical properties of selected high entropy alloys, Mater. Chem. Phys. 242 (2020) 1–13, https://doi.org/10.1016/j.matchemphys.2019.122555
[15] M. Wu, R.C. Setiawan, D.Y. Li, Benefits of passive element Ti to the resistance of AlCrFeCoNi high-entropy alloy to corrosion and corrosive wear, Wear (2022) 492–493, https://doi.org/10.1016/j.wear.2021.204231
[16] Y.J. Chang, A.C. Yeh, The evolution of microstructures and high temperature properties of AlxCo1.5CrFeNi1.5Tiy high entropy alloys, J. Alloy. Compd. 653 (2015) 379–385, https://doi.org/10.1016/j.jallcom.2015.09.042
[17] W. Guo, J. Li, M. Qi, Y. Xu, H.R. Ezatpour, Effects of heat treatment on the microstructure, wear behavior and corrosion resistance of AlCoCrFeNiSi high-entropy alloy, Intermetallics 138 (2021) 1–14, https://doi.org/10.1016/j.intermet.2021.107324
[18] J.M. Zhu, H.M. Fu, H.F. Zhang, A.M. Wang, H. Li, Z.Q. Hu, Synthesis and properties of multiprincipal component AlCoCrFeNiSix alloys, Mater. Sci. Eng. A 527 (2010) 7210–7214, https://doi.org/10.1016/j.msea.2010.07.049

[19] B. Xin, A. Zhang, J. Han, J. Meng, Improving mechanical properties and tribological performance of Al0.2Co1.5CrFeNi1.5Ti0.5 high entropy alloys via doping Si, J. Alloy. Compd. 869 (2021) 1–15, https://doi.org/10.1016/j.jallcom.2021.159122

[20] Y. Chen, S. Zhu, X. Wang, B. Yang, G. Han, L. Qiu, Microstructure evolution and strengthening mechanism of Al0.4CoCu0.6NiSix (x=0–0.2) high entropy alloys prepared by vacuum arc melting and copper injection fast solidification, Vacuum 150 (2018) 84–95, https://doi.org/10.1016/j.vacuum.2018.01.031

[21] W. Łoński, M. Spilka, M. Kądziołka-Gaweł, P. Gębara, A. Radoń, T. Warski, K. Młynarek-Żak, R. Babilas, The effect of cooling rate on the structure and selected properties of AlCoCrFeNiSix (x = 0; 0.25; 0.5; 0.75) high entropy alloys, J. Alloy. Compd. 905 (2022) 1–10, https://doi.org/10.1016/j.jallcom.2022.164074

[22] P. Shi, Y. Li, Y. Wen, Y. Li, Y. Wang, W. Ren, T. Zheng, Y. Guo, L. Hou, Z. Shen, Y. Jiang, J. Peng, P. Hu, N. Liang, Q. Liu, P.K. Liaw, Y. Zhong, A precipitate-free AlCoFeNi eutectic high-entropy alloy with strong strain hardening, J. Mater. Sci. Technol. 89 (2021) 88–96, https://doi.org/10.1016/j.jmst.2021.03.005

[23] H. Wu, J. Xie, H.Y. Yang, D.L. Shu, G.C. Hou, J.G. Li, Y.Z. Zhou, X.F. Sun, Comparative study of mechanical and corrosion behaviors of cost-effective AlCrFeNi high entropy alloys, J. Mater. Eng. Perform. 31 (2022) 4472–4482, https://doi.org/10.1007/s11665-021-06563-w

[24] Y. Lu, Y. Dong, S. Guo, L. Jiang, H. Kang, T. Wang, B. Wen, Z. Wang, J. Jie, Z. Cao, H. Ruan, T. Li, A promising new class of high-temperature alloys: eutectic high-entropy alloys, Sci. Rep. 4 (2014) 1–5, https://doi.org/10.1038/srep06200

[25] J. Hou, X. Shi, J. Qiao, Y. Zhang, P.K. Liaw, Y. Wu, Ultrafine-grained dual phase Al0.45CoCrFeNi high-entropy alloys, Mater. Des. 180 (2019) 1–8, https://doi.org/10.1016/j.matdes.2019.107910

[26] Q. An, J. Wang, Y. Liu, B. Liu, W. Guo, Q. Fang, Y. Nie, Effects of C and Mo on microstructures and mechanical properties of dual-phase high entropy alloys, Intermetallics 110 (2019) 1–8, https://doi.org/10.1016/j.intermet.2019.04.014

[27] C. Xu, N. Geng, Q. Xiang, Y. Qu, B. Yu, K. Qiu, A novel dual phase high entropy casting alloy with high damping capacity, Mater. Res. Express 8 (2021) 1–13, https://doi.org/10.1088/2053-1591/abf390

[28] X. Han, Q. Chen, Q. Chen, Q. Wu, Z. Xu, T. Zheng, W. Li, D. Cui, Z. Duan, J. Zhang, J. Li, H. Li, Z. Wang, J. Wang, Z. Xia, Eutectic dual-phase microstructure modulated porous high-entropy alloys as high-performance bifunctional electrocatalysts for water splitting, J. Mater. Chem. A 10 (2022) 11110–11120, https://doi.org/10.1039/D2TA01701F

[29] D. Gorniewicz, H. Przygucki, M. Kopec, K. Karczewski, S. Jóźwiak, TiCoCrFeMn (BCC + C14) high-entropy alloy multiphase structure analysis based on the theory of molecular orbitals, Materials 14 (2021) 1–16, https://doi.org/10.3390/ma14185285

[30] N. Wang, FeCoNiMnCuTi high entropy amorphous alloys and M50Ti50 (M = Fe, Cu, FeCoNiMnCu) amorphous alloys: novel and efficient catalysts for heterogeneous photo-Fenton decomposition of Rhodamine B, Surf. Interfaces 33 (2022) 1–19, https://doi.org/10.1016/j.surfin.2022.102265

[31] A. Radoń, S. Łoński, M. Kądziołka-Gaweł, P. Gębara, M. Lis, D. Łukowiec, R. Babilas, Influence of magnetite nanoparticles surface dissolution, stabilization and functionalization by malonic acid on the catalytic activity, magnetic and electrical properties, Colloids Surf. A Physicochem. Eng. Asp. 607 (2020) 1–9, https://doi.org/10.1016/j.colsurfa.2020.125446

[32] B. Pieczykolan, I. Płonka, K. Barbusiński, Discoloration of dye wastewater by modified Uv-Fenton process with sodium percarbonate, Archit. Civ. Eng. Environ. 9 (2016) 135–140, https://doi.org/10.21307/acee-2016-060

[33] K. Brząkalik, J.E. Frąckowiak, A Mössbauer and structural study of disordered alloys Fe3-xTixAl (0 < x < 1), Nukleonika 48 (2003) 13–16.

[34] K. Brząkalik, J.E. Frąckowiak, Mössbauer spectroscopy and X-ray diffraction study of the Fe3-xTixAl ternary alloys, Hyperfine Interact. 168 (2006) 973–977, https://doi.org/10.1007/s10751-006-9384-4

[35] J.E. Frackowiak, Mössbauer effect study of the hyperfine fields and isomer shift of ordered Fe-Co alloys, Hyperfine Interact. 60 (1990) 757–760, https://doi.org/10.1007/BF02399863

[36] V.V. Serikov, N.M. Kleinerman, O.A. Golovnya, NMR and Mössbauer study of peculiarities of the structure formation in Fe–Co alloys, Phys. Met. Metallogr. 118 (2017) 1040–1047, https://doi.org/10.1134/S0031918×1711014X

[37] M. Kądziołka-Gaweł, A. Bajorek, J. Goraus, P. Łopadczak, M. Oboz, Magnetic properties and structure of (Fe100-xGex)0.95Ni0.05 alloys (x = 0, 5, 10, 15, 20), Intermetallics 132 (2021) 1–6, https://doi.org/10.1016/j.intermet.2021.107141

[38] N. Hamada, Magnetic-local-environment effect on the atomic magnetic moment in ferromagnetic transition-metal alloys, J. Magn. Magn. Mater. 15–18 (1980) 61–62, https://doi.org/10.1016/0304-8853(80)90949-X

[39] H. Man-Gui, D. Long-Jiang, Mössbauer studies on the shape effect of Fe84 94Si 9.68Al5.38 particles on their microwave permeability, Chin. Phys. B 22 (2013) 1–6, https://doi.org/10.1088/1674-1056/22/8/083303

[40] Y. Jiraskova, N. Pizurova, A. Titov, D. Janickovic, M. Friak, Phase separation in Fe-Ti-Al alloy – structural, magnetic, and Mössbauer study, J. Magn. Magn. Mater. 468 (2018) 91–99, https://doi.org/10.1016/j.jmmm.2018.07.065

[41] G.K. Wertheim, J.H. Wernick, R.C. Sherwood, Model for the composition-dependent ferromagnetic to antiferromagnetic transition in Fe2Ti, Solid State Commun. 7 (1969) 1399–1402, https://doi.org/10.1016/0038-1098(69)90380-9

[42] S.L.C.L. Chien, Crystalline and amorphous FeTi and Fe2T, Phys. Rev. 31 (1985) 8238–8241, https://doi.org/10.1103/PhysRevB.31.8238

[43] M. Singh, I.P. Jain, Mossbauer and positron life-time studies of FeTi and Fe46Ti50Mn4 hydride systems, Int. J. Hydrog. Energy 21 (1996) 367–372, https://doi.org/10.1016/0360-3199(95)00088-7

[44] J. Pelloth, R.A. Brand, W. Keune, Local magnetic properties of the Fe2Ti Laves phase, J. Magn. Magn. Mater. 140–144 (1995) 59–60, https://doi.org/10.1016/0304-8853(94)00836-1

[45] I.A. Manakova, M.F. Vereshchak, L.S. Sergeeva, A.K. Shokanov, V.I. Antonyuk, V.S. Rusakov, K.K. Kadyrzhanov, Laws of thermally induced formation of phases in α-Fe with a titanium coating upon isochronous annealings, Phys. Met. Metallogr. 109 (2010) 447–460, https://doi.org/10.1134/S0031918×10050054

[46] R.A. Dunlap, Mössbauer effect studies of hume-rothery stabilization mechanisms in decagonal Al-Fe-Ni quasicrystals, Philos. Mag. B 67 (1993) 69–75, https://doi.org/10.1080/13642819308230219

[47] S.D. Kaloshkin, V.V. Tcherdyntsev, I.A. Tomilin, D.V. Gunderov, V.V. Stolyarov, Y.V. Baldokhin, I.G. Brodova, E.V. Shelekhov, Composed phases and microhardness of aluminium-rich aluminium-iron alloys obtained by rapid quenching, mechanical alloying and high pressure torsion deformation, Mater. Trans. 43 (2002) 2031–2038, https://doi.org/10.2320/matertrans.43.2031

[48] S. Enzo, R. Frattini, G. Mulas, G. Principi, Structural transformation of Al-Fe alloys analysed by neutron diffraction and Mössbauer spectroscopy, J. Mater. Sci. 39 (2004) 6333–6339, https://doi.org/10.1023/b:jmsc.0000043603.28152.bc

[49] I. Dézsi, C. Fetzer, L. Bujdosó, J. Brötz, A.G. Balogh, Mechanical alloying of Fe-Si and milling of α- And β-FeSi 2 bulk phases, J. Alloy. Compd. 508 (2010) 51–54, https://doi.org/10.1016/j.jallcom.2010.07.178

[50] P. Mono, A.S. Lahamer, Mössbauer study of the half-metallic ferromagnet Fe 1-x Co x Si, J. Ky. Acad. Sci. 69 (2008) 170–177, https://doi.org/10.3101/1098-7096-69.2.170

[51] S. Liu, P. Cao, D.Y. Lin, F. Tian, Stability of L21 (NiM)2TiAl (M=Co, Fe) in high-entropy alloys, J. Alloy. Compd. 764 (2018) 650–655, https://doi.org/10.1016/j.jallcom.2018.06.113

[52] O. Stryzhyboroda, V.T. Witusiewicz, S. Gein, D. Röhrens, U. Hecht, Phase equilibria in the Al–Co–Cr–Fe–Ni high entropy alloy system: thermodynamic description and experimental study, Front. Mater. 7 (2020) 270, https://doi.org/10.3389/fmats.2020.00270

[53] R. Krein, M. Palm, M. Heilmaier, Characterization of microstructures, mechanical properties, and oxidation behavior of coherent A2 + L21 Fe-Al-Ti, J. Mater. Res. 24 (2009) 3412–3421, https://doi.org/10.1557/jmr.2009.0403

[54] N.G. Jones, R. Izzo, P.M. Mignanelli, K.A. Christofidou, H.J. Stone, Phase evolution in an Al0.5CrFeCoNiCu high entropy alloy, Intermetallics 71 (2016) 43–50, https://doi.org/10.1016/j.intermet.2015.12.001

[55] Q. Wang, Y. Lu, Q. Yu, Z. Zhang, The exceptional strong face-centered cubic phase and semi-coherent phase boundary in a eutectic dual-phase high entropy alloy AlCoCrFeNi, Sci. Rep. 8 (2018) 1–8, https://doi.org/10.1038/s41598-018-33330-0

[56] T.T. Zuo, R.B. Li, X.J. Ren, Y. Zhang, Effects of Al and Si addition on the structure and properties of CoFeNi equal atomic ratio alloy, J. Magn. Magn. Mater. 371 (2014) 60–68, https://doi.org/10.1016/j.jmmm.2014.07.023

[57] A. Parakh, M. Vaidya, N. Kumar, R. Chetty, B.S. Murty, Effect of crystal structure and grain size on corrosion properties of AlCoCrFeNi high entropy alloy, J. Alloy. Compd. 863 (2021) 1–10, https://doi.org/10.1016/j.jallcom.2020.158056

[58] A. Kumar, A. Arora, R. Chandrake, K.R. Rao, M. Chopkar, Effect of silicon addition on alcocrfeni high entropy alloys prepared by vacuum arc melting, AIP Conf. Proc. 2247 (2020) 1–6, https://doi.org/10.1063/5.0003829

[59] L. Huang, X.J. Wang, B.X. Huang, C.Z. Wang, Study on microstructure and corrosion resistance of AlCoCrFeNiTi(x) high-entropy alloys, IOP Conf. Ser. Mater. Sci. Eng. 774 (2020) 2–8, https://doi.org/10.1088/1757-899X/774/1/012058

[60] M. Dada, P. Popoola, O. Aramide, N. Mathe, S. Pityana, Optimization of the corrosion property of a high entropy alloy using response surface methodology, Mater. Today Proc. 38 (2021) 1024–1030, https://doi.org/10.1016/j.matpr.2020.05.618

[61] Y. Qiu, S. Thomas, M.A. Gibson, H.L. Fraser, N. Birbilis, Corrosion of high entropy alloys, Npj Mater. Degrad. 1 (2017) 1–17, https://doi.org/10.1038/s41529-017-0009-y

[62] C.M. Lin, H.L. Tsai, Evolution of microstructure, hardness, and corrosion properties of high-entropy Al0.5CoCrFeNi alloy, Intermetallics 19 (2011) 288–294, https://doi.org/10.1016/j.intermet.2010.10.008

[63] Y.F. Kao, T.D. Lee, S.K. Chen, Y.S. Chang, Electrochemical passive properties of AlxCoCrFeNi (x = 0, 0.25, 0.50, 1.00) alloys in sulfuric acids, Corros. Sci. 52 (2010) 1026–1034, https://doi.org/10.1016/j.corsci.2009.11.028

[64] B. Ren, R.F. Zhao, Z.X. Liu, S.K. Guan, H.S. Zhang, Microstructure and properties of Al0.3CrFe 1.5MnNi0.5Ti x and Al0.3CrFe 1.5MnNi0.5Si x high-entropy alloys, Rare Met. 33 (2014) 149–154, https://doi.org/10.1007/s12598-014-0224-4

[65] A.C. Martin, J.P. Oliveira, C. Fink, Elemental effects on weld cracking susceptibility in AlxCoCrCuyFeNi high-entropy alloy, Metall. Mater. Trans. A Phys. Metall. Mater. Sci. 51 (2020) 778–787, https://doi.org/10.1007/s11661-019-05564-8

[66] M.A. Suarez, I. Figueroa, A. Cruz, A. Hernandez, J.F. Chavez, Study of the Al-Si-X system by different cooling rates and heat treatment, Mater. Res. 15 (2012) 763–769, https://doi.org/10.1590/S1516-14392012005000103

[67] O.T. Onawale, P.V. Cobbinah, W.R. Matizamhuka, R.A. Nzeukou, Synthesis route, microstructural evolution, and mechanical property relationship of high-entropy alloys (HEAs): a review, Materials 14 (2021) 1–35, https://doi.org/10.3390/ma14113065

[68] S.-K. Chen, P.-H. Lee, C.-H. Lin, AlCoCrFeNiTi and its equal-molar five-component alloys in a metal mixological enthalpy-entropy plane, Q, Phys. Rev. 3 (2017) 1–28, https://doi.org/10.18103/qpr.v3i1.1184

[69] D.H. Xiao, P.F. Zhou, W.Q. Wu, H.Y. Diao, M.C. Gao, M. Song, P.K. Liaw, Microstructure, mechanical and corrosion behaviors of AlCoCuFeNi-(Cr,Ti) high entropy alloys, Mater. Des. 116 (2017) 438–447, https://doi.org/10.1016/j.matdes.2016.12.036

[70] Y. Qiu, S. Thomas, D. Fabijanic, A.J. Barlow, H.L. Fraser, N. Birbilis, Microstructural evolution, electrochemical and corrosion properties of Al x CoCrFeNiTi y high

entropy alloys, Mater. Des. 170 (2019) 1–15, https://doi.org/10.1016/j.matdes.2019.107698
[71] I. Basu, J.T.M. De Hosson, Strengthening mechanisms in high entropy alloys: fundamental issues, Scr. Mater. 187 (2020) 148–156, https://doi.org/10.1016/j.scriptamat.2020.06.019
[72] F. Tian, L.K. Varga, N. Chen, J. Shen, L. Vitos, Empirical design of single phase high-entropy alloys with high hardness, Intermetallics 58 (2015) 1–6, https://doi.org/10.1016/j.intermet.2014.10.010
[73] B. Jin, N. Zhang, Y. Zhang, D. Li, Microstructure, phase composition and wear resistance of low valence electron concentration AlxCoCrFeNiSi high-entropy alloys prepared by vacuum arc melting, J. Iron Steel Res. Int. 28 (2021) 181–189, https://doi.org/10.1007/s42243-020-00398-w
[74] A. Babuponnusami, K. Muthukumar, Advanced oxidation of phenol: a comparison between Fenton, electro-Fenton, sono-electro-Fenton and photo-electro-Fenton processes, Chem. Eng. J. 183 (2012) 1–9, https://doi.org/10.1016/j.cej.2011.12.010
[75] H.N. Quan, A.L. Teel, R.J. Watts, Effect of contaminant hydrophobicity on hydrogen peroxide dosage requirements in the Fenton-like treatment of soils, J. Hazard. Mater. 102 (2003) 277–289, https://doi.org/10.1016/S0304-3894(03)00214-0
[76] Q. Wang, Y. Yang, S. Ma, J. Wu, T. Yao, Preparation of Fe3O4@Prussian blue core/shell composites for enhanced photo-Fenton degradation of rhodamine B, Colloids Surf. A Physicochem. Eng. Asp. 606 (2020) 1–8, https://doi.org/10.1016/j.colsurfa.2020.125416
[77] Y. Zhong, X. Liang, Z. He, W. Tan, J. Zhu, P. Yuan, R. Zhu, H. He, The constraints of transition metal substitutions (Ti, Cr, Mn, Co and Ni) in magnetite on its catalytic activity in heterogeneous Fenton and UV/Fenton reaction: from the perspective of hydroxyl radical generation, Appl. Catal. B Environ. 150–151 (2014) 612–618, https://doi.org/10.1016/j.apcatb.2014.01.007
[78] K. Barbusiński, The modified fenton process for decolorization of dye wastewater, Pol. J. Environ. Stud. 14 (2005) 281–286.
[79] K. Barbusiński, J. Majewski, Discoloration of Azo Dye acid red 18 by Fenton reagent in the presence of iron powder, Pol. J. Environ. Stud. 12 (2003) 151–155.
[80] C. Zhang, G. Ren, W. Wang, X. Yu, F. Yu, Q. Zhang, M. Zhou, A new type of continuous-flow heterogeneous electro-Fenton reactor for Tartrazine degradation, Sep. Purif. Technol. 208 (2019) 76–82, https://doi.org/10.1016/j.seppur.2018.05.016
[81] E. Pesman, S. Imamoglu, E.E. Kalyoncu, H. Kırcı, The effects of sodium percarbonate and perborate usage on pulping and flotation deinking instead of hydrogen peroxide, BioResources 9 (2014) 523–536, https://doi.org/10.15376/biores.9.1.523-536
[82] L. Zhang, Y. Nie, C. Hu, J. Qu, Enhanced Fenton degradation of Rhodamine B over nanoscaled Cu-doped LaTiO3 perovskite, Appl. Catal. B Environ. 125 (2012) 418–424, https://doi.org/10.1016/j.apcatb.2012.06.015
[83] S. Guo, G. Zhang, J. Wang, Photo-Fenton degradation of rhodamine B using Fe2O3-Kaolin as heterogeneous catalyst: characterization, process optimization and mechanism, J. Colloid Interface Sci. 433 (2014) 1–8, https://doi.org/10.1016/j.jcis.2014.07.017
[84] Y. Ye, H. Yang, H. Zhang, J. Jiang, A promising Ag2CrO4/LaFeO3 heterojunction photocatalyst applied to photo-Fenton degradation of RhB, Environ. Technol. 41 (2020) 1486–1503, https://doi.org/10.1080/09593330.2018.1538261
[85] Y. Zhang, T. He, S. Ding, H. Li, W. Song, J. Ding, J. Lu, Photo-fenton degradation of RhB via transition metal oxides composite catalyst Fe3O4/CuO under visible light optimized using response surface methodology, Mater. Technol. 37 (2022) 2347–2359, https://doi.org/10.1080/10667857.2022.2035144
[86] X. Wu, Z. Nan, Degradation of rhodamine B by a novel Fe3O4/SiO2 double-mesoporous-shelled hollow spheres through photo-Fenton process, Mater. Chem. Phys. 227 (2019) 302–312, https://doi.org/10.1016/j.matchemphys.2019.02.023
[87] X. Tao, Q. Chen, L. Ji, G. Huang, The synergy of chromium and molybdenum on the stable catalysis of Fe-based amorphous alloy powder, J. Non Cryst. Solids 570 (2021) 1–8, https://doi.org/10.1016/j.jnoncrysol.2021.121010

Załącznik IV

A(IV)

Sylwester Łoński, Dariusz Łukowiec, Krzysztof Barbusiński, Rafał Babilas, Bartosz Szeląg, Adrian Radoń

Flower-like magnetite nanoparticles with unfunctionalized surface as an efficient catalyst in photo-Fenton degradation of chemical dyes

Applied Surface Science Volume 638, 30, November 2023, 158127

Doi: 10.1016/j.apsusc.2023.158127 Impact Factor: **6,3** Punkty MNiSW: 140

Applied Surface Science 638 (2023) 158127

Contents lists available at ScienceDirect

Applied Surface Science

journal homepage: www.elsevier.com/locate/apsusc

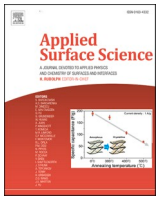

Full Length Article

Flower-like magnetite nanoparticles with unfunctionalized surface as an efficient catalyst in photo-Fenton degradation of chemical dyes

Sylwester Łoński [a], Dariusz Łukowiec [b], Krzysztof Barbusiński [c], Rafał Babilas [b], Bartosz Szeląg [d], Adrian Radoń [b,e,*]

[a] PhD School, Department of Water and Wastewater Engineering, Silesian University of Technology, Konarskiego 2a St., 44-100 Gliwice, Poland
[b] Faculty of Mechanical Engineering, Silesian University of Technology, Konarskiego 18 a St., 44-100 Gliwice, Poland
[c] Department of Water and Wastewater Engineering, Silesian University of Technology, Konarskiego 18 St., 44-100 Gliwice, Poland
[d] Warsaw University of Life Sciences, Nowoursynowska 166, 02-787 Warsaw, Poland
[e] Łukasiewicz Research Network - Institute of Non-Ferrous Metals, Sowinskiego 5 St., 44-100, Gliwice, Poland

ARTICLE INFO

Keywords:
Magnetite nanoparticles
photo-Fenton
Sodium percarbonate
Dye removal
Logistic regression

ABSTRACT

Flower-like magnetite nanoflowers (Fe_3O_4 NFs) were synthesized in this study using a new, highly scalable, modified co-precipitation method. The heterogeneous photo-Fenton process was optimized for the degradation of Rhodamine B using sodium percarbonate as an alternative source of H_2O_2. The low dosage of NPs (0.6 mg/ml) can ensure the high Rhodamine B degradation of about 93.6% at pH 4 and sodium percarbonate concentration of 8.3 mg/ml. Studies confirm the high cyclic stability of Fe_3O_4 NFs and the possibility of using optimized reaction condition in the degradation of Lissamine Green B (97.3%) and Naphthol Green B (61.8%). Moreover, it was confirmed that $O_2^{\cdot-}$ and $HO^{\bullet}$ are the primary radicals oxidizing Rhodamine B, while the ultrafast Lissamine Green B degradation corresponds to their oxidation by $O_2^{\cdot-}$. Finally, surface functionalization was confirmed as one of the most critical parameters in designing catalysts for heterogeneous photo-Fenton processes. The study confirms that in the case of surface functionalization, the degradation of dyes is slowed down (reduction of active sites on the magnetite surface by the organic molecules). Accordingly, the ultrafine, spherical-shaped magnetite nanoparticles functionalized by thrietylene glycol were characterized by above 3 times lower catalytic activity than unfunctionalized Fe_3O_4 NFs.

1. Introduction

Controlling the properties of nanoparticles by modifying their morphology (shape, degree of agglomeration) is one of the leading research issues in nanotechnology, especially in nanostructure engineering [1]. This is closely related to the possibility of developing precise methods of synthesizing nanomaterials with specific properties such as catalytic, magnetic, and electrical [2]. The control of the shape, size, and degree of agglomeration of nanoparticles is one of the most widely developed issues due to the wide application possibilities of magnetite nanoparticles. A properly selected synthesis method allows for the synthesis of nanoparticles with a controlled efficiency. However, the balance between the efficiency and morphology of the obtained product must be considered depending on the applications. This problem was discussed, for example, by Majetich et al. [3]. They noted that chemical synthesis methods in an aqueous environment (such as co-precipitation and hydrothermal methods) lead to the formation of less monodisperse nanoparticles than in the case of other synthesis methods; however, these methods allow to obtain nanoparticles with high efficiency (at the level of hundreds of grams).

On the other hand, methods based on synthesis in an organic environment make it possible to obtain monodispersive nanoparticles, but with much lower efficiency. The current possibilities of controlling the shape of magnetite nanoparticles (Fe_3O_4 NPs) through appropriately selected methods of their synthesis were presented by Roca et al. [4]. They showed that it is possible to synthesize Fe_3O_4 nanoparticles of different shapes, from cubic to octahedral, the shape of disks, nanoflowers, and hollow structures. The methods of synthesizing nanostructures of different shapes are mainly based on the high-temperature decomposition of organic precursors in high-boiling organic liquids using appropriate chemical modifiers such as sodium acetate, oleic acid, and oleylamine.

* Corresponding author.
E-mail address: adrian.radon@imn.lukasiewicz.gov.pl (A. Radoń).

https://doi.org/10.1016/j.apsusc.2023.158127
Received 11 April 2023; Received in revised form 14 July 2023; Accepted 26 July 2023
Available online 27 July 2023

The synthesis of magnetite-based nanocatalysts is very interesting, according to the high surface area of the nanoparticles and the possibility of removing the catalyst from the reaction solution by a magnetic field. Moreover, according to the highly reactive surface of Fe_3O_4 NPs, they found numerous applications in the oxidation of organic compounds in heterogenous Fenton-like processes. For example, Radon et al. [5] confirmed that non-spherical magnetite nanoparticles could be used to degrade Rhodamine B and Methylene Blue dyes in alkaline pH with a high degradation rate above 97 %. The possibility of removing phenol was confirmed by Wang et al. [6]. They showed that the Fe_3O_4 nanoparticles could be used in a wide pH range, from acidic to alkaline. Moreover, other organic and inorganic compounds can modify the nanoparticles' highly reactive surface to obtain a broader catalyst range [7–9].

Unfortunately, most synthesis methods, which allow obtaining magnetite nanoparticles with a defined shape, need organic modifiers, which spontaneously functionalize their surface. This process blocks the active sites for the Fenton reaction (i.e., Fe ions) by the organic molecules, which can change the catalytic activity of the magnetite nanoparticles [10]. Accordingly, this study developed a new synthesis method of flower-like magnetite nanoparticles without surface functionalization and tested them in heterogeneous photo-Fenton catalysts. Pure hydrogen peroxide is one of the most used oxidants in the Fenton and photo-Fenton processes. However, the hydrogen peroxide is corrosive and harmful. Accordingly, some alternatives were proposed. One is sodium percarbonate (solid and crystalline carrier of hydrogen peroxide) with potential use in the wide pH range. This oxidant is also much safer, especially during transport and handling; the reaction between this oxidant and organic compounds is non-toxic and non-polluting, and above that, the carbonate formed under the sodium percarbonate decomposition act as buffering agent [11,12]. The possibility of using this oxidant was confirmed by Sajjadi et al. [13] in the catalytic degradation of Methylene Blue dye catalyst by magnetite nanoparticles incorporated into the zeolitic imidazolate framework and by Chen et al. [11] in the degradation of Rhodamine B in the presence of FeOCl and visible light.

According to our knowledge, it is the first study in which flower-like magnetite nanoparticles with unfunctionalized surface were tested in decolorizing dyes using sodium percarbonate as an oxidant. Moreover, to better understand the proposed synthesis methods' advantages, nanoparticles were compared with ultrafine spherical nanoparticles functionalized by triethylene glycol and cubic nanoparticles with surface modified by oleic acid. Furthermore, the role of pH, nanoparticles dose, sodium percarbonate concentration, and stirring was evaluated to obtain optimum reaction conditions. Moreover, these variables' role was also studied using logistic regression models. Finally, the applicability of the flower-like magnetite nanoparticles in the heterogenous photo-Fenton process was also evaluated for the degradation of various dyes typically used in the industry. As a result, it was confirmed that the dyes' chemical structure also plays a crucial role in the efficiency of the decolorization process, and their degradation can be related to the different radicals formed in the studied system.

2. Materials and methods

2.1. Rod-shaped β-FeOOH precursor synthesis

20 mmol of $FeCl_3{\cdot}6H_2O$ was dissolved in 40 ml of deionized (DI) water. Separately 10 mmol of hexamethylenetetramine was dissolved in 60 ml of DI water and mixed with a solution containing Fe^{3+} ions. The received red–orange solution was heated to boiling temperature and kept for 2 h under reflux. Next, the yellow-brownish product was cooled to room temperature, and 20 ml of DI water was added.

2.2. Synthesis of flower-like magnetite nanoparticles (Fe_3O_4 NFs)

The yellow-brownish dispersion of β-FeOOH was sonicated at 50 ℃ for 10 min. Afterward, 60 ml of a solution containing 15 mmol of $FeSO_4{\cdot}7H_2O$ was added and sonicated for 10 min. Next, 0.1 mol of NaOH was dissolved in 60 ml of DI water and dropwise to the dispersion of β-FeOOH with Fe^{2+} ions under continuous sonication to form a dark-green precipitate. Finally, obtained dispersion was sonicated for 1 h at 50 ℃ to form a black magnetic precipitate and stored at room temperature for 24 h. Synthesized flower-like magnetite nanoparticles were removed from the reaction solution using a neodymium magnet and washed three times with DI water, two times with ethanol, and two times with acetone. The powder was stored under acetone to minimize the air's highly-reactive surface contact with oxygen.

2.3. Structure analysis

The phase composition and crystalline structure of the β-FeOOH precursor and flower-like magnetite nanoparticles were determined using the X-ray diffraction (XRD) method. The measurements were performed using Rigaku MiniFlex 600 (Rigaku Corporation, Tokyo, Japan) diffractometer equipped with copper tube Cu Kα($\lambda = 0.15406$ nm) as a radiation source (tube voltage 40 kV, current 15 mA). The data were analyzed using the dedicated Rigaku PDXL software suite. The morphology and structure of synthesized nanomaterials were described based on the transmission electron microscopy (TEM) images analysis. Measurements were also performed using high-angle annular dark-field scanning transmission electron microscopy (HAADF STEM) mode. In addition, the chemical composition of the β-FeOOH precursor was investigated based on the energy dispersive X-ray (EDX) spectra collected in STEM mode.

2.4. Catalytic activity measurements

Catalytic activity was determined for the heterogenous photo-Fenton process using sodium percarbonate as an oxidant. The role of the pH, oxidant and catalyst concentration, and stirring on the catalytic activity of flower-like magnetite nanoparticles were described in the Rhodamine B (RhB) decolorization reaction. All experiments were performed in similar ways. To avoid measurement errors, all nanoparticles were redispersed in the water to obtain stable dispersions and ensure the repeatability of measurements. Generally, 30 ml of RhB solution with a concentration equal to 10 mg/l was mixed with 30 ml of nanoparticle dispersion to receive the final concentration of nanoparticles in solution from 0.3 to 2.6 mg/ml. The pH of the solution (from 3 to 6.5) was then established using sulfuric acid. The sodium percarbonate in the powder form was added before the experiment started to obtain the oxidant's final concentration from 1.7 mg/ml to 37.5 mg/ml. Afterward, stirring the reaction solution was established at 0 or 400 rpm. The photo-Fenton process was performed using the 365 nm UV source with power equal to 36 W. In the case of the reactions without the catalyst, the 30 ml nanoparticle dispersion was replaced by DI water. The radicals responsible for the dyes' degradation were determined in the same way by introduction into reaction solution 0.5 mol of 2-propanol ($HO^{\bullet}$ scavenger), 0.2 mol of *tert*-Butanol ($HO^{\bullet}$ scavenger), 5 mmol of ascorbic acid (O_2^{-}scavenger) and 5 mmol of KI (hole, h^+ interfering species). The cyclic stability was determined for chosen reaction conditions using the same catalyst in 5 processes without any purification between degradation efficiency tests. For this purpose, the nanoparticles were collected after the degradation test (60 min of the reaction) by centrifugation, redispersed in the DI water to form a stable dispersion, and added to the dye solution.

The free H_2O_2 concentration in the reaction solution was determined based on the following procedure. First, 0.2 g of the tested solution was weighed with an accuracy of 0.0002 g. Next, 10 ml of sulfuric acid solution (10% m/m) was added. Finally, the solution was titrated with the

potassium permanganate 0.0125 M solution to a light pink permanent color.

The decolorization of other organic dyes was performed similarly to the one described above for RhB. The 30 ml of RhB solution was replaced by the solutions of Phloxine B (PhB, 12 mg/L), Acid Red 1 (AR1, 20 mg/L), Lissamine Green B (LGB, 4.5 mg/L), and Naphthol Green B (NGB, 10 mg/L). The pH, sodium percarbonate and nanoparticles concentrations were constant and equal to 4, 8.3 mg/ml, and 0.6 mg/ml. Stirring the reaction solution was established at 400 rpm.

The adsorption tests were performed for all dyes. For this purpose, 30 ml of dye solution with a known concentration was mixed with 30 ml of nanoparticle dispersion to receive the final concentration of nanoparticles in the solution of 0.6 mg/ml. The pH of the solution was then established using sulfuric acid to 4, and the solution was kept in the dark under continuous stirring (400 rpm) for 60 min.

Finally, the role of the surface chemistry on the heterogenous photo-Fenton process and the applicability of flower-like magnetite nanoparticles in conventional processes with H_2O_2 as an oxidant were tested in the degradation of methylene blue (MB). The details about these tests can be found in Appendix A..

2.5. Modeling and optimization process

2.5.1. Logistic regression model (LRM)

Logistic regression, also known as the logit model, is a tool used for classification. Its benefits in comparison to widely used methods (neural network, regression tree, and their modification) arise from the fact that computation results range from 0 to 1 and represent probability values. In this study, sensitivity (Sens), specificity (Spec), and accuracy (Acc) were used to assess the fit of the results to the measurements. In the present analyses, six independent logistic regression models were developed for decolorization D equal to 25, 50, 60, 70, 80, and 90%. The approach adopted allowed the identification of decolorization values with corresponding ranges of variation in D. A detailed description of the model is given in section 5.1 in Appendix A.

Furthermore, a local sensitivity analysis was performed using the developed logit models. In this approach, sensitivity coefficients (S_{xi}) were determined according to the formula:

$$S_{xi} = \frac{\partial p}{\partial x_i} \bullet \frac{x_i}{p(x_i)} \quad (1)$$

where: $p(x_i)$ - the probability of exceeding decolorization (D) at point x_i; S_{xi} – sensitivity coefficient for the influence of the independent variable x_i on the degree of decolorization. A detailed description of the calculation methodology is given in Section 5.2 in Appendix A.

3. Results and discussion

3.1. Structural analysis

The phase composition of solid-state Fe^{3+} precursor was determined based on the XRD patterns analysis. Obtained results are presented in Fig. S1. The applied hydrolysis of the $FeCl_3$ in the presence of HMTA results in the formation of akageneite phase - β-FeO(OH)•Cl_n, hollandite-type material with the channel, in which Cl^- ions are presented. The morphology and chemical composition analysis results are presented in Fig. S2. As seen in Fig. S2a applied synthesis method results in the formation of β-FeO(OH)•Cl_n nanorods with a length of about 22.3 ± 4.6 nm and a diameter of 5.4 ± 1.0 nm. The presence of Cl^- ions was additionally confirmed using EDX spectra analysis (Fig. S2b). The presence of Cl can be noted, together with the peaks characteristic for Fe and O. Unfortunately, the synthesized nanorods are characterized by a high agglomeration ratio, which can be especially seen in Fig. S2c and d. Moreover, as observed in Fig. S2d highly disordered structure of these rods complies with the broadness of the diffraction peaks for the synthesized sample.

In this study, synthesized rods were used as a solid-state precursor for the synthesis of magnetite nanoparticles. Generally, iron oxyhydroxides are used to synthesize magnetite nanoparticles with rod-shape by the controlled reduction using hydrogen, hydrazine, or reducing organic solvents. For example, Adhikari et al. used hydrazine to produce Fe_3O_4 nanorods from β-FeO(OH) nanoneedles [14]. At the same time, Choi et al. [15] proposed that ethylene glycol reduction can produce solid nanospheres, hollow nanoellipsoids, and solid nanoellipsoids by adding sodium acetate or using β-FeO(OH) with or without Cl ions in their structure. Herein different method was used to prepare magnetite nanoparticles. While in the examples mentioned above formation of Fe^{2+} ions is related to the reduction of the Fe^{3+} ions presented in β-FeO(OH)Cl, in this work, Fe^{2+} ions were introduced as $FeSO_4$ and ultrasound-assisted co-precipitation at elevated temperature was performed to obtain a magnetically removable powder. The X-ray diffraction pattern of the synthesized material is presented in Fig. 1. As can be seen, this new method forms a spinel structure characteristic of pure magnetite. Moreover, the absence of additional diffraction peaks on the XRD patterns confirms the obtained samples' phase purity. Also, while in the case of the co-precipitation method, synthesized nanoparticles are characterized by ultrafine size, the average crystallite size calculated according to the Halder-Wagner method [16,17] was equal to 44.3 nm.

Interestingly, when the spherical or eventually rod-shaped magnetite nanoparticles were expected using the proposed methods, as seen in Fig. 2. magnetite nanoflowers composed of ultrafine nanoparticles were formed. Based on the TEM images analysis, the diameter of these nanoflowers was equal to 83.7 ± 16.6 nm, which is approximately two times higher than the average crystallite size calculated based on the XRD patterns analysis, indicating the multi-crystalline nature of these nanoflowers. Generally, magnetite nanoflowers are formed by the controlled agglomeration of nanoparticles in high-temperature decomposition reactions of organic precursors and using specific organic modifiers [18,19]. In the case of the typical co-precipitation methods, spherical, cuboidal, or octahedral shapes were described in the literature [20,21]. Accordingly, the proposed new method synthesis should be tested in producing the nanostructured catalysts, especially for heterogeneous Fenton processes.

3.2. Degradation of RhB in UV/sodium percarbonate system

The various advanced oxidation processes and reagents are presented and widely studied in the literature. Generally, one of the most common is the Fenton-like process, in which the reaction catalyst produces hydroxyl radicals by Fe^{2+} ions, which are oxidized to Fe^{3+} and

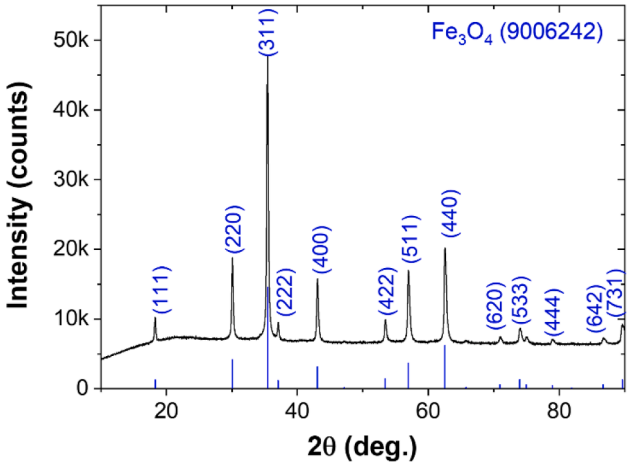

Fig. 1. X-ray diffraction pattern of synthesized Fe_3O_4 NFs with characteristic Miller indices and theoretical diffraction pattern of Fe_3O_4 spinel structure.

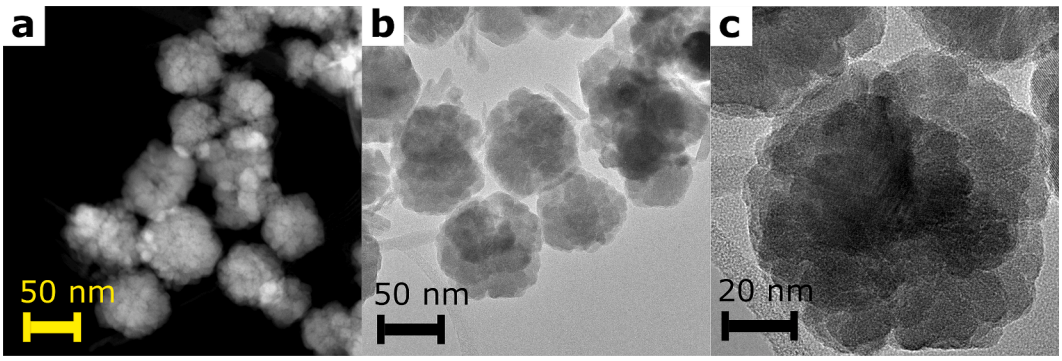

Fig. 2. Transmission electron microscopy analysis: (**a**) HAADF STEM and (**b, c**) TEM images of synthesized Fe_3O_4 NFs.

slowly back into Fe^{2+} form. Also, these radicals can be produced by the UV illumination of the reaction solution containing only H_2O_2 as the oxidant. In this study, sodium percarbonate ($Na_2CO_3{\cdot}1.5H_2O_2$) was applied as the hydrogen peroxide source. Recently this oxidant was tested, for example, in the degradation of CI Reactive Red 195 in the presence of tetraacetylethylenediamine [22]. Accordingly, the process optimization was performed in the decolorization of RhB in the presence of UV irradiation. Firstly, the role of the sodium percarbonate concentration on the decolorization rate was measured for three oxidant concentrations, and analysis results are presented in Fig. 3a. As can be seen, with increasing concentration from 8.3 mg/ml to 37.5 mg/ml, the decolorization rate also increases from 53.6 to 95.9 % at nearly neutral solution pH.

Interestingly, the pH value does not influence the process efficiency and is close to 84.6 % for all tested acidic environments (Fig. 3b). The significant changes observed in the case of the parameter, which is not commonly tested in the literature and is related to the stirring of the reaction solution. Generally, stirring of the reaction solution is applied in various catalytic activity tests; however, sometimes, in real applications, it is difficult to obtain rapid stirring or catalytic reaction is performed in different systems such as flow reactors. Therefore, the tests were performed for the near neutral pH equal to 6.5 and oxidant concentration equal to 37.5 mg/ml. The results are presented in Fig. 3c and d. As shown in Fig. 3c, the decolorization efficiency increases while the reaction solution is stirred and achieves 95.9 %. On the other hand, the decolorization rate in the system without stirring was much lower (83.0 % after 60 min.), which is visible mainly for shorter reaction times. These changes can be related to the nature of the oxidant, sodium percarbonate, which can dose the H_2O_2 under the whole reaction. As can be seen in Fig. 3d, while the solution is stirring, the concentration of free hydrogen peroxide is nearly constant, while in the case of the reaction performed without stirring increases and achieve about 4% after 30 min of the reaction. Accordingly, the dose of hydrogen peroxide is not consumed in the hydroxyl radicals generation process and acts like a scavenger, which will be discussed later in this study.

3.3. Optimization of catalytic degradation of RhB by flower-like magnetite nanoparticles

3.3.1. Influence of pH on catalytic degradation of RhB

One of the important parameter influences on the catalytic activity of magnetite nanoparticles is the solution pH. Unal et al. [23] have shown that the optimum pH depends on the dye type. In the case of the removal of Basic Red 18, the highest Fenton oxidation (76%) was observed for pH 3.5, whereas 100% of Acid Red 8 removals for pH 6.0. On the other hand, the highest Rhodamine B decolorization efficiency was observed for the ultralow pH value, which is related to the changes in the interaction of dye molecules with the catalyst's surface [24]. Interestingly, in

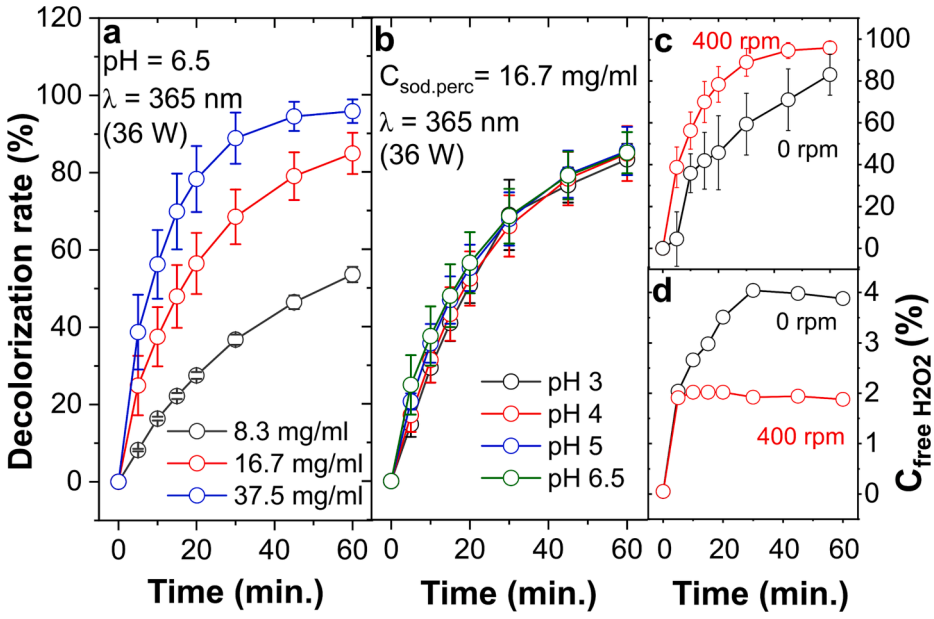

Fig. 3. RhB decolorization results obtained for UV/ sodium percarbonate system: (**a**) influence of the sodium percarbonate concentration, (**b**) influence of the pH value, and (**c**) role of the reaction solution stirring on the process efficiency; (**d**) free H_2O_2 concentration (in %) in the reaction solution.

the studied, modified photo-Fenton process catalyzed by magnetite nanoflowers, the influence of the pH on the Rhodamine B degradation is slight. The highest decolorization rate was observed for pH 4.0 during the whole reaction time; however, after 60 min of the reaction, the dye removal efficiency is similar for all pH values and not lower than 95.1% (Fig. 4). Generally, changes in the removal of RhB by various catalysts are related to the presence of the cationic form of this dye at a pH lower than 3.7 and the zwitterionic form in higher pH values [24]. Radon et al. [5] have shown that the catalytic degradation of rhodamine B with high efficiency of about 99.5% by non-spherical shaped magnetite nanoparticles is possible at a high pH value equal to 10, while Ansari et al. [25] have confirmed that the pH 3 is the most optimal for the spherical magnetite nanoparticles and sodium dodecyl sulfate coated magnetite nanoparticles. Accordingly, the possibility of application of magnetite nanoflowers in a wide pH range from 3 to 6.5 significantly improves the applicability of the synthesized nanoparticles in the industry without the significant loss of dye removal efficiency at 60 min. However, pH 4 improves the decolorization efficiency for much lower reaction times than much acidic and alkaline pH. For example, the decolorization rate of 72.9% was observed for pH 4, while 67.9% of the RhB was removed from the solution at pH 6.5 (for 20 min).

3.3.2. *Influence of sodium percarbonate concentration in catalytic degradation of RhB*

Generally, oxidants in the Fenton and photo-Fenton processes nonlinear influence the degradation dyes rate. In the case of H_2O_2 use, this behavior is related to the scavenging properties of hydrogen peroxide in much higher oxidant concentrations (eq.2) [26]. The formed in this process, $HOO^{\bullet}$ radicals are characterized by much lower oxidation properties than hydroxyl radicals and decrease the organic compounds' degradation rate [27].

$$H_2O_2 + HO^{\bullet} \rightarrow HOO^{\bullet} + H_2O \quad (2)$$

The first advantage of using sodium percarbonate is the possibility of generating three different radicals under UV illumination ($HO^{\bullet}$, O_2^{-} and CO_3^{-}) [28]. The role of them will be discussed later. The second one, as was mentioned previously, is related to the concentration of hydrogen peroxide changes over time - one of the most significant advantages of this process is the possible dosage of H_2O_2 under the whole reaction. Accordingly, the changes generated by sodium percarbonate concentration on the decolorization rate were studied for a concentration range from 1.7 to 37.5 mg/ml. In this experiment, the pH was established at 4, and the final concentration of magnetite nanoparticles was also constant and equal to 1.3 mg/ml. As shown in Fig. 5, the decolorization rate increases from 13.3 to 95.9% with the increasing sodium percarbonate concentration in the analyzed dose range. Unfortunately, the oxidant concentration equal to 37.5 mg/ml is too high for applying this reaction for the degradation of organic pollutants; however, in terms of pure H_2O_2 moles, this is still a lower concentration than for other similar tested processes [29,30]. Accordingly, further optimization of this process was carried out for a much lower concentration, equal to 8.3 mg/ml, for which the decolorization rate was around 55.2 % after 60 min and the concentration of pure H_2O_2 equal only to 78 mM.

3.3.3. *Influence of flower-like magnetite nanoparticles concentration on catalytic degradation of RhB*

The catalyst concentration is another parameter significantly influencing the organic compounds' oxidation rate. Unfortunately, the changes generated by increasing the Fe^{2+} ions concentration are nonlinear in this case. First, these ions' presence is important in the degradation of the organic compounds, according to the eq. (3) allowing highly reactive hydroxyl radicals to form with a rate constant of 78 $M^{-1}s^{-1}$. However, the amount produced by this method of hydroxyl radicals is much lower than the theoretical one and decreases with the increasing Fe^{2+} concentration, which is related to the occurrence of the reactions (4)–(5) [31].

$$Fe^{2+} + H_2O_2 \rightarrow Fe^{3+} + HO^{-} + HO\bullet \quad (3)$$

$$Fe^{2+} + H_2O_2 \rightarrow FeO^{2+} + H_2O \quad (4)$$

$$2Fe^{2+} + H_2O_2 \rightarrow 2Fe^{3+} + 2HO^{-} \quad (5)$$

Accordingly, the role of the magnetite nanoflowers concentration in reaction solution on the decolorization efficiency of rhodamine B was studied for 0.3, 0.6, 1.3, and 2.6 mg/ml of Fe_3O_4 NFs and compared with the degradation without the addition of iron ions. As can be seen in Fig. 6a, the addition of the magnetite nanoflowers increases the decolorization rate in comparison to the reference reaction; however, the most visible changes observed for 0.6 mg/ml, which is related to the spontaneous occurrence of the reactions (4)–(5) in the case of higher catalyst concentrations. While the decolorization rate equal to 93.6% was observed for 0.6 mg/ml, for the 2.6 mg/ml, only 60.1% of the RhB was removed from the reaction solution. Interestingly, adding the low amount of magnetite nanoparticles (0.3 mg/ml) into the reaction solution as well as higher ones (1.3 and 2.6 mg/ml) does not significantly

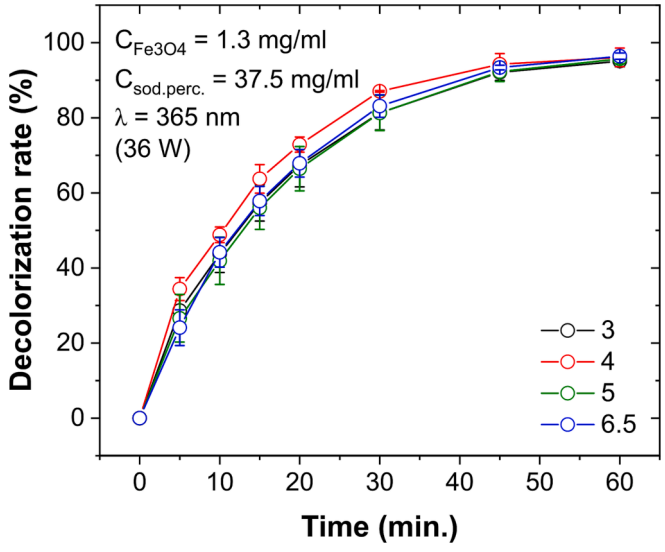

Fig. 4. Influence of pH on the decolorization rate of Rhodamine B in the photo-Fenton reaction catalyzed by Fe_3O_4 NFs.

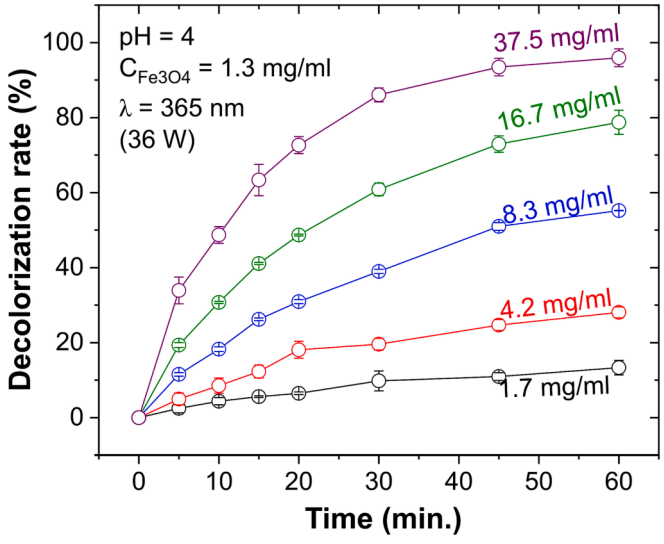

Fig. 5. Influence of sodium percarbonate concentration on the decolorization rate of Rhodamine B in the photo-Fenton reaction catalyzed by Fe_3O_4 NFs.

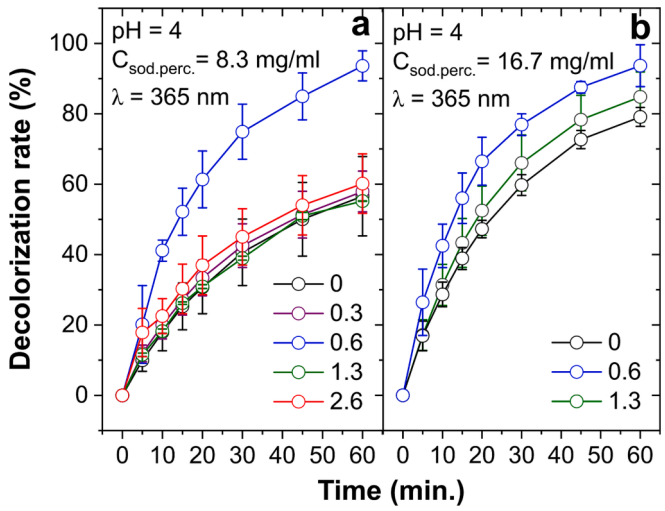

Fig. 6. Influence of Fe_3O_4 NFs concentration on the decolorization rate of RhB in the photo-Fenton reaction catalyzed by magnetite nanoflowers: (**a**) for oxidant concentration equal to 8.3 mg/ml and (**b**) for concentration equal to 16.7 mg/ml.

change the decolorization rate in comparison to the system without the magnetite addition (Fig. 3a). Accordingly, the improvement of the decolorization rate by the magnetite nanoflowers in reaction with 16.7 mg/ml addition of sodium percarbonate was studied to confirm the role of the Fe_3O_4 NPs in the analyzed system. As shown in Fig. 6b, in this case, adding 0.6 mg/ml of flower-like magnetite nanoparticles improves the decolorization rate from 79.1% (for the reaction without catalyst addition) to 93.6%. Interestingly, the catalytic activity was similar to the reaction performed using nearly twice the lower sodium percarbonate concentration, equal to 8.3 mg/ml. Accordingly, the most favorable reaction condition was determined based on the above studies. It was noted that the high decolorization rate (93.6%) could be received after 60 min using a low concentration of sodium percarbonate (8.3 mg/ml) in pH 4 and using flower-like magnetite nanoparticles with a concentration equal to 0.6 mg/ml.

The catalyst stability was tested for this optimal reaction condition, and the results are shown in Fig. 7. The recyclability and reusability strongly depend on the catalyst composition [32]. In some cases, the decolorization of magnetite nanoparticles can drop drastically, mainly related to the iron leaching in the reaction solution or deactivation of catalytic sites [24]. A slight decrease in decolorization rate (94.7 to 89.5%) was observed between 1st and 5th experiments using the same nanoparticles. A similar situation was noted for the test performed for higher Fe_3O_4 NFs concentration. In this case, the decolorization decreased from 58.9 to 50.6% (Fig. 7a). To understand these changes, the FTIR spectrum of Fe_3O_4 NFs collected from the dispersion, which was used in the catalytic activity tests was compared with the spectrum recorded for the catalyst after 5th test. As shown in Fig. 7b, the unfunctionalized, highly reactive surface of flower-like magnetite nanoparticles also interacts with pure water and forms a Fe-OH-rich surface (two vibrational modes characteristic for goethite at 796 and 895 cm^{-1} [33]). After the catalytic reaction, some new, overlapping vibrational modes can be observed for the sample measured after tests. These modes were not assigned to the absorption of rhodamine B molecules, which confirms that the observed decrease in the decolorization rate is only related to the degradation of this compound. Analysis of these spectra confirms that the observed vibrations are probably related to the formation of complex carbonate-rich surface. The formation of this structure is related to the degradation of RhB and sodium percarbonate under UV illumination. Formed in these processes gaseous CO_2 and $CO_3^{\cdot-}$ radicals react with the magnetite surface forming carbonates [28]. As was recently shown, this carbonate-rich surface of oxides is a complex structure for which the occurrence of different vibrational modes is related to the formation of unidentate, bidentate, bridged, and polydentate carbonates under the reaction with the oxide surface [34,35]. Interestingly, the formation of this carbonate layer on the Fe_3O_4 NFs surface only slightly decreases this catalyst's catalytic activity.

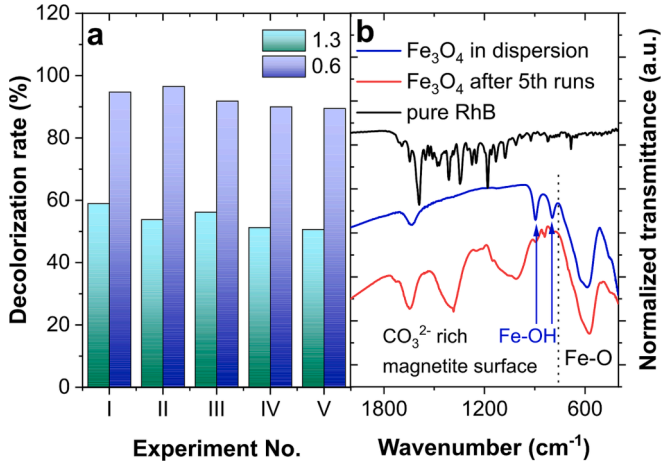

Fig. 7. Stability of Fe_3O_4 NFs: (**a**) changes in the decolorization rate of RhB recorded for the optimal reaction condition (pH 4, stirring 400 rpm, C_{Fe3O4} = 0.6 mg/ml and $C_{sod.perc.}$ = 8.3 mg/ml) and reaction with higher catalyst concentration (pH 4, stirring 400 rpm, C_{Fe3O4} = 1.3 mg/ml and $C_{sod.perc.}$ = 8.3 mg/ml); (**b**) FTIR spectra of RhB, magnetite nanoparticles collected from water dispersion and nanoparticles collected after the 5th stability experiment.

3.3.4. *Role of stirring on the catalytic degradation of RhB by flower-like magnetite nanoparticles*

The role of the stirring on the catalytic activity was confirmed previously for the system without nanoparticles. Accordingly, in this study, stirring was also tested for catalytic degradation of RhB using a photo-Fenton reaction, magnetite nanoparticles as a catalyst, and sodium percarbonate as an oxidant. The tests were performed for the optimal condition, i.e., pH equal to 4, Fe_3O_4 NFs and oxidant concentrations equal to 0.6 and 8.3 mg/ml, respectively. The results are presented in Fig. 8. As shown in Fig. 8a, the decolorization rate is comparable for both experiments only until 5 min. Afterward, the decolorization efficiency drastically increases while the reaction solution is stirred and achieves 93.6%. The decolorization rate in the system without stirring

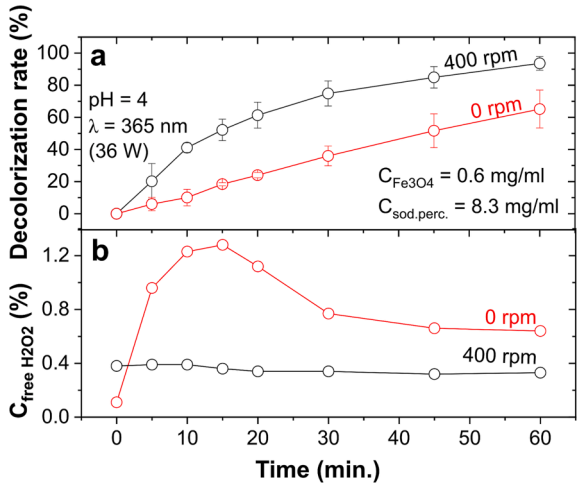

Fig. 8. Role of the reaction solution stirring on the catalytic activity of Fe_3O_4 NFs: (**a**) comparison of decolorization rate obtained for the reaction without (0 rpm) and with (400 rpm) stirring; (**b**) free hydrogen peroxide concentration in reaction solution in the reaction time function.

was much lower (only 65.2%). To understand the mechanism responsible for this drastic change, the concentration of the free H_2O_2 in the reaction solution was determined, and the results are presented in Fig. 8b. As was mentioned previously, in the case of sodium percarbonate, the hydrogen peroxide is dosed by whole reaction time. Under the stirring, the free H_2O_2 concentration ($C_{freeH2O2}$) is nearly constant throughout the reaction. Accordingly, the degradation is efficient in the whole process and consumes the same amount of hydrogen peroxide. While the solution is not stirred, the $C_{freeH2O2}$ increases drastically to 1.28% at 15 min and then decreases to 0.64% at 60 min. It can be assumed that few mechanisms can be responsible for the low decolorization rate in the case of the reaction without stirring. Firstly, when the solution is stirred, there is a much higher probability that the Fenton reaction (eq.3) appears because the nanoparticles and hydrogen peroxides molecules are continuously moving. That process results in the consumption and decomposition of hydrogen peroxide to the hydroxyl radical and hydroxide ions. Secondly, when the reaction solution was stirred, there was a much higher probability that the hydroxyl radical would react with the organic molecules (in this case, RhB dye). According to eq (2), the free hydrogen peroxide can be a scavenger for these radicals in the static case.

3.4. Modelling of the catalytic degradation process of rhodamine B by sodium percarbonate in the presence of flower-like magnetite nanoparticles

3.4.1. LRM model

A logistic regression model (LRM) of the catalytic degradation process of Rhodamine B by sodium percarbonate in the presence of Fe_3O_4 NFs was developed; the obtained values of coefficients (α_i) and standard deviations (σ) are given in Table S1. The LRMs obtained for decolorization limits D = 25, 50, 60, 70, 80, and 90% had a high predictive capability, as confirmed by values of SPEC = 81.25 – 99.20%, SENS = 85.60 – 99.5% and Acc = 83.20 – 99.60%. The best fit of the calculation results to the measurements for the LRMs was for p_{Dcr} = 0.40. Decolorization degree, as confirmed experimentally in section 3.3. changes in the reaction time (t) and was influenced by pH (Fig. 4), sodium percarbonate concentration $C_{sod.perc}$ (Fig. 5) and nanoparticles concentration C_{Fe3O4} (Fig. 6). Based on the $D = f(t, pH = 4.0, C_{Fe3O4} = 1.3$ mg/ml, $C_{sod.perc} = 16.7$ mg/ml) for D = 50%, an increase in time from 15 min to 45 min, leads to an increase of p from 0.01 to 0.67 (Figure S3). The increasing of $C_{sod.perc.}$ from 16.7 to 24.0 mg/ml (for t = 45 min) resulted in an increase p from 0.77 to 0.96 (Figure S3). An increased pH from 4.0 to 4.5 for t = 45 min (C_{Fe3O4} = 1.3 mg/ml and $C_{sod.perc.}$ = 16.7 mg/ml) leads to a decrease in p from 0.77 to 0.72, while an increase of the C_{Fe3O4} from 0.6 to 1.3 mg/ml results in an increase the probability of exceeding from 0.58 to 0.77 (for D equal to 50%).

Due to limitations of the LRM (lack of possibility to determine the value of D from x_i), based on equations S6 and S7 for pH = 6.5, C_{Fe3O4} = 0.6 mg/ml, t from 5 to 60 min, $C_{sod.perc.}$ from 5 to 36 mg/ml, the relationship D_m = f(t, $Cs_{od.perc}$) was determined, in which: D_m is the minimum degree of decolorization for the assumed independent variables (Fig. 9). The increase in $Cs_{od.perc.}$ from 5 to 15 mg/ml for t = 60 min leads to an increase in decolorization from 25% to 90%. Moreover, the increase of $C_{sod.perc.}$ from 25 to 35 mg/ml reduces reaction time from 35 to 25 min, for which D_m equal to 90% was observed. For $C_{sod.perc.}$ equal to 5 mg/ml and t = 60 min a D_m = 25% was gained, and a similar decolorization effect was obtained for $Cs_{od.perc.}$ equal to 0.035 and reaction time to 23 min.

3.4.2. Sensitivity analysis

To evaluate the influence of reaction time on the degree of decolorization as a function of percarbonate and nanoparticle dose, the relationships $S_{Fe3O4} = f(t^*, C_{sod.perc}, C_{Fe3O4}, pH^*)$ and $S_{sod.perc} = f(t^*, C_{sod.perc}, C_{Fe3O4}, pH^*)$ were determined; t^* = 15, 30 min, pH^* = 6.5 (Fig. 9a and b). It was observed that the increment of reaction time from 15 to 30 min leads to a decrease in the influence of C_{Fe3O4}, $C_{sod.perc}$ on the

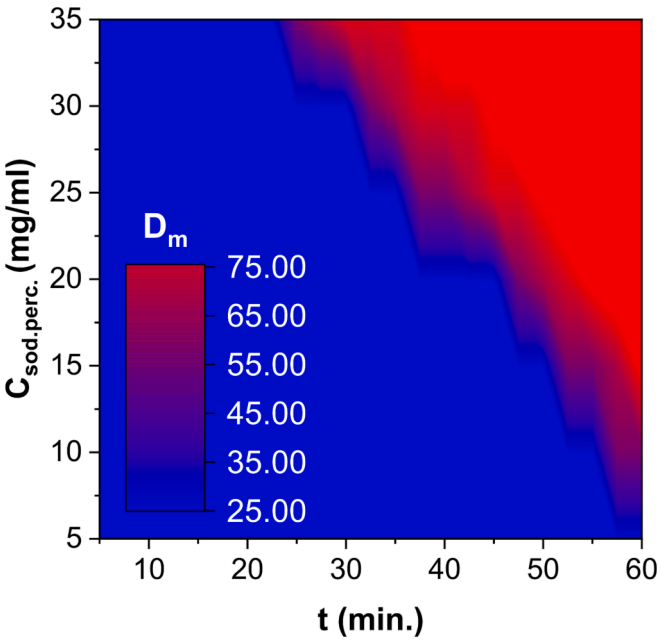

Fig. 9. Influence of the reaction time (t) and sodium percarbonate concentration ($C_{sod.perc.}$) on decolorization value (D_m).

degree of decolorization. For a reaction time equal to 15 min, an increase in C_{Fe3O4} from 0.2 to 1.2 in the range of $C_{sod.perc}$ = 5 – 31 mg/ml leads to an increase in S_{Fe3O4} from 0.25 to 1.54 (Fig. 10a). For sodium percarbonate concentration greater than 27.75 mg/ml, the influence of percarbonate dose on S_{Fe3O4} is demonstrated, and it was found that an increase in $C_{sod.\ perc}$ to 37.5 mg/ml (for C_{Fe3O4} equal to 1.2 mg/ml) results in a decrease in S_{Fe3O4} to 1.05 (Fig. 10a). For t = 30 min, the influence of sodium percarbonate concentration on S_{Fe3O4} was shown over the entire range of nanoparticle variation (Fig. 10b). For C_{Fe3O4} = 0.2, it was found that an increase in $C_{sod.perc}$ from 5 to 37.5 mg/ml leads to a decrease in S_{Fe3O4} from 0.25 to 0.10, and for C_{Fe3O4} equal to 1.2 mg/ml there is a decrease in S_{Fe3O4} from 1.54 to 0.15.

For C_{Fe3O4} from 0.2 to 1.2 mg/ml with increasing percarbonate concentration, the sensitivity coefficients of $S_{sod.perc}$ increased to a maximum value, followed by a slight decrease depending on the nanoparticles concentration (Fig. 10c). For C_{Fe3O4} equal to 0.2 mg/ml, an increase in $C_{sod.perc}$ led to an increase in $S_{sod.perc}$ from 1.4 to 9.0. For C_{Fe3O4} = 1.2 mg/ml, it was found that the sensitivity coefficient of $S_{sod.perc}$ increased from 1.4 to 7.6 in the range $C_{sod.perc.}$ from 5 to 34.25 mg/ml. Further increases in $C_{sod.perc}$ resulted in a decrease of $S_{sod.perc}$ to 7.0. An increase in $C_{sod.perc}$ from 5 to 27.75 (for t = 30 min and C_{Fe3O4} = 0.2 mg/ml) leads to an increase in $S_{sod.perc}$ from 1.25 to a maximum value of 6.37; an increase in $C_{sod.perc}$ to 37. 5 mg/ml results in a decrease in $S_{sod.perc}$ to 1.27 (Fig. 10d). In contrast, for nanoparticle concentration equal to 1.2 mg/ml it was found that for $C_{sod.perc}$ from 5 to 24.5 mg/ml there is an increase in $S_{sod.perc}$ from 1.25 to 6.0, once $C_{sod.perc}$ equal to 24.5 mg/ml is exceeded, the effect of $C_{sod.perc}$ on decolorization (D) decreases.

3.5. Influence of the dye structure on the catalytic decolorization process using optimal reaction condition

Magnetite nanoparticles with different shapes have been tested recently in the degradation of various chemical dyes. The analysis performed herein confirmed that pH, stirring, sodium percarbonate, and magnetite concentrations play a crucial role in the catalytic degradation and decolorization of Rhodamine B, a model dye widely described in the literature. However, the possible applicability of these nanoparticles in the degradation of other organic compounds cannot be assumed based only on the optimization process of one dye. Therefore, for the

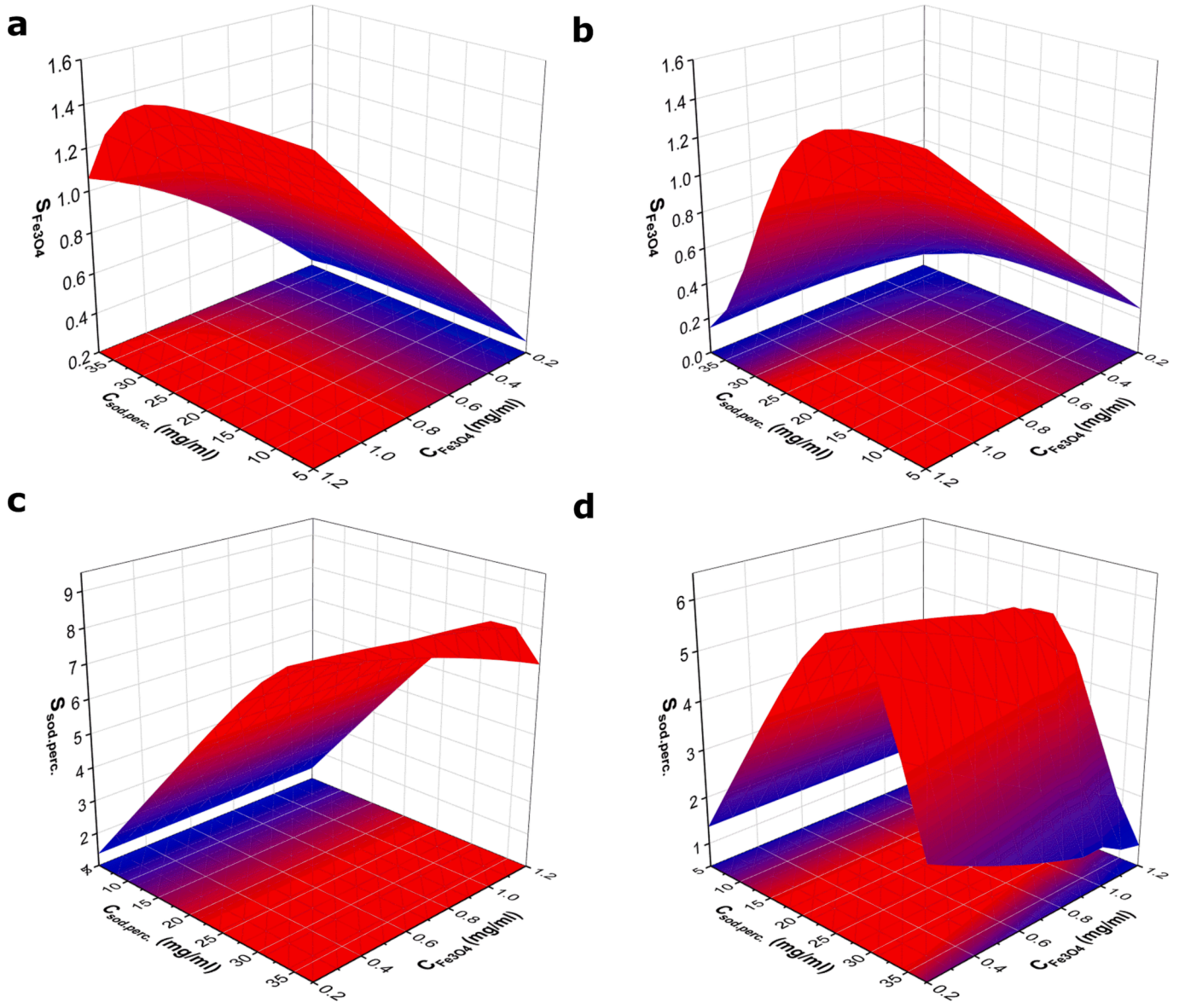

Fig. 10. Influence of magnetite nanoparticles (C_{Fe3O4}) and sodium percarbonate ($C_{sod.perc.}$) concentration on the $S_{Fe3O4} = f(C_{Fe3O4}, C_{sod.perc})$ (**a** and **b**) and $S_{sod.perc.} = f(C_{Fe3O4}, C_{sod.perc})$ (**c** and **d**) determined for reaction time equal to 15 min. (**a** and **c**) and 30 min. (**b** and **d**).

experimentally optimal reaction condition (i.e., pH equal to 4, stirring of 400 rpm, sodium percarbonate concentration equal to 8.3 mg/ml and nanoparticles concentration to 0.6 mg/ml), tests of the possible application of this process were conducted for additional widely used in the industry chemical dyes. The decolorization rates of four tested dyes are presented in Fig. 11. As can be seen, the same reaction condition can show ultrahigh efficiency and also cannot allow degradation of some of them. Naphthol Green B and Lissamine Green B are dyes that can be degraded by the proposed herein system. In the case of Lissamine Green B, the decolorization rate of 100% was achieved after 5 min, while for the Naphthol Green B observed a high, but not as good, rate of 61.8% after 60 min. Naphthol Green B is a Fe(III) complex dye with high degradation resistance, which is widely present in wastewater concerning its application as a coloring agent in the leather and fur industries. This dye degradation processes mainly focus on biodegradation by bacteria [36] and combined adsorption and degradation by complex systems [37].

Li et al. [38] have also shown that metallic glasses can be used to degrade this dye by activating peroxymonosulfates. The second dye, Lissamine Green B, a dye commonly used for coloring wool, silk, and leather, was successfully degraded using, for example, TiO_2 thin films [39]; however, this process was not as efficient as proposed in this study (the dye was entirely degraded after 2 h). Interestingly, Phloxine B and Acid Red 1 were not degraded with high efficiency using flower-like magnetite nanoparticles as catalysts (decolorization rate about near 0%). This is unusual because some studies indicate that these dyes, especially Acid Red 1, can be removed using heterogeneous Fenton and photo-Fenton reactions [39]. To understand this behavior, two additional tests were performed. Firstly, adsorption tests (Fig. S5) confirm that the dyes with a higher tendency to be adsorbed on the surface of Fe_3O_4 nanoflowers can be degraded with a higher ratio, even if the adsorption is low (5.69%, 1.76% and 0.22% for RhB, LGB, and NGB, respectively). No adsorption process was observed in the case of PhB and AR1. This can be related to the higher degradation rate observed in the case of the molecules, which are adsorbed by the magnetite nanoparticles.

Scavengers and interfering species were tested in the Lissamine Green B and Rhodamine B degradation in the second test. This experiment is widely used in the case of the catalytic degradation of various organic compounds. However, the role of the different compounds,

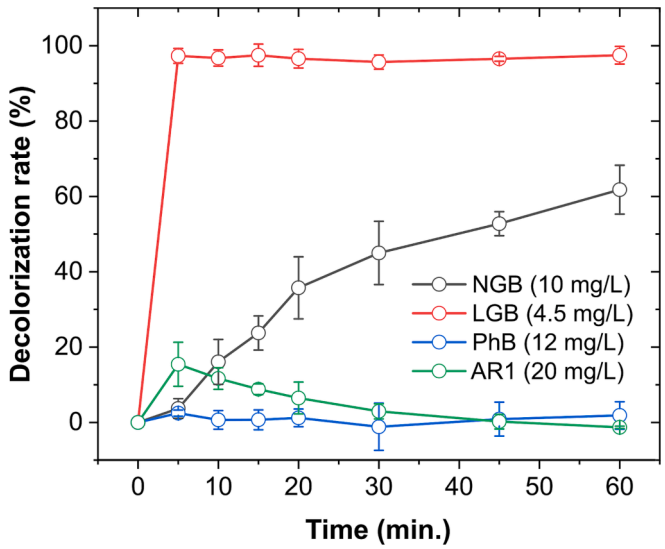

Fig. 11. Decolorization rate of various chemical dyes measured for the optimal reaction condition (pH 4, stirring 400 rpm, C_{Fe3O4} = 0.6 mg/ml and $C_{sod.perc.}$ = 8.3 mg/ml).

added as scavengers and interfering species, is controversial, sometimes unknown, and many studies oppose their selectivity [40]. Therefore, different scavengers should be tested, and the results can only approximate a possible mechanism rather than describe it in detail. As shown in Fig. 12 a, only adding ascorbic acid changes the LGB dye's degradation process.

Interestingly, adding 2-propanol and *tert*-Butanol does not result in a drop in Lissamine Green B's decolorization ratio. These two alcohols are widely used to scavenge the $HO^{\bullet}$ radicals [41–43], therefore observed ultrafast degradation of this dye is not related to the oxidation by the hydroxyl radicals but can be related to the degradation by O_2^{-} radicals, which are also formed from the sodium percarbonate under the activation of this compound by metal ions (such as iron and copper ions) and UV light [28,44]. On the other hand, the mechanism of the RhB degradation is related to the oxidation by both radicals (Fig. 12b). The addition of ascorbic acid, 2-propanol, and *tert*-Butanol results stopped

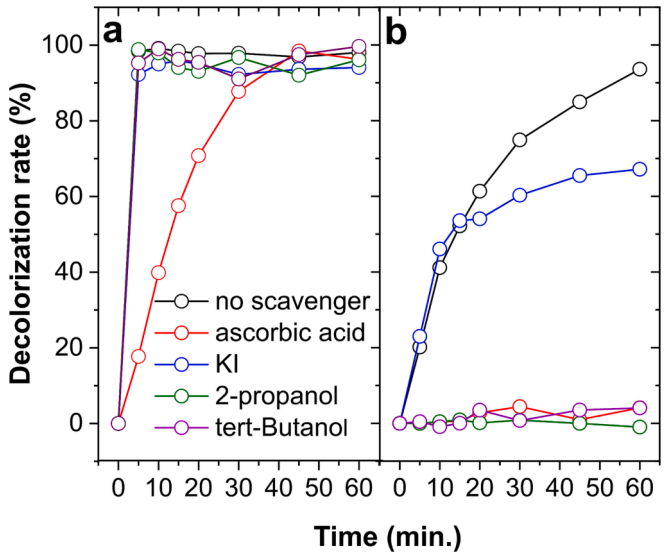

Fig. 12. Effect of the scavengers and interfering species (ascorbic acid, KI, 2-propanol, and *tert*-Butanol) addition on the decolorization rate of Lissamine Green B (**a**) and Rhodamine B (**b**) for optimal reaction condition (pH 4, stirring 400 rpm, C_{Fe3O4} = 0.6 mg/ml and $C_{sod.perc.}$ = 8.3 mg/ml.

the degradation process totally, which is typical for this reaction type. Interestingly, in the case of RhB, electron holes h^{+} generated by the UV illumination of magnetite nanoparticles also participate in this dye's degradation process. This can be related to the occurrence of the reaction between these holes generated by the UV light in the magnetite valence bands and hydroxyl ions, which results in the formation of hydroxyl radicals (according to reactions (3) and (6), one of the main radicals response for the RhB degradation [45]. Moreover, the iodide ions can also be used as the hydroxyl radicals scavenger according to the reaction (7).

$$h^{+}+HO^{-}\rightarrow HO^{\bullet} \quad (6)$$

$$2HO^{\bullet}+2I^{-}+2H^{+}\rightarrow 2H_2O + I_2 \quad (7)$$

3.6. Role of the surface functionalization on the catalytic activity of magnetite nanoparticles

As presented above, nanoparticle reaction conditions and adsorption capabilities must be considered in the degradation processes. However, there is still a question: Why should flower-like nanoparticles synthesized using the proposed method be considered an efficient catalyst in photo-Fenton reaction? In the literature, many methods of synthesis of nanoparticles are presented. Using the various organic modifiers in the thermal degradation of organic precursors allows for synthesizing magnetite nanoparticles with various shapes and properties. Unfortunately, these methods result in nanoparticle synthesis spontaneously functionalized by these organic molecules [46]. While, as was described above, in the Fenton-based processes, the crucial role plays iron ions, this surface functionalization drastically changes the catalytic activity of nanoparticles. Radon et al. [10] have shown that despite the reduction in the size of the magnetite nanoparticle agglomerates from 2384 nm to 240 nm, the catalytic activity of the thus synthesized materials did not increase. However, it decreased from 86% to 35% for the heterogeneous Fenton process and 93 to 85.5% for the UV-assisted heterogeneous Fenton process. Studies using FTIR spectroscopy clearly indicated that it is related to the functionalization of the Fe_3O_4 surface by small, organic malonic acid molecules. This functionalization blocks the active sites, i. e. Fe^{2+} and Fe^{3+} ions on the surface of nanoparticles, and despite the increase in the active surface area by reducing the size of the agglomerates, the catalytic activity in the decomposition of rhodamine B decreases. Accordingly, in this study magnetite nanoflowers synthesized without any organic modifiers were compared with two other nanoparticle types – ultrafine spherical Fe_3O_4 NPs (Fig. S6) synthesized using polyol method and magnetite nanocubes (Fig. S7) synthesized by thermal degradation of $Fe(acac)_3$ in presence of the oleic acid. As can be seen in Fig. 13 the Fe_3O_4 nanoflowers can be also used in the catalytic degradation of Methylene Blue using photo-Fenton process with H_2O_2 as the oxidant. In studied case (see Supporting Information for details) the 72% of the methylene blue can be removed from the reaction solution, while application of the oleic acid functionalized magnetite nanocubes allowed to remove only 44% of MB. Interestingly, hydrophilic ultrafine magnetite nanoparticles (with size below 10 nm) synthesized in polyol process were characterized by the lowest degradation rate of 21%. These changes can be related to the functionalization of the magnetite surface by oleic acid and by the triethylene glycol.

The presence of these organic molecules on the surface of magnetite can decrease the catalytic activity for two reasons: (i) the active centers (Fe ions) are inactive in the Fenton process by bonding with organic molecules, and (ii) the produced hydroxyl radicals are consumed to degrade the attached to the magnetite surface organic molecules (Fig. 14). While in the case of the nanoflowers Fenton reaction and formation of hydroxyl radicals in UV/H_2O_2 occurs spontaneously (Fig. 14a) in the case of the ultrafine nanospheres and cubic nanoparticles Fenton reaction is stopped firstly by the inactive catalytic sites.

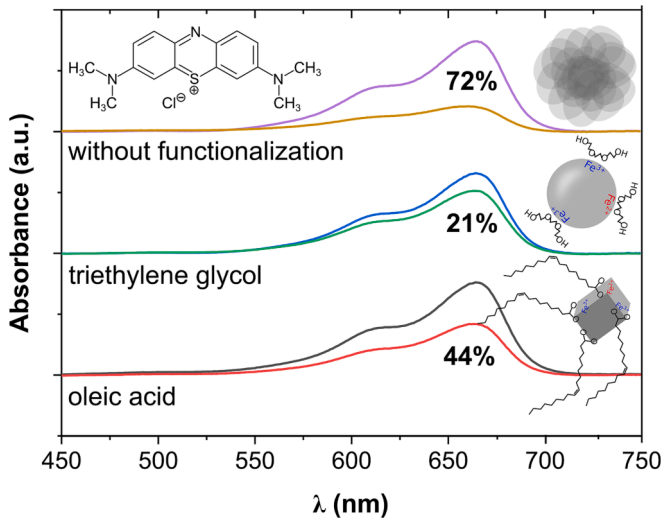

Fig. 13. UV–Vis spectra recorded at 0 and 60 min of reaction decolorization of Methylene Blue with decolorization rate and models of the applied magnetite nanoparticles.

Moreover, as can be seen, the functionalization by glycol molecules drastically decreases catalytic activity, which is related to the high ratio of the surface functionalization and agrees with obtained FTIR spectra (Fig. S8). The presence of an organic modifier was also confirmed for the nanoparticles synthesized in the presence of oleic acid, while in the case of nanoflowers, the additional vibrations in the analyzed range were attributed only to the adsorbed water. Furthermore, Günay et al. confirmed that triethylene glycol could easily functionalize the Fe_3O_4 NPs surface by the covalent interaction between oxygens in glycol and metal ions. Therefore, in the case of the functionalized magnetite nanoparticles, hydroxyl radicals not only react with the dye molecules and oxidize them but also with the triethylene glycol and oleic acid. Afterward, when the organic layer on the surface of magnetite is decomposed, both processes (Fenton and UV/H_2O_2 reactions) occur spontaneously and decompose the dyes molecules (Fig. 14b and c); however, the degradation rate is much lower than in the case of the pure, highly active surface of magnetite nanoflowers.

Despite the differences between the degradation mechanism, the proposed unfunctionalized flower-like magnetite nanocatalyst can be used to degrade organic dyes with different structures with high degradation rates. Table 1 presents a comparison between the optimized herein reaction condition and other systems recently tested in literature in the degradation of Rhodamine B, Lissamine Green B, and Naphthol Green B. As can be seen, the decolorization rate of RhB is similar to other tested reactions, and the most visible advantages can be observed for the degradation of NGB and LGB. In the case of Lissamine Green B degradation, the 97.3% dye was oxidized after 5 min. The decolorization rate of Naphthol Green B is lower than for the other processes; however, the concentration of this dye is much higher than tested currently (ppm) in the degradation processes, or the reaction time is much shorter than shown in the literature.

4. Conclusions

The catalytic activity of flower-like magnetite nanoparticles synthesized using a new, co-precipitation-based method was measured in the decolorization of rhodamine B dye in the heterogenous photo-Fenton reaction using sodium percarbonate as oxidant. It was confirmed that using β-FeO(OH)•Cl_n nanorods as Fe^{3+} ions source in the co-precipitation method allows obtaining 83.7 ± 16.6 nm magnetite nanoflowers without impurities. Optimizing the catalytic degradation process allowed us to state that Fe_3O_4 NFs could be used as a catalyst in a wide pH range; however, the highest catalytic activity can be obtained at pH 4. The decolorization rate increase when the concentration of sodium percarbonate increases, contrary to magnetite nanoparticles concentration, for which optimum was observed for 0.6 mg/ml. It was shown that using this concentration can significantly improve the decolorization rate from 56.6 to 93.6% for sodium percarbonate concentration equal to 8.3 mg/ml and pH equal to 4. The slightly higher degradation

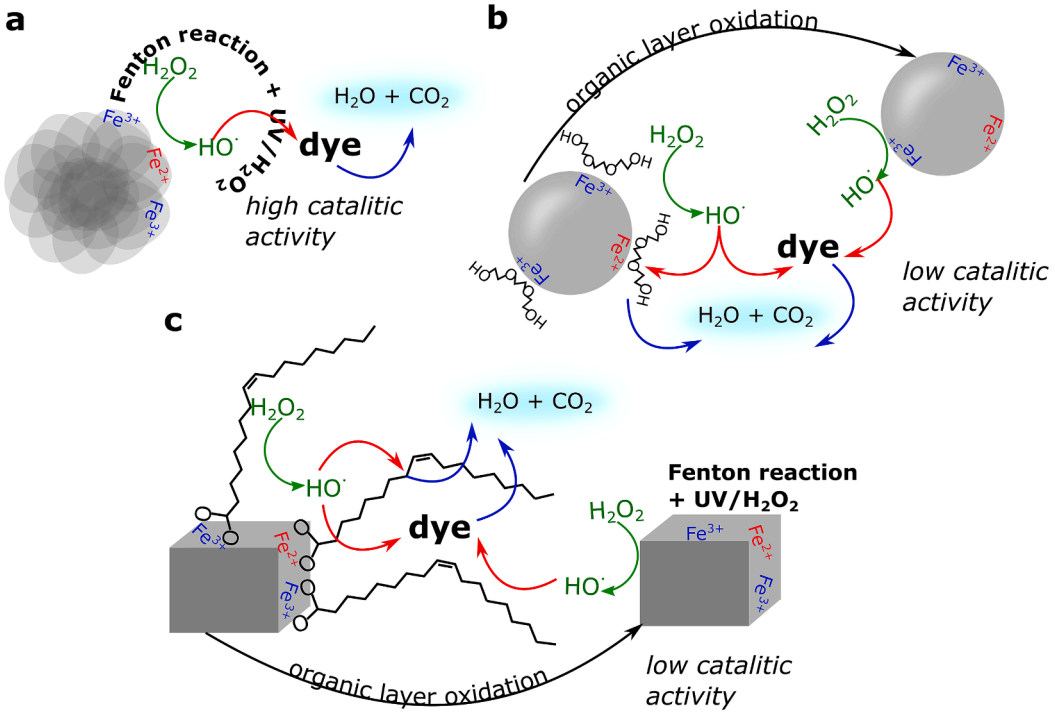

Fig. 14. Schematic representation of the influence of magnetite nanoparticle surface functionalization on the catalytic activity and dye decomposition process for (**a**) Fe_3O_4 NFs, (**b**) ultrafine spherical magnetite nanoparticles functionalized by triethylene glycol and (**c**) magnetite nanocubes functionalized by oleic acid.

Table 1
Comparison of different degradation processes of Rhodamine B (RhB), Naphthol Green B (NGB), and Lissamine Green B (LGB).

Catalyst	Dye	Reaction condition	Decolorization (%)	Time (min.)	Ref.
$CoFe_2O_4$ NPs	RhB	[RhB] = 10 mg/L [catalyst] = 1 g/L [H_2O_2] = 15 ml/L (30%) 30 W LED lamps	90.6	270	[47]
Fe_3O_4/SiO_2 double-mesoporous-shelled hollow spheres		[RhB] = 20 mg/L [catalyst] = 0.2 g/L [H_2O_2] = 20 ml/L (30%) pH = 6.12 T = 25℃ Vis radiation	97	180	[48]
Cu–Fe_3O_4 MNPs		[RhB] = 10 μM [catalyst] = 0.5 g/L [H_2O_2] = 80 mM pH = 6.9 T = 25℃	~100	120	[49]
Fe_2O_3–Fe_3O_4/SiO_2		[RhB] = 20 mg/L [catalyst] = 2 g/L [H_2O_2] = 1 ml/L pH = 6.5—7 T = 25℃ 296 nm / 30 W	~99	60	[50]
Fe_3O_4 NFs		[RhB] = 10 mg/L [catalyst] = 0.6 g/L [sodium percarbonate] = 8.3 g/L pH = 4 T = 25℃ stirring = 400 rpm 365 nm / 36 W	93.6	60	This study
$ZnS/MoS_2/Fe_3O_4$	NGB	[NGB] = 20 ppm [catalyst] = 0.1 g/L pH = 3 UV and Vis irradiation	84 (Vis)97 (UV)	75	[51]
$Fe_{78}Si_9B_{13}$ metallic glass		[NGB] = 50 ppm [catalyst] = 0.5 g/L [peroxymonosulfates] = 1.0 mmol/L irradiation intensity: 7.7 μW/cm^2	92.1	8	[38]
Pseudoalteromonas sp CF10-13		[NGB] = 100 mg/L pH = 7.5 concentrated solution of *P.* sp CF10-13 T = 25℃ anaerobic condition acetate as an electron donor	> 95	4200	[36]
Fe_3O_4 NFs		[NGB] = 10 mg/L [catalyst] = 0.6 g/L [sodium percarbonate] = 8.3 g/L pH = 4 T = 25℃ stirring = 400 rpm 365 nm / 36 W	61.8	60	This study
$FeSO_4{\cdot}7H_2O$	LGB	[catalyst] = 0.2 mM pH = 3 graphite electrodes potential = 5 V [Na_2SO_4] = 0.1 M	80	180	[52]
iron-based amberlite catalyst		[LGB] = 7.5 mg/L [catalyst] = 30 g/L [$Na_2S_2O_8$] = 1 mM	>90	20	[53]
TiO_2 film		[LGB] = 7.3 mg/ml [catalyst] = 57.93 g/L pH = 7.2 T = 25℃ 365 nm	~100	120	[54]

(*continued on next page*)

Table 1 (*continued*)

Catalyst	Dye	Reaction condition	Decolorization (%)	Time (min.)	Ref.
Fe alginate beads		pH = 2 graphite electrodes air flow = 1 L/min Potential = 14.19 V	>95	60	[55]
Fe_3O_4 NFs		[LGB] = 4.5 mg/L [catalyst] = 0.6 g/L [sodium percarbonate] = 8.3 g/L pH = 4 T = 25℃ stirring = 400 rpm 365 nm / 36 W	97.3	5	This study

rate (95.9%) was observed for 4.5 times higher oxidant concentration (37.5 mg/ml), which confirms the high catalytic activity and the appropriateness of using flower-like magnetite nanoparticles in the tested advanced oxidation process. This applicability potential also was confirmed by the stability test, in which the drop in the decolorization rate was slight after five cycles. Moreover, their possible applicability was confirmed for the degradation of two other dyes: Lissamine Green B (decolorization rate near 100% after 5 min.) and Naphthol Green B (decolorization rate of 61.8% after 60 min.), using optimized in this study reaction condition. Interestingly, this ultrafast Lissamine Green B decolorization can be related to the oxidation of this compound by the O_2^{-} radicals. Finally, the high catalytic activity of flower-like Fe_3O_4 NPs was connected with their unfunctionalized surface. It was shown that the use of the much smaller (below 10 nm) magnetite nanoparticles with surface functionalized by triethylene glycol results in a much lower degradation rate (21%) than 8-times bigger nanoflowers, for which reaction efficiency was equal to 72 % in the case of the methylene blue decolorization. It was confirmed that an increase in percarbonate dose and nanoparticle leads to an increase in decolorization, and LRM models allowed interpolation of the degree of decolorization for t = 0——60 min, pH = 3.0——6.5, C_{Fe3O4} = 0.0002——0.0012 and $C_{sod.perc.}$ = 0.005——0.0375. The results of the sensitivity analysis complemented the simulations and allowed the influence of the correction of the independent variables (C_{Fe3O4}, $C_{sod.perc}$) on the degree of decolorization to be determined, which is essential from the point of view of optimizing process conditions.

Funding

This work was supported by the grant from the Polish Ministry of Science and Higher Education - Diamond Grant (0220/DIA/2018/47).

CRediT authorship contribution statement

Sylwester Łoński: Conceptualization, Methodology, Investigation, Writing – original draft. **Dariusz Łukowiec:** Investigation, Writing – review & editing. **Krzysztof Barbusiński:** Validation, Investigation, Writing – review & editing. **Rafał Babilas:** Conceptualization, Writing – review & editing. **Bartosz Szeląg:** Conceptualization, Methodology, Writing – original draft. **Adrian Radoń:** Conceptualization, Methodology, Investigation, Writing – original draft, Visualization, Supervision.

Declaration of Competing Interest

The authors declare the following financial interests/personal relationships which may be considered as potential competing interests: [Adrian Radon reports financial support was provided by Ministry of Education and Science of the Republic of Poland].

Data availability

Data will be made available on request.

Appendix A. Supplementary data

Supplementary data to this article can be found online at https://doi.org/10.1016/j.apsusc.2023.158127.

References

[1] M. Goyal, M. Singh, Size and shape dependence of optical properties of nanostructures, Appl. Phys. A Mater. Sci. Process. (2020), https://doi.org/10.1007/s00339-020-3327-9.
[2] E.A. Kwizera, E. Chaffin, X. Shen, J. Chen, Q. Zou, Z. Wu, Z. Gai, S. Bhana, R. Oconnor, L. Wang, H. Adhikari, S.R. Mishra, Y. Wang, X. Huang, Size- and shape-controlled synthesis and properties of magnetic-plasmonic core-shell nanoparticles, J. Phys. Chem. C. 120 (2016) 10530–10546, https://doi.org/10.1021/acs.jpcc.6b00875.
[3] S.A. Majetich, T. Wen, O.T. Mefford, Magnetic nanoparticles, MRS Bull. 38 (2013) 899–903, https://doi.org/10.1557/mrs.2013.230.
[4] A.G. Roca, L. Gutiérrez, H. Gavilán, M.E. Fortes Brollo, S. Veintemillas-Verdaguer, M. del P. Morales, Design strategies for shape-controlled magnetic iron oxide nanoparticles, Adv. Drug Deliv. Rev. (2019), https://doi.org/10.1016/j.addr.2018.12.008.
[5] A. Radoń, S. Łoński, T. Warski, R. Babilas, T. Tański, M. Dudziak, D. Łukowiec, Catalytic activity of non-spherical shaped magnetite nanoparticles in degradation of Sudan I, Rhodamine B and Methylene Blue dyes, Appl. Surf. Sci. 487 (2019), https://doi.org/10.1016/j.apsusc.2019.05.091.
[6] W. Wang, Q. Mao, H. He, M. Zhou, Fe_3O_4 nanoparticles as an efficient heterogeneous fenton catalyst for phenol removal at relatively wide pH values, Water Sci. Technol. (2013), https://doi.org/10.2166/wst.2013.497.
[7] A.N. Chishti, L. Ni, F. Guo, X. Lin, Y. Liu, H. Wu, M. Chen, G.W. Diao, Magnetite-Silica core-shell nanocomposites decorated with silver nanoparticles for enhanced catalytic reduction of 4-nitrophenol and degradation of methylene blue dye in the water, J. Environ. Chem. Eng. (2021), https://doi.org/10.1016/j.jece.2020.104948.
[8] H. Qin, R. Xiao, W. Shi, Y. Wang, H. Li, L. Guo, H. Cheng, J. Chen, Magnetic core-shell-structured Fe_3O_4@CeO_2 as an efficient catalyst for catalytic wet peroxide oxidation of benzoic acid, RSC Adv. (2018), https://doi.org/10.1039/c8ra07144f.
[9] P.B. Rathod, K.S.A. Kumar, A.A. Athawale, A.K. Pandey, S. Chattopadhyay, Polymer-shell-encapsulated magnetite nanoparticles bearing hexamethylenetetramine for catalysing Aza-Michael addition reactions, European J. Org. Chem. (2018), https://doi.org/10.1002/ejoc.201801095.
[10] A. Radoń, S. Łoński, M. Kądziołka-Gaweł, P. Gębara, M. Lis, D. Łukowiec, R. Babilas, Influence of magnetite nanoparticles surface dissolution, stabilization and functionalization by malonic acid on the catalytic activity, magnetic and electrical properties, Colloids Surfaces A Physicochem. Eng. Asp. (2020), https://doi.org/10.1016/j.colsurfa.2020.125446.
[11] M. Chen, H. Xu, Q. Wang, D. Li, D. Xia, Activation mechanism of sodium percarbonate by FeOCl under visible-light-enhanced catalytic oxidation, Chem. Phys. Lett. (2018), https://doi.org/10.1016/j.cplett.2018.06.004.
[12] R.G. De La Calle, O. Gimeno, J. Rivas, Percarbonate as a hydrogen peroxide carrier in soil remediation processes, Environ. Eng. Sci. (2012), https://doi.org/10.1089/ees.2011.0237.
[13] S. Sajjadi, A. Khataee, R. Darvishi Cheshmeh Soltani, N. Bagheri, A. Karimi, A. Ebadi Fard Azar, Implementation of magnetic Fe3O4@ZIF-8 nanocomposite to activate sodium percarbonate for highly effective degradation of organic compound in aqueous solution, J. Ind. Eng. Chem. (2018), https://doi.org/10.1016/j.jiec.2018.08.016.
[14] M. Adhikari, E. Echeverria, G. Risica, D.N. McIlroy, M. Nippe, Y. Vasquez, Synthesis of magnetite nanorods from the reduction of iron oxy-hydroxide with hydrazine, ACS Omega. (2020), https://doi.org/10.1021/acsomega.0c02928.
[15] J. Choi, J. Cha, J.K. Lee, Synthesis of various magnetite nanoparticles through simple phase transformation and their shape-dependent magnetic properties, RSC Adv. (2013), https://doi.org/10.1039/c3ra40283e.
[16] A. Rebhi, T. Makhlouf, N. Njah, X-Ray diffraction analysis of 99.1% recycled aluminium subjected to equal channel angular extrusion, Phys. Procedia. 2 (2009) 1263–1270, https://doi.org/10.1016/j.phpro.2009.11.090.

[17] C.M. Patel, M. Chakraborty, Z.V.P. Murthy, Study on the stability and microstructural properties of barium sulfate nanoparticles produced by nanomilling, Adv. Powder Technol. 25 (2014) 226–235, https://doi.org/10.1016/j.apt.2013.04.003.

[18] F. Hu, K.W. MacRenaris, E.A. Waters, E.A. Schultz-Sikma, A.L. Eckermann, T. J. Meade, Highly dispersible, superparamagnetic magnetite nanoflowers for magnetic resonance imaging, Chem. Commun. (2010), https://doi.org/10.1039/b916562b.

[19] C. Lu, H. Wang, J. Ma, H. Yuan, H. Liang, L. Wu, K.Y. Chai, S. Li, Facile synthesis of superparamagnetic magnetite nanoflowers and their applications in cellular imaging, RSC Adv. (2016), https://doi.org/10.1039/c6ra06532e.

[20] K. Petcharoen, A. Sirivat, Synthesis and characterization of magnetite nanoparticles via the chemical co-precipitation method, Mater. Sci. Eng. B Solid-State Mater. Adv. Technol. (2012), https://doi.org/10.1016/j.mseb.2012.01.003.

[21] H. Fatima, D.W. Lee, H.J. Yun, K.S. Kim, Shape-controlled synthesis of magnetic Fe_3O_4 nanoparticles with different iron precursors and capping agents, RSC Adv. (2018), https://doi.org/10.1039/c8ra02909a.

[22] Y. Dong, L. Bian, C. Zhang, B. Li, Comparison of four oxidants activated through tetraacetylethylenediamine for developing sustainable and rapid degradation of organic dye, Color. Technol. (2020), https://doi.org/10.1111/cote.12474.

[23] B. Ozbey Unal, Z. Bilici, N. Ugur, Z. Isik, E. Harputlu, N. Dizge, K. Ocakoglu, Adsorption and Fenton oxidation of azo dyes by magnetite nanoparticles deposited on a glass substrate, J. Water Process Eng. (2019), https://doi.org/10.1016/j.jwpe.2019.100897.

[24] B.G.H. Briton, L. Duclaux, Y. Richardson, K.B. Yao, L. Reinert, Y. Soneda, Effectiveness of the dispersion of iron nanoparticles within micropores and mesopores of activated carbon for Rhodamine B removal in wastewater by the heterogeneous fenton process, Appl. Water Sci. (2019), https://doi.org/10.1007/s13201-019-1047-0.

[25] M.S. Ansari, K. Raees, M.A. Khan, M.Z.A. Rafiquee, M. Otero, Kinetic studies on the catalytic degradation of rhodamine b by hydrogen peroxide: Effect of surfactant coated and non-coated iron (III) oxide nanoparticles, Polymers (Basel). (2020), https://doi.org/10.3390/polym12102246.

[26] T. Maezono, M. Tokumura, M. Sekine, Y. Kawase, Hydroxyl radical concentration profile in photo-fenton oxidation process: Generation and consumption of hydroxyl radicals during the discoloration of azo-dye Orange II, Chemosphere. (2011), https://doi.org/10.1016/j.chemosphere.2010.11.052.

[27] M. Noorjahan, V. Durga Kumari, M. Subrahmanyam, L. Panda, Immobilized Fe(III)-HY: An efficient and stable photo-Fenton catalyst, Appl. Catal. B Environ. (2005), https://doi.org/10.1016/j.apcatb.2004.11.006.

[28] X. Liu, S. He, Y. Yang, B. Yao, Y. Tang, L. Luo, D. Zhi, Z. Wan, L. Wang, Y. Zhou, A review on percarbonate-based advanced oxidation processes for remediation of organic compounds in water, Environ. Res. (2021), https://doi.org/10.1016/j.envres.2021.111371.

[29] A. Choquehuanca, J.G. Ruiz-Montoya, A. La Rosa-Toro Gómez, Discoloration of methylene blue at neutral pH by heterogeneous photo-Fenton-like reactions using crystalline and amorphous iron oxides, Open Chem. (2021), https://doi.org/10.1515/chem-2021-0077.

[30] P. Van Viet, D. Van Chuyen, N.Q. Hien, N.N. Duy, C.M. Thi, Visible-light-induced photo-fenton degradation of rhodamine B over Fe_2O_3-diatomite materials, J. Sci. Adv. Mater. Devices. (2020), https://doi.org/10.1016/j.jsamd.2020.07.007.

[31] Y. Mizuta, T. Masumizu, M. Kohno, A. Mori, L. Packer, Kinetic analysis of the fenton reaction by ESR-spin trapping, Biochem. Mol. Biol. Int. (1997), https://doi.org/10.1080/15216549700204931.

[32] X. Zhu, L. Zhang, G. Zou, Q. Chen, Y. Guo, S. Liang, L. Hu, M. North, H. Xie, Carboxylcellulose hydrogel confined-Fe_3O_4 nanoparticles catalyst for Fenton-like degradation of Rhodamine B, Int. J. Biol. Macromol. (2021), https://doi.org/10.1016/j.ijbiomac.2021.04.067.

[33] M. Stoia, R. Istratie, C. Păcurariu, Investigation of magnetite nanoparticles stability in air by thermal analysis and FTIR spectroscopy, J. Therm. Anal. Calorim. (2016), https://doi.org/10.1007/s10973-016-5393-y.

[34] H. Du, C.T. Williams, A.D. Ebner, J.A. Ritter, In situ FTIR spectroscopic analysis of carbonate transformations during adsorption and desorption of CO_2 in K-promoted HTlc, Chem. Mater. (2010), https://doi.org/10.1021/cm100703e.

[35] E.M. Köck, M. Kogler, T. Bielz, B. Klötzer, S. Penner, In situ FT-IR spectroscopic study of CO_2 and CO adsorption on Y_2O_3, ZrO_2, and yttria-stabilized ZrO_2, J. Phys. Chem. C. (2013), https://doi.org/10.1021/jp405625x.

[36] S. Cheng, N. Li, L. Jiang, Y. Li, B. Xu, W. Zhou, Biodegradation of metal complex Naphthol Green B and formation of iron–sulfur nanoparticles by marine bacterium Pseudoalteromonas sp CF10-13, Bioresour. Technol. (2019), https://doi.org/10.1016/j.biortech.2018.10.082.

[37] Y. Chen, Z. Lin, R. Hao, H. Xu, C. Huang, Rapid adsorption and reductive degradation of Naphthol Green B from aqueous solution by Polypyrrole/Attapulgite composites supported nanoscale zero-valent iron, J. Hazard. Mater. (2019), https://doi.org/10.1016/j.jhazmat.2019.02.096.

[38] X.F. Li, S.X. Liang, X.W. Xi, Z. Jia, S.K. Xie, H.C. Lin, J.P. Hu, L.C. Zhang, Excellent performance of $Fe_{78}Si_9B_{13}$ metallic glass for activating peroxymonosulfate in degradation of naphthol green B, Metals (Basel). (2017), https://doi.org/10.3390/met7070273.

[39] S. Thomas, R. Sreekanth, V.A. Sijumon, U.K. Aravind, C.T. Aravindakumar, Oxidative degradation of Acid Red 1 in aqueous medium, Chem. Eng. J. (2014), https://doi.org/10.1016/j.cej.2014.01.037.

[40] J.T. Schneider, D.S. Firak, R.R. Ribeiro, P. Peralta-Zamora, Use of scavenger agents in heterogeneous photocatalysis: Truths, half-truths, and misinterpretations, Phys. Chem. Chem. Phys. (2020), https://doi.org/10.1039/d0cp02411b.

[41] L. Yan, J. Du, C. Jing, How TiO_2 facets determine arsenic adsorption and photooxidation: Spectroscopic and DFT studies, Catal. Sci. Technol. (2016), https://doi.org/10.1039/c5cy01679g.

[42] Z. Gao, D. Zhang, Y.S. Jun, Does tert-butyl alcohol really terminate the oxidative activity of •OH in inorganic redox chemistry? Environ. Sci. Technol. (2021) https://doi.org/10.1021/acs.est.1c01578.

[43] X. Li, J. Li, J. Bai, Y. Dong, L. Li, B. Zhou, The inhibition effect of Tert-butyl alcohol on the TiO_2 nano assays photoelectrocatalytic degradation of different organics and its mechanism, Nano-Micro Lett. (2016), https://doi.org/10.1007/s40820-015-0080-2.

[44] S. Som, C. Raha, I.B. Chatterjee, Ascorbic acid: A scavenger of superoxide radical, Acta Vitaminol, Enzymol, 1983.

[45] S.J. Olusegun, T.G.F. Souza, G. de O. Souza, M. Osial, N.D.S. Mohallem, V.S. T. Ciminelli, P. Krysinski, Iron-based materials for the adsorption and photocatalytic degradation of pharmaceutical drugs: A comprehensive review of the mechanism pathway, J. Water Process Eng. (2023), https://doi.org/10.1016/j.jwpe.2022.103457.

[46] A. Rajan, N.K. Sahu, Hydrophobic-to-hydrophilic transition of Fe_3O_4 nanorods for magnetically induced hyperthermia, ACS Appl. Nano Mater. (2021), https://doi.org/10.1021/acsanm.1c00274.

[47] N.T.T. Loan, N.T.H. Lan, N.T. Thuy Hang, N.Q. Hai, D.T.T. Anh, V.T. Hau, L. Van Tan, T. Van Tran, $CoFe_2O_4$ nanomaterials: Effect of annealing temperature on characterization, magnetic, photocatalytic, and photo-fenton properties, Processes. (2019). https://doi.org/10.3390/PR7120885.

[48] X. Wu, Z. Nan, Degradation of rhodamine B by a novel Fe_3O_4/SiO_2 double-mesoporous-shelled hollow spheres through photo-Fenton process, Mater. Chem. Phys. (2019), https://doi.org/10.1016/j.matchemphys.2019.02.023.

[49] W. Du, R. Huang, X. Huang, R. Chen, F. Chen, Copper-promoted heterogeneous Fenton-like oxidation of Rhodamine B over Fe_3O_4 magnetic nanocatalysts at mild conditions, Environ. Sci. Pollut. Res. (2021), https://doi.org/10.1007/s11356-020-12264-z.

[50] I. Fatimah, S.N. Amaliah, M.F. Andrian, T.P. Handayani, R. Nurillahi, N.I. Prakoso, W.P. Wicaksono, L. Chuenchom, Iron oxide nanoparticles supported on biogenic silica derived from bamboo leaf ash for rhodamine B photodegradation, Sustain. Chem. Pharm. (2019), https://doi.org/10.1016/j.scp.2019.100149.

[51] N. Khorasanipour, P. Iranmanesh, S. Saeednia, S. Tabatabai Yazdi, Photocatalytic degradation of Naphthol Green in aqueous solution through the reusable ZnS/MoS_2/Fe_3O_4 magnetic nanocomposite, Surfaces and Interfaces. (2023), https://doi.org/10.1016/j.surfin.2022.102613.

[52] E. Rosales, M. Pazos, M.A. Longo, M.A. Sanromán, Influence of operational parameters on electro-Fenton degradation of organic pollutants from soil, J. Environ. Sci. Heal. - Part A Toxic/Hazardous Subst. Environ. Eng. (2009). https://doi.org/10.1080/10934520903005111.

[53] M. Arellano, M. Pazos, M.Á. Sanromán, Sulfate radicals-based technology as a promising strategy for wastewater, Water (Switzerland). (2019), https://doi.org/10.3390/w11081695.

[54] L. Ćurković, D. Ljubas, S. Šegota, I. Bačić, Photocatalytic degradation of Lissamine Green B dye by using nanostructured sol-gel TiO_2 films, J. Alloys Compd. (2014), https://doi.org/10.1016/j.jallcom.2014.03.148.

[55] E. Rosales, O. Iglesias, M. Pazos, M.A. Sanromán, Decolourisation of dyes under electro-Fenton process using Fe alginate gel beads, J. Hazard. Mater. (2012), https://doi.org/10.1016/j.jhazmat.2012.02.005.

Załącznik V

A(V)

Sylwester Łoński, Wojciech Łoński, Rafał Babilas, Krzysztof Barbusiński

Photocatalytic Decolourization of Rhodamine B by Modified Photo-Fenton Process with Quasicrystals – Preliminary Research

Architecture, Civil Engineering, Environment, Volume 16 (2023): ISSUE 2 (JUNE 2023)

Doi: 10.2478/acee-2023-0026 Impact Factor: **0,5** Punkty MNiSW: 70

ARCHITECTURE CIVIL ENGINEERING ENVIRONMENT
The Silesian University of Technology No. 2/2023

doi: 10.2478/ACEE-2023-0026

PHOTOCATALYTIC DECOLOURIZATION OF RHODAMINE B BY MODIFIED PHOTO-FENTON PROCESS WITH QUASICRYSTALS – PRELIMINARY RESEARCH

Sylwester ŁOŃSKI [a*], Wojciech ŁOŃSKI [b], Rafał BABILAS [c], Krzysztof BARBUSIŃSKI [d]

[a] MSc; Department of Water and Wastewater Engineering, PhD School, Silesian University of Technology, Konarskiego 18, 44-100 Gliwice, Poland
*Corresponding author. E-mail address: *Sylwester.Lonski@polsl.pl*

[b] MSc; Department of Engineering Materials and Biomaterials, Silesian University of Technology, Konarskiego 18a, 44-100 Gliwice, Poland

[c] Prof.; Department of Engineering Materials and Biomaterials, Silesian University of Technology, Konarskiego 18a, 44-100 Gliwice, Poland

[d] Prof.; Department of Water and Wastewater Engineering, Silesian University of Technology, Konarskiego 18, 44-100 Gliwice, Poland

Received: 15.05.2023; Revised: 26.05.2023; Accepted: 28.05.2023

Abstract

A novel photocatalytic process using a modification of photo-Fenton reaction, with sodium percarbonate (SP), as an alternative source of H_2O_2, and alloy $Al_{65}Cu_{20}Fe_{15}$ containing, among others, quasicrystals (of the percentage composition $Al_{65}Cu_{20}Fe_{15}$), being a source of iron ions, effectively decolourizes the aqueous solution of rhodamine B (RB; solution of 5 mg/l). The source of UV radiation was a lamp with a power of 36 W. The experiments were carried out at pH = 7 and reaction time (from 5 to 60 min). The increase in SP concentration (in the range of 8.3 to 33.3 g/l) significantly increased the degree of degradation of RB and the reaction rate. However, the use of quasicrystals, in the range of 8.3 to 33.3 g/l, was also important in the modified photocatalytic photo-Fenton process. The best degradation effects of RB (95%) were obtained for the highest SP concentration of 33.3 g/l and the lowest quasicrystal concentration of 8.3 g/l. On the other hand, visual decolourization of RB was obtained with an efficiency of 70% for SP and quasicrystal concentrations of 16.7 g/l and 16.7 g/l, respectively, after 45 minutes, and for SP and quasicrystal concentrations of 33.3 g/l and 8.3 g/l, respectively, after the time of 20 minutes. The best RB degradation effects in the comparative method (UV/$Na_2CO_3 \cdot 1.5H_2O_2$ without the addition of quasicrystals) were only 52.7%. The obtained results encourage further research to optimize the conditions of the proposed method and to investigate its applicability to other types of dyes and pollutants.

Keywords: **Advanced oxidation processes; Quasicrystals; Rhodamine B; Decolourization; Modified photo-Fenton.**

1. INTRODUCTION

Rhodamine B (RB) is a commonly used dye that can be found in various industries, including food[1, 2], textiles [3–6], and cosmetics [1, 7]. However, its presence in wastewater can have detrimental effects on aquatic ecosystems [8, 9]. Using photocatalytic reactions, particularly the photo-Fenton reaction, to remove RB from wastewater is both efficient and ecological. This process uses iron's photocatalytic abilities. In photo-Fenton reaction catalyst absorbs light energy and creates reactive oxygen species from hydrogen peroxide. The dye molecules are therefore oxidised by these reactive oxygen species into less dangerous compounds [10]. This makes it suitable for treating wastewater in various industries. The process

is efficient not only in the degradation of various dyes, but also other organic pollutants. Discovered in 1894 by H.J.H. Fenton, the reaction of H_2O_2 with iron ions [11], later named the Fenton reaction after him, became one of the most effective treatment processes for many types of industrial wastewater. Various modifications of the Fenton reaction have also been studied for a long time in order to intensify the effects of the degradation of many types of pollutants in wastewater. There are numerous variations of the Fenton reaction. Catalysing iron can be supplied in a variety of forms, including metallic [12–14], nanoparticle [15, 16], amorphous alloys [17], and high entropy alloys [18].

In the presented study the authors applied a new approach, the use of alloy $Al_{65}Cu_{20}Fe_{15}$ containing quasicrystals I-AlCuFe as a catalyst in the photo-Fenton reaction applied to degradation rhodamine B from aqueous solution. Quasicrystals are a type of material with unique atomic structures important in various applications, including catalysis. The atomic composition of $Al_{65}Cu_{20}Fe_{15}$ was chosen for its stability and durability in harsh environments [19], making it applicable for industrial wastewater treatment.

Further modifications of the classic Fenton reaction are the methods of supplying the oxidant and the method of supplying the possible light. Hydrogen peroxide [15, 16] and sodium percarbonate [18, 20, 21] are just two examples of the numerous oxidants that can be used to carry out the reaction. Light, of which there are many different kinds, from UV light [15, 16, 18, 21] to sunlight [22], may catalyse the process even further. In these studies, it was decided to use sodium percarbonate $Na_2CO_3 \cdot 1.5H_2O_2$ (SP) as the alternative source of H_2O_2 in the Fenton reaction and UV light to catalyse this process. The purpose of the work was to verify the viability of effectively using quasicrystals in the modification of the photo-Fenton reaction with SP, as an alternative source of H_2O_2.

2. EXPERIMENTAL

2.1. Materials

The material for the tests was the $Al_{65}Cu_{20}Fe_{15}$ alloy produced by casting the liquid alloy into a copper mould cooled with water. This method of producing the material results in the formation of many different intermetallic phases in the alloy, such as Cu_3Al, Al_2Cu, $Al_{13}Fe_4$, Al_7Cu_2Fe, AlFe, Al_2Fe and the quasicrystal line icosahedral phase of I-AlCuFe. The phase composition of the material produced by this technique is confirmed by X-ray diffraction studies. In addition, the presence of a quasicrystal line icosahedral phase was confirmed by electron diffraction [23, 24]. This phase composition of the alloy causes significant differences in relation to classic aluminium-based alloys. First of all, the very high hardness and brittleness of these alloys are noticeable. The most interesting part of the steppes is the occurrence of the quasi-crystalline phase. Quasicrystals are a relatively new form of crystal. Discovered by Dan Shechtman in 1984, for which he was awarded the Nobel Prize in 2011. Quasicrystals are an ordered structure, but not periodic. A quasicrystal line pattern can continuously fill all available space, but it shows lack of translational symmetry. While the crystals, according to the classical crystallographic restriction theorem, can only possess two-, three-, four-, and six-fold rotational symmetry, the Bragg diffraction pattern for quasicrystals shows sharp peaks with the other orders of symmetry—for example, five-fold. Along with the unusual spatial arrangement of atoms in quasicrystals, there are numerous differences between quasicrystals and traditional crystalline phases. This phase, however, has many unique properties, such as: low electrical and thermal conductivity, high oxidation resistance, low coefficient of friction, high abrasion resistance, high tensile strength and brittleness at room temperature. These unique properties mean that quasicrystals can be used as anti-adhesive materials, protective coatings or composite reinforcements [24–27].

2.2. Photocatalytic experiment

The studies were aimed at determining the effect of the concentration of quasicrystals and SP on the decolourization efficiency of the RB solution. For this purpose, different amounts of quasicrystals and doses of SP were introduced into the reactor (Fig. 1) containing 60 ml of an aqueous solution of RB at a concentration of 5 mg/l, irradiated with UV light with 4 bulbs (36 W in total; λ= 365 nm) additionally foil reflecting UV light into the solution was placed behind the lamps. The reaction solution was constantly stirred (at 400 RPM). Although the concentration of RB was low, the colour of the solution was intense pink. In addition, the results of studies using similar concentrations of this dye can be found in the literature [28, 29].

Samples for measuring dye concentration were collected at 0, 5, 10, 15, 20, 30, 45, and 60 minutes. The dye concentration was measured by spectrophotometry using a Shimadzu UV-1800 spectrophotometer.

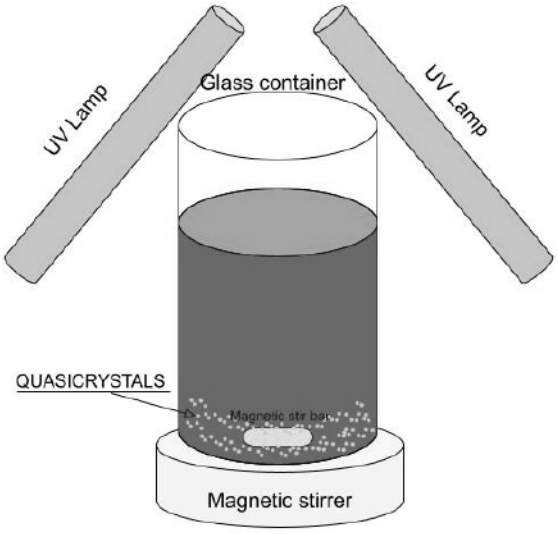

Figure 1.
Schematic diagram of lab-scale reactor

The initial pH = 7 has not been modified, because the addition of SP no effect on its value [18]. Due to the lack of publications on the degradation of dyes using quasicrystals, the authors used the experience gained while working with high entropy alloys [18] regarding the adoption of the concentration of SP and quasicrystals (8.3; 16.7; 33.3 g/l and 8.3; 16.7; 33.3 g/l, respectively). The UV/Na_2CO_3·1.5H_2O_2 process without the addition of quasicrystals was used as a comparative reaction.

3. RESULTS AND DISCUSSION

3.1. Effect of quasicrystals dose

Figures 2 and 3 show the average values (from two experiments) of the decolourization efficiency for different concentrations of the tested quasicrystals and SP, respectively. The difference in the obtained decolourization efficiency values did not exceed 5%. To ascertain the impact of the catalyst on decolourization efficiency, the following quasicrystals concentrations were used: 8.3, 16.7 and 33.3 g/l, at a constant SP concentration of 16.7 g/l (Fig. 2). After 60 minutes of the process, the decolourization efficiency was 84.2%, 78.4% and 84% for quasicrystal doses of 8.3, 16.7 and 33.3 g/l, respectively. At that time, the comparative method had a decolourization degree of 52.7%. For all the used reaction times and doses of quasicrystals, no significant differences in decolourization efficiency were observed. Therefore, for further tests to determine the effect of SP on the decolourization efficiency, the smallest quasicrystal dose of 8.3 g/l was selected.

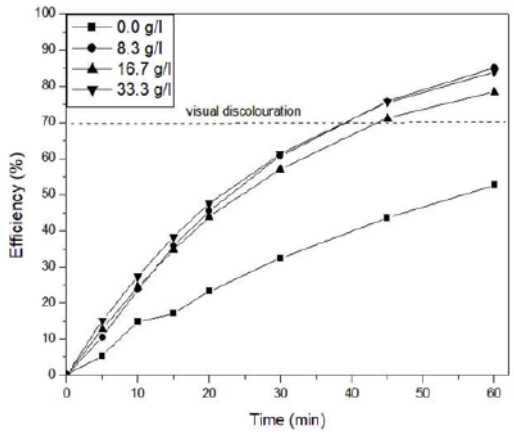

Figure 2.
Influence of catalyst dose on decolourization efficiency (16.7 g/l sodium percarbonate)

3.2. Effect of sodium percarbonate dose

In the next part of the research a series of tests using various SP concentrations (8.3, 16.7 and 33.3 g/l), at a constant quasicrystal dose of 8.3 g/l (Fig. 3), were conducted to examine the effect of the alternative source of hydrogen peroxide in the photo-Fenton process on decolourization degree. After 60 minutes of the process, the decolourization efficiency was 63.3%, 85.1% and 93.6% for SP doses of 8.3, 16.7 and 33.3 g/l, respectively. Practically throughout the entire test, the efficiency of dye degradation for individual doses of SP clearly differed, which proves the significant impact of SP doses on the effects of RB degradation. The greatest increase in the effects of RB degradation was observed during the first 30 minutes of the process.

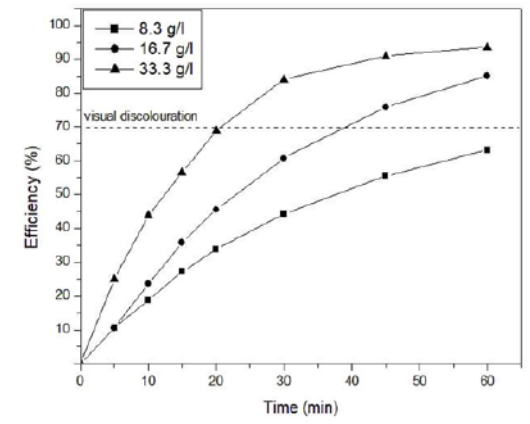

Figure 3.
Influence of sodium percarbonate dose on decolourization efficiency (8.3 g/l quasicrystals)

Table 1.
Reaction rate constant

Quasicrystals concentration 8.3 g/l				Sodium percarbonate concentration 16.7 g/l				
SP concentration (g/l)	8.3	16.7	33.3	Quasicrystals concentration (g/l)	0.0	8.3	16.7	33.3
Reaction order	I	I	I	Reaction order	I	I	I	I
Reaction rate constant	0.017	0.032	0.048	Reaction rate constant	0.012	0.032	0.026	0.031
Unit	s^{-1}	s^{-1}	s^{-1}	Unit	s^{-1}	s^{-1}	s^{-1}	s^{-1}

Even at the lowest doses of catalyst used in the experiments (8.3 g/l), it has an impact on the reaction. The concentration of the oxidant significantly increases the rate of decolourization of the dye relative to the comparative method. The addition of the catalyst affects the rate of degradation very similarly regardless of the dose of the added catalyst Fig. 2. The highest rate of decolourization was observed at the highest concentration of oxidant (33.3 g/l). The decolourization process accelerates with an increase in the dose of the oxidant. However, the difference in decolourization between the highest and the second highest concentration (16.7 g/l) is 10 percentage points (see Fig. 2), which is not significant, taking into account the double dose of the oxidant. The results suggest that the use of a catalyst is essential to achieve a fast and efficient decolourisation of the dye.

3.3. Reaction kinetics

Table 1 shows the values of the reaction rate constants for both types of tests. Reaction order and reaction rate constants were estimated from a linear fit of the data matching to characteristic functions for reaction order. For the 0 order reaction C_0-C_t; 1st order $Ln(\frac{c_0}{c_t})$; 2nd order $\frac{1}{c_t}-\frac{1}{c_0}$ [30]. For a constant concentration of quasicrystals (8.3 g/l), a two-fold increase in the concentration of SP from 8.3 to 16.7 g/l caused also an approximately two-fold increase in the value of the reaction rate constant from 0.017 to 0.032 s^{-1}. Another two-fold increase in SP concentration (from 16.7 to 33.3 g/l) resulted in only one and a half times increase in the value of the reaction rate constant (from 0.032 to 0.048 s^{-1}). Generally, the increase in SP concentration significantly increased the degree of degradation of RB (Fig. 2 and 3) and the reaction rate. In the case of tests using a constant concentration of SP (16.7 g/l), similar relationships were not observed. The values of the reaction rate constants when increasing the concentration of quasicrystals from 8.3 to 33.3 g/l did not show an upward trend, remaining at almost the same level. This is also confirmed by the results presented in Fig. 2, which show that the degradation efficiencies of RB for individual quasicrystal concentrations differed to a small extent. On this basis, it can also be concluded that in the presented studies the concentration of SP had a greater impact on the rate and efficiency of dye degradation compared to the concentration of quasicrystals.

4. SUMMARY

The results of the presented studies clearly show that a new photocatalytic process using a modification of the photo-Fenton reaction, with SP as an alternative source of H_2O_2 and quasicrystals as a source of iron ions, effectively decolourizes the aqueous solution of RB. The increase in SP concentration significantly increased the degree of degradation of RB and the reaction rate. However, the use of quasicrystals was also important in the photocatalytic photo-Fenton process. The best degradation effects of RB (95%) were obtained for the highest SP concentration of 33.3 g/l and the lowest quasicrystal concentration of 8.3 g/l. On the other hand, visual decolourization of the aqueous solution of RB was obtained with an efficiency of 70% for SP and quasicrystal concentrations of 16.7 g/l and 16.7 g/l, respectively, after 45 minutes, and for SP and quasicrystal concentrations of 33.3 g/l and 8.3 g/l, respectively, after the time of 20 minutes. The obtained results encourage further research to optimize the conditions of the proposed method and to investigate its application to the other types of dyes and pollutants.

In general, the doses of quasicrystals and SP used were very high in relation to the concentration of RB. It should be noted, however, that these were preliminary studies, mainly aimed at confirming the assumption that it is possible to use quasicrystals for photocatalytic decolourization of dyes in the modified photo-Fenton process. Therefore, in future experiments, a higher power medium pressure lamp (150 W) will be used to intensify the decolourization efficiency at lower doses of SP. However, the use of quasicrystals in excess will be continued to confirm that this catalyst can be used many times to decolorize successive portions of the dye solution. Due to

the fact that quasicrystals consist of metals, after a decrease in efficiency, it is possible to remelt them to obtain a new catalyst. It is also assumed that tests will be carried out at a higher concentration of RB solution of 100 mg/l. Moreover, the effectiveness of the tested process should also be compared with the effects obtained in the classical UV-Fenton process ($UV/H_2O_2 + Fe^{2+}$).

REFERENCE

[1] M. Soylak, Y.E. Unsal, E. Yilmaz, M. Tuzen, (2011). Determination of rhodamine B in soft drink, waste water and lipstick samples after solid phase extraction. *Food and Chemical Toxicology*, 4, 1796–1799. https://doi.org/10.1016/J.FCT.2011.04.030.

[2] M. Alesso, G. Bondioli, M.C. Talío, M.O. Luconi, L.P. Fernández, (2012). Micelles mediated separation fluorimetric methodology for Rhodamine B determination in condiments, snacks and candies. *Food Chem*. 134, 513–517. https://doi.org/10.1016/J.FOODCHEM.2012.02.110.

[3] A.K. Al-Buriahi, A.A. Al-Gheethi, P. Senthil Kumar, R.M.S. Radin Mohamed, H. Yusof, A.F. Alshalif, N.A. Khalifa, (2022). Elimination of rhodamine B from textile wastewater using nanoparticle photocatalysts: A review for sustainable approaches. *Chemosphere*, 287, 132162. https://doi.org/10.1016/J.CHEMOSPHERE.2021.132162.

[4] A.A. Al-Gheethi, Q.M. Azhar, P. Senthil Kumar, A.A. Yusuf, A.K. Al-Buriahi, R.M.S. Radin Mohamed, M.M. Al-shaibani, (2022). Sustainable approaches for removing Rhodamine B dye using agricultural waste adsorbents: *A review, Chemosphere*. 287, 132080. https://doi.org/10.1016/J.CHEMOSPHERE.2021.132080.

[5] H. Lee, S.H. Park, Y.K. Park, B.H. Kim, S.J. Kim, S.C. Jung, (2013). Rapid destruction of the rhodamine B using TiO_2 photocatalyst in the liquid phase plasma. *Chem Cent J*., 7. https://doi.org/10.1186/1752-153X-7-156.

[6] M.A. Hossain, M.S. Alam, (2012). Adsorption kinetics of Rhodamine-B on used black tea leaves. *Iranian J Environ Health Sci Eng*, 9, 1–7. https://doi.org/10.1186/1735-2746-9-2/TABLES/1.

[7] S. Arris, I. Brahmia, L. Bousbaa, (2012). Experimental Study of Removal of Rhodamine B by an Activated Cereal by Product. *Energy Procedia*, 18 1208–1219. https://doi.org/10.1016/J.EGYPRO.2012.05.136.

[8] P.M. Rowiński, M.M. Chrzanowski, (2011). Influence of selected fluorescent dyes on small aquatic organisms. *Acta Geophysica*, 59, 91–109. https://doi.org/10.2478/S11600-010-0024-7/METRICS.

[9] F.H. AlHamedi, M.A. Rauf, S.S. Ashraf, (2009). Degradation studies of Rhodamine B in the presence of UV/H_2O_2. *Desalination*, 239, 159–166. https://doi.org/10.1016/J.DESAL.2008.03.016.

[10] G. Ruppert, R. Bauer, G. Heisler, (1993). The photo-Fenton reaction — an effective photochemical wastewater treatment process. *J Photochem Photobiol A Chem*, 73, 75–78. https://doi.org/10.1016/1010-6030(93)80035-8.

[11] H.J.H. Fenton, (1894). LXXIII. – Oxidation of tartaric acid in presence of iron. *Journal of the Chemical Society, Transactions*, 65, 899–910. https://doi.org/10.1039/CT8946500899.

[12] L.G. Devi, M. Srinivas, M.L. ArunaKumari, (2016) Heterogeneous advanced photo- Fenton process using peroxymonosulfate and peroxydisulfate in presence of zero valent metallic iron: A comparative study with hydrogen peroxide photo-Fenton process. *Journal of Water Process Engineering*, 13, 117–126. https://doi.org/10.1016/J.JWPE.2016.08.004.

[13] K. Barbusiński, J. Majewski, (2003). Discoloration of Azo Dye Acid Red 18 by Fenton Reagent in the Presence of Iron Powder. *Pol J Environ Stud.* 12, 151–155. http://www.pjoes.com/Discoloration-of-Azo-Dye-Acid-Red-18-by-Fenton-r-nReagent-in-the-Presence-of-Iron,87538,0,2.html (accessed May 7, 2023).

[14] K. Barbusiński, (2005), The modified Fenton process for decolorization of dye wastewater. *Pol J Environ Stud.,* 14, 281–285.

[15] A. Radoń, S. Łoński, T. Warski, R. Babilas, T. Tański, M. Dudziak, D. Łukowiec, (2019). Catalytic activity of non-spherical shaped magnetite nanoparticles in degradation of Sudan I, Rhodamine B and Methylene Blue dyes. *Appl Surf Sci.*, 487, 1018–1025. https://doi.org/10.1016/J.APSUSC.2019.05.091.

[16] A. Radoń, S. Łoński, M. Kądziołka-Gaweł, P. Gębara, M. Lis, D. Łukowiec, R. Babilas, (2020). Influence of magnetite nanoparticles surface dissolution, stabilization and functionalization by malonic acid on the catalytic activity, magnetic and electrical properties. *Colloids Surf A Physicochem Eng Asp*, 607, 125446. https://doi.org/10.1016/J.COLSURFA.2020.125446.

[17] Z. Jia, J. Kang, W.C. Zhang, W.M. Wang, C. Yang, H. Sun, D. Habibi, L.C. Zhang, (2017). Surface ageing behaviour of Fe-based amorphous alloys as catalysts during heterogeneous photo Fenton-like process for water treatment. *Appl Catal B*. 204, 537–547. https://doi.org/10.1016/J.APCATB.2016.12.001.

[18] W. Łoński, M. Spilka, M. Kądziołka-Gaweł, P. Gębara, A. Radoń, T. Warski, S. Łoński, K. Barbusiński, K. Młynarek-Żak, R. Babilas, (2023) . Microstructure, magnetic properties, corrosion resistance and catalytic activity of dual-phase AlCoNiFeTi and AlCoNiFeTiSi high entropy alloys. *J Alloys Compd,* 934, 167827. https://doi.org/10.1016/J.JALLCOM.2022.167827.

[19] V.N. Balbyshev, D.J. King, A.N. Khramov, L.S. Kasten, M.S. Donley, (2004). Investigation of quaternary Al-based quasicrystal thin films for corrosion protection. *Thin Solid Films*, 447–448, 558–563. https://doi.org/10.1016/J.TSF.2003.07.026.

[20] Sodium percarbonate as an agent for effective treatment of industrial wastewater, (n.d.). https://www.researchgate.net/publication/291155615_Sodium_percarbonate_as_an_agent_for_effective_treatment_of_industrial_wastewater (accessed May 7, 2023).

[21] B. Pieczykolan, I. Płonka, K. Barbusiński, (2016). Discoloration of dye wastewater by modified UV-Fenton process with sodium percarbonate, *Architecture, Civil Engineering, Environment, 9*(4). https://doi.org/10.21307/acee-2016-060.

[22] R. Bauer, H. Fallmann, (1997). The Photo-Fenton oxidation – A cheap and efficient wastewater treatment method. *Research on Chemical Intermediates*, 23, 341–354. https://doi.org/10.1163/156856797X00565/METRIC.

[23] R. Babilas, A. Bajorek, M. Spilka, A. Radoń, W. Łoński, (2020). Structure and corrosion resistance of Al–Cu–Fe alloys. *Progress in Natural Science: Materials International*, 30, 393–401. https://doi.org/10.1016/J.PNSC.2020.06.002.

[24] D. V. Louzguine-Luzgin, A. Inoue, (2008). Formation and properties of quasicrystals. *Annu Rev Mater Res, 38,* 403–423. https://doi.org/10.1146/ANNUREV.MATSCI.38.060407.130318.

[25] L. Lityńska-Dobrzyńska, M. Mitka, A. Góral, K. Stan-Głowińska, J. Dutkiewicz, (2016). Microstructure and mechanical properties of aluminium matrix composites reinforced by Al62Cu25.5Fe12.5 melt spun ribbon. *Mater Charact*, 117, 127–133. https://doi.org/10.1016/J.MATCHAR.2016.04.025.

[26] K. Młynarek-Żak, W. Pakieła, D. Łukowiec, A. Bajorek, P. Gębara, A. Szakál, I. Dhiman, R. Babilas, (2022). Structure and selected properties of Al–Cr–Fe alloys with the presence of structurally complex alloy phases. *Scientific Reports, 12*, 1–12. https://doi.org/10.1038/s41598-022-17870-0.

[27] R. Babilas, K. Młynarek, W. Łoński, D. Łukowiec, M. Kadziołka-Gaweł, T. Czeppe, L. Temleitner, (2020). Structural Characterization of $Al_{65}Cu_{20}Fe_{15}$ Melt-Spun Alloy by X-ray, Neutron Diffraction, High-Resolution Electron Microscopy and Mössbauer Spectroscopy. *Materials* 14, 54. https://doi.org/10.3390/MA14010054.

[28] Q. Wang, Y. Yang, S. Ma, J. Wu, T. Yao, (2020). Preparation of Fe_3O_4@Prussian blue core/shell composites for enhanced photo-Fenton degradation of rhodamine B. *Colloids Surf A Physicochem Eng Asp*, 606, 125416. https://doi.org/10.1016/J.COLSURFA.2020.125416.

[29] J. Zhang, M. Yan, G. Sun, X. Li, B. Hao, K. Liu, (2022). Mg–Fe–Al–O spinel: Preparation and application as a heterogeneous photo-Fenton catalyst for degrading Rhodamine B. *Chemosphere*, 304, 135318. https://doi.org/10.1016/J.CHEMOSPHERE.2022.135318.

[30] F. Chen, S. Xie, X. Huang, X. Qiu, (2017). Ionothermal synthesis of Fe_3O_4 magnetic nanoparticles as efficient heterogeneous Fenton-like catalysts for degradation of organic pollutants with H_2O_2. *J Hazard Mater*, 322, 152–162. https://doi.org/10.1016/J.JHAZMAT.2016.02.073.